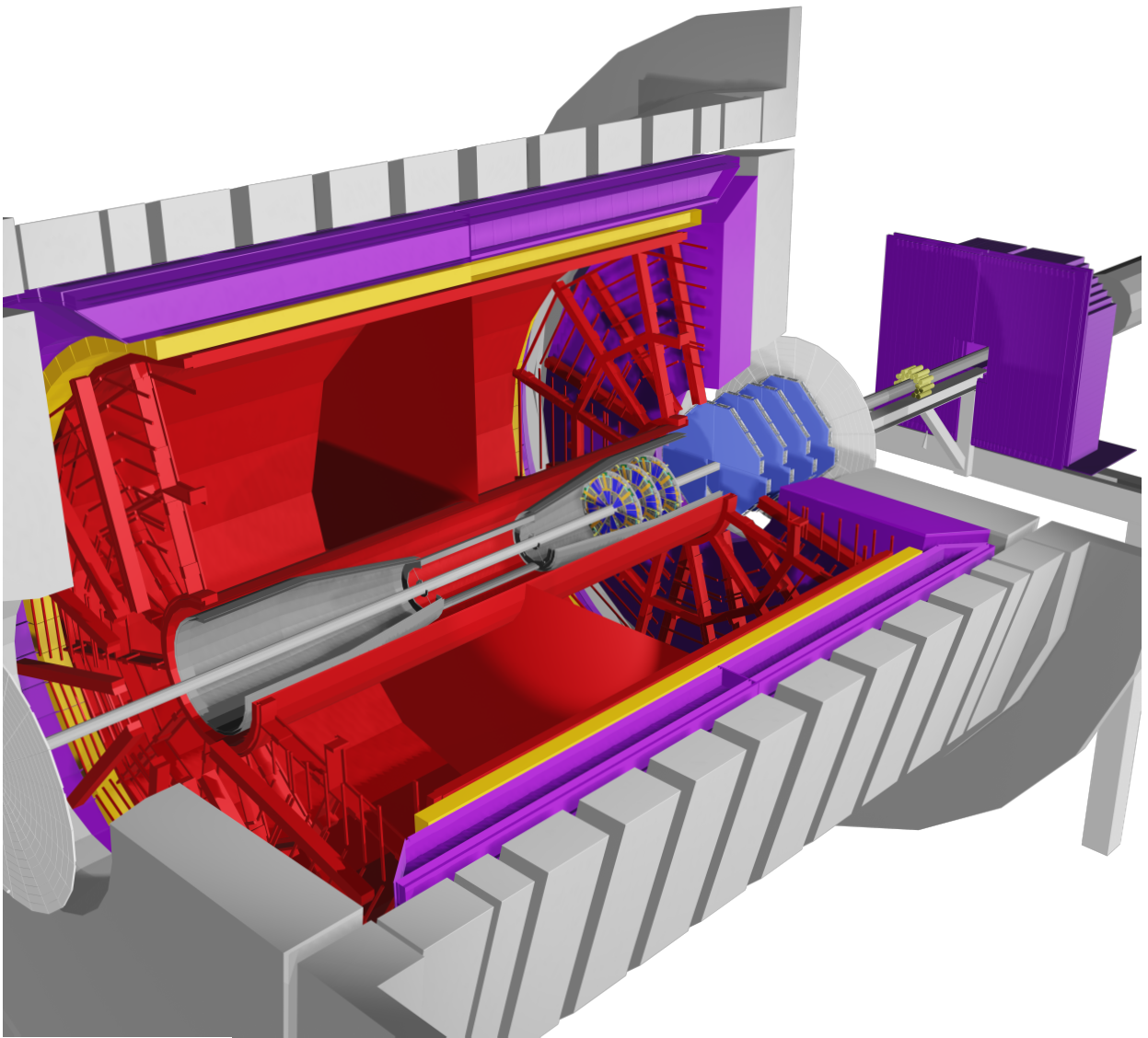


# The STAR Beam Use Request for Run-21, Run-22 and data taking in 2023-25

The STAR Collaboration



# 1 Executive Summary

2 This Beam Use Request outlines the physics programs that compels the STAR collaboration  
3 to request data taking during the years 2021-2025.

4 STAR's **highest scientific priorities** for Run-21 and Run-22 are to complete the NSAC-  
5 endorsed second phase of the Beam Energy Scan (BES-II) program, and initiate the "must-  
6 do" Cold QCD forward physics program enabled by the newly completed suite of forward  
7 detectors via the collection of transversely polarized  $p+p$  data at 510 GeV. From 2023-25 we  
8 will use a combination of soft and hard probes to explore the microstructure of the QGP  
9 and continue the forward physics program via the collection of high statistics Au+Au,  $p+Au$   
10 and  $p+p$  data at  $\sqrt{s_{NN}} = 200$  GeV.

11 The BES-II program has so far been very successful. As shown in Table 1, we have  
12 recorded collisions at  $\sqrt{s_{NN}} = 9.2-27$  GeV in collider mode, and  $\sqrt{s_{NN}} = 3-7.7$  GeV in fixed  
13 target (FXT) mode. We expect to complete data collection at  $\sqrt{s_{NN}} = 9.2$  GeV by the end  
14 of Run-20b. In Run-21, as shown in Table 2, our number one priority is to complete the  
15 BES-II by recording 100 M good events at  $\sqrt{s_{NN}} = 7.7$  GeV.

**Table 1:** Summary of all BES-II and FXT Au+Au beam energies, equivalent chemical potential, event statistics, run times, and date collected.

Beam Energy (GeV/nucleon)	$\sqrt{s_{NN}}$ (GeV)	$\mu_B$ (MeV)	Run Time	Number Events Requested (Recorded)	Date Collected
13.5	27	156	24 days	(560 M)	Run-18
9.8	19.6	206	36 days	400 M (582 M)	Run-19
7.3	14.6	262	60 days	300 M (324 M)	Run-19
5.75	11.5	316	54 days	230 M (235 M)	Run-20
4.59	9.2	373	102 days	160 M (162 M) <sup>1</sup>	Run-20+20b
31.2	7.7 (FXT)	420	0.5+1.1 days	100 M (50 M+112 M)	Run-19+20
19.5	6.2 (FXT)	487	1.4 days	100 M (118 M)	Run-20
13.5	5.2 (FXT)	541	1.0 day	100 M (103 M)	Run-20
9.8	4.5 (FXT)	589	0.9 days	100 M (108 M)	Run-20
7.3	3.9 (FXT)	633	1.1 days	100 M (117 M)	Run-20
5.75	3.5 (FXT)	666	0.9 days	100 M (116 M)	Run-20
4.59	3.2 (FXT)	699	2.0 days	100 M (200 M)	Run-19
3.85	3.0 (FXT)	721	4.6 days	100 M (259 M)	Run-18
3.85	7.7	420	11-20 weeks	100 M	Run-21 <sup>2</sup>

<sup>1</sup> Run-20b data taking completed 7:30am Sept 1.

<sup>2</sup> Data not yet collected, Run-21 forms part of this year's BUR.

16 Based on guidance from the Collider-Accelerator Department (CAD) and past experience  
17 we expect that the bulk of Run-21 will be devoted to Au+Au collisions at  $\sqrt{s_{NN}} = 7.7$  GeV,

**Table 2: Proposed Run-21** assuming 24-28 cryo-weeks, including an initial one week of cool-down, one week for CeC, a one week set-up time for each collider energy and 0.5 days for each FXT energy.

Single-Beam Energy (GeV/nucleon)	$\sqrt{s_{NN}}$ (GeV)	Run Time	Species	Events (MinBias)	Priority
3.85	7.7	11-20 weeks	Au+Au	100 M	1
3.85	3 (FXT)	3 days	Au+Au	300 M	2
44.5	9.2 (FXT)	0.5 days	Au+Au	50 M	2
70	11.5 (FXT)	0.5 days	Au+Au	50 M	2
100	13.7 (FXT)	0.5 days	Au+Au	50 M	2
100	200	1 week	O+O	400 M 200 M (central)	3
8.35	17.1	2.5 weeks	Au+Au	250 M	3
3.85	3 (FXT)	3 weeks	Au+Au	2 B	3

18 the lowest collider energy of the program. Collection of these events is our highest priority.  
 19 However, if we assume optimistic, but not overly so, rates and up-times, and 28 cryo-weeks,  
 20 we project that the opportunity to collect of other exciting datasets will arise.

21 The *second highest priority* for Run-21 identified by the STAR collaboration is four short  
 22 FXT runs; the collection of 300 M good events at  $\sqrt{s_{NN}} = 3$  GeV and 50 M good events  
 23 at each of three higher beam energies ( $\sqrt{s_{NN}} = 9.2, 11.5, \text{ and } 13.7$  GeV). In the second  
 24 highest priority block shown in Table 2, the 3 GeV FXT system is listed first for reasons  
 25 of logistics. It is recognized that the opportunity to address the topics listed as second and  
 26 third priorities will be contingent on the performance of the 7.7 GeV collider run. Should  
 27 it become evident early on in that run (in the first 4-8 weeks or so), that performance is  
 28 exceeding the conservative projections and that time will be available at the end of Run-21,  
 29 then it would be beneficial to take three days to complete the 3 GeV FXT run. This system  
 30 uses the same single beam energy (3.85 GeV) as the 7.7 GeV collider program, so there would  
 31 be no time lost transitioning, and acquiring these data early in the run would give sufficient  
 32 time to analyze the results of the ExpressStream production to investigate the acceptance  
 33 and background for the search of the double- $\Lambda$  hypernucleus and determine the statistics  
 34 necessary to pursue this physics topic (currently estimated to be three weeks). 300 M events  
 35 at 3 GeV with the enhanced iTPC and eTOF coverage gives access to the proton higher  
 36 moments, precision  $\phi$ , hypernuclei, and dilepton measurements. The higher  $\sqrt{s_{NN}}$  FXT data  
 37 combined with the collider data at the same energy will provide full proton rapidity coverage  
 38 allowing us to probe in detail the mechanisms of stopping at play in heavy-ion collisions. We  
 39 estimate the total run time required to collect all these datasets is 6 days.

40 The STAR collaboration also finds important scientific opportunities are presented by  
 41 the collection of our *third highest priority* datasets:

- 42 • O+O data at  $\sqrt{s_{\text{NN}}} = 200$  GeV, in the context of understanding the early-time condi-  
43 tions of small systems. These data would allow for a direct comparison with a similarly  
44 proposed higher-energy O+O run at the LHC, and further motivate the case for a small  
45 system scan complementary to ongoing efforts by the NA61/SHINE collaboration at  
46 SPS energies, and other proposed light-ion species at the LHC.
- 47 • A sixth collider beam energy at  $\sqrt{s_{\text{NN}}} = 17.1$  GeV. These data will provide for a finer  
48 scan in a range where the energy dependence of the net-proton kurtosis and neutron  
49 density fluctuations appear to undergo a sudden change.
- 50 • 2 B good events at  $\sqrt{s_{\text{NN}}} = 3$  GeV in FXT mode. The enhanced statistics enables  
51 the measurements of mid-rapidity proton 5-th/6-th order moments/cumulants and the  
52 system size dependence of  $\phi$  meson production. Furthermore, the large dataset has the  
53 potential to make the first measurement of (or put limits on) the production rate of  
54 the double- $\Lambda$  hypernuclei.

55 The sequence with which we collect these datasets is currently somewhat fluid and are  
56 listed in the order of the requested run time; we do not want to take partial datasets. We  
57 expect to refine the ordering of our goals as Run-21 progresses. Collection of these data  
58 during future RHIC running periods is also of interest to the collaboration.

59 For Run-22, as shown in Table 3, we propose **a dedicated 20 cryo-week transversely**  
60 **polarized  $p+p$  run at  $\sqrt{s} = 510$  GeV.** This run will take full advantage of STAR's new  
61 forward detection capabilities, consisting of a Forward Calorimeter System (FCS) and a  
62 Forward Tracking System (FTS) located between  $2.5 < \eta < 4$ , and further capitalizes on the  
63 recent BES-II detector upgrades.

64 These data will enable STAR to explore, with unprecedented precision, forward jet  
65 physics that probe both the high-x (largely valence quark) and low-x (primarily gluon)  
66 partonic regimes.

**Table 3: Proposed Run-22** assuming 20 cryo-weeks, including an initial one week of cool-down and a two weeks set-up time.

$\sqrt{s}$ (GeV)	Species	Polarization	Run Time	Sampled Luminosity	Priority
510	$p+p$	Transverse	16 weeks	$400 \text{ pb}^{-1}$	1

67 Looking further out, the STAR collaboration has determined that there is a compelling  
68 scientific program enabled by the first opportunity to capitalize on the combination of the  
69 BES-II and Forward Upgrades in the data collected from Au+Au,  $p$ +Au, and  $p+p$  collisions  
70 at  $\sqrt{s_{\text{NN}}} = 200$  GeV as outlined in Table 4.

71 Significantly increased luminosities, the extended acceptance at mid-rapidity due to the  
72 iTPC, improved event plane and triggering capabilities of the EPD, and the ability to probe

73 the previously inaccessible forward region are all exploited in our Hot QCD program, that  
 74 informs on the microstructure of the QGP, and our Cold QCD program that will utilize  
 75 transverse polarization setting the stage for related future measurements at the EIC.

**Table 4: Proposed Run-23 - Run-25** assuming 24 (28) cryo-weeks of running every year, and 6 weeks set-up time to switch species in 2024. Sampled luminosities assume a "take all" triggers.

$\sqrt{s_{NN}}$ (GeV)	Species	Number Events/ Sampled Luminosity	Date
200	Au+Au	10B / 38 nb <sup>-1</sup>	2023
200	<i>p+p</i>	235 pb <sup>-1</sup>	2024
200	<i>p+Au</i>	1.3 pb <sup>-1</sup>	2024
200	Au+Au	10B / 52 nb <sup>-1</sup>	2025

# 76 Contents

77	<b>1 Highlights from the STAR Program</b>	<b>1</b>
78	1.1 Highlights from the Heavy Ion Program . . . . .	1
79	1.1.1 Heavy-Ion Jet Measurements . . . . .	1
80	1.1.2 Bulk Correlations . . . . .	5
81	1.1.3 Light Flavor Spectra and Ultra-peripheral Collisions . . . . .	12
82	1.1.4 Heavy-Flavor . . . . .	16
83	1.2 CME Search and Isobar Run . . . . .	22
84	1.2.1 Introduction . . . . .	22
85	1.2.2 Modality of Isobar Running at RHIC . . . . .	22
86	1.2.3 Blinding of Data Sets and Preparation for Analyses . . . . .	23
87	1.2.4 Methods for the Isobar Blind Analyses . . . . .	24
88	1.2.5 Observables for Isobar Blind Analyses . . . . .	25
89	1.2.6 Prospect of CME Search Beyond the Isobar-era . . . . .	28
90	1.3 Highlights from the Spin and Cold QCD Program . . . . .	31
91	1.3.1 Introduction . . . . .	31
92	1.3.2 Longitudinal program . . . . .	31
93	1.3.3 Transverse program . . . . .	33
94	1.3.4 Unpolarized Results . . . . .	35
95	1.4 Run-20 Performance . . . . .	38
96	<b>2 Proposed Program - Hot QCD in Run-21, 23, and 25</b>	<b>42</b>
97	2.1 Beam Request for Run-21 . . . . .	42
98	2.1.1 Completion of the BES-II Program . . . . .	42
99	2.1.2 Au+Au Collisions in FXT Mode at $\sqrt{s_{NN}} = 3.0$ GeV - I: 300 million	
100	goal . . . . .	43
101	2.1.3 Au+Au Collisions in FXT Mode at $\sqrt{s_{NN}} = 9.2, 11.5,$ and $13.7$ GeV .	47
102	2.2 Further Opportunities in Run-21 . . . . .	48
103	2.2.1 Small System Run: O+O at $\sqrt{s_{NN}} = 200$ GeV . . . . .	49
104	2.2.2 Au+Au Collisions at $\sqrt{s_{NN}} = 17.1$ GeV . . . . .	57
105	2.2.3 Au+Au Collisions in FXT Mode at $\sqrt{s_{NN}} = 3.0$ GeV - II: 2 Billion Goal	61
106	2.3 Future Possibilities . . . . .	62
107	2.3.1 Exploring the Nuclear Equation-of-State (EoS) with Heavy Ion Collisions	62
108	2.4 Exploring the Microstructure of the QGP (Run-23 and Run-25 Au+Au) . .	64
109	2.4.1 Correlation Measurements Utilizing Extended Acceptance . . . . .	66
110	2.4.2 Correlation Measurements Utilizing the Enhanced Statistics . . . . .	71
111	2.4.3 Electromagnetic Probes . . . . .	73
112	2.4.4 Deconfinement and Thermalization With Charmonia Measurements .	77
113	2.4.5 Jet Probes . . . . .	80

114	<b>3</b>	<b>Cold QCD Physics with <math>p^\uparrow+p^\uparrow</math> and <math>p^\uparrow+A</math> Collisions at 510 and 200 GeV</b>	<b>86</b>
115	3.1	Run-22 Request for $p^\uparrow+p^\uparrow$ Collisions at 510 GeV . . . . .	87
116	3.1.1	Inclusive transverse spin asymmetries at forward rapidities . . . . .	87
117	3.1.2	Sivers and Efremov-Teryaev-Qiu-Sterman Function . . . . .	89
118	3.1.3	Transversity, Collins Function and Interference Fragmentation Function	91
119	3.1.4	Spatial Imaging of the Nucleon . . . . .	96
120	3.2	Run-24 Request for Polarized $p+p$ and $p+A$ Collisions at 200 GeV . . . . .	99
121	3.2.1	Spin Physics with Polarized $p+p$ and $p+Au$ Collisions at 200 GeV . .	99
122	3.2.2	Physics Opportunities with Unpolarized proton-Nucleus Collisions . .	104
123	<b>4</b>	<b>Detector Updates, Operations, and Opportunities</b>	<b>118</b>
124	4.1	Status and Performance of the eTOF . . . . .	118
125	4.2	Forward Upgrade . . . . .	119
126	4.2.1	Status . . . . .	120
127	4.2.2	Forward Calorimetry System . . . . .	120
128	4.2.3	Forward Silicon Tracking . . . . .	121
129	4.2.4	sTGC Tracking . . . . .	122
130	4.2.5	Software . . . . .	122

# 1 Highlights from the STAR Program

## 1.1 Highlights from the Heavy Ion Program

### 1.1.1 Heavy-Ion Jet Measurements

Jet quenching, the modification of parton showers due to interactions in the QGP, is manifest in several distinct ways: energy transport to large angles, observable via jet energy loss and large-angle energy recovery; multiple-soft and single-hard coherent scatterings off of plasma constituents, observable via jet deflection or acoplanarity; and the modification of jet substructure. This broad spectrum of phenomena provides unique and incisive probes of the microscopic structure of the QGP. It also provides a robust experimental program, in which different observables with different systematic sensitivity probe the same underlying physics, providing stronger constraints on theoretical models of jet quenching than single measurements. STAR has a comprehensive jet quenching program which covers the full spectrum of these phenomena, using hadrons, direct photons, and reconstructed jets as probes.

STAR has led the development of essential analysis techniques for the challenging task of measuring reconstructed jet observables in heavy-ion collisions at RHIC. These include a data-driven Mixed-Event technique to measure uncorrelated jet background for semi-inclusive observables [1], enabling unbiased jet measurements over a broad phase space in heavy-ion collisions, notably low jet  $p_T$  ( $\sim 10$  GeV/ $c$ ) and large jet resolution parameter ( $R \sim 0.5$ ); and sub-jet observables that are robust to the underlying event and yet sensitive to the jet splitting kinematics, applying them as a tool to access the resolution scale in jet-medium interactions [2].

Jet quenching measurements have traditionally utilized  $p+p$  collisions to provide an unmodified reference, and  $p+A$  collisions to measure initial state effects that may mask signals of quenching in the final state. More recently it has become evident that small systems themselves exhibit QGP-like flow signatures for event selection corresponding to high Event Activity (EA), and an urgent question in the field is whether evidence can likewise be found for jet quenching in such systems. The STAR jet quenching program therefore includes measurements in (unpolarized)  $p+p$  and  $p+Au$  collisions, as well as Au+Au collisions.

In this section we present recent highlights of the STAR jet quenching program. The STAR papers published in this area in the past year can be found in Refs. [3–7].

**Inclusive and semi-inclusive jet yield suppression:** Inclusive jet yield suppression is a hallmark of jet quenching in heavy-ion collisions. STAR has recently reported the first measurement at RHIC of inclusive charged-particle jet distributions in central and peripheral Au+Au collisions at  $\sqrt{s_{NN}} = 200$  GeV [7], together with measurements of their yield suppression,  $R_{AA}$  (normalized by the yield in  $p+p$  collisions calculated by PYTHIA tuned to other STAR data [8]) and  $R_{CP}$ . Figure 1 shows the extracted  $R_{CP}$  compared to a similar measurement by ALICE, and to charged-hadron  $R_{CP}$  measured at both colliders. A striking similarity is seen between the two inclusive jet measurements, and between the two

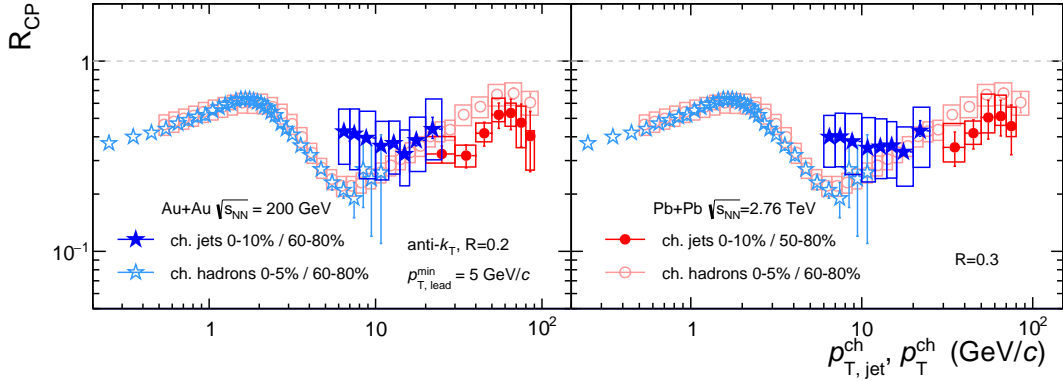


**Figure 1:** Measurement of  $R_{CP}$  as a function of  $p_{T,jet}^{ch}$  for charged-particle jets (anti- $k_T$ ,  $R = 0.2$  and  $0.3$ ) measured by STAR (blue points) [7], compared to charged-jet  $R_{CP}$  at the LHC and to inclusive hadron  $R_{CP}$  at RHIC and the LHC. Note the different centrality selections.

170 inclusive hadron measurements. The  $p_T$ -dependence of  $R_{CP}$  is stronger for hadrons in the  
 171 region of overlap. While there remain differences in centrality selection between the datasets,  
 172 this is the most direct comparison to date of reconstructed jet measurements at RHIC and  
 173 the LHC.

174 This paper also reported the ratio of jet yields in central and peripheral Au+Au collisions  
 175 for  $R = 0.2$  and  $0.4$ , which is a probe of jet shape and its in-medium modification. Consis-  
 176 tency to theoretical calculations is found within uncertainties. However, the calculations  
 177 exhibit significant spread in the jet shape ratio, presenting an opportunity for more precise  
 178 measurements to discriminate between them. A measurement of the inclusive jet yield in  
 179 Au+Au collisions including both charged and neutral particle constituents using the much  
 180 larger data set recorded in 2014, corresponding to  $9.9 \text{ nb}^{-1}$  [9] is underway. STAR also has  
 181 full jet measurements in  $p+p$  collisions for use for the  $R_{AA}$  normalization.

182 A recent STAR measurement, likewise using the  $9.9 \text{ nb}^{-1}$  2014 dataset, extends the semi-  
 183 inclusive measurement of charged jets (anti- $k_T$ ,  $R = 0.2$  and  $0.5$ ) recoiling from a high- $E_T$   
 184 photon trigger to photon triggers in the range  $15 < E_T^{trig} < 20 \text{ GeV}$  [10]. Currently, the  
 185 recoil jet yield suppression for 0–15% Au+Au collisions ( $I_{AA}$ ) is determined by comparison to  
 186 the yield in  $p+p$  collisions calculated using PYTHIA-6 (STAR tune [8]) and PYTHIA-8 [11].  
 187 Significant yield suppression in central Au+Au collisions is observed for  $R = 0.2$ , with less  
 188 suppression for  $R = 0.5$ . Theoretical calculations predict a stronger dependence of  $I_{AA}$  on  
 189  $p_{T,jet}^{ch}$  for  $R = 0.5$  than observed. A measurement of this observable in  $p+p$  collisions is in  
 190 progress, to provide a data reference rather than PYTHIA calculations for  $I_{AA}$ .

191 Jet yield suppression is an indirect measurement of energy loss, because it convolutes  
 192 out-of-cone energy loss with the shape of the jet spectrum – a fixed energy loss generates  
 193 greater suppression for a steeper spectrum. Since the jet spectrum shape depends strongly on  
 194 the choice of observable (inclusive, semi-inclusive) and collision energy, direct comparison of  
 195 different jet quenching measurements requires this effect to be taken into account. Figure 2

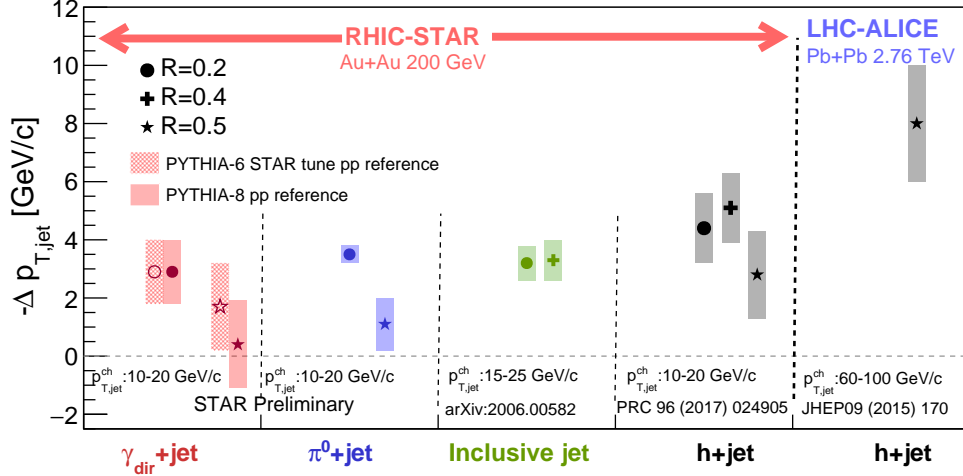


**Figure 2:** Out-of-cone jet energy loss derived from jet yield suppression measurements in A+A collisions (see text) for  $\gamma_{dir}+jet$ ,  $\pi^0+jet$ , inclusive jet, and h+jet measurements at RHIC, and h+jet measurements at the LHC [9, 10]. Note the different  $p_{T,jet}$  ranges.

196 shows the  $p_{T,jet}$  shift needed between jet spectra measured in a reference system ( $p+p$  or  
 197 peripheral A+A collisions) and in central A+A collisions, for several jet yield suppression  
 198 measurements at RHIC and the LHC [9, 10]. The absolute magnitude of medium-induced  
 199 jet energy loss is similar for several different observables at RHIC, and is smaller than the  
 200 LHC measurement. Note that the  $p_{T,jet}^{ch}$  range is significantly higher for the LHC h+jet  
 201 measurement, so that the *relative* energy loss is smaller than at RHIC.

202 This is a first look at comparing medium-induced out-of-cone radiation at RHIC and the  
 203 LHC. Clearly, as the measured  $p_{T,jet}$  range at RHIC moves up and that at the LHC moves  
 204 down in upcoming measurements, more precise comparisons can be made. Nevertheless,  
 205 Fig. 2 already provides significant constraints on jet quenching calculations that seek to  
 206 model RHIC and LHC measurements in a unified way.

207 **Jet-structure modifications:** The Fragmentation Function (FF), normalized per jet,  
 208 provides information of the longitudinal momentum fraction ( $z = p_{T,trk} \cos(\Delta r)/p_{T,jet}$ ) of  
 209 charged particles projected along the jet axis. While FF have been measured previously at  
 210 the LHC [12, 13], STAR has utilized the semi-inclusive approach to measure the FF of charged  
 211 jets for the first time at RHIC [14]. The Mixed-Event approach developed in [1] is extended  
 212 for the FF measurement, and utilized for the correction of uncorrelated jet contributions.  
 213 The fully corrected FF are shown in Fig. 3 for jets of varying  $p_{T,jet}^{ch}$  for mid-peripheral 40-60%  
 214 collisions compared to PYTHIA-8 predictions shown by the dashed curved. The FF shape in  
 215 data is reproduced by PYTHIA-8 in these peripheral collisions. Measurements are ongoing  
 216 to extend to central collisions where one expects a larger path length for the recoil jet and  
 217 enhanced medium effects.

218 Another observable of the jet transverse profile is the differential jet shape, measured in

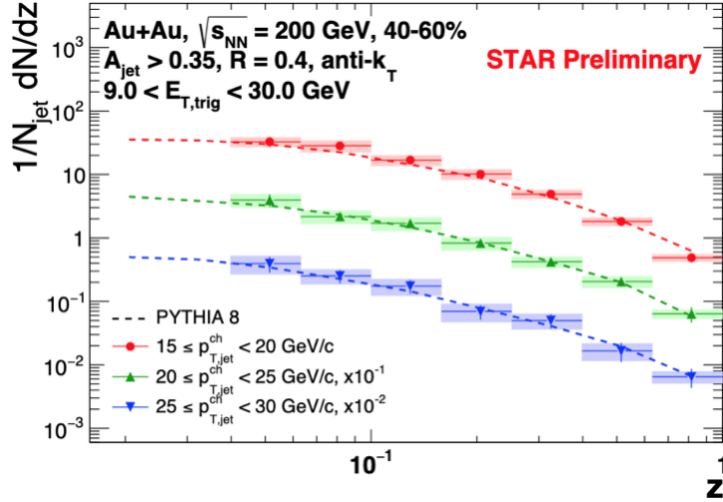


**Figure 3:** Fragmentation functions for recoil charged-particle jets of varying  $p_{\text{jet},T}^{\text{ch}}$  with trigger  $9.0 < E_T < 30.0$  GeV in 40–60% peripheral events compared to PYTHIA-8 simulations in the dashed curves.

219 radial annuli around the jet axis ( $\rho(\Delta r)$ ). Utilizing the hard-core jet selection [15] which  
 220 provides a pure sample of hard-scattered jets with a high constituent threshold, the fully  
 221 corrected  $\rho$  as a function of  $\Delta r$  (distance between the constituent tracks and the jet axis)  
 222 of leading jet with  $20 < p_{T,\text{jet}} < 40$  GeV/c for central (0–10%) and mid-central (20–50%)  
 223 events are calculated. To probe possible in-medium modification of the jet structure and  
 224 its dependence on the path length in medium, this observable is also differentially measured  
 225 based on the jet’s orientation with respect to the event plane for 20–50% mid-central colli-  
 226 sions, as shown in Fig 4. High- $p_{T,\text{trk}}$  particles are found closer to the jet core, whilst softer  
 227 constituents are more evenly distributed around the jet. In comparing the soft particle pro-  
 228 duction for in-plane vs. out-of-plane jets one finds subtle hints of path-length dependence.

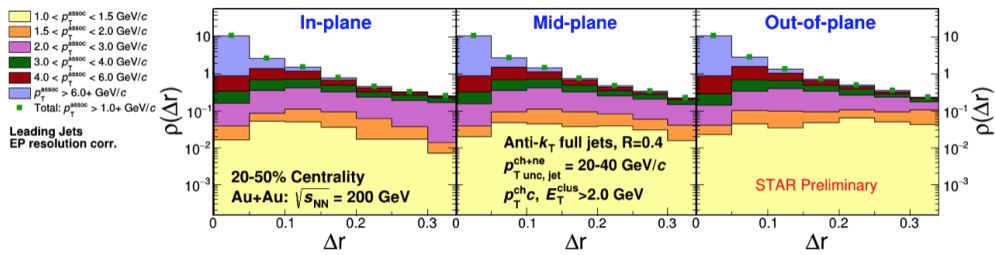


**Figure 4:** Differential measurement of the leading jet ( $20 < p_{T,\text{jet}} < 40$  GeV/c) shapes in 20–50% central Au+Au collisions shown for different jet azimuthal angles with respect to the event-plane angle. The  $p_{T,\text{trk}}$ -dependence of the associated tracks are shown in the different stacked histograms. Results are corrected for event-plane resolution effects.

230 **Jets in  $p+Au$  collisions:** STAR has searched for jet-medium interactions in  $p+Au$  colli-  
 231 sions by looking at potential modifications of semi-inclusive charged-particle jet yields and  
 232 jet substructure observables such as the jet mass and SoftDrop groomed jet mass.  $p+Au$  col-  
 233 lisions are classified as low or high event-activity (EA) according to the particle multiplicity  
 234 in the Au-going direction as measured by the BBC-East detectors.

235 The charged-particle jet spectra, normalized per HT trigger (uncorrected for detector  
 236 effects) are shown on the left of Fig. 5 where the open (full) markers correspond to low (high)  
 EA. The different colored markers represent the azimuthal separation between the trigger and

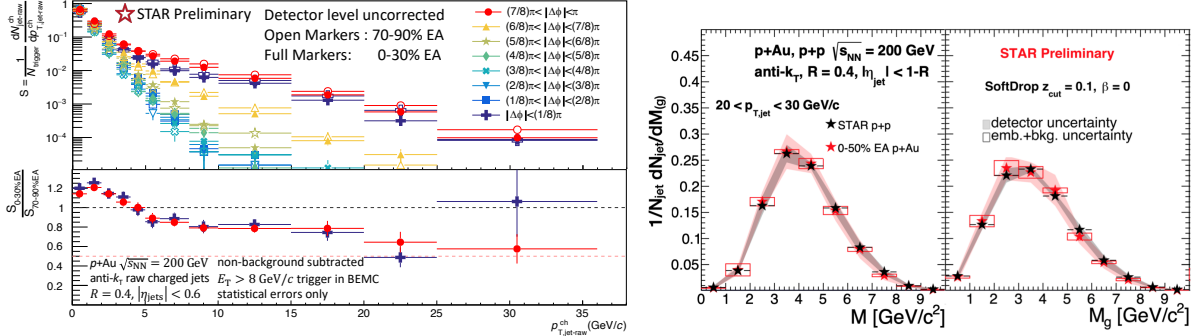


**Figure 5:** Left: Semi-inclusive charged jet spectra in  $p+Au$  collisions for high and low event-activity (EA) events, the ratio is shown in the bottom panel. Right: Fully corrected (groomed) jet-mass distributions in  $p+Au$  with high EA and  $p+p$  collisions.

237 the recoil jet. We see for jet with  $p_{T, \text{jet-raw}} > 10$  GeV/c, a significant suppression in high to  
 238 low EA events for both the trigger-side and recoil-side spectra. These suppression ratios are  
 239 qualitatively different from jet suppression in Au+Au collisions, where the recoil jets traverse  
 240 more QGP on average and are suppressed compared to the trigger-side. In investigating if  
 241 this suppression is a result of modification of jet structure, STAR also measured the fully  
 242 corrected jet-mass and groomed jet-mass distributions, normalized per jet, on the right of  
 243 Fig. 5. The distribution in high EA  $p+Au$  collisions is comparable to that in  $p+p$  collisions  
 244 within the systematic uncertainties, and this leads to the conclusion that CNM effects do not  
 245 significantly affect the jet substructure. The jet mass measurements in  $p+Au$  will be followed  
 246 in a more differential fashion by studying finer EA classes and rapidity selections which can  
 247 isolate jets originating from the Au vs p side. Both of these measurements from STAR point  
 248 to lack of jet modification from nuclear effects and also to a more fundamental selection bias  
 249 when identifying classes of high vs low activity events in asymmetric collisions.

### 251 1.1.2 Bulk Correlations

252 Over the past years, the STAR collaboration has performed a series of correlation measure-  
 253 ments directed towards a comprehensive understanding of the QCD phase diagram and the  
 254 bulk properties of the QGP phase. Here we highlight the most recent STAR results on bulk  
 255 correlations, which are expected to shed light on the QCD phase diagram as well as on the  
 256 transport properties of the QGP.

257 **Net-proton number fluctuations and the QCD critical point:** One of the main  
 258 goals of the STAR Beam Energy Scan (BES) program is to search for possible signatures  
 259 of the QCD critical point (CP) by scanning the temperature (T) and the baryonic chemical  
 260 potential ( $\mu_B$ ) plane by varying the collision energy. When the system produced in the heavy  
 261 ion collisions approaches the CP, the correlation length diverges. Higher order cumulants  
 262 of conserved net-particle multiplicity distributions are sensitive to such correlation lengths  
 263 as the divergence of correlation length leads to enhanced fluctuations in the net-particle  
 multiplicity distributions.

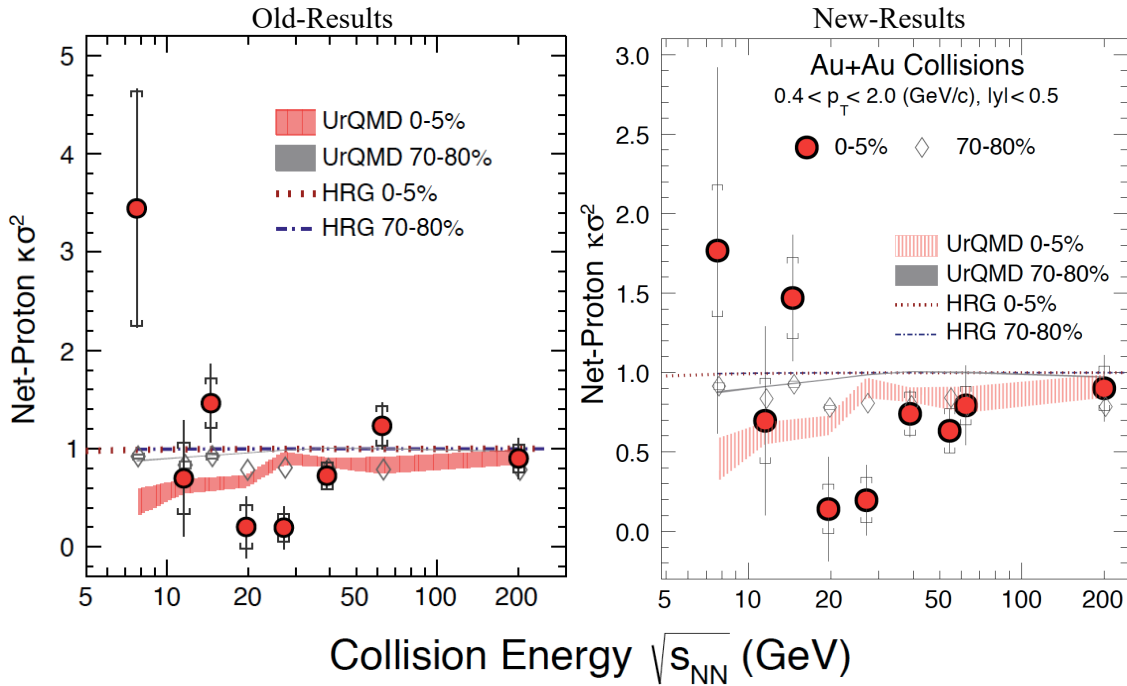


**Figure 6:**  $\kappa\sigma^2$  as a function of collision energy for net-proton distributions measured in central (0-5%) and peripheral (70-80%) Au+Au collisions within  $0.4 < p_T$  (GeV/c)  $< 2.0$  and  $|y| < 0.5$ . The error bars and caps show statistical and systematic uncertainties, respectively. The dashed and dash-dotted lines correspond to results from a hadron resonance gas (HRG) model. The shaded bands are the results of a transport model calculation (UrQMD). The model calculations utilize the experimental acceptance and incorporate conservation laws for strong interactions, but do not include the dynamics of phase transition or critical point. **The new results are obtained after removing the spoiled events, the largest changes are seen in central Au+Au collisions at 7.7 and 62.4 GeV.**

264  
 265  
 266

The ratios of the cumulants of identified net-particle multiplicity distributions, such as net-protons, have been predicted to be ideal observables sensitive to the onset of the QCD

267 phase transition and the location of the CP. A non-monotonic variation of these ratio of  
 268 cumulants, such as  $C_4/C_2$  ( $=\kappa\sigma^2$ ), as a function of collision energy has been proposed to be  
 269 an experimental signature of the CP. Taking the ratios of cumulants has advantages as it  
 270 cancels the volume fluctuations to first order. Further, these ratios of cumulants are related  
 271 to the ratio of baryon-number susceptibilities at a given T and  $\mu_B$ . Near the critical point,  
 272 QCD-based calculations predict the net-baryon number distributions to be non-Gaussian  
 273 and susceptibilities to diverge, causing these ratios to have non-monotonic variation as a  
 274 function of collision energy. However, the finite-size and finite-time effects in heavy-ion  
 275 collisions limit the growth of correlation length, and hence it could restrict the values of  $\kappa\sigma^2$   
 276 from its divergence as a function of collision energy.

277 Figure 6 shows the collision energy variation of net-proton  $\kappa\sigma^2$  for central and peripheral  
 278 Au+Au collisions within the acceptance of  $0.4 < p_T < 2.0$  GeV and  $|y| < 0.5$ . In central  
 279 collisions, a non-monotonic variation with beam energy is observed for  $\kappa\sigma^2$  with a significance  
 280 of  $3.0 \sigma$ . In contrast, monotonic behavior with beam energy is observed for the statistical  
 281 hadron gas (HRG) model, and for a nuclear transport UrQMD model without a critical  
 282 point, and experimentally in peripheral collisions.

283 High statistics data from the ongoing BES-II program can provide precision measure-  
 284 ments at higher  $\mu_B$  region in the QCD phase diagram. In addition, due to the iTPC [16]  
 285 and eTOF [17] upgrades, a differential measurement in  $|y| < 1.5$  and  $p_T > 0.15$  GeV/c will be  
 286 explored. The study of acceptance dependence of net-proton  $\kappa\sigma^2$  and other cumulants ra-  
 287 tios are important to understand critical fluctuation. Furthermore, the forward Event-Plan  
 288 Detector (EPDs) [18] can also be used to determine the centrality selection in heavy-ion  
 289 collisions for this measurement.

290 **Global polarization measurements at 27 GeV:** In heavy-ion collisions, many theoret-  
 291 ical models propose that the large angular momentum in the collisions of two nuclei [19–21]  
 292 can be transferred to the microscopic constituent of the created matter. Consequently, the  
 293 spin of the produced quarks and gluons might be polarized along the direction of the global  
 294 angular momentum due to spin-orbit coupling. The direction of the global angular momen-  
 295 tum is perpendicular to the reaction plane, as defined by the incoming beam and the impact  
 296 parameter vector. This direction can be determined from directed flow measurements of the  
 297 spectators. STAR observed significant non-zero polarization of hyperons [20] with increasing  
 298 strength with decreasing collision energy (from 200 to 7.7 GeV).

299 We recently report more differential measurements using our newly installed EPDs in  
 300 Au+Au collisions at 27 GeV as functions of the hyperon’s transverse momentum, and pseudo-  
 301 rapidity. In Fig. 7 left panel we observe that the polarization does not show a strong  
 302 dependence on  $p_T$ , albeit large uncertainties. There are several expectations on the  $p_T$   
 303 dependence on the polarization. If global polarization is generated by the vorticity of the  
 304 initial state that does not have a strong  $p_T$  dependence then the result is compatible with  
 305 expectations. Alternatively, at lower  $p_T$ , due to the smearing effect caused by scattering at  
 306 later stages of the collisions, we might expect a decrease of the polarization. In addition,  
 307 one might expect a decrease in the polarization at higher  $p_T$  due to the expected larger

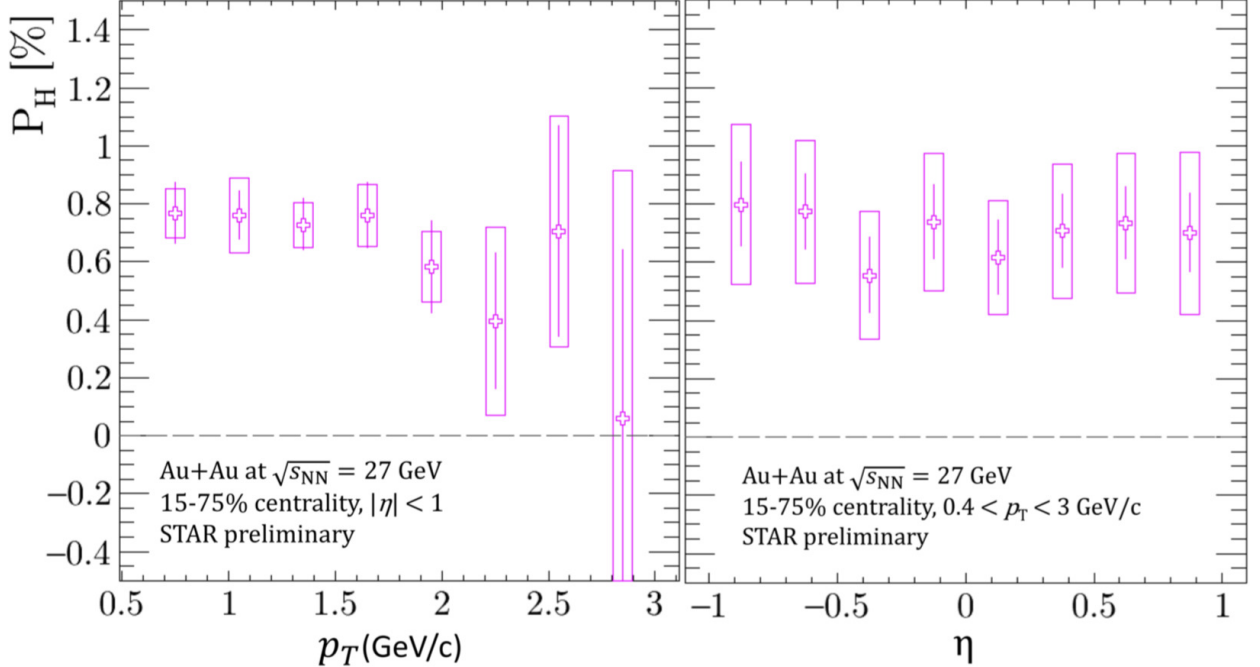


**Figure 7:** The global polarization measurements as a function of  $p_T$  and  $\eta$  in 15-75% central Au+Au collisions at  $\sqrt{s_{NN}} = 27$  GeV. The figure is taken from Ref [22].

308 contribution from jet fragmentation. Fig 7 right panel shows the pseudo-rapidity dependence  
 309 of the polarization measurement, no  $\eta$ -dependence of the polarization is observed within  
 310 uncertainties. The vorticity is expected to decrease at larger rapidity, but might also have a  
 311 local minimum at  $\eta=0$  due to complex shear flow structure [21, 23, 24] however, this might  
 312 be difficult to observe within STAR's acceptance. This preliminary observation of no  $p_T$  or  $\eta$   
 313 dependence of the polarization is consistent with our previous measurements at 200 GeV [19].  
 314 STAR plans to perform the same measurement with an extended pseudo-rapidity coverage  
 315 using the iTPC detector upgrade and with higher statistics BES-II data set enabling higher  
 316 a precision result.

317 **Global spin alignment of  $K^{*0}$  and  $\phi$ :** Unlike the self-analyzing (anti) $\Lambda$ , the polarization  
 318 of vector mesons such as  $\phi(1020)$  and  $K^{*0}(892)$  cannot be directly measured since vector  
 319 mesons mainly decay through the strong interaction in which parity is conserved. The spin  
 320 alignment of vector mesons can be given by a  $3 \times 3$  spin density matrix with unit trace [25].  
 321 The spin density matrix diagonal elements  $\rho_{nn}$ ,  $n=0,1$  and  $-1$ , represent the probabilities  
 322 for the spin component along the quantization axes. When there is no spin alignment this  
 323 means that all three spin states ( $\rho_{nn}$ ) have equal probability to be occupied meaning  $\rho_{nn} =$   
 324  $1/3$ . Out of the three diagonal elements, only the  $n=0$  case is independent of the other two.  
 325 Consequently, it is intriguing to experimentally investigate the  $\rho_{00}$  of vector mesons.

326 Figure 8 shows the centrality dependence of  $\rho_{00}$  for both vector meson species for Au  
 327 + Au collisions at 200 GeV. The  $\phi$ -meson results are presented for transverse momentum

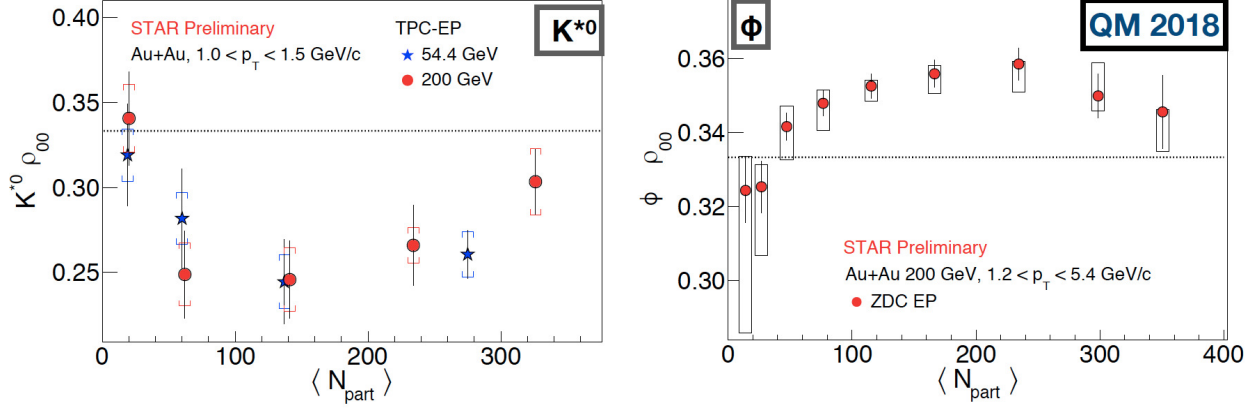


**Figure 8:** The spin alignment  $\rho_{00}$  measurements of vector mesons  $K^{*0}$  and  $\phi$  as a function of  $N_{part}$  for the indicated  $p_T$  range of the Au+Au collisions at 200 and 54.4 GeV. The figure is taken from Ref [26].

328  $1.2 < p_T < 5.4$  GeV/c, and  $\rho_{00}$  for this species is significantly above 1/3 for mid-central  
 329 collisions, indicating finite global spin alignment. The  $K^{*0}$ -meson results are presented for  
 330 transverse momentum  $1.0 < p_T < 1.5$  GeV/c, and the magnitude of  $\rho_{00}$  for this particle  
 331 species is observed to be significantly less than 1/3 for mid-central collisions.

332 The distinction between the global spin alignment for  $K^{*0}$  and  $\phi$  may be assigned to  
 333 different in-medium interactions due to the difference in the lifetime ( $\phi$ -meson is 10 times  
 334 larger than  $K^{*0}$ -mesons), and/or a different response to the vector meson field. These global  
 335 spin alignment results are expected to shed light on the possible vector meson fields [27, 28].  
 336 Such investigations are extremely important since vector meson fields are a crucial part of  
 337 the nuclear force that binds nucleons to atomic nuclei and are also central in describing  
 338 properties of nuclear structure and nuclear matter.

339 **Nuclear deformation measurements:** Deformation is a fundamental property of atomic  
 340 nuclei that reflects the correlated nature of the dynamics of nucleons within the quantum  
 341 many-body system. The majority of atomic nuclei possess an intrinsic deformation, most of  
 342 which is an axial quadrupole, or ellipsoidal, deformation.

343 Prior relativistic heavy-ion collision measurements from STAR reported strong signatures  
 344 of nuclear deformation using detailed comparisons between Au+Au collisions and U+U col-  
 345 lisions [29]. These measurements suggest that U+U collisions being much more deformed  
 346 in their ground state. Consequently, we can say that these detailed comparisons between  
 347 Au+Au and U+U collisions enabled us to examine the geometry of the colliding nuclei.

348 The study of mean transverse momentum dependence of the elliptic and triangular flow  
 349 harmonics in Au+Au and U+U collisions are recently proposed by theory calculations [31]  
 350 that are more sensitive to the deformation of the colliding nuclei.

351 Figure 9 shows the scaled mean  $p_T$  dependence of  $v_2$  and  $v_3$  for the central Au+Au and  
 352 U+U collisions. STAR preliminary data show a clear positive correlation for  $v_2$  and  $v_3$  in  
 353 Au+Au collisions that is in agreement with the  $v_3$  from U+U collisions. In contrast, a  
 354 nontrivial negative correlation is observed in  $v_2$  as a function of scaled mean  $p_T$  in U+U

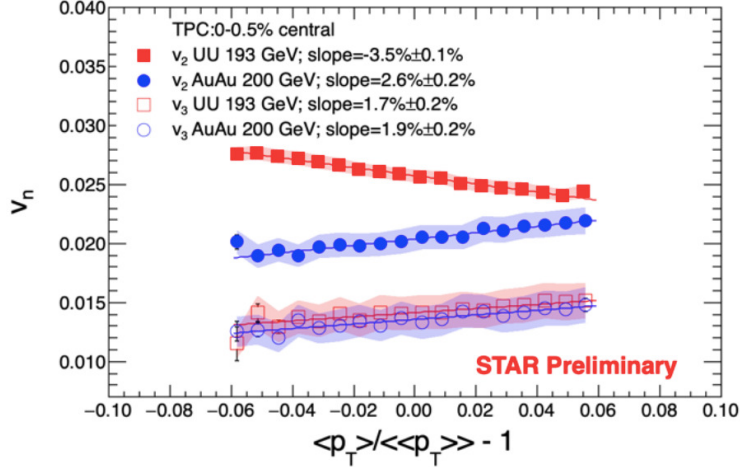


**Figure 9:** The scaled mean  $p_T$  dependence of the elliptic and triangular flow harmonics for 0-0.5% central Au+Au and U+U collisions. The figure is taken from Ref [30].

355 collisions. Also these preliminary results are consistent with the theoretical expectation for  
 356 a deformed U nuclei [31].

357 **Flow correlations and fluctuations measurements:** Flow harmonics ( $v_n$ ) calculated  
 358 from the Fourier expansion of the particle azimuthal distributions are commonly employed  
 359 to quantify the azimuthal anisotropy of particle emission relative to the collision symmetry  
 360 planes. While the lower-order Fourier coefficients ( $v_2$  and  $v_3$ ) are more directly related to the  
 361 corresponding eccentricities of the initial state, the higher-order flow harmonics ( $v_{n>3}$ ) can  
 362 be induced by a non-linear (mode-coupled) response to its lower-order harmonics and also  
 363 with a linear response to the same-order anisotropy. These higher-order flow harmonics and  
 364 their linear and mode-coupled contributions can be used to constrain the initial conditions  
 365 and the transport properties of the medium in the theoretical calculations.

366 The  $v_2$  and  $v_3$  harmonics are sensitive to the respective influence of the initial-state  
 367 eccentricity and the final-state viscous attenuation, which have proven difficult to disentangle.  
 368 The mode-coupled coefficients show characteristically different dependencies on the viscous  
 369 attenuation and the initial-state eccentricity [32]. Therefore, they can be used in conjunction  
 370 with measurements for the  $v_2$  and  $v_3$  harmonics to leverage additional unique constraints for  
 371 initial-state models, as well as reliable extraction of transport coefficient.

372 Figure 10 shows the mode-coupled response coefficients,  $\chi_{4,22}$  and  $\chi_{5,23}$ , with a weak  
 373 centrality dependence, akin to the patterns observed for similar measurements at the LHC  
 374 for Pb+Pb collisions at 2.76 TeV [34]. These patterns suggest that the mode-coupled response  
 375 coefficients are dominated by initial-state eccentricity couplings which is known from models  
 376 to have a weak dependence on beam energy. The correlations of the event plane angles,  $\rho_{4,22}$   
 377 and  $\rho_{5,23}$  show a strong centrality dependence that agrees well with the LHC measurements  
 378 for Pb+Pb collisions at 2.76 TeV. The predictions from viscous hydrodynamic models [35,  
 379 36] give a good qualitative description of the mode-coupled response coefficients and the

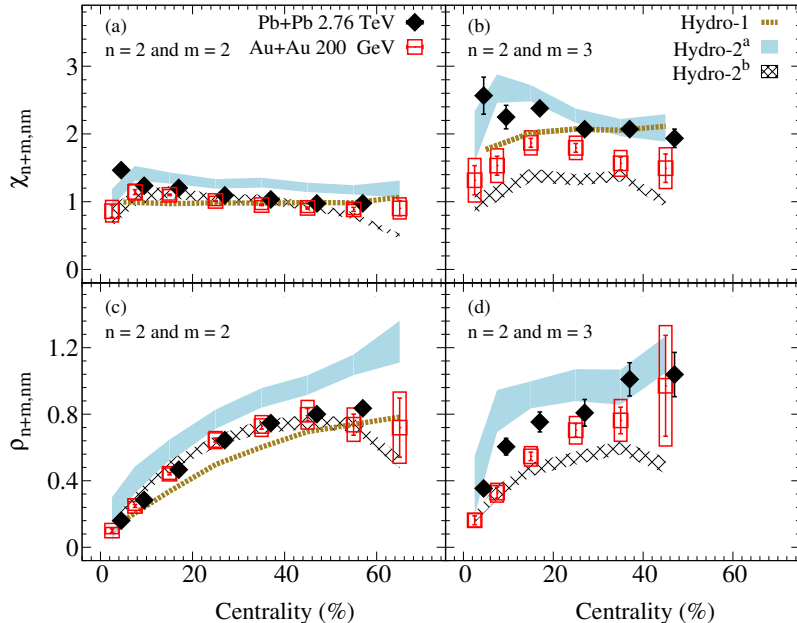


**Figure 10:** Results as a function of centrality for Au+Au collisions at 200 GeV [33]. Panels (a) and (b) shows the mode-coupled response coefficients, and panels (c) and (d) show the correlations of event plane angles. The closed-symbols represents similar LHC measurements [34]. The shaded bands indicate hydrodynamic model predictions Hydro-1 [35], Hydro-2<sup>a</sup> and Hydro-2<sup>b</sup> [36].

380 correlation of event plane angles.

381 **Small system measurements:** The comparisons of theoretical models to the flow har-  
 382 monics,  $v_n$ , continue to be an essential avenue to evaluate the transport properties of partonic  
 383 matter produced in large to moderate-sized collision systems [37–39]. For the small collision-  
 384 systems formed in  $p/d/{}^3\text{He}+\text{Au}$  and  $p+\text{Pb}$  collisions, collective flow might not develop due  
 385 to the presence of large gradients in the energy-momentum tensor that could trigger non-  
 386 hydrodynamic modes [40, 41]. Certainly, the most important question that divided our field  
 387 is whether an alternative initial-state-driven mechanism [42] dominates over hydrodynamic  
 388 expansion for these collision systems.

389 Current measurements for  $p/d/{}^3\text{He}+\text{Au}$  collisions, which supplement earlier measure-  
 390 ments at both RHIC [43] and the LHC [44] aim to address the respective influence of collision-  
 391 system size and its subnucleonic fluctuations, and viscous attenuation on the measured  $v_n$ .

392 Figure 11 shows the  $v_2(p_T)$  and  $v_3(p_T)$  values for  $p/d/{}^3\text{He}+\text{Au}$  collisions at 200 GeV  
 393 before and after non-flow subtraction, compared for all three subtraction techniques. The  
 394 presented results show non-flow contributions which are system-dependent, but the non-  
 395 flow subtracted  $v_2$  (top panels) and  $v_3$  (bottom panels) are method-independent within the  
 396 uncertainties.

397 These STAR measurements with non-flow subtracted show that for the comparable  
 398 charged-hadron multiplicity ( $N_{ch}$ ) events  $v_2$  and  $v_3$ , values are independent of collision sys-

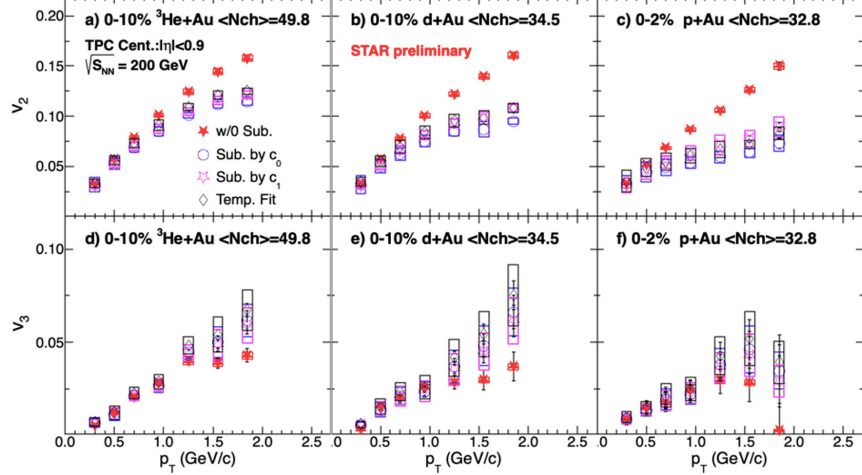


**Figure 11:** Comparison of the  $v_{2,3}(p_T)$  values for p/d/ $^3\text{He}$ +Au collisions at 200 GeV, before and after non-flow subtraction. The figure is taken from Ref [45].

tem. These observations are compatible with the significant influence of the subnucleonic  
fluctuations-driven eccentricities,  $\epsilon_{2,3}$ , in a system whose size is primarily determined by  
 $N_{ch}$ . However, they are incompatible with the notion of shape engineering in p/d/ $^3\text{He}$ +Au  
collisions.

### 1.1.3 Light Flavor Spectra and Ultra-peripheral Collisions

The Light Flavor Spectra and Ultra-peripheral Collisions (LFSUPC) physics working group  
is responsible for the measurements of calibrated production yields and spectra in inclusive  
ion-ion collisions, ultra-peripheral collisions, and exclusive p+p collisions.

In ion-ion collisions, analysis efforts can be grouped based on the methodology and physics  
issues. The general categories include light charge hadrons ( $\pi$ ,  $K$ ,  $p$ ), strange hadrons ( $\phi$ ,  
 $\Lambda$ ,  $\Xi$ ,  $\Omega$ ), light nuclei (d, t,  $^3\text{He}$ ,  $^4\text{He}$ ), and hyper-nuclei ( $^3_\Lambda H$  and  $^4_\Lambda H$ ). Examples of recent  
results from light nuclei and hyper-nuclei are shown in other sections (see sections 2.2.3 and  
2.2.2). Here some recent results will be presented from the light charged hadron and strange  
hadron analyses.

**Light hadron production:** Light charged hadron spectra and yields are measured using  
particle identification through  $dE/dx$  in the TPC,  $1/\beta$  in the time-of-flight detectors and  
careful study of the acceptance and efficiency of the detectors. These studies are particularly  
useful in defining the basic thermal properties ( $T$  and  $\mu_B$ ) of the system. Previous studies  
of the light charged hadrons from BES-I measured the spectra and yields at midrapidity.  
The newest results now include rapidity dependence which allows for a better understanding  
of baryon stopping, which is key to the dependence of  $\mu_B$  with  $\sqrt{s_{NN}}$ . New preliminary  $\pi$ ,  
K, and p transverse mass spectra are shown as a function of rapidity in Fig. 12 for Au+Au  
collisions at  $\sqrt{s_{NN}} = 27$  GeV. Additional pre-preliminary results have been produced from  
fast offline pre-calibration quality assurance productions from the other BES-II collider and

423 fixed-target energies.

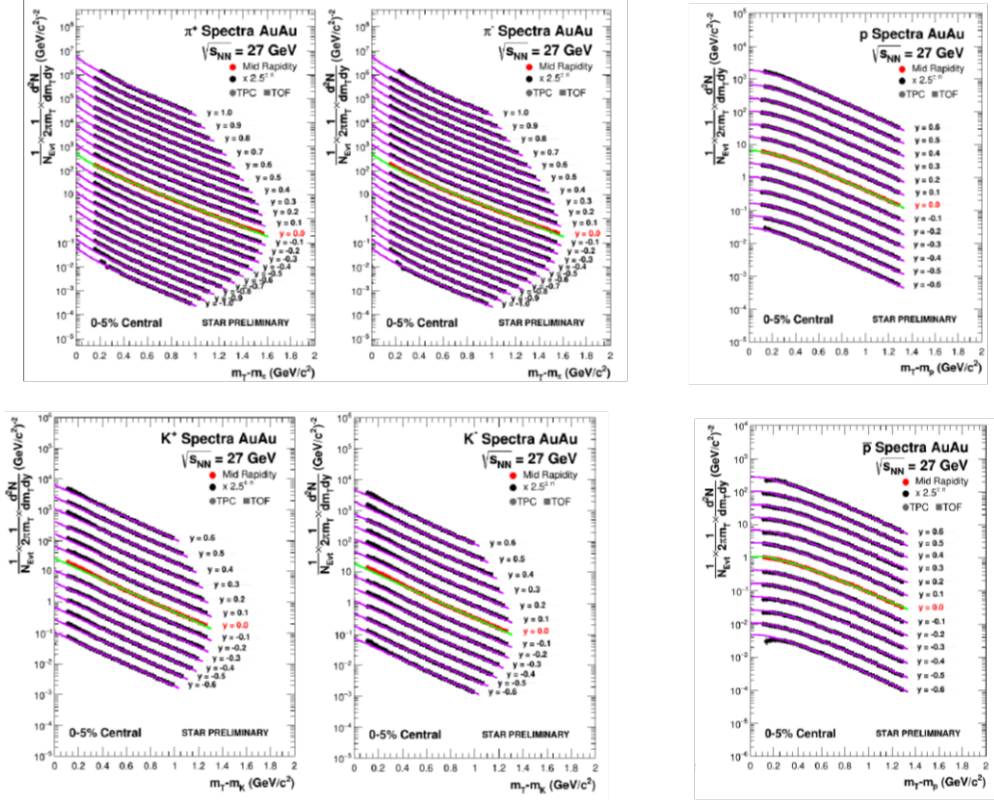


**Figure 12:** Transverse mass spectra for pions, Kaons, and protons from Au+Au collisions at  $\sqrt{s_{NN}} = 27$  GeV as a function of rapidity.

424 **Strange hadron production:** Strange hadron spectra and yields are measured by deter-  
 425 mining the invariant mass from the charged daughters from weak decays of neutral strange  
 426 hadrons. These studies define the role of the strange quark in the thermodynamic evolution  
 427 of the system. STAR has recently implemented a new  $V^0$  finding routine called *KFparticle*  
 428 which increases the sensitivity of our strange hadron studies. The highlights of recent  
 429 measurements have come from the newest fixed-target data. The fixed-target energy range  
 430 covers the production threshold energies for  $\Xi^-$  (3.247 GeV),  $\Omega^-$  (4.09 GeV),  $\Xi^+$ ,  $\Xi^-$  (4.52  
 431 GeV), and  $\Omega^+$ ,  $\Omega^-$  (5.22 GeV). Figure 13 shows the invariant mass plots for measurements  
 432 of  $\Lambda$ 's,  $\Xi$ 's, and  $\Omega$ 's for fixed-target Au+Au at  $\sqrt{s_{NN}}$  of 3.0 and 7.2 GeV. Additional pre-  
 433 preliminary measurements have been made at other collider and fixed-target energies. In  
 434 addition, studies of the production of the  $\phi$  meson have been made at 3.0 and 7.2 GeV.

435 **Central exclusive production:** Central exclusive production is measured in p+p colli-  
 436 sions using the very forward roman pot detectors to identify the the two colliding protons  
 437 and the TPC to measure the products. Figure 14 shows the invariant mass of pion pairs

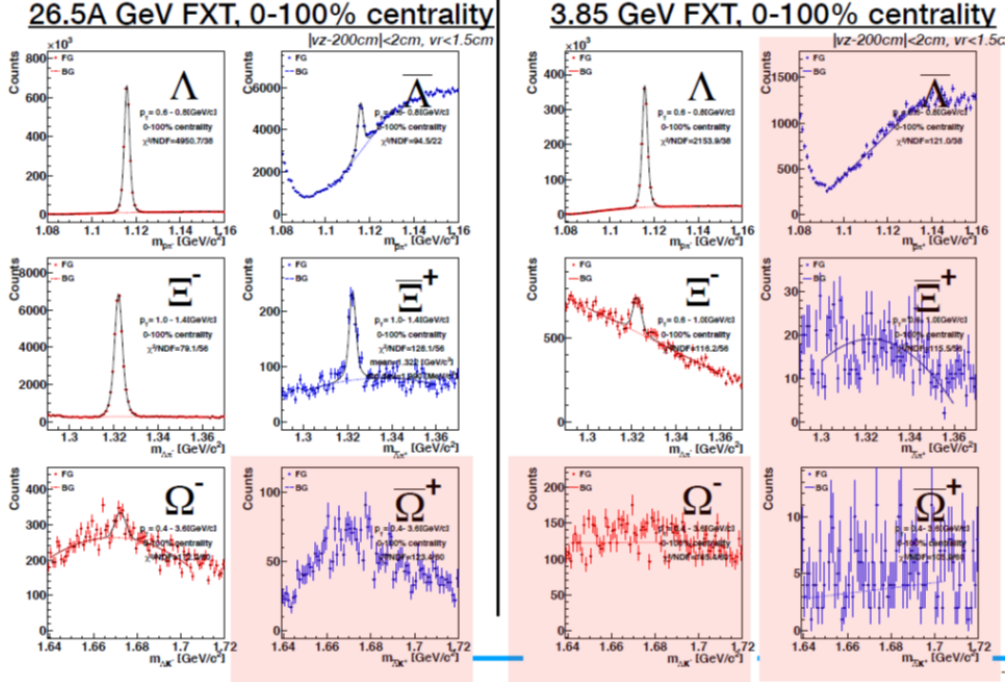


**Figure 13:** Invariant mass plots for measurements of  $\Lambda$ 's,  $\Xi$ 's, and  $\Omega$ 's for fixed-target Au+Au collisions at  $\sqrt{s_{NN}}$  of 3.0 and 7.2 GeV (single beam energies of 3.85 and 26.5 GeV respectively).

438 in exclusive p+p events at 200 GeV. These are the first measurements at this energy and  
 439 show significant peaks in the invariant mass spectra that were not predicted by the models.  
 440 Similar results are available for kaon and proton pairs.

441 **Electromagnetic probes:** Electromagnetic radiation from high-energy heavy-ion colli-  
 442 sions provides rich information about the properties of the produced medium. Dileptons  
 443 directly probe the in-medium electromagnetic correlator of hadronic currents [46, 47]. Dy-  
 444 namical information on in-medium spectral functions encodes not only changes in degrees  
 445 of freedom, chiral symmetry restoration [48–50], and transport properties of medium like  
 446 the electrical conductivity [51, 52], but also the life time and average temperature of the  
 447 interacting fireball [53], and the emission history and origin of the radiation [54–57].

448 STAR reported measurement of thermal dilepton radiation ranging from  $\sqrt{s_{NN}} = 200$   
 449 GeV down to 19.6 GeV [58–61]. A significant excess in the low-mass region when compared  
 450 to the known hadronic sources has been observed. It was shown that the predictions of  
 451 hadronic manybody theory for a melting  $\rho$  meson, coupled with QGP emission utilizing  
 452 a modern lattice QCD-based equation of state [51, 62], yield a quantitative description of  
 453 dilepton spectra in heavy-ion collisions [58, 61]. This is demonstrated in Fig. 15 (left panel).  
 454 Moreover, it has been shown that the integrated low-mass excess radiation provides a direct  
 455 measure of the total fireball lifetime [60]. Secondary vertex rejection employing information  
 456 provided by the Heavy Flavor Tracker installed for Run-14 and Run-16 will enable unique

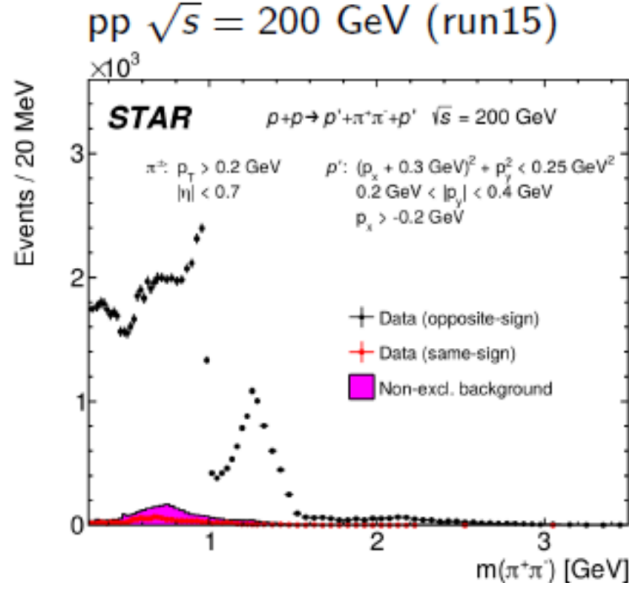


**Figure 14:** Invariant mass spectra for pion pairs from exclusive p+p events at 200 GeV.

457 temperature measurements of the QGP.

458 The low-mass line shape will provide a critical test of the  $\rho$ -melting scenario (which is  
 459 consistent with expectations of chiral symmetry restoration) at vanishing baryon chemical  
 460 potential. A precision measurement at top RHIC energy will provide additional constraints  
 461 that can be directly tested against the lattice QCD predictions and will be put in focus via  
 462 the additional data collected in 2023-2025 (see section 2.4.3).

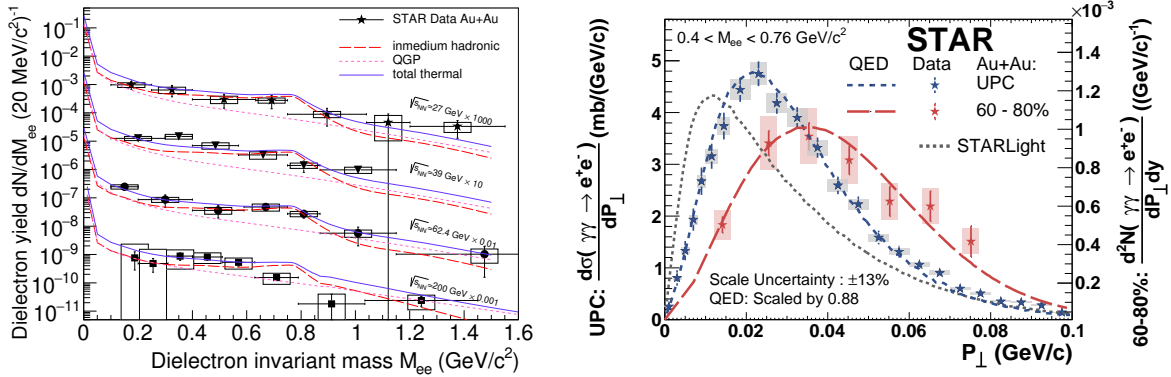


**Figure 15:** Left: Acceptance-corrected dielectron excess mass spectra, normalized by  $dN_{ch}/dy$ , for Au+Au collisions at  $\sqrt{s_{NN}} = 27, 39, 62.4, 200$  GeV. Right: Comparison of the  $P_T$  distribution in 60–80% central Au+Au collisions with that in UPCs [63].

463 Dileptons generated by the intense electromagnetic fields accompanying the relativistic  
 464 heavy nuclei at large impact parameters [64], in ultra-peripheral collisions (UPC) where  
 465 there is no nuclear overlap has recently become experimentally accessible, offering several  
 466 opportunities. According to the equivalent photon approximation (EPA), the electromag-

467 netic field generated by an ultra-relativistic nucleus can be viewed as a spectrum of quasi-real  
 468 photons coherently emitted by the entire nucleus and the dilepton production process can be  
 469 represented as  $\gamma + \gamma \rightarrow l^+ + l^-$ . Recently, the STAR and ATLAS collaborations made mea-  
 470 surements of dileptons at small impact parameters with nuclear overlap, and found that the  
 471 electromagnetic production of dileptons can also occur in hadronic collisions. Furthermore,  
 472 a significant  $P_\perp$  broadening as shown in Fig. 15 (right panel) effect for lepton pairs produced  
 473 by the two photon scattering process has been observed in hadronic collisions compared to  
 474 measurements in UPC and to EPA calculations. Precision measurements will provide an im-  
 475 portant constraints for quantitative theoretical analyses of magnitude and duration of initial  
 476 magnetic fields. It was perceived that photons participating in such collisions are quasi-real  
 477 with transverse-momentum  $k_t \simeq 1/R$  (30 MeV/c) reflecting the virtuality and uncertainty  
 478 principle of their origin. This led to the implementation in many EPA models that the initial  
 479 transverse momentum of the dilepton pairs does not depend on impact parameter and the  
 480 transverse space coordinates where the pair are created are randomly distributed due to the  
 481 same principles. Our new measurements of centrality dependence and azimuthal distribu-  
 482 tions have shown that the photons behave like real photons in all observables and the renewed  
 483 models and theories have demonstrated that correction to the real photon approximation is  
 484 suppressed at the order of  $1/\gamma^2$  even to the pair's transverse momentum distribution. The  
 485 discovery of the Breit-Wheeler process and the utilization of linearly polarized photons in  
 486 UPC are conceptually and experimentally highly nontrivial. With future high statistics data  
 487 with larger TPC acceptance in UPC, we can explore the phase space of photon collisions  
 488 in transverse momentum, rapidity and momentum-space-spin correlations in extreme QED  
 489 field [65,66] (see section 2.4.3).

#### 490 1.1.4 Heavy-Flavor

491 The production of heavy-flavor (HF) quarks proceeds predominately via the hard scatterings  
 492 of partons in  $p(A)+p(A)$  collisions. This fact gives rise of the utility of heavy-flavor hadron  
 493 measurements in heavy-ion experiments since they are produced independently of the QCD  
 494 medium and probe it's properties by scattering with the medium constituents. Topics of  
 495 medium-induced parton energy loss, QGP transport properties, hadronization mechanisms,  
 496 and quarkonia melting are some of the pivotal studies that have emerged within the HF  
 497 category. Besides the highlights discussed in detail below, the following measurements have  
 498 been recently published: First Measurement of  $\Lambda_c$  Baryon Production in Au+Au Collisions  
 499 at  $\sqrt{s_{NN}} = 200$  GeV [67]; Measurement of inclusive  $J/\psi$  suppression in Au+Au collisions at  
 500  $\sqrt{s_{NN}}=200$  GeV through the dimuon channel at STAR [68]; First Observation of the Directed  
 501 Flow of  $D^0$  and  $\bar{D}^0$  in Au+Au Collisions at  $\sqrt{s_{NN}} = 200$  GeV [69].

502 **Charm coalescence:** Recent measurements of  $D^0$  [70] and  $D^+$  meson yields (shown at  
 503 Hard Probes 2020) as a function of transverse momentum ( $p_T$ ) in heavy-ion collisions show a  
 504 significantly suppressed spectrum with respect to  $p+p$  collisions. The two mechanisms that  
 505 predominately produce suppressed meson distributions are parton energy loss in the QGP  
 506 and different hadronization schemes. The latter is nicely illustrated via the measurement

507 of the  $\Lambda_c^+/D^0$  yield ratio [67], which is significantly enhanced with respect to the expecta-  
 508 tion in  $p+p$  collisions and is attributed to baryon production via coalescence hadronization.  
 509 Recently, STAR has measured the ratio of  $D_s^+/D^0$  yields in heavy-ion collisions, which is  
 510 important as it probes charm hadronization and strangeness enhancement mechanisms. Utili-  
 511 zing the excellent pointing resolution resolution of the Heavy Flavor Tracker (HFT), the  
 512  $D_s$  is measured in 2014 and 2016 data via topological reconstruction using a multi-variate  
 513 analysis (MVA). The final results of  $D_s^+$  yield with respect to  $D^0$  were reported in the 2019  
 514 Quark Matter conference, and are shown in Figure 16. The ratios for 0-10% (blue points)  
 515 and 10-40% (red points) centrality regions are consistent within experimental uncertainties.  
 516 Also shown in the left panel are the ratios averaged over  $p+p/e+p/e+e$  collisions, PYTHIA,  
 517 and a model calculation (TAMU) including coalescence hadronization for 10-40% centrality.  
 518 The  $D_s$  yield is significantly enhanced in Au+Au collisions with respect to that of elemen-  
 519 tary  $p+p/e+p/e+e$  collisions. Shown in the right panel are model calculations including  
 520 sequential (solid lines) and simultaneous (dashed lines) coalescence for both Au+Au colli-  
 521 sions at RHIC and Pb+Pb collisions at LHC energies. The ALICE data, also shown in the  
 522 right panel, are consistent within uncertainties with the STAR data. The model including  
 523 sequential coalescence is able to best capture the trends in the data.

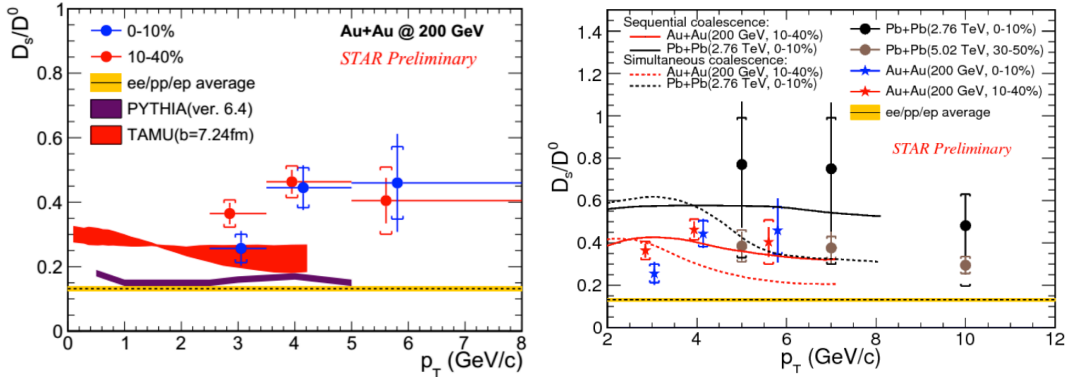


**Figure 16:** Left: STAR measurement of the  $D_s/D^0$  ratio in 0-10% (blue circles) and 10-40% (red circles) centrality Au+Au collisions as a function of  $D_s$   $p_T$ . The yellow shaded band shows the average from  $p+p/e+p/e+e$  collisions. The purple and red shaded bands show the expectations from PYTHIA and TAMU model calculations, respectively. Right: STAR  $D_s/D^0$  ratio measurements compared to model calculations including sequential (solid lines) and simultaneous coalescence (dotted lines) hadronization, and data from the ALICE measurements (blue and brown circles) and the respective model calculations at LHC energies.

524 **Mass dependence of partonic energy loss:** The mass dependence of parton energy  
 525 loss has been probed in heavy-ion collisions with the measurements of light- and heavy-flavor  
 526 hadron nuclear modifications factors ( $R_{AA}$ ). At high  $p_T$ , where mass effects are predicted  
 527 to significantly modify the quark energy loss from gluon radiation in the QGP, the values  
 528 of light-flavor and charm hadron  $R_{AA}$  are measured to be degenerate, and can be explained

529 by mechanisms that are not related to parton energy loss (e.g, see [71]). In that respect  
 530 systematic comparisons of both bottom and charm hadron nuclear modification factors are  
 531 predicted to be a clean probe of the mass dependence of parton energy loss by several model  
 532 calculations [72–75]. However, from an experimental point of view measuring bottom hadrons  
 533 have been difficult at RHIC due to the low bottom quark production cross-section, and have  
 534 only been accessible via the measurement of displaced electrons or charmed hadrons. STAR  
 535 has now reported at the 2019 Quark Matter conference an updated measurement of single  
 536 electrons from bottom semileptonic decays utilizing both 2014 and 2016 data sets. The  
 537 contribution of bottom- and charm-decayed electrons, and backgrounds, are topologically  
 538 separated using the three-dimensional distance-of-closest approach (DCA) utilizing the HFT  
 539 detector. In contrast to previous measurements utilizing the transverse dimension DCA  
 540 ( $DCA_{xy}$ ), the 3D DCA is able to separate charm- and bottom-decay electrons with greater  
 541 significance since the longitudinal and transverse DCA have similar resolution. The updated  
 542 STAR measurement also includes an improved electron identification selection, which is based  
 543 off a projective likelihood MVA. The improvement in the mis-identified hadron fraction is a  
 544 factor of two when compared to traditional cut-based particle identification. The results of  
 545 bottom- and charm-decayed electron  $R_{AA}$  are shown in Figure 17 in the top panel, and their  
 546 ratio in the bottom panel. A constant fit to the double ratio is used to quantify the enhanced  
 547  $b \rightarrow e R_{AA}$  and is measured to be  $1.92 \pm 0.25(\text{stat.}) \pm 0.21(\text{syst.})$ . Shown in the bottom panel as  
 548 the hashed blue curve is a null hypothesis where we assume equal values of  $R_{AA}$  for charm and  
 549 bottom hadrons and then fold the distributions to the decay-electron, and subsequently take  
 550 a double ratio. Performing this exercise shows the effects from different production spectra,  
 551 fragmentation, and decay phase-space of charm and bottom hadrons, and it is clearly seen  
 552 these effects have a small impact on the double ratio. The double ratios of  $b \rightarrow e$  to  $c \rightarrow e$   
 553  $R_{CP}$  are also measured and a similar constant fit as in the  $R_{AA}$  case is performed and found  
 554 to be  $1.68 \pm 0.15(\text{stat.}) \pm 0.12(\text{syst.})$  and  $1.38 \pm 0.08(\text{stat.}) \pm 0.03(\text{syst.})$  for the ratios of  $R_{CP}(0-$   
 555  $20\%/40-80\%)$  and  $R_{CP}(0-20\%/20-40\%)$ , respectively. We additionally compare the data to  
 556 a modified Langevin transport model (DUKE) [73] which includes the mass dependence  
 557 of parton energy loss, and within uncertainties the data and model are consistent in both  
 558 the absolute  $R_{AA}$  data and the double ratios of  $R_{AA}$  and  $R_{CP}$ . Combining the agreement  
 559 between model and experiment, and the quality of the data, these observations represent,  
 560 for the first time, evidence of mass-ordering of parton energy loss in heavy-ion collisions.

561 **Charm and bottom flow:** Measurements of heavy-flavor flow are also essential to under-  
 562 standing the QGP properties as particle flow and yield provide a test-bed for model calcula-  
 563 tions to simultaneously describe the data. It has already been established by STAR [76] in  
 564 200 GeV Au+Au collisions that  $D^0$  hadrons have a significant elliptic flow that is compara-  
 565 ble to light-flavor hadrons after taking into account particle mass and number of constituent  
 566 quarks. Measurements of heavy-flavor hadron flow at lower collision energies have been ex-  
 567 plored via the measurements of single electron elliptic flow in the 2017 and 2018 data sets,  
 568 and was reported at the 2020 Hard Probes conference. Previous STAR measurements of  
 569 heavy-flavor electron  $v_2$  in 62.4 and 39 GeV Au+Au collisions [77] were statistically limited

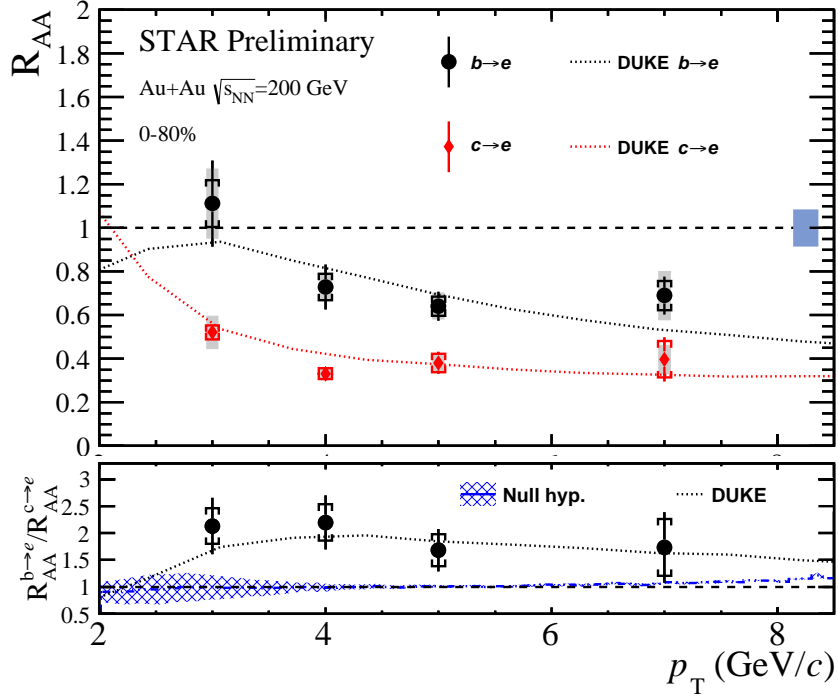


**Figure 17:** Top: Data for bottom- (blue stars) and charm-decay (red diamonds) electron  $R_{AA}$  as a function of electron  $p_T$ . The DUKE model calculation are shown as the respectively colored dotted lines. Bottom: The double ratio of bottom to charm  $R_{AA}$ , and the null hypothesis (explained in the text) shown as the blue shaded band and DUKE calculation as the dotted line.

570 and within experimental uncertainties consistent with zero. The data collected during Run-  
571 17 and Run-18 at  $\sqrt{s_{NN}}$  54.4 and 27 GeV Au+Au collisions, respectively, are more than  
572 an order of magnitude larger in statistics and allow for a more precise measurement. The  
573 heavy-flavor decay electron  $v_2$  is extracted from the inclusive electron  $v_2$  by correcting for  
574 electron  $v_2$  from hadron and photon decays. The data are shown in Figure 18 for both 54.4  
575 and 27 GeV Au+Au collisions, and compared to previously published STAR data in 200  
576 GeV Au+Au collisions [77]. The 54.4 GeV data show a significant  $v_2$  that is comparable to  
577 200 GeV Au+Au collisions, indicating heavy-flavor hadrons gain significant collective flow  
578 in the produced medium in 54.4 GeV Au+Au collisions. The data at 27 GeV indicate a hint  
579 of non-zero  $v_2$ , but still have considerable uncertainties due to a lower signal-to-background  
580 ratio.

581 STAR has also recently reported at the 2019 Quark Matter conference charm-decayed  
582 electron  $v_1$  and  $v_2$ , and bottom-decay electron  $v_2$  in 200 GeV Au+Au collisions utilizing  
583 the HFT to isolate charm- or bottom-decayed electrons, respectively. The measurement of  
584 charm-decayed electron  $v_1$  and  $v_2$  was compared to previous STAR data of  $D^0$  mesons, and  
585 show consistency between the two measurements. In the former case the measured slope  
586 of the charm-decayed electron  $v_1$  versus rapidity corroborated the recently measured large

587 negative  $v_1$  slope by STAR [69], and with an improved significance of  $5\sigma$ . The bottom-decay  
 588 electron  $v_2$  was measured to have a non-zero  $v_2$  with a significance of about  $3.4\sigma$ , and is  
 589 consistent in magnitude with expectations from the DUKE model [73]. This is the first  
 590 significant measurement of bottom hadron  $v_2$  at RHIC.

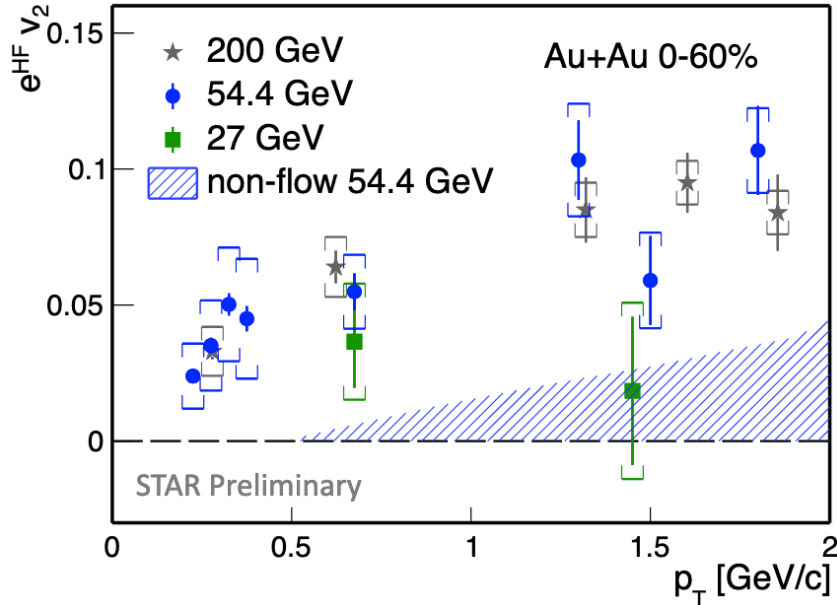


**Figure 18:** Heavy-flavor electron  $v_2$  as a function of electron  $p_T$  in 54.4 (blue circles) and 27 (green squares) GeV Au+Au collisions. The STAR published data at 200 GeV are also shown as the gray stars. The shaded blue histogram shows the estimated non-flow contribution in the 54.4 GeV data.

591 Recent measurements of quarkonia have opened up new ways to probe production mech-  
 592 anisms by measuring their distributions with jets. It has been observed that there is no  
 593 simultaneous description of models to the  $J/\psi$  spectra and polarization data. It has also  
 594 been shown that measurements of quarkonia fragmentation functions in jets can have good  
 595 discriminating power between different models. Recently reported at the 2020 Hard Probes  
 596 conference, was the measurement of  $J/\psi$  mesons within jets as a function of the  $J/\psi$   $p_T$   
 597 fraction ( $z = p_T(J/\psi)/p_T(jet)$ ). The results are shown in Figure 19 for a given set of jet  
 598 reconstruction requirements, and unfolded to account for detector smearing. The depen-  
 599 dence on cone size was also investigated and the data showed as the cone sized is increased  
 600 the  $z$  distribution became more populated at lower values. Compared with the data in the  
 601 same plot is the expectation of PYTHIA simulations (shown as the gray shaded histogram).  
 602 The data show a clear discrepancy with PYTHIA, suggesting  $J/\psi$  mesons are not produced  
 603 mostly in isolation. This new measurement is expected to provide valuable input to the  
 604 theory community.

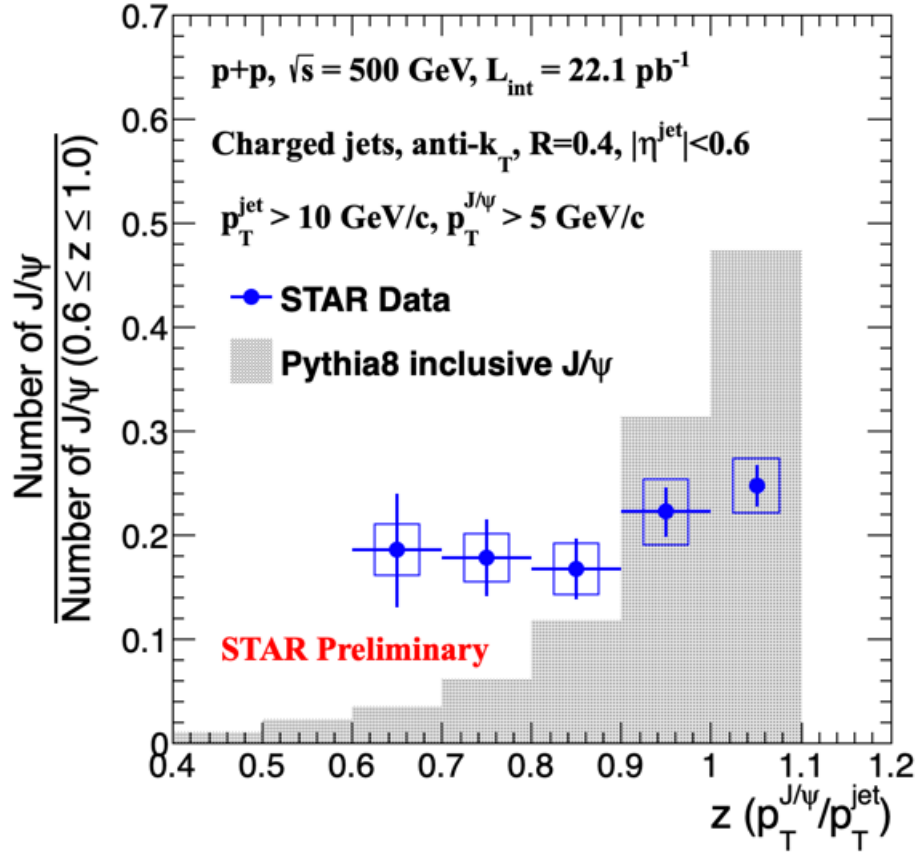


**Figure 19:**  $J/\psi$  momentum fraction in jets in 500 GeV  $p+p$  data for a given set of jet reconstruction parameters listed. Also shown is the expectation from PYTHIA simulation as the gray histogram.

## 605 1.2 CME Search and Isobar Run

### 606 1.2.1 Introduction

607 A decisive experimental test of the Chiral Magnetic Effect (CME) has become one of the  
 608 major scientific goals of the heavy-ion physics program at RHIC. The existence of CME  
 609 will be a leap towards an understanding of the QCD vacuum, establishing a picture of  
 610 the formation of a deconfined medium where chiral symmetry is restored, and will also  
 611 provide unique evidence of the strongest known electromagnetic fields created in relativistic  
 612 heavy-ion collisions [78, 79]. The impact of such a discovery goes beyond the community of  
 613 heavy-ion collisions and will possibly be a milestone in physics. The remaining few years  
 614 of RHIC running and analyses of already collected data probably provide the only chance  
 615 for dedicated CME searches in heavy-ion collisions in the foreseeable future. Significant  
 616 efforts from STAR, as well as other collaborations, have been dedicated towards developing  
 617 methods and observables to isolate possible CME-driven signals from non-CME background  
 618 contributions in measurements of charge separation across the reaction plane. Many clever  
 619 ideas have been proposed and applied to existing data. However, a general consensus is that  
 620 measurements from isobar collisions, Ruthenium+Ruthenium (Ru+Ru) that has 10 – 18%  
 621 higher B-field than Zirconium+Zirconium (Zr+Zr), provide the best solution. At the time  
 622 of writing this BUR document, analysts from STAR are proceeding to the final step of  
 623 the (three-step) blind analysis of the isobar data that we discuss at length in the following  
 624 section.

### 625 1.2.2 Modality of Isobar Running at RHIC

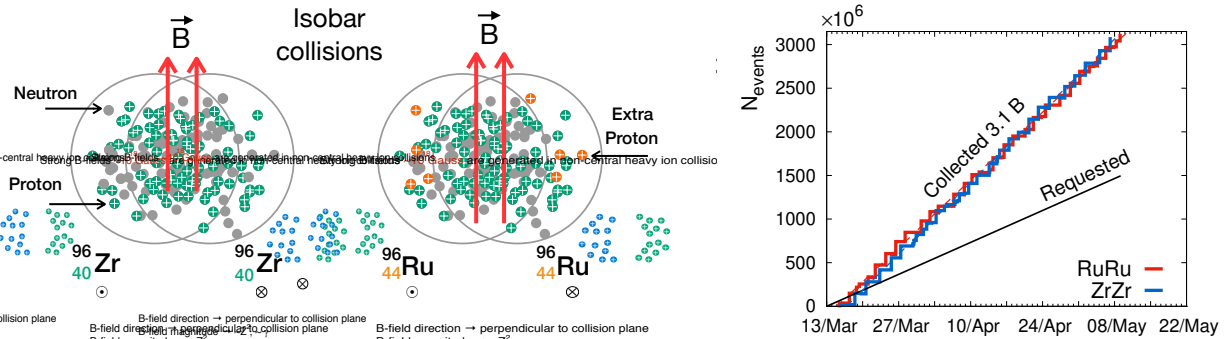


**Figure 20:** Left: Cartoon of the isobar collisions, about 10 – 18% stronger B-field is expected in Ru+Ru collisions as compared to Zr+Zr. Right: Summary of the Isobar data collected during Run-18.

626 Colliding isobars, particularly Ru+Ru and Zr+Zr, to make a decisive test of CME was  
 627 proposed by Voloshin in Ref [80], the same paper also proposed to use Uranium collisions  
 628 to disentangle signal and background of CME. The possible difference in the signals relies

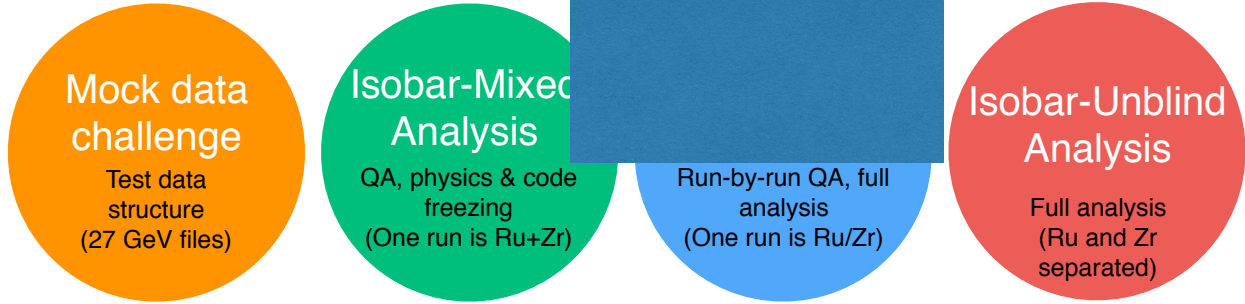


**Figure 21:** Cartoon showing steps of analysis consisting of the mock-data challenge and the three-step isobar blind analysis. This cartoon is based on the procedure for the blind analysis of isobar data that have been outlined in Ref [85]. At the time of writing STAR has begun the final step of isobar-unblind analysis (shown in red).

629 on the 10 – 18% higher B-field in Ru+Ru compared to Zr+Zr, due to four extra protons  
 630 in each Ru nucleus [81], in contrast to about 4% difference in flow driven background [36].  
 631 Such estimates are sensitive to details of the shape, charge distribution and neutron skin  
 632 thickness of the two isobar nuclei [81–83]. In the 2017-18 RHIC BUR [84] STAR proposed to  
 633 collect data for two 3.5 week periods in Run-18. The projection was based on the prospect  
 634 of achieving five-sigma significance in a scenario where the measurement of  $\Delta\gamma$  has 80%  
 635 non-CME background. This, however, relies on the assumption that the systematic uncer-  
 636 tainties of the measurements are only a few percent, and much smaller than the statistical  
 637 uncertainty. This started a large scale collaboration wide effort in synergy with the RHIC  
 638 collider accelerator department to plan for the isobar running in 2018. Based on the studies  
 639 of previous years of data from Au+Au and U+U collisions several major sources of sys-  
 640 tematics in the measurement of  $\Delta\gamma$  were identified. The major sources include: run-to-run  
 641 variation of detector response due to loss of acceptance, change in efficiency and variation  
 642 in luminosity that affects the number of reconstructed tracks in the TPC. This eventually  
 643 leads to uncorrectable systematic uncertainties in  $\Delta\gamma$ , the main observable to measure charge  
 644 separation across the event plane. In order to minimize such systematics a running proposal  
 645 was developed to: 1) switch species between each store and, 2) keep long stores with a level  
 646 luminosity; aiming for specific rates in the coincidence measurements of beam fragments  
 647 via zero-degree calorimeters. The aim was to maintain exact balance of run and detector  
 648 conditions for the two species so that observations in the two systems are equally affected  
 649 and can later on be largely eliminated in the ratios of observables.

### 650 1.2.3 Blinding of Data Sets and Preparation for Analyses

651 The procedure to blind the isobar data was already in place well ahead of the actual data  
 652 taking to limit the access of the data to the analysts to eliminate possible unconscious biases.  
 653 At the successful conclusion of the isobar run in 2018 STAR had collected more than 3 billion  
 654 events for each isobar species. A total of five institutional groups agreed to perform blind  
 655 analyses on the data. The analysts from each group will focus on a specific analysis described

656 in the following section. The substantial overlap of some analyses will help cross check the  
657 results.

658 The details of the blinding procedure and data structure were decided an analysis blinding  
659 committee (ABC) who are not part of the team of analysts but work in close collaboration  
660 with STAR experts who are part of the production team. The idea is to provide the analysts  
661 access to data where species-specific information are disguised or removed prior to the final  
662 step, shown in red in Fig. 21. Careful consideration is taken by the ABC to make sure only  
663 the essential information to do the analysis-specific quality assurance of the data is available  
664 to the analysts, to ensure the integrity of the CME Isobar analyses. The quality assurance,  
665 calibration and centrality determination work, that require species information, are done  
666 only by STAR experts who are not a part of the blind analysis team.

#### 667 1.2.4 Methods for the Isobar Blind Analyses

668 The detailed procedure for the blind analyses of isobar data have been outlined in Ref [85].  
669 Figure 21 is a cartoon that summarizes the mock-data challenge and three steps of the blind  
670 analysis.

671 The zeroth step shown, in the extreme left of Fig. 21 (orange circle), was the mock-  
672 data challenge; a crucial step to familiarize the analysts with the technicalities of the data  
673 structures that have been specifically designed for blind analysis, and ensure the blinding  
674 worked.

675 The first step shown in Fig. 21 (green circle) as the “isobar-mixed analysis” was truly the  
676 first step of the blind analysis. This was also the most challenging step from the point of  
677 view of the analysts. In this step they were provided with a data sample where each “run”  
678 comprised of events that were a mixed sample of the two species. In this step the analysts  
679 performed the full quality assurance (QA) and physics analysis of the data, documented every  
680 detail of their procedures and froze the codes. After the completion of this step, no changes  
681 to the analysis code or procedures are permissible. The only permissible change in the  
682 following step is to reject bad runs or pile-up events. However, in order to avoid unconscious  
683 bias, such rejections could not be done arbitrarily. Instead, an automated algorithm for bad  
684 run rejection was developed and corresponding codes frozen. The stability of the automated  
685 QA algorithm was tested on existing Au+Au and U+U data.

686 The second step shown in Fig. 21 (blue circle) is referred to as the “isobar-blind analysis”.  
687 For this the analysts were provided with files each of which contained data from a single,  
688 but blinded, species. From this step on-wards, the analysts were only allowed to run their  
689 previously frozen codes. The main purpose of this step was to perform run-by-run QA of  
690 the data. The files each contained a limited number of events that could not lead to any  
691 statistically significant result. Although a pseudo-run-number was used for each file, the  
692 time ordering was preserved with a unique mapping that was unknown to the analysts. It  
693 was important to maintain the time ordering to identify time-dependent changes in detectors  
694 and run conditions as a part of the run-by-run QA. A similar automated algorithm was also  
695 used for identifying and rejecting bad runs. After this step no more changes are allowed in  
696 terms of QA.

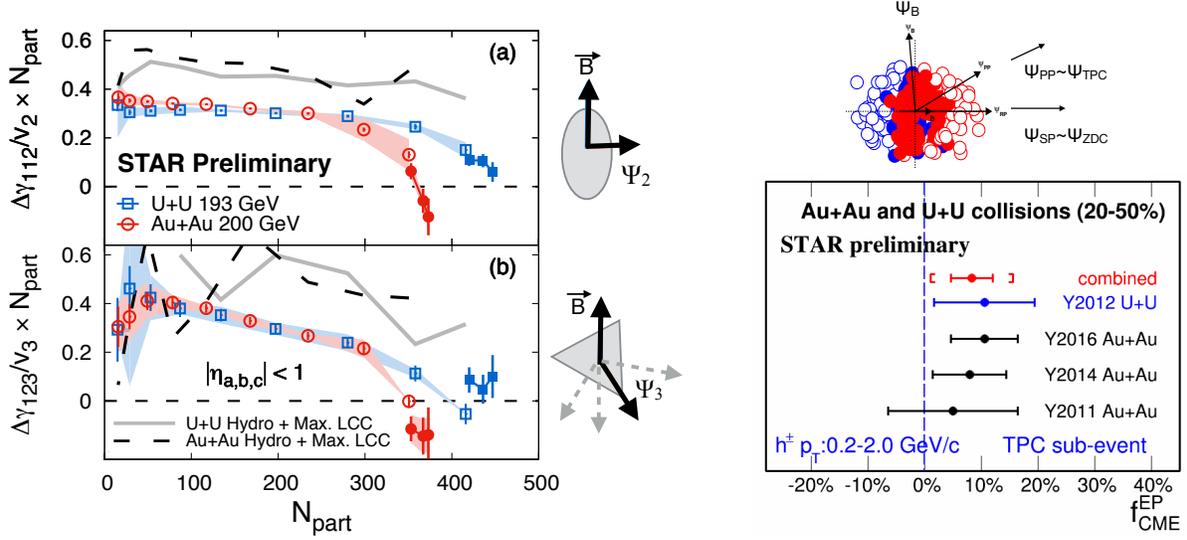


**Figure 22:** (Left) Measurement of charge separation along second and third order event planes in Au+Au and U+U collisions. (Right) Fraction of possible CME signal in the measurement of  $\Delta\gamma$  with respect to spectator and participant planes [86].

697 The final step of isobar blind analysis shown by red circle in Fig. 21 is referred to as  
 698 “isobar-unblind” analysis. In this step, the species information will be revealed and the  
 699 physics results will be produced by the analysts using the previously frozen codes. The  
 700 findings from this step will be directly submitted for publication without alteration. If a  
 701 mistake is found in the analysis code, the erroneous results will also accompany the corrected  
 702 results.

### 703 1.2.5 Observables for Isobar Blind Analyses

704 Isobar blind analysis will specifically focus on the following observables. The general strategy  
 705 is to compare two isobar species to search for a significant difference in whatever observable  
 706 used. The following sections describe these procedures in brief with comments on the out-  
 707 look for isobar blind analysis: 1) measurement of higher order harmonics of  $\gamma$ -correlator, 2)  
 708 exploiting the relative charge separation across participant and spectator planes, 3) differ-  
 709 ential measurements of  $\Delta\gamma$  to identify and quantify backgrounds, 4) the use of R-observable  
 710 to measure charge separation. The first three approaches are based on the aforementioned  
 711 three-particle correlator and the last employs slightly different approaches to quantify charge  
 712 separation. There is also another analysis which will be performed using the signed balance  
 713 function, but this is not part of the blind analyses.

#### 714 Mixed harmonics measurements with second and third order event planes:

715 In order to proceed in this section, it is better to rewrite the conventional  $\gamma$ -correlator  
 716 by a more general notation as  $\gamma_{112} = \langle \cos(\phi_a^\alpha + \phi_b^\beta - 2\Psi_2) \rangle$ . The idea is to measure

717 charge separations across the third harmonic event plane by constructing a new correla-  
 718 tor  $\Delta\gamma_{123} = \gamma_{123}(OS) - \gamma_{123}(SS)$ , where  $\gamma_{123} = \langle \cos(\phi_a^\alpha + 2\phi_b^\beta - 3\Psi_3) \rangle$  was introduced  
 719 by CMS collaboration in Ref [87]. Since the  $\Psi_3$  plane is random and not correlated to  
 720 B-field direction (see Fig. 22),  $\gamma_{123}$  is purely driven by non-CME background, the contri-  
 721 bution of which should go as  $v_3/N$ . This is very useful to contrast signal and background  
 722 scenarios by comparing measurements in the two isobaric collision systems. Since Ru+Ru  
 723 has larger B-field than Zr+Zr but comparable background, the case for CME would be  
 724 as follows:  $(\Delta\gamma_{112}/v_2)^{\text{Ru+Ru}}/(\Delta\gamma_{112}/v_2)^{\text{Zr+Zr}} > 1$  and  $(\Delta\gamma_{112}/v_2)^{\text{Ru+Ru}}/(\Delta\gamma_{112}/v_2)^{\text{Zr+Zr}} >$   
 725  $(\Delta\gamma_{123}/v_3)^{\text{Ru+Ru}}/(\Delta\gamma_{123}/v_3)^{\text{Zr+Zr}}$ . Fig. 22 (left) shows the measurement of these observables  
 726 in U+U and Au+Au collisions. Within the uncertainties of the measurements, no significant  
 727 difference in the trend of  $\Delta\gamma_{112}/v_2$  and  $\Delta\gamma_{123}/v_3$  is observed for the two collision systems  
 728 except for the very central events. Predictions from hydrodynamic model calculations with  
 729 maximum possible strength of local charge conservation [36] is shown on the same plot.  
 730 Overall observation indicates the backgrounds dominate the measurements and a similar  
 731 analysis of the isobar data is highly anticipated.

732 **Charge separation along participant and spectator planes:** This analysis makes use  
 733 of the fact that the B-field driven signal is more correlated to the spectator plane, in contrast  
 734 to flow-driven backgrounds which are maximal along the participant plane. The idea was  
 735 first introduced in Ref. [88] and later on followed up in Ref. [89]. It requires measurement  
 736 of  $\Delta\gamma$  with respect to the plane of produced particles, a proxy for the participant plane, as  
 737 well as with respect to the plane of spectators. In STAR, the two measurements can be done  
 738 by using  $\Psi_2$  from the TPC and  $\Psi_1$  from the ZDCs, respectively. The approach is based on  
 739 three main assumptions: 1) the measured  $\Delta\gamma$  has contributions from signal and background,  
 740 which can be decomposed as  $\Delta\gamma = \Delta\gamma^{\text{bkg}} + \Delta\gamma^{\text{sig}}$ , 2) the background contribution to  $\Delta\gamma$   
 741 should follow the scaling  $\Delta\gamma^{\text{bkg}}(\text{TPC})/\Delta\gamma^{\text{bkg}}(\text{ZDC}) = v_2(\text{TPC})/v_2(\text{ZDC})$  and, 3) the signal  
 742 contribution to  $\Delta\gamma$  should follow the scaling  $\Delta\gamma^{\text{sig}}(\text{TPC})/\Delta\gamma^{\text{sig}}(\text{ZDC}) = v_2(\text{ZDC})/v_2(\text{TPC})$ .  
 743 The first two have been known to be working assumptions, widely used for a long time and  
 744 can be used to test the case of CME [89] if  $(\Delta\gamma/v_2)(\text{ZDC})/(\Delta\gamma/v_2)(\text{TPC}) > 1$ . The validity  
 745 of the last one was studied and demonstrated in Ref. [88]. Using all three equations one can  
 746 extract [86] the fraction of possible CME signal  $f_{\text{CME}} = \Delta\gamma^{\text{sig}}/\Delta\gamma$  in a fully data-driven  
 747 way as shown in Fig. 22(right). This analysis will be done with the isobar data and the case  
 748 for CME will be  $f_{\text{CME}}^{\text{Ru+Ru}} > f_{\text{CME}}^{\text{Zr+Zr}} > 0$ .

749 **Differential measurements of  $\Delta\gamma$  to identify and quantify background:** *Invariant*  
 750 *mass dependence of charge separation:* Differential measurements of  $\Delta\gamma$  with invariant mass  
 751 and relative pseudorapidity provide interesting prospects to identify and quantify the sources  
 752 of flow and non-flow driven backgrounds. The idea to use invariant mass is simple and was  
 753 first introduced in Ref. [90]. Resonances are widely identified by observing structures in the  
 754 invariant mass spectra of the decay daughters. Consider a pair of opposite sign pions for  
 755 example, it is known that a large fraction of them come from the neutral resonances that  
 756 show up in the invariant mass spectrum of  $m_{\text{inv}}(\pi^+ + \pi^-)$ . If we restrict the analysis to

757 pairs of pions, differential measurements of  $\Delta\gamma$  with  $m_{inv}(\pi^+ + \pi^-)$  should also show similar  
758 peak like structures if background from neutral resonances dominate the charge separation.  
759 Indeed similar peak structures are observed and an analysis has been performed to extract  
760 the possible fraction of CME signals from the current measurements [91]. This analysis relies  
761 on the assumption that CME signals do not show peak like structures in  $m_{inv}(\pi^+ + \pi^-)$  and  
762 also requires an assumption of  $m_{inv}$  dependence of the CME signal, therefore calls for more  
763 theoretical insight in this direction have been made.

764 *Relative pseudorapidity dependence:* The relative pseudorapidity dependence of azimuthal  
765 correlations are widely studied to identify sources of long-range components that are domi-  
766 nated by early time dynamics as compared to late time correlations that are prevented by  
767 causality to appear as short-range correlations. The same can be extended to charge depen-  
768 dent correlations which provide the impetus to explore the dependence of  $\Delta\gamma$  on the pseudo-  
769 rapidity gap between the charge carrying particles  $\Delta\eta_{ab} = |\eta_a - \eta_b|$  in  $\langle \cos(\phi_a^\alpha + \phi_b^\beta - 2\Psi_{RP}) \rangle$ .  
770 Such measurements have been performed in STAR with Au+Au and U+U data. It turns  
771 out that the possible sources of short-range correlations due to photon conversion to  $e^+ - e^-$ ,  
772 HBT and Coulomb effects can be identified and described as Gaussian peaks at small  $\Delta\eta_{ab}$ ,  
773 the width and magnitude of which strongly depend on centrality and system size. Going to  
774 more peripheral centrality bins, it becomes harder and harder to identify such components  
775 as they overlap with sources of di-jets fragmentation that dominates both same-sign and  
776 opposite sign correlations. An effort to decompose different components of  $\Delta\gamma$  via study of  
777  $\Delta\eta_{ab}$  can be challenging although a clear sign of different sources of correlations are visible in  
778 change of shape of individual same-sign and opposite sign measurements of  $\gamma$ -correlator [92].

779 In any case, these differential measurements of  $\Delta\gamma$  in isobar collisions provide the prospect  
780 to extract the  $m_{inv}(\pi^+ + \pi^-)$  and  $\Delta\eta$  dependence of CME signals that will provide much  
781 deeper insights on the origin of the effect. Comparing the differential measurements in  
782 Ru+Ru and Zr+Zr it will be possible to extract the invariant mass and the relative pseu-  
783 dorapidity distribution of the CME signal that will provide deeper insight into the origin of  
784 the phenomenon.

785 **Alternate measure: The novel R-observable:** The  $R$ -observable is actually a dis-  
786 tribution, introduced in Ref. [95], and defined as the ratio of two distribution functions  
787 of the quantity  $\Delta S$  parallel and perpendicular to B-field direction defined as  $R_{\Psi_m}(\Delta S) =$   
788  $C_{\Psi_m}(\Delta S)/C_{\Psi_m}^\perp(\Delta S)$ . Here  $\Delta S$  measures the difference in the dipole moment of the positive  
789 and negative charge in an event (see Ref. [95] for details). The shape of  $R_{\Psi_2}(\Delta S)$  will be  
790 sensitive to CME as well as non-CME background, whereas  $R_{\Psi_3}(\Delta S)$  is purely driven by  
791 non-CME background and serves as a baseline. Model calculations have established several  
792 unique features of this observable: 1) presence of CME signal will lead to a concave shape of  
793 the  $R_{\Psi_2}(\Delta S)$ , 2) increasing strength of CME signal will increase the concavity of  $R_{\Psi_2}(\Delta S)$ ,  
794 3) in the presence of CME, the concavity of  $R_{\Psi_2}(\Delta S)$  will be larger than that of  $R_{\Psi_3}(\Delta S)$ .  
795 The measurement of  $R_{\Psi_m}$  is shown in Fig.23. The quantity  $\Delta S''$  shown is a slight variant of  
796 ( $\Delta S$ ) that incorporates correction for particle number fluctuations and event plane resolution.  
797 The observation of Fig.23 indicates more concave shape for  $R_{\Psi_2}$  compared to  $R_{\Psi_3}$  in Au+Au

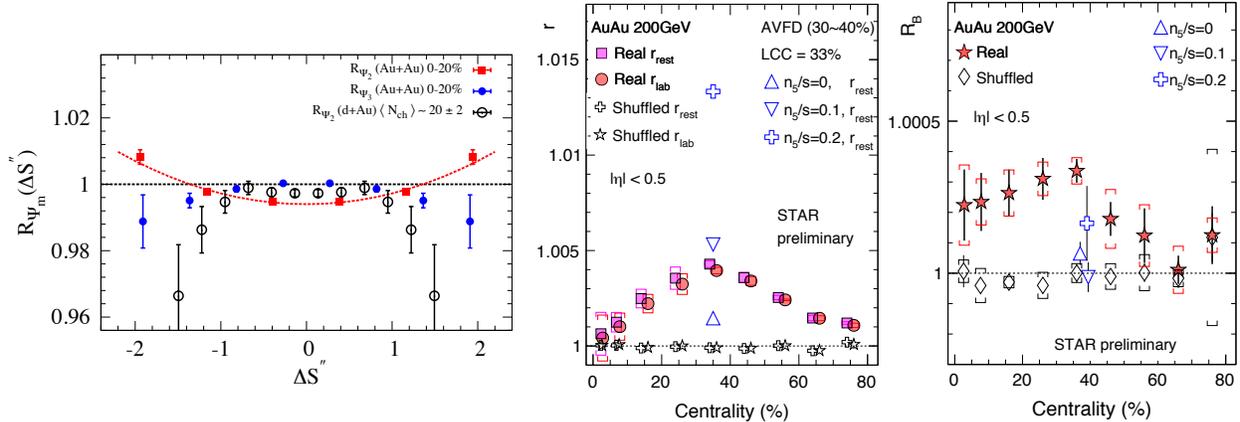


**Figure 23:** (Left) The R-observable shown for different collision systems, a concave shape is consistent with CME expectation [93]. (Right) The two main quantities  $r$  and  $R_B$  derived from the signed balance function, deviation from unity is consistent with CME expectations [94].

798 whereas flat or convex shapes for  $p/d$ +Au indicates that the measurements are consistent  
 799 with expectations of CME [93]. For isobar collisions, the case of CME will be confirmed if:  
 800 1) a concave shape is observed for the ratio of the observables  $R_{\Psi_2}(\Delta S)^{\text{Ru+Ru}}/R_{\Psi_2}(\Delta S)^{\text{Zr+Zr}}$   
 801 and 2) the concavity should be weaker for  $R_{\Psi_3}(\Delta S)^{\text{Ru+Ru}}/R_{\Psi_3}(\Delta S)^{\text{Zr+Zr}}$ .

802 **Alternate measure: The signed Balance function:** A very recently proposed observ-  
 803 able to search for CME via the signed balance function (SBF) [96]. The idea is to account  
 804 for the ordering of the momentum of charged pairs measured by the width of SBF that  
 805 is expected to be different for out-of-plane as compared to in-plane measurement captured  
 806 in the ratio  $r_{\text{lab}}$ . In addition, one can also account for the boost due to collective expansion  
 807 of the system that forces all pairs to move in the same direction and measure the  
 808 ratio in pair rest frame  $r_{\text{rest}}$ . In the presence of CME, the individual ratios, as well as the  
 809 double ratio  $R_B = r_{\text{rest}}/r_{\text{lab}}$ , are expected to be greater than unity. Preliminary measure-  
 810 ments, shown in Fig. 23 (right), from STAR in Au+Au 200 GeV data seem to be consistent  
 811 with CME expectation. This observable will be studied with the isobar data but not as a  
 812 part of the blind analysis. The CME expectation is: 1)  $r(\text{Ru} + \text{Ru}) > r(\text{Zr} + \text{Zr})$ , and 2)  
 813  $R_B(\text{Ru} + \text{Ru}) > R_B(\text{Zr} + \text{Zr})$ .

## 814 1.2.6 Prospect of CME Search Beyond the Isobar-era

815 It is important to discuss the strategy for CME search beyond the isobar-era. While it is true  
 816 that such a strategy needs to be finalized based on the outcome of the isobar program, we  
 817 would like to get started by considering two possible scenarios at top RHIC energy: 1) isobar  
 818 program results in a significance of  $3\sigma$  and below, 2) isobar program results in a significance  
 819 of  $3\sigma$  and above.

820 In the first scenario one can infer from the projection plot of Fig. 24(left) that the upper

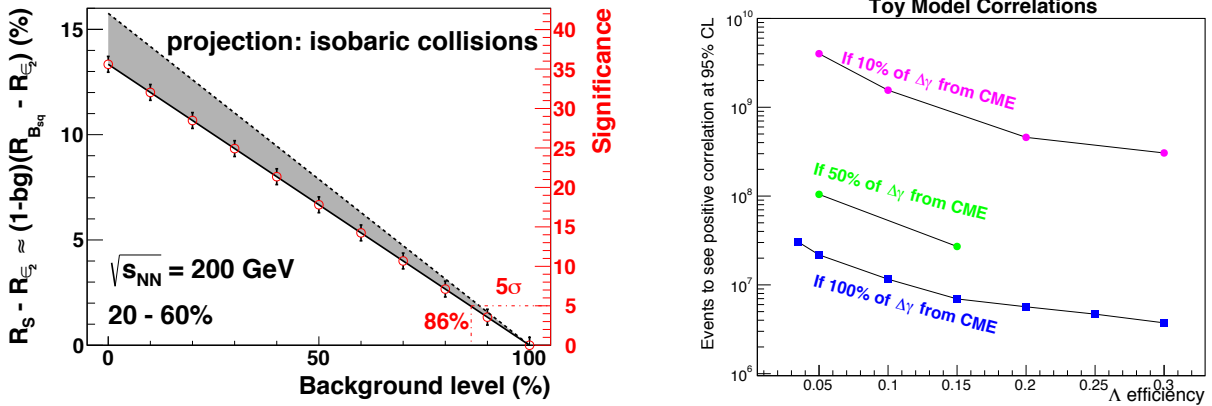


**Figure 24:** (Left) Projection plot taken from a previous beam user request document [84] indicating the anticipated significance in the measurement of charge separation as a function of the CME signal fraction prepared using 2.5 B simulated events. (Right) Estimation of the number of events required to see positive correlation between net  $\Lambda$  helicity with out-of-plane charge separation sensitive to local parity violation at 95% confidence level, plotted against the efficiency of  $\Lambda(\bar{\Lambda})$  reconstruction (see [97] for details).

821 limit of the fraction of CME signal should be less than or equal to 8%. Under such a scenario  
822 can STAR perform a follow up measurement to achieve a decisive  $5\sigma$  significance and establish  
823 a conclusive evidence of CME? It turns out such a measurement is possible even with a  
824 single Au+Au 200 GeV data set during the year 2023 running of STAR concurrently with  
825 sPHENIX. Current CME related analyses of the aforementioned Au+Au 200 GeV extraction  
826 using elliptic flow and charge separation with respect to spectator and participant planes  
827 yields 4% statistical uncertainty with 2.4 B events ( $2 - 3\sigma$  significance). In order to get  $5\sigma$   
828 significance with the same analysis one needs to have a statistical uncertainty of order 1.6%  
829 which would require about  $(4/1.6)^2 \times 2.4 = 15$  Billion events. Therefore, as per the previous  
830 estimates of anticipated 10 Billion events that can be collected by STAR during Run-23, one  
831 can achieve about  $4\sigma$  significance on the upper limit of a possible CME signal fraction in  
832 the measurement of charge separation. This estimate does not account for two important  
833 facts that can lead to higher significance and a decisive measurement. The first is that the  
834 magnitude of the projected B-field on the reaction plane is higher in Au+Au collisions as  
835 compared to isobar collisions. The second one is that the iTPC upgrade enhances the charge  
836 particle multiplicity by 50% and therefore triplet ( $\sim dN/d\eta^3$ ) (pair  $\sim dN/d\eta^2$ ) statistics by  
837 a factor of 3.4 (2.3). So the final conclusion is that even if isobar program results in a  $3\sigma$   
838 measurement running STAR in 2023 will result in a  $> 4\sigma$  measurement. This conclusion  
839 assumes that the systematic uncertainty can be controlled to be smaller than the statistical  
840 uncertainty, i.e. below 2%.

841 For the second scenario ( $> 3\sigma$  measurement from isobar program) we will also be able  
842 to establish an upper limit of the fraction of CME signal. For example, in Fig. 24(left)  
843 we see that a  $5\sigma$  significance will establish 13% CME signal and a discovery of the CME

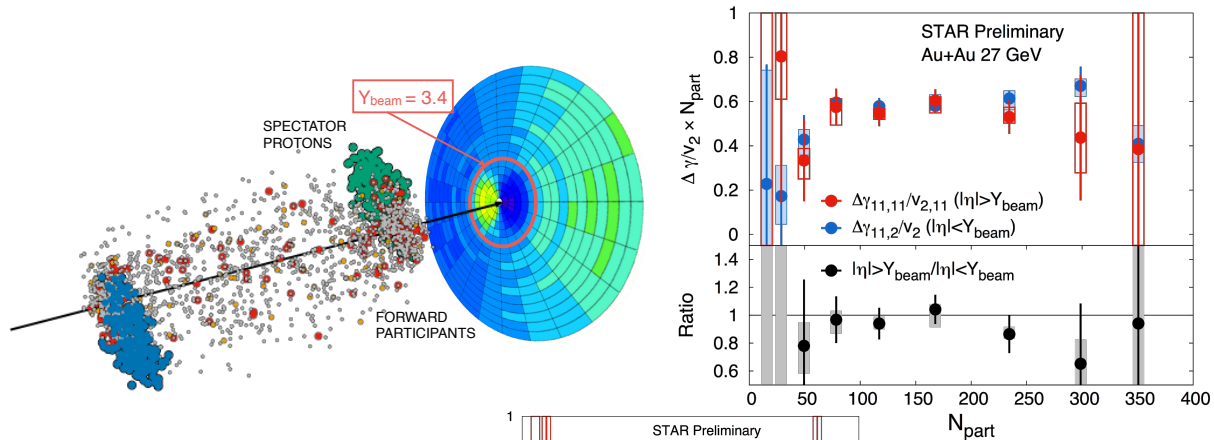


**Figure 25:** Prospect of precision CME search with the BES-II data. (Left) Single simulated UrQMD event and EPD detector acceptance that covers beam rapidity and detects both forward participants and spectators in 27 GeV Au+Au collisions that have large directed flow which changes sign at  $\eta = Y_{\text{beam}} = 3.4$ . (Right)  $\gamma$ -correlators scaled by  $v_2$  across different event-planes and double ratio of spectators/participant event planes which should be unity for no-CME scenario.

844 phenomenon in heavy-ion collisions. The impact of such a discovery will be a significant  
 845 milestone. Running STAR in 2023 concurrently with sPHENIX would be essential to perform  
 846 dedicated precision measurements to further investigate and characterize the phenomena. In  
 847 this context the STAR collaboration has started a new analysis to understand the origin  
 848 of parity violation in hot QCD by measuring the correlation of net- $\Lambda$  helicity with charge  
 849 separation across reaction plane [97]. The difference between the number of positive and  
 850 negative helicity  $\Lambda(\bar{\Lambda})$   $N_L^\Lambda - N_R^\Lambda$  should be associated with net-chirality, i.e. the difference  
 851 between right and left handed quarks, in a given event. Since net-chirality in the event also  
 852 drives out-of-plane charge separation ( $a_1$ ) in the presence of B-field, one expects a correlation  
 853 between  $a_1$  and  $N_L^\Lambda - N_R^\Lambda$  as a results of local parity violation. Currently available data sets  
 854 do not allow us to perform a significant measurement for this observable. Using a toy model  
 855 simulation, shown in Fig. 24(right), we estimate the number of events required to see non-  
 856 zero correlations between  $a_1$  and  $N_L^\Lambda - N_R^\Lambda$  at the 95% confidence level as a function of  
 857 the efficiency of  $\Lambda(\bar{\Lambda})$  reconstruction. Different curves correspond to different magnitudes  
 858 of CME fraction in the measurement of the  $\gamma$ -correlator. With about 10 B Au+Au 200  
 859 GeV events in Run-23 it will be possible to perform a significant measurement to study this  
 860 phenomenon.

861 Regardless of the outcome of the measurements with the isobar program, that will be  
 862 performed at the top RHIC energy, one question will remain. What happens at lower collision  
 863 energy? In this context a new idea has emerged. The newly installed event-plane detector  
 864 (EPD) upgrade provides a new capability at STAR towards CME search at lower collision  
 865 energy and for the Beam Energy Scan phase-II program [18]. The idea is simple, at lower  
 866 energies EPD acceptance ( $2.1 < |\eta| < 5.1$ ) falls in the region of beam rapidity ( $Y_{\text{beam}}$ ) and  
 867 can measure the plane of strong directed flow ( $\Psi_1$ ) of spectator protons, beam fragments and

868 stopped protons, therefore strongly correlated to the B-field direction (See Fig. 25). The next  
 869 step is to measure  $\Delta\gamma$  with respect to  $\Psi_1$  and compare it with the measurement of  $\Delta\gamma$  along  
 870  $\Psi_2$  planes from outer regions of EPD and TPC at mid-rapidity that are weakly correlated  
 871 to the B-field directions. A test of CME scenario will be to see if large difference is observed  
 872 in the measurements. First preliminary measurements from STAR as shown in Fig, 25 are  
 873 dominated by uncertainty but seem to show a lot of prospects for the CME search at lower  
 874 energies. With the higher statistics data from the BES-II (7.7-19.6 GeV) and fixed target  
 875 programs more precise measurements are possible.

## 876 1.3 Highlights from the Spin and Cold QCD Program

### 877 1.3.1 Introduction

878 The goal of the STAR Cold QCD program is to probe the spin and flavor structure of  
 879 the proton and understand the role of spin in Quantum Chromodynamics, exploiting the  
 880 unique capability of RHIC to provide longitudinally and transversely polarized  $p+p$  and  
 881  $p+A$  collisions at multiple energies. Measurements with longitudinal beam polarizations  
 882 have given new insights into the helicity structure of the proton, while measurements with  
 883 transverse polarizations have provided new ways to probe polarized parton distribution func-  
 884 tions (PDFs) in the collinear and transverse momentum dependent frameworks. Addition-  
 885 ally, cross-section measurements in unpolarized  $p+p$  collisions provide valuable information  
 886 to constrain collinear and transverse momentum dependent unpolarized PDFs. This pro-  
 887 gram is complemented by studies of polarized  $p+p$  elastic scattering and central exclusive  
 888 production, in which a far-forward proton is detected intact.

889 Since 2009, RHIC STAR has completed several highly successful polarized  $p+p$  runs both  
 890 at  $\sqrt{s} = 200$  GeV and  $\sqrt{s} = 500/510$  GeV. Moreover,  $p+Au$  and  $p+Al$  datasets with a trans-  
 891 versely polarized proton beam have been recorded in 2015 at  $\sqrt{s} = 200$  to address important  
 892 physics problems, including the ridge phenomenon and the possible onset of gluon satura-  
 893 tion effects. Table 5 summarizes the STAR sampled luminosity and the luminosity averaged  
 894 beam polarization as measured by the hydrogen jet (H-jet) polarimeter.

895

### 896 1.3.2 Longitudinal program

897 Since last year's PAC meeting, the STAR spin and cold QCD physics working group has  
 898 released preliminary results focused on double-spin asymmetries  $A_{LL}$  of inclusive jet [98] and  
 899 dijet [99] production in longitudinally polarized  $p+p$  collisions at a center-of-mass energy  
 900  $\sqrt{s} = 200$  GeV based on the 2015 data set. These analyses are aimed at providing additional  
 901 constraints to the gluon helicity distribution  $\Delta G(x, Q^2)$ , especially for the medium gluon  
 902 momentum fractions in the range from  $x \simeq 0.05$  to  $x \simeq 0.5$ . Figures 26 and 27 show the  
 903 preliminary results of inclusive jet  $A_{LL}$  together with the 2009 data results of Ref. [100] and  
 904 dijet  $A_{LL}$  together with the 2009 results from [101], respectively. Expected  $A_{LL}$  values for  
 905 the DSSV14 [102] and NNPDF-pol1.1 [103] parton distributions are also presented. The

**Table 5:** Summary of polarized  $p+p$  and  $p+A$  running periods at RHIC since 2009, including center-of-mass energy, STAR’s integrated luminosity and the average beam polarization for blue (B) and yellow (Y) beams from the H-jet polarimeter.

Year	System	$\sqrt{s}$ (GeV)	Recorded Lumi. ( $\text{pb}^{-1}$ )	Polarization	B/Y $\langle P \rangle$ (%)
2009	$p+p$	200	25	Longitudinal	55/55
2009	$p+p$	500	10	Longitudinal	39/39
2011	$p+p$	500	12	Longitudinal	48/48
2011	$p+p$	500	25	Transverse	48/48
2012	$p+p$	200	22	Transverse	61/56
2012	$p+p$	510	82	Longitudinal	50/53
2013	$p+p$	510	300	Longitudinal	51/52
2015	$p+p$	200	52	Transverse	53/57
2015	$p+p$	200	52	Longitudinal	53/57
2015	$p+\text{Au}$	200	0.45	Transverse	60/-
2015	$p+\text{Al}$	200	1	Transverse	54/-
2017	$p+p$	510	320	Transverse	55/55

906 results are in good agreement with previous measurements at  $\sqrt{s} = 200$  GeV and with the  
 907 theoretical evaluations of prior world data. They have better precision and thus provide  
 908 further evidence that  $\Delta G(x, Q^2)$  is positive for  $x > 0.05$ .

909 The results for the inclusive jet and dijet  $A_{LL}$  based on the 2012  $\sqrt{s} = 510$  GeV longi-  
 910 tudinally polarized  $p+p$  data, which enabled exploration of  $\Delta G(x, Q^2)$  down to  $x \simeq 0.015$ ,  
 911 were discussed in the previous PAC report and have since been published in Physical Review  
 912 D [104].

913

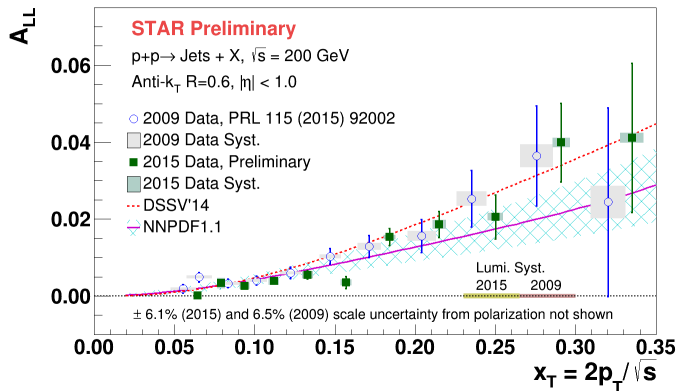


**Figure 26:**  $A_{LL}$  for inclusive jets with  $|\eta| < 1.0$  versus  $x_T$ . The filled points show 2015 preliminary results [98], whereas the open points show the 2009 data of Ref. [100]. The bars show the size of the statistical uncertainties, whereas the boxes indicate the size of systematic uncertainties. The curves show the expected  $A_{LL}$  values for the DSSV14 [102] and NNPDF-poll1.1 [103] parton distributions.

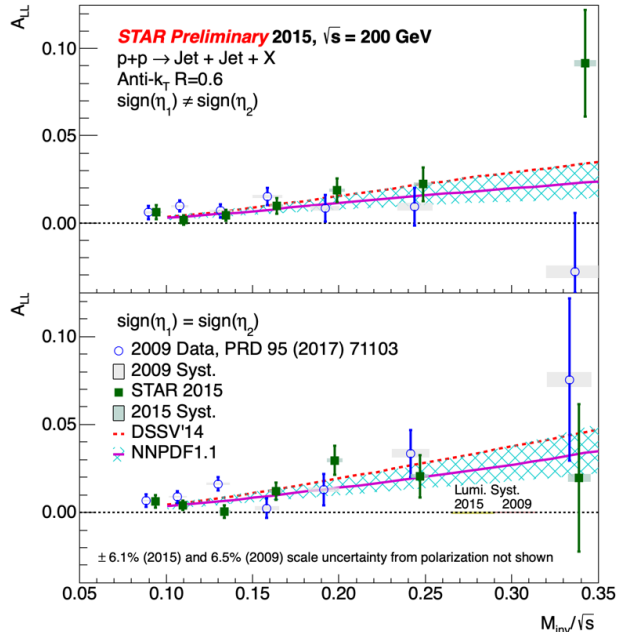


**Figure 27:**  $A_{LL}$  as a function of the parton-level invariant mass for dijets with the opposite-sign (top) and same-sign (bottom) event topologies. The filled points show 2015 preliminary results [99], whereas the open points show the 2009 data of Ref. [101]. The bars show the size of the statistical uncertainties, whereas the boxes indicate the size of systematic uncertainties. The curves show the expected  $A_{LL}$  values for the DSSV14 [102] and NNPDF-pol1.1 [103] parton distributions.

### 914 1.3.3 Transverse program

915 There have been several new STAR preliminary results on transverse spin physics released  
 916 since the last PAC meeting. Highlights include the Collins asymmetry for charged pions  
 917 inside a jet [105] and the dijet Sivvers asymmetry [106] in  $\sqrt{s} = 200$  GeV  $p+p$  collisions.  
 918 Moreover, the final publications of the transverse single spin asymmetries (TSSA) for neutral  
 919 pions produced at forward rapidity in  $\sqrt{s} = 200$  GeV for  $p+p$ ,  $p+Au$  and  $p+Al$  [107], and  
 920 500 GeV  $p+p$  [108] collisions are in God Parent Committees.

921 The Collins asymmetry in  $p+p$  collisions combines the collinear quark transversity in the  
 922 proton with the transverse momentum dependent Collins fragmentation function [109–111],  
 923 and thus provides a cleaner probe of the Collins fragmentation function than that in semi-  
 924 inclusive deep inelastic scattering (SIDIS) and enables tests of evolution, universality and  
 925 factorization breaking in the TMD formalism. Figure 28 shows the preliminary Collins  
 926 asymmetries for charged pions inside jets that scatter forward ( $x_F > 0$ ) to the polarized  
 927 beam from 2015. The measured asymmetries are consistent with previous measurements  
 928 from 2012 [112], but have 30% smaller statistical uncertainty.

929 The Sivvers effect describes the correlation of the parton transverse momentum with the  
 930 transverse spin of the nucleon. Figure 29 shows the first observation of non-zero Sivvers  
 931 asymmetries in dijet production of transversely polarized proton collisions using the STAR  
 932 2012+2015 polarized  $p+p$  data. Compared to the previous 2006 result [113], fully recon-  
 933 structed jets are analyzed with 33 times more statistics. Charge-tagging methods are em-  
 934 ployed in order to separate the  $u$  and  $d$  quark signals. With detailed simulation, the individual  
 935 parton spin-dependent  $\langle k_T \rangle$  are extracted for  $u$ ,  $d$  and  $gluon + sea$  quarks, and indicates that  
 936  $\langle k_T^u \rangle \approx 32$  MeV/ $c$ ,  $\langle k_T^d \rangle \approx -67$  MeV/ $c$  and  $\langle k_T^{g+sea} \rangle \approx 0$  MeV/ $c$ .

937 The transverse single spin asymmetry (TSSA) for forward neutral pions produced in

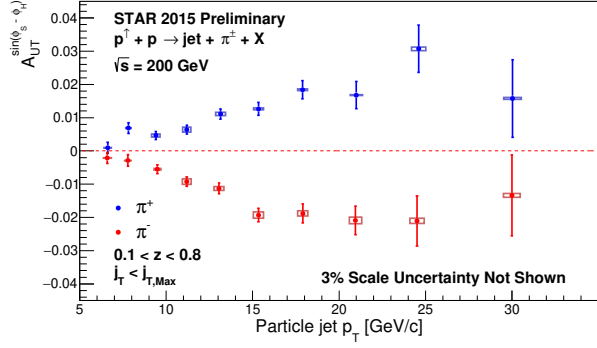


**Figure 28:** Preliminary results for the Collins asymmetry plotted for identified  $\pi^+$  (blue) and  $\pi^-$  (red) particles as a function of jet  $p_T$  for jets that scatter forward to polarized beam ( $x_F > 0$ ) [105]. The full range of both  $z$  and  $j_T$  are integrated over.

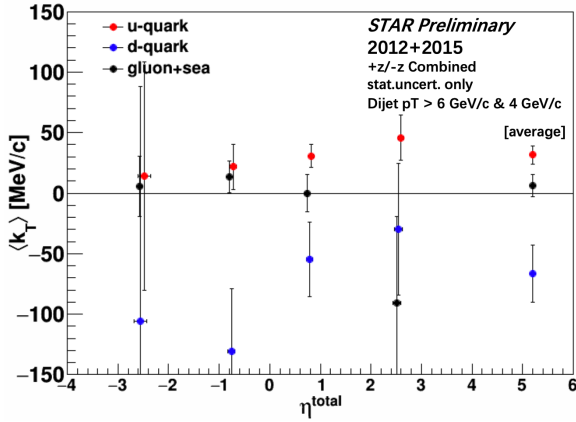


**Figure 29:** Preliminary results for the spin-dependent  $k_T$  values for  $u$ ,  $d$  and  $gluon + sea$  from the dijet Sivers measurement as a function of the sum of dijet pseudorapidities  $\eta_1 + \eta_2 \sim \ln(\frac{x_1}{x_2})$  [106].

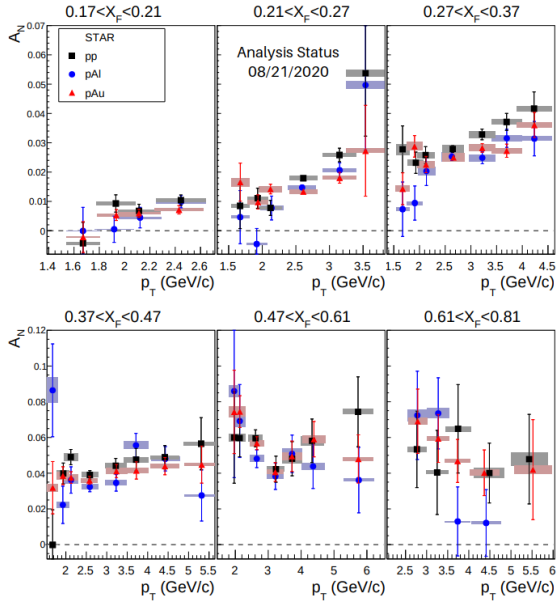


**Figure 30:** Transverse single spin asymmetry for forward  $\pi^0$  production as a function of transverse momentum for six Feynman  $x_T$  regions. Results for three collisions systems are shown, black squares for  $p+p$ , blue circles for  $p+Al$  and red triangles for  $p+Au$  collisions. The statistical uncertainties are shown with vertical error bars and the filled boxes indicate the horizontal and vertical systematic uncertainties. Analysis status on 08/21/2020. Preliminary results available in Ref. [107].

938 polarized proton collisions with protons ( $p+p$ ), with aluminum nuclei ( $p+Al$ ) and with gold  
 939 nuclei ( $p+Au$ ) at  $\sqrt{s} = 200$  GeV from FMS data are also measured using the data taken in  
 940 2015. The preliminary results for ( $p+p$ ) and ( $p+Au$ ) have been released [107], and the final  
 941 publication is soon to be submitted to Physical Review D. Measured asymmetries presented  
 942 in Fig. 30 are found to rise with transverse momentum at  $x_F < 0.5$ , while they flatten or  
 943 fall at larger  $x_F$ . The results are consistent with a weak nuclear  $A$  dependence. Moreover,  
 944 a further observation is that the TSSA is significantly larger for isolated  $\pi^0$ s than for non-  
 945 isolated  $\pi^0$ s, which are accompanied by additional jet-like fragments.

946 The transverse single-spin asymmetry of neutral pions at  $\sqrt{s} = 200$  GeV and 500 GeV  
 947 from FMS data are compared in Fig. 31. The 200 GeV data are from 2015, while the 500  
 948 GeV data are from 2011. The theoretical calculations presented in the plot are based on  
 949 the Transverse Momentum Dependent (TMD) and collinear twist-3 functions from a recent  
 950 global analysis [114], which also includes previous forward  $\pi^0$  and charged hadron TSSA data  
 951 from RHIC in the fit. The theoretical calculation differs from our measurement and only  
 952 provides a reasonable description of the non-isolated  $\pi^0$  in the low- $x_F$  region. A continu-  
 953 ous increase of the TSSA with Feynman- $x$  indicates the independence on the center-of-mass  
 954 energy. Pions with no nearby particles, which may not arise from conventional jet fragmen-  
 955 tation, tend to have a higher TSSA than non-isolated pions, which suggests that a different  
 956 mechanism other than the Sivers or Collins effects is required to explain these results.

957

### 958 1.3.4 Unpolarized Results

959 The azimuthal correlation of forward di-pions produced in  $p+p$  and  $p+Au$  collisions provides  
 960 an essential tool to access the underlying gluon dynamics in the nonlinear evolution region.

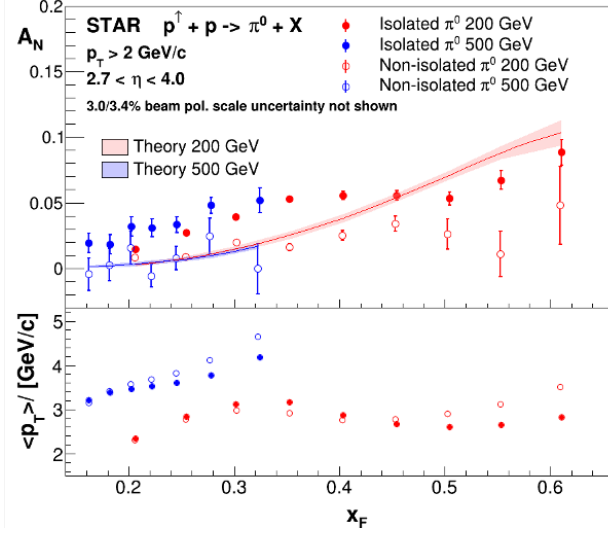


**Figure 31:** Preliminary results for the transverse single-spin asymmetry as function of Feynman- $x$  for the isolated and non-isolated  $\pi^0$  in transversely polarized  $p+p$  collisions at 200 and 500 GeV [108]. Theory curves based on a recent global fit [114] are also shown. The average transverse momentum of the  $\pi^0$  for each  $x_F$  bin is shown in the lower panel.

961  $\pi^0$  measured in the FMS in the pseudorapidity region  $2.5 < \eta < 4.0$  probe low momentum  
962 fraction partons down to  $x \approx 0.001$  at  $\sqrt{s} = 200 \text{ GeV}$ , which are dominated by gluons. 2015  
963  $p+Au$  collisions have a unique opportunity to study this phenomenon with much higher  
964 luminosities and smaller background than 2008  $d+Au$  [115]. Figure 32 shows the status  
965 of di-pion correlation measurement from Run-15  $p+p$  and  $p+Au$  collisions. The away-side  
966 peak is suppressed in high activity  $p+Au$  collisions compared with  $p+p$ . This effect is more  
967 significant when the more central part of the nucleus is probed (with higher multiplicity as  
968 indicated by BBCE). Further analysis to characterize the  $p_T$  dependence and compare with  
969 theoretical expectations is ongoing.

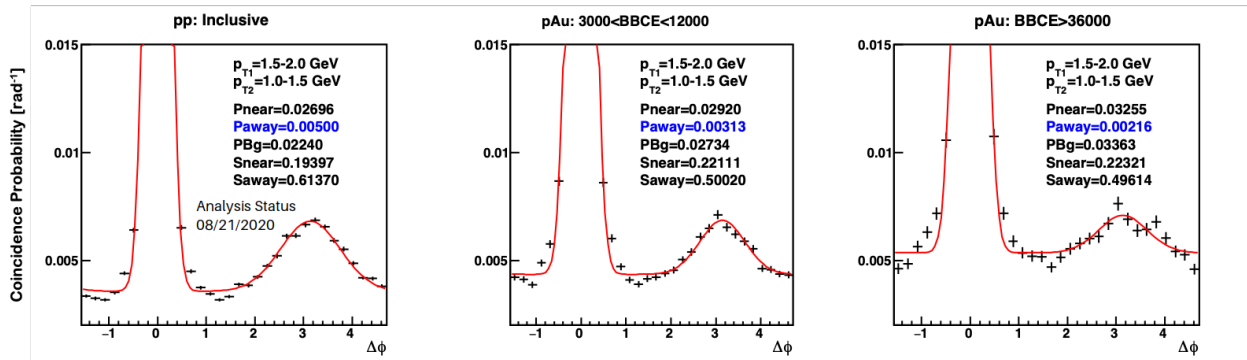


**Figure 32:** Coincidence probability as a function of azimuthal angle difference between two forward neutral pions in  $p+p$ , compared to low- and high-activity  $p+Au$  collisions. Analysis status on 08/21/2020.

970 The STAR measurement of the unpolarized cross-section ratio of the  $W^+$  and  $W^-$  bosons  
971 from the STAR 2011 to 2013 data at  $\sqrt{s} = 500/510 \text{ GeV}$  has released preliminary results [116]  
972 and is soon to be submitted to Physical Review D. Figure 33 shows the ratio plotted as a  
973 function of lepton pseudorapidity. This unique measurement is sensitive to the unpolarized

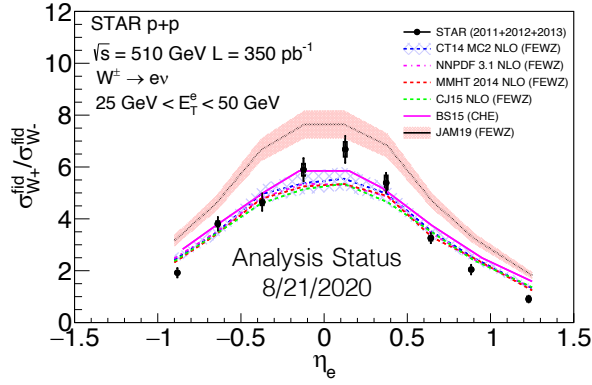


**Figure 33:**  $W^+$  and  $W^-$  cross-section ratio as a function of lepton pseudorapidity for the combined 2011, 2012, and 2013 datasets. The central values correspond to the mean value of  $\eta_e$  distribution for that bin. The error bars represent the statistical uncertainty, whereas the rectangular boxes represent the systematic uncertainty for the respective data point. These measurements are compared to various theory frameworks, which use several different PDF inputs. Analysis status on 08/21/2020. Preliminary results available in Ref. [116].

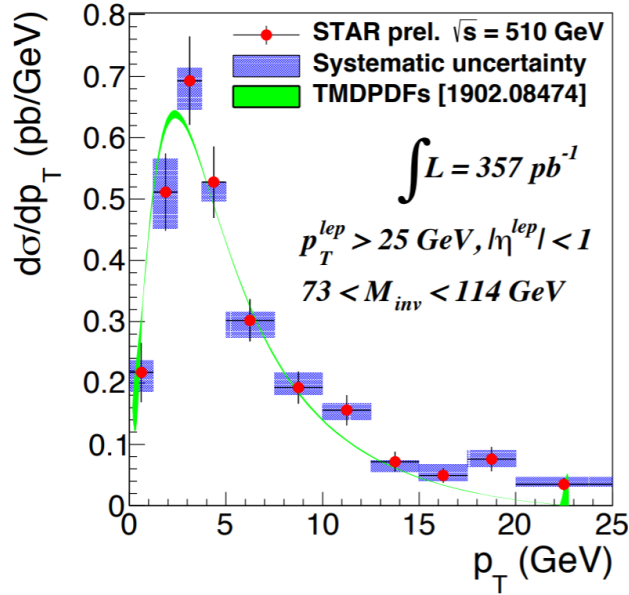


**Figure 34:** Preliminary results for the differential cross-section of  $Z^0$ -bosons as function of transverse momentum  $p_T$  [119] and comparison with theory predictions based on calculations developed in [120]. Results are based on data from 2011-2013.

974  $\bar{d}/\bar{u}$  quark distribution and will provide insights into unpolarized light quark distributions  
 975  $\bar{d}(x)$  and  $\bar{u}(x)$  at  $x > 0.05$ . The measurement at STAR is complementary to the Drell-Yan  
 976 results from NuSea [117] and SeaQuest [118], covering the overlapping  $x$  region of about  
 977  $0.1 - 0.3$  at higher  $Q^2 = M_W^2$ .

978 Differential cross sections of  $Z^0$ -boson production as function of transverse momentum  
 979 are valuable input to global fits of TMD parton distribution functions, and STAR kinematics  
 980 ( $0.1 < x < 0.3$ ) are complementary to LHC and Tevatron data. Figure 34 shows preliminary  
 981 results from 2011-2013 data with an integrated luminosity of  $350 \text{ pb}^{-1}$  [119]. Data on disk  
 982 from 2017 comprise about the same luminosity, and preliminary results are expected soon  
 983 along with transverse single-spin asymmetries. While the measurement of  $Z^0$ -bosons is an  
 984 experimentally very clean observable, it requires a good understanding of the calorimeter  
 985 performance. These will inform the on-going background studies of the measurements of  
 986 Sivers asymmetries for  $W$ -bosons, which are also expected very soon.

## 1.4 Run-20 Performance

In this section, we will review the BES-II collider and fixed-target performance to date. Careful study of these performance metrics will be used to make projections about the required time to complete the 7.7 GeV collider system in Run-21.

The BES-II collider program performance is over-viewed in Table 6. The 27 GeV system, which was run in 2018, was not officially part of the BES-II physics program, however it is close enough in energy to help provide some performance evaluation. The most important lines in the table from the point of view of performance evaluation are the *good event rate*, which is a measure of the useful luminosity, and the *data hours per day*. In general, we had seen improvements over the luminosities recorded in 2010/2011 of a factor of three to four. For the 27 GeV system, which was run in 2018 we saw the good event rate rise to 620 Hz, which implies a luminosity increase of factor of 3.3 over the 2011 performance.

The 19.6 GeV system was completed in 2019. For this system, the good event rate rose from 100 Hz in 2011 to 400 Hz in 2019 for a factor of 4.0 increase. We should note that it took 5.1 calendar weeks to complete the energy, however during the running period for the 19.6 GeV system, the facility was dedicating two twelve hour shifts per week to LEReC development. Correcting the 5.1 calendar weeks by 6/7 means that 4.4 beam weeks were used to complete this energy which should be compared to the 4.5 weeks which was requested in the STAR BUR for 2019. Historically, it has been shown that the luminosities scale with  $\gamma^2$  above injection energy (9.8 GeV) and with  $\gamma^3$  below injection energy. Scaling the 27 GeV performance would have predicted a good event rate of 330 Hz at 19.6 GeV. One should also note that the number of events recorded exceeded the required number significantly. Overall, the performance for the 19.6 GeV system significantly exceeded expectations.

The 14.6 GeV system was completed in 2019. This energy had been run previously in 2014, however the STAR good event rate was unusually low at that time so comparing the 23 Hz rate from 2014 to the 170 Hz rate in 2019 is not a good metric for performance. It required 8.6 calendar weeks to complete the required number of events, however during the running of the 14.6 GeV system, 40% of the beam time was used for LEReC development. Scaling the 8.6 calendar weeks by 60% yields effectively 5.1 weeks of beam time which favorably compares with the 5.5 weeks estimated in the BUR for 2019. Using the performance at 19.6 GeV (good event rate of 400 Hz), and the  $\gamma^3$  scaling, we would have expected a good event rate at 14.6 GeV of 165 Hz. This compares well the the 170 Hz rate which was achieved for this energy. Performance at this energy slightly exceeded expectations.

The 11.5 GeV system was completed in 2020. The good event rate rose from 30 Hz in 2010 to 80 Hz in 2020 for a factor of 2.67 increase. It took 8.9 calendar weeks achieve the required event statistics. In the BUR for 2020 a range from 7.5 (optimistic) to 10 (pessimistic) was proposed. The actual time required fell in the middle of the expected range. Scaling the good event rate from 14.6 GeV by  $\gamma^3$  predicted that the good event rate for 11.5 GeV would be 83 Hz, which compares favorably with the 80 Hz actually achieved for the run. Overall, performance at this energy met expectations.

The 9.2 GeV system was completed on September 1st, 2020. This energy was not run during BES-I, so there is not a historical comparison. Scaling the good event rate from

1029 11.5 GeV by  $\gamma^3$  predicts that we should have seen a good event rate of 38 Hz. Prior to  
1030 the shutdown of the laboratory in March, we had achieved an average good event rate of  
1031 38 Hz and we had been averaging 16 hours of data taking per day, however the challenges  
1032 of running in the summer have reduced the average number of hours of data taking to 13  
1033 and the average good event rate to 33. The 14.5 weeks taken to achieve the required event  
1034 statistics, is at the high end of the range that was included in the BUR for 2020.

1035 Quality assurance studies of the BES-II and FXT data indicate that roughly 98% of the  
1036 data recorded will ultimately be used in physics analyses. The quality assurance takes place  
1037 on multiple levels. At the time of data acquisition, online performance plots are reviewed  
1038 as each run starts by the shift crew member. There are two levels of online plots; the first  
1039 use the raw detector specific data to overview the performance of all systems; the second  
1040 level does event-by-events tracking and vertex reconstruction using the High Level Trigger  
1041 (HLT) computer farm to generate event level performance plots and to tag the good Au+Au  
1042 collision events. The next level of quality assurance uses a FastOffline production of a small  
1043 percentage of all recorded events. The plots generated by this review take place on a daily  
1044 basis a provide the opportunity for corrections to any issues that might arise. A third level  
1045 of quality assurance takes place in a weekly QA meeting which reviews the overlap between  
1046 the events flagged as good from the HLT system, a significant fraction of which are recorded  
1047 and available to preliminary offline physics analysis, and the events identified as good using  
1048 the FastOffline processed data, which utilizes a more sophisticated tracking algorithm. The  
1049 overlap of good events has been at the 98% level for all BES-II collider and FXT systems.  
1050 The QA meeting also reviews preliminary physics working group quality assurance analysis  
1051 of the FastOffline data sets. The final level of quality assurance comes from preliminary  
1052 physics analyses using the FastOffline and the ExpressStream data sets. This multi-level to  
1053 quality assurance guarantees that the data will meet the needs of the physics analyses for  
1054 the BES-II science program.

1055 The relevant data sets recorded in 2018 have been fully calibrated and produced. These  
1056 data sets are the 27 GeV collider system and the 3.0 and 7.2 GeV FXT data sets. Preliminary  
1057 results for all of the key physics analyses have been performed and highlights of these new  
1058 results are reviewed in the previous section of this document. The 2019 data sets have  
1059 required extensive calibrations of the new detector systems, the iTPC and the eTOF. The  
1060 large volume of cosmic ray data that were recorded have been used to do the fine spatial  
1061 alignment of the new iTPC modules. New methods needed to be developed to calibrate  
1062 the precise start timing for each event, which is needed to get the correct reconstruction of  
1063 the  $z$ -location of the hits in the TPC to account for the long bunches used to maximize the  
1064 luminosity for BES-II and the FXT programs. The complete set of calibrations for the first  
1065 collider energy from 2019, the 19.6 GeV system, have been completed and a test production  
1066 using these calibrations has been generated and are undergoing quality control.

1067 As several of the physics opportunities discussed in the following sub-sections utilize fixed-  
1068 target systems, it is best to review the performance in this mode of operation. An overview of  
1069 the performance for all fixed-target energies is shown in table 7. The first fixed-target physics  
1070 run was in 2018 using a 3.85 GeV beam. A total of four and half days was spent on this

**Table 6:** Achieved and projected experiment performance criteria for the BES-II collider program.

Collision Energy (GeV)	7.7	9.2	11.5	14.6	17.1	19.6	27
Performance in BES-I	2010	NA	2010	2014	NA	2011	2011
Good Events (M)	4.3	NA	11.7	12.6	NA	36	70
Days running	19	NA	10	21	NA	9	8
Data Hours per day	11	NA	12	10	NA	9	10
Fill Length (min)	10	NA	20	60	NA	30	60
Good Event Rate (Hz)	7	NA	30	23	NA	100	190
Max DAQ Rate (Hz)	80	NA	140	1000	NA	500	1200
Performance in BES-II ( <b>achieved</b> )	2021	2020	2020	2019	2021	2019	2018
Required Number of Events	100	160	230	300	250	400	NA
<b>Achieved Number of Events</b>	2.9	<b>162</b>	<b>235</b>	<b>324</b>	TBD	<b>582</b>	<b>560</b>
fill length (min)	20-45	<b>45</b>	<b>25</b>	<b>45</b>	50	<b>60</b>	<b>120</b>
Good Event Rate (Hz)	16-24	<b>33</b>	<b>80</b>	<b>170</b>	265	<b>400</b>	<b>620</b>
Max DAQ rate (Hz)	400	<b>700</b>	<b>550</b>	<b>800</b>	1300	<b>1800</b>	<b>2200</b>
Data Hours per day	12-15	<b>13</b>	<b>13</b>	<b>9</b>	15	<b>10</b>	<b>9</b>
Projected number of weeks	11-20	8.5-14	7.6-10	5.5	2.5	4.5	NA
weeks to reach goals	TBD	<b>14.6</b>	<b>8.9</b>	<b>8.6</b>	TBD	<b>5.1</b>	<b>4.0</b>

1071 system; first developing the conduct of operation and then recording a robust data sample.  
1072 The lowest energy beam was selected for this first run in 2018 because at that time the  
1073 iTPC and eTOF upgrades were not yet available; the lowest beam energy means the lowest  
1074 center-of-mass boost, which meant that we could still complete the physics program even  
1075 without the detector upgrades. Additionally in 2018, fixed-target data were recorded with  
1076 a single beam energy of 26.5 GeV. Obviously, at such a high energy the detector upgrades  
1077 would be essential for the mid-rapidity physics program. However, the 26.5 GeV beam  
1078 was not requested by STAR; this beam was being using by the Coherent Electron Cooling  
1079 program, and STAR was simply taking these data parasitically. This parasitic data taking  
1080 gave us further opportunities to refine the fixed-target conduct of operations, which gave us  
1081 confidence going forward that we could average 100 M good events per day in fixed-target  
1082 mode. This is limited by the STAR data acquisition system and not by RHIC.

1083 In 2019, eTOF detector upgrade system suffered damage at the start of the 14.6 GeV  
1084 collider system. This meant that it would be unavailable for any fixed-target energies taken  
1085 that year. It was felt that the physics program could still be achieved using the 4.59 GeV  
1086 beam, but that for all higher energies the loss of the eTOF system would compromise the  
1087 physics, so only modest samples at 5.75 and 31.2 GeV were taken.

1088 The eTOF detector was repaired for 2020, and relatively early in the run it was decided  
1089 to spend one week cycling through the seven remaining fixed-target energies. Roughly one  
1090 day was spent at each energy. The conclusion from this series of fixed target energies is

1091 that the collider and the experiment can quickly and efficiently set up and run fixed-target  
 1092 systems. STAR can efficiently trigger on good fixed-target events with roughly 80-90% of  
 1093 triggers passing the HLTgood test. The operators monitor the STAR event rate to keep the  
 1094 current on target at a level to keep the STAR DAQ system running at full capacity and  
 1095 minimizing the pile-up of multiple collisions in the target. Stores last for many hours (8-24  
 1096 hours) and refill and realignment are fast and efficient.

1097 Preliminary physics results from the 3.0 and 7.2 GeV data sets recorded in 2018 are  
 1098 available and highlights have been shown the the previous sections. Internal preliminary  
 1099 physics analyses of the ExpressStream and FastOffline data sets have been performed and  
 1100 these confirm the quality of the data taken.

**Table 7:** Event statistics (in millions) needed in the fixed-target part of the BES-II program for various observables, and the total number of events acquired (those events taken in 2018 did not include the iTPC or eTOF detectors; those taken in 2019 did not include the eTOF).

$\sqrt{s_{NN}}$ (GeV)	3.0	3.2	3.5	3.9	4.5	5.2	6.2	7.2	7.7
Beam Energy	3.85	4.59	5.75	7.3	9.8	13.5	19.5	26.5	31.2
$\mu_B$ (MeV)	721	699	666	633	589	541	487	443	420
Rapidity $y_{CM}$	1.06	1.13	1.25	1.37	1.52	1.68	1.87	2.02	2.10
<b>Observables</b>									
Elliptic Flow	300	150	80	40	20	40	60	70	80
CME	70	60	50	50	50	70	80	90	100
Directed Flow	20	30	35	45	50	60	70	80	90
Femtoscopy	60	50	40	50	65	70	80	90	100
Kurtosis	36	50	75	125	200	400	950	NA	NA
Strange hadrons	300	100	60	40	25	30	50	75	100
Hypertritons	200	100	80	50	50	60	70	85	100
<b>Event Totals</b>									
Good events (2018)	258							158	
Good events (2019)	3.7	200	53						50
Good events (2020)			116	117	108	103	118	TBD	112

## 1101 2 Proposed Program - Hot QCD in Run-21, 23, and 25

### 1102 2.1 Beam Request for Run-21

#### 1103 2.1.1 Completion of the BES-II Program

1104 The highest priority for Run-21 is the completion of the proposed BES-II program. At  
1105 this time, the only system that remains to be taken is the 7.7 GeV collider data set. This  
1106 energy is extremely important for several reasons. First, theoretical calculations suggest  
1107 that the highest baryon density is achieved in collisions at this energy; second, several of the  
1108 BES-I experimental signatures which have been put forth to be sensitive to the presence of  
1109 deconfined matter either lose significance or are no longer present at this energy; third, the  
1110 BES-I data showed enhanced fluctuations at this energy; finally, this energy provides the  
1111 best acceptance overlap with the fixed-target program. Although the 7.7 GeV collider data  
1112 set is extremely important from the point of view of the science, it is also technically the  
1113 most challenging data set. The technical challenge of achieving a viable collision rate at this  
1114 energy was the motivation to develop the Low Energy RHIC electron Cooling (LEReC) and  
1115 is the reason that this energy has been left to the final year of the program.

1116 The specific physics goals (and required statistics) include: measurement of the elliptic  
1117 flow of the phi meson for which the the constituent quark scaling was suggested to break  
1118 down in the lowest energy BES-I data (80 M events required); measurement of the correlators  
1119 associated with the charge separation induced by the chiral magnetic effect which were seen  
1120 to collapse at the lowest BES-I energies (50 M events required); differential measurements of  
1121 the directed flow of protons which was seen to show evidence of a softening of the equation of  
1122 state in the lowest BES-I data (20 M events required); Azimuthal femtoscopy measurements  
1123 of protons to study the tilt angle of the source (35 M events required); measurement of the  
1124 net-proton kurtosis which showed significant enhanced fluctuations at 7.7 GeV in the BES-I  
1125 data (70 M events required); measurements of the di-lepton invariant mass distributions to  
1126 determine in the excess in the low mass region is proportional to the total baryon density  
1127 (100 M events required); and the global lambda polarization to determine the magnetic field  
1128 significance (50 M events required). These analyses are being pursued at all of the BES-II  
1129 collider energies; for several of the physics measurements, the 7.7 GeV energy is expected to  
1130 be either the most significant or the most challenging.

1131 The 7.7 GeV collider system provides the essential bridge between the collider and fixed-  
1132 target energy scans. Although in later sections we detail a request to acquire fixed-target  
1133 data at higher overlap energies, there is the largest region of common coverage at this energy.  
1134 This will provide critical cross checks between the different modes.

1135 Although the 7.7 GeV collider system is the most technically challenging system of the  
1136 suite of BES-II and FXT energies, one can use the performances which have already been  
1137 achieved during the BES-II program to help develop projections for the 7.7 GeV collider  
1138 energy. These BES-II performance trends have been detailed in 6. In 2010, STAR achieved  
1139 a good event rate of 7 Hz; a factor of three improvement would result in a 21 Hz rate. Scaling  
1140 the performance at 9.2 GeV by  $\gamma^3$  would predict a good event rate of 19.3 Hz. We project the

1141 good event rate to fall between 16 and 24 Hz. We project the range of hours of data taking  
 1142 per day to fall between 12 and 15. These numbers suggest a range in the expected number  
 1143 of weeks to reach the goals from 11 to 20 weeks. We should note that CAD has provided  
 1144 projections which suggest that it will take 28 weeks to reach the goals. Our projections are  
 1145 more optimistic. Although we recognize that it is likely that running the 7.7 system will  
 1146 require all the available beam time in 2021, the optimistic range of our predictions suggests  
 1147 that we should prepare for success and we have therefore considered and prioritized other  
 1148 programs which could be run in 2021 if time were to be available.

### 1149 **2.1.2 Au+Au Collisions in FXT Mode at $\sqrt{s_{\text{NN}}} = 3.0$ GeV - I: 300 million goal**

1150 QCD matter at high baryon chemical potential region contains a wealth of unexplored physics  
 1151 and is one the central focus of current and future heavy-ion collision programs in few GeV  
 1152 energy range around the world. RHIC has been able to deliver beams with the energy  
 1153 as low as 3.85 GeV per nucleon. Utilizing the gold fixed target (FXT) installed in the  
 1154 STAR experiment, we were able to record collision events at the center-of-mass-energy as  
 1155 low as  $\sqrt{s_{\text{NN}}} = 3.0$  GeV, which corresponds to baryon chemical potential of  $\mu_B \sim 720$  MeV  
 1156 in central collisions. The STAR detector configuration (including the iTPC and eTOF) has  
 1157 full midrapidity coverage ( $|y| < 0.5$ ) at this energy and enables us to carry a systematic  
 1158 investigation of the dynamics of the QCD matter created in these collisions at  $\sqrt{s_{\text{NN}}}$  from  
 1159 3.0 up to 200 GeV.

1160 At such a high  $\mu_B$  region and moderate temperatures, baryon dynamics become important  
 1161 or even dominant in understanding the QCD matter properties. Strange quarks, due to their  
 1162 heavier masses, play an important role in study the high net-baryon density QCD matter.  
 1163 The combination of increased sensitivity of strange quarks with the existing high baryon  
 1164 density in low energy heavy-ion collisions offers a unique condition to create various light  
 1165 hypernuclei, which enables us to study *e.g.* the hyperon-nucleon ( $Y$ - $N$ ) interactions, which  
 1166 have potential implications for the inner structure of compact stars in nuclear astrophysics.

1167 STAR has collected  $\sim 250$  million FXT Au+Au events at  $\sqrt{s_{\text{NN}}} = 3.0$  GeV in 2018  
 1168 before iTPC and eTOF were installed.. We propose to collect a minimum of 300 million  
 1169 events with the extended phase-space coverage enabled by iTPC and eTOF for the following  
 1170 measurements:

- 1171 • high moments of proton multiplicity distributions covering the same midrapidity ac-  
 1172 ceptance  $|y| < 0.5$ ,  $0.4 < p_T < 2.0$  GeV/ $c$ , comparable to that with the BES-I and BES-II  
 1173 measurements in collider mode.
- 1174 • precision  $\phi$  meson production at midrapidity to test the validity of Canonical Ensemble  
 1175 (CE) for strangeness production at high baryon density region.
- 1176 • systematic measurements of lifetime, binding energy, production yield, collective flow  
 1177 of light hypernuclei ( ${}^3_{\Lambda}\text{H}$ ,  ${}^4_{\Lambda}\text{H}$ ,  ${}^5_{\Lambda}\text{He}$  etc.).
- 1178 • measurement of low- and intermediate-mass dileptons to extract fireball lifetime, its  
 1179 average temperature and to access the microscopic properties of matter. This would

1180  
1181

be the first measurement of electromagnetic radiation at this energy which will guide the future high  $\mu_B$  facilities at FAIR and NICA.

1182  
1183

With additional beam time allowed, we would like to further collect up to 2 billion Au+Au FXT events at  $\sqrt{s_{NN}} = 3.0$  GeV which will be elaborated in the next section.

1184  
1185  
1186  
1187

One feature we would like to point out is that the single beam energy for FXT collisions at  $\sqrt{s_{NN}} = 3.0$  GeV is 3.85 GeV per nucleon, the same beam energy to be used for colliding to collect the major 7.7 GeV collision dataset in Run-21. This leads to a negligible transition time for operation between  $\sqrt{s_{NN}} = 7.7$  GeV collider mode and  $\sqrt{s_{NN}} = 3.0$  GeV FXT mode.

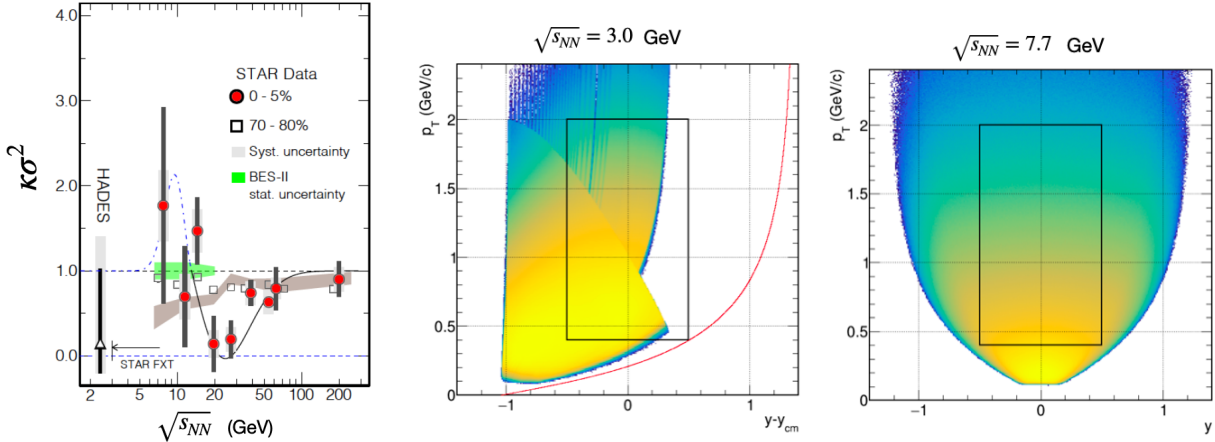


**Figure 35:** (Left) The net-proton  $\kappa\sigma^2$  in most central (0-5%) and peripheral (70-80%) Au+Au collisions as a function of collision energy. (Middle/Right) Proton acceptance plot  $p_T$  vs.  $y$  in the center-of-mass frame at  $\sqrt{s_{NN}} = 3.0$  GeV (FXT data from Run-18) and 7.7 GeV (collider data from Run-10), respectively. The red curve in the middle panel indicates the acceptance boundary with iTPC and eTOF.

1188  
1189  
1190  
1191  
1192  
1193  
1194  
1195  
1196  
1197  
1198  
1199  
1200  
1201

**High moments of proton multiplicity distributions:** A non-monotonic behavior of net-proton high moments  $\kappa\sigma^2$  as a function of collision energy has been suggested to be an evidence of the existence of QCD critical point [121, 122]. Figure 35 (left panel) shows the final STAR measurement from the BES-I data as a function of energy exhibiting a suggestive non-monotonic behavior [123, 124]. A complete picture of the non-monotonic behavior requires measurements at collision energies below the lowest collider mode energy (7.7 GeV) by utilizing the FXT mode collisions. STAR detector configuration has the best midrapidity coverage for fixed target collisions at the lowest collision energy  $\sqrt{s_{NN}} = 3.0$  GeV. Figure 35 middle and right panels show the proton acceptance with TPC and barrel TOF in Run-18 FXT data at 3.0 GeV and Run-10 collider data at 7.7 GeV, respectively. In the 2018 FXT data, to ensure  $> 95\%$  purity of the proton sample, one needs to utilize the barrel TOF for high momentum particle identification. With this requirement, the proton acceptance in Run-18 covers full negative rapidity region ( $-0.5 < y < 0$ ,  $0.4 < p_T < 2.0$  GeV/c), while missing a considerable acceptance in the positive rapidity region. A new run, with

1202 eTOF and iTPC, would allow for phase space coverage comparable to the one in collider  
 1203 mode (indicated by the box in the middle panel). The estimated acceptance boundary for  
 1204 protons is indicated by the red line shown in Fig. 35 middle panel. We can therefore cover  
 1205 the full midrapidity  $|y| < 0.5$  region from  $0.4 < p_T < 2.0$  GeV/ $c$  which will be the same as  
 1206 these measurements conducted in collider mode data, shown in the right panel. This would  
 1207 allow to perform a systematic scan of the net-proton high moments analysis within the same  
 1208 mid-rapidity acceptance across the collision energy from 3.0 up to 200 GeV. In the meantime,  
 1209 the increased rapidity coverage will also enable us to investigate the rapidity-window ( $\Delta y$ )  
 1210 dependence of these fluctuations, which will offer us deep understanding on the physics origin  
 1211 through the development of these fluctuations vs.  $\Delta y$  [125].

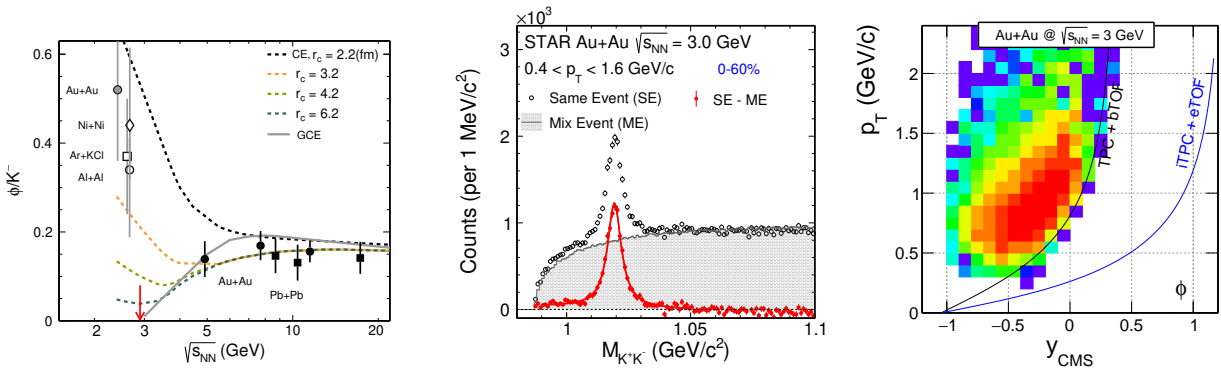


**Figure 36:** (Left)  $\phi/K^-$  ratio as a function of collision energy from several heavy-ion experiments in comparison to thermal model calculations assuming strangeness following GCE and CE with different canonical radius. (Middle) Invariant mass distributions of  $K^+K^-$  pairs and the  $\phi$  meson signal in Run-18 FXT data at  $\sqrt{s_{NN}} = 3.0$  GeV. (Right) Reconstructed  $\phi$  meson candidate phase space distributions using Run-18 FXT data taken at  $\sqrt{s_{NN}} = 3.0$  GeV. The black line shows the boundary of combining the TPC and barrel TOF detector for kaon identification. The blue line indicates the anticipated boundary extended by iTPC and eTOF for kaon identification in the proposed Run-21 FXT run at  $\sqrt{s_{NN}} = 3.0$  GeV.

1212  **$\phi$  meson production:** Yields of strange hadron produced in relativistic heavy-ion collisions  
 1213 from RHIC BES-I energies up to the LHC energy ( $\sqrt{s_{NN}} = 7.7-5500$  GeV) can be  
 1214 well described by thermal model with Grand Canonical Ensemble (GCE) in which strange  
 1215 quark number is conserved on average [126–129]. It has been argued that at low energy  
 1216 heavy-ion collisions when the fireball created in these collisions becomes small enough the  
 1217 GCE for strange quarks will break down. Strangeness needs to be conserved on the event-  
 1218 by-event basis, therefore only Canonical Ensemble (CE) is applicable to strange hadron  
 1219 production [127, 129]. Strange hadrons with finite strangeness number (e.g.  $K$ ,  $\Lambda$  etc.) will  
 1220 suffer from a suppression due to the strangeness number conservation, often characterized  
 1221 by a canonical radius ( $r_c$ ) for strange quark profile in comparison to the regular radius ( $r$ )  
 1222 for light quarks [130, 131]. The  $\phi$  meson is the lightest bound state of  $s$  and  $\bar{s}$  quarks with  
 1223 zero net-strangeness number. Its production yield, on the contrary, will not suffer from the

1224 canonical suppression. Therefore CE models predict the  $\phi/K^-$  ratio will show an enhance-  
 1225 ment in very low energy heavy-ion collisions while GCE models calculate the  $\phi/K^-$  ratio will  
 1226 gradually drop to zero at the  $\phi$  production threshold in  $p+p$  collisions. ( $\sqrt{s_{\text{NN}}} = 2.89$  GeV).

1227 Experimentally, the measured  $\phi/K^-$  values stay around 0.15 at  $\sqrt{s_{\text{NN}}} > 5$  GeV up to  
 1228 the LHC energy. At collision energies below the  $\phi$  production threshold in  $p+p$  collisions,  
 1229 measurements from HADES and FOPI suggest an enhancement compared to those at high  
 1230 energies, consistent with the CE description for strange quarks at such low energies within  
 1231 appreciable uncertainties [132, 133]. High precision measurement of the  $\phi/K^-$  at such low  
 1232 energies will be of great interest to systematic investigate the  $\phi$  meson and strangeness  
 1233 production mechanism in heavy-ion collisions.

1234 We have performed such a measurement using the FXT data at  $\sqrt{s_{\text{NN}}} = 3$  GeV taken  
 1235 in 2018. Fig. 36 middle panel shows the reconstructed  $K^+K^-$  invariant mass distributions  
 1236 in 0-60% centrality. The shaded histogram shows the  $K^+K^-$  pair distributions from the  
 1237 mixed-event technique while normalized at the mass region above the  $\phi$  meson signal. The  
 1238 red data points show the mixed-event background subtracted distributions and the  $\phi$  meson  
 1239 signal obtained in this data is about  $60\sigma$ . The right panel shows the  $\phi$  meson acceptance  
 1240 coverage in center-of-mass frame. Due to the small production yield of kaons, one needs to  
 1241 rely on clean particle identification using TOF detector to obtain a control background in  
 1242 the  $\phi$  meson reconstruction. The black curve indicates the single track acceptance boundary  
 1243 from TPC and barrel TOF in 2018 year run. One can see the  $\phi$  meson  $p_T$  acceptance at  
 1244 midrapidity is limited at  $\sim 0.6$ - $0.8$  GeV/ $c$ . This covers roughly only 40% of the  $\phi$  meson yield  
 1245 in the full  $p_T$  region, leading to a considerable amount of systematic uncertainty due to the  
 1246  $p_T$  extrapolation. The blue curve in the same panel indicates the anticipated single track  
 1247 boundary with iTPC and eTOF. The  $p_T$  lower limit can be extended down to  $\sim 0.2$  GeV/ $c$ ,  
 1248 yielding a  $p_T$  coverage of  $\sim 90\%$  of total  $dN/dy$  at midrapidity. This will greatly reduce the  
 1249 systematic uncertainty in the total  $\phi$  meson yield measurement.

1250 We therefore request to take the FXT data at  $\sqrt{s_{\text{NN}}} = 3$  GeV with iTPC and eTOF  
 1251 detectors in RHIC Run-21. A roughly similar amount of statistics (300 million) will allow  
 1252 us to perform the measurement of  $\phi/K^-$  ratio with high precision both statistically and  
 1253 systematically.

1254 **Hypernuclei production:** Hypernuclei are those nuclei with one or more nucleons re-  
 1255 placed with hyperons (typically  $\Lambda$ s). The study of hypernuclei lifetime, binding energy and  
 1256 their production mechanism offer insights to the understanding of hyperon-nucleon ( $Y-N$ )  
 1257 interactions. The  $Y-N$  interactions could have significant implications to our understanding  
 1258 of the internal structure of compact stars in nuclear astrophysics.

1259 Heavy-ion collisions have shown great potential in studying the light hypernuclei proper-  
 1260 ties and their production mechanism. There have been unprecedented measurements from  
 1261 RHIC and LHC on both the lifetime and binding energy (anti-)hypertriton ( ${}^3_{\Lambda}\text{H}$  and  ${}^3_{\bar{\Lambda}}\text{H}$ ). At  
 1262 low energy heavy-ion collisions, due to the high baryon density and high strangeness popu-  
 1263 lation, statistical hadronization thermal model predicts a significant enhancement of various  
 1264 light hypernuclei production yield, shown in Fig. 37 left panel [134]. The STAR FXT energy

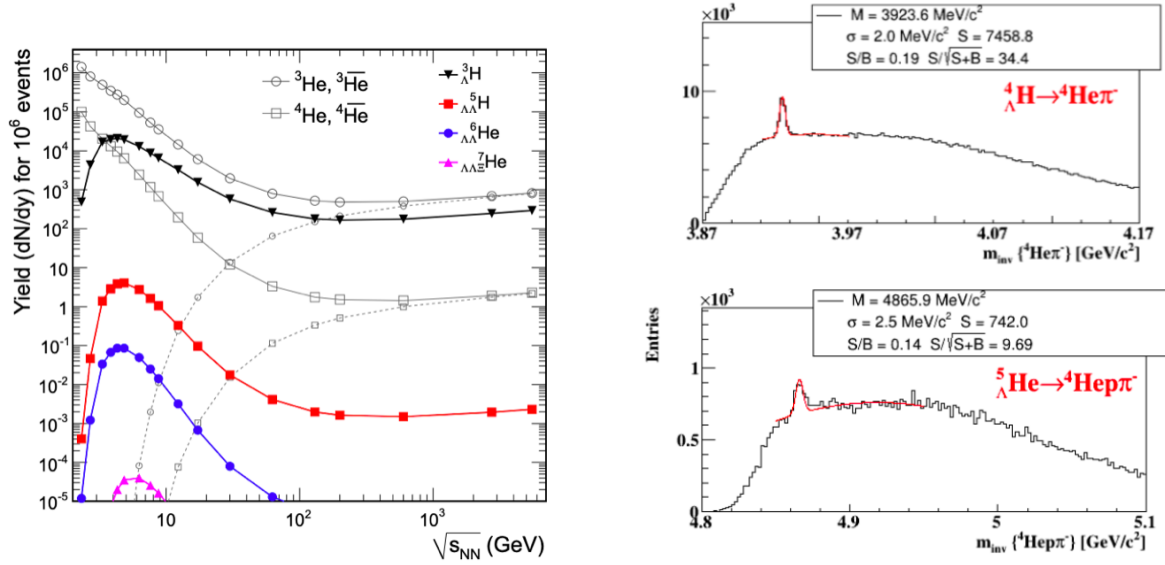


**Figure 37:** (Left) Thermal model predictions of various light nuclei and hypernuclei production yield at midrapidity in central heavy-ion collisions as a function of collision energy [134]. (Right) Invariant mass distribution of  ${}^4\text{He}\pi^-$  (top)  ${}^4\text{He}\pi^-$  (bottom) from 2018 FXT data at  $\sqrt{s_{NN}} = 3.0$  GeV. The  ${}^4_{\Lambda}\text{H}$  and  ${}^5_{\Lambda}\text{He}$  hypernuclei signal is clearly visible on top of background.

1265 region from  $\sqrt{s_{NN}} = 3.0 - 7.7$  GeV sits nicely in the maximum mid-rapidity production yield  
 1266 of various hypernuclei while STAR detector layout has the best midrapidity acceptance cov-  
 1267 erage at 3.0 GeV. Figure 37 right panel shows the reconstructed  ${}^4_{\Lambda}\text{H}$  and  ${}^5_{\Lambda}\text{He}$  signal from the  
 1268 Run-18 FXT dataset at  $\sqrt{s_{NN}} = 3.0$  GeV. These are so far the most unprecedented statistics  
 1269 on these light nuclei that will allow us to systematically investigate their lifetimes, binding  
 1270 energies as well as their production yield and collective flow behavior in heavy-ion collisions.

### 1271 2.1.3 Au+Au Collisions in FXT Mode at $\sqrt{s_{NN}} = 9.2, 11.5, \text{ and } 13.7$ GeV

1272 The BES-II program aims to study the nature of QCD matter by varying the temperature  
 1273 and baryon chemical potential. High baryon chemical potentials are achieved by ‘stopping’  
 1274 the baryons which made up the two colliding nuclei. To better understand the development  
 1275 of the baryon chemical potential and its profile through the interaction region, it is necessary  
 1276 to study the rapidity density distribution of the protons across a broad range in rapidity. It  
 1277 is important that the rapidity range covered includes the peak of the participant distribution  
 1278 which have been accelerated during the collision process. For all collider energies available  
 1279 at RHIC (7.7 GeV and above), the peak of the rapidity distribution of the stopped protons  
 1280 is outside or at the edge of the acceptance of the STAR TPC (which only extends 0.6 units  
 1281 beyond mid-rapidity with particle identification via  $dE/dx$ , this is extended to 1.0 units  
 1282 of rapidity using eTOF particle ID); for  $\sqrt{s_{NN}} = 9.2, 11.5, \text{ and } 13.7$  GeV, the shifted 0.9,  
 1283 1.0, and 1.1 units away from mid-rapidity respectively. However, in fixed-target mode the  
 1284 STAR detector is excellent for studies of stopping as the acceptance extends 1.7 units from

1285 target rapidity (see figure 38) toward mid-rapidity; for  $\sqrt{s_{\text{NN}}} = 9.2, 11.5, \text{ and } 13.7$  GeV,  
1286  $y_{\text{CM}} = 2.28, 2.50, \text{ and } 2.68$  respectively. Combining collider and fixed-target measurements  
1287 at each energy will provide full coverage from target rapidity to center-of-mass rapidity. The  
1288 stopping of the incident protons is the key to changing the baryon chemical potential in the  
1289 interaction region and the changing baryon chemical potential is the key to mapping out the  
1290 phase diagram of QCD matter.

1291 Complete rapidity density distribution for identified particles will provide important con-  
1292 straints for models. It has been noted by Shen [135] that the high rapidity tails of the  $dN/dy$   
1293 distributions are very important and that high rapidity data are rare. In the energy range  
1294 from  $\sqrt{s_{\text{NN}}} = 5.0$  to 200 GeV, the only available proton rapidity density distribution mea-  
1295 surements are from NA49 at 8.77 and 17.3 GeV [136] and from BRAHMS at 62.4 and 200  
1296 GeV [137]. Shen used these data to constrain his 3-D models of the collisions to better un-  
1297 derstand the elliptic flow measurements in heavy-ion collisions. In the BES-II energy range,  
1298 around 10 GeV, these models can set strong constraints on the dependence of Quark-Gluon  
1299 Plasma shear viscosity on temperature and net baryon chemical, however, in order to do so,  
1300 it is necessary to have knowledge of the rapidity distributions of net-protons and produced  
1301 particles.

1302 It has been proposed that the trend of the rapidity shift of the stopped protons with  
1303 collision energy will provide a signature of the softening of the equation of state at the phase  
1304 transition [138]. Specifically, the model which has a two phase equation of state shows that  
1305 the increase in the rapidity shift with collision energy stalls in the  $\sqrt{s_{\text{NN}}} = 8$  to 12 GeV  
1306 range.

1307 We proposed to extend the studies to proton stopping through the BES-II energy regime.  
1308 Specifically we propose to add three more energies to the high end of the FXT energy range.  
1309 These energies are chosen to provide three more overlap energies with the collider program.  
1310 Single beam energies of 44.5, 70, and 100 GeV will provide interactions at  $\sqrt{s_{\text{NN}}} = 9.2,$   
1311  $11.5, \text{ and } 13.7$  GeV (the top energy is not quite an overlap energy with the 14.6 GeV  
1312 collider system). Combining the midrapidity coverage from the collider mode and the target  
1313 rapidity coverage from the fixed-target mode will provide full rapidity coverage for inclusive  
1314 observables. Since the focus for program will be inclusive observables, 50 M events will be  
1315 sufficient at each energy. We propose that at each of these three energies, twelve hours be  
1316 spent on beam development and twelve hours be spent taking data.

## 1317 2.2 Further Opportunities in Run-21

1318 S

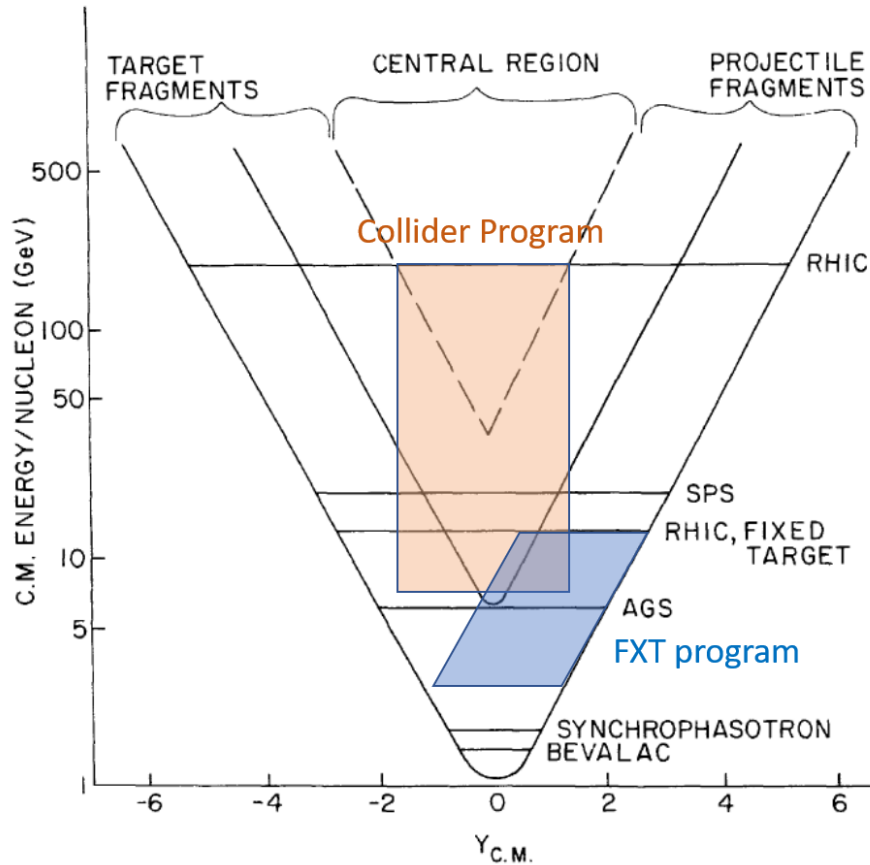


**Figure 38:** This figure has been modified from a figure in the introduction of the Conceptual Design Report for the RHIC facility. The black lines indicate different regions in the rapidity - center of mass energy space. The ‘V’ shaped region in the top center of the figure which is labeled at the central region have been predicted and demonstrate to be a low baryon chemical potential region characterized by a continuous phase transition between the QG and the hadron gas. The outer ‘V’ shaped region is dominated by the target fragments. Colored regions are overlaid to indicate the coverage of the STAR detector for collider (Orange) and FXT (Blue) modes. For the three higher energies currently being proposed, the FXT acceptance covers the region dominated by target fragments while the collider acceptance covers the equilibrated central region.

1319 **2.2.1 Small System Run: O+O at  $\sqrt{s_{NN}} = 200$  GeV**

1320 **Introduction:** Collective long-range azimuthal correlations in A+A collisions have been  
 1321 successfully described as a hydrodynamic response by a fluid-like system to geometric shape  
 1322 fluctuations in the initial state. In recent years, observation of similar collective phenomena  
 1323 in small-system collisions, such as  $p+p$  and  $p+A$  collisions, have attracted wide interest in the  
 1324 community. The interpretation of a fluid-like state formed there has been challenged, as the  
 1325 small size and short lifetime might prevent the system from quickly thermalizing and evolu-  
 1326 ting hydrodynamically. Instead, collectivity arising either from initial momentum correlations

1327 motivated by gluon saturation models [139] or via a few scatterings among partons (without  
 1328 hydrodynamization) [140–142] has been proposed as alternative sources that may be domi-  
 1329 nant in small systems. Lots of experimental and theoretical efforts have been devoted to the  
 1330 study of collectivity in small-system collisions, with the goal of understanding the time-scale  
 1331 for the emergence of collectivity and the mechanism for early-time hydrodynamization in  
 1332 large collision systems.

1333 One key feature that distinguishes initial momentum correlation models (ISM) from final-  
 1334 state interaction models (FSM, including hydrodynamics or a few scatterings) is the connec-  
 1335 tion to the initial-state geometry [143]. In FSM, the collectivity is a geometrical response to  
 1336 initial shape fluctuations, i.e.,  $v_n$  is approximately proportional to the  $n^{\text{th}}$ -order initial-state  
 1337 eccentricity  $\varepsilon_n$ . In ISM, such a geometrical response is expected to be absent [144]. It was  
 1338 proposed that a geometry scan of various colliding systems with different spatial eccentricities  
 1339 can help distinguish between contributions of these two scenarios [145].

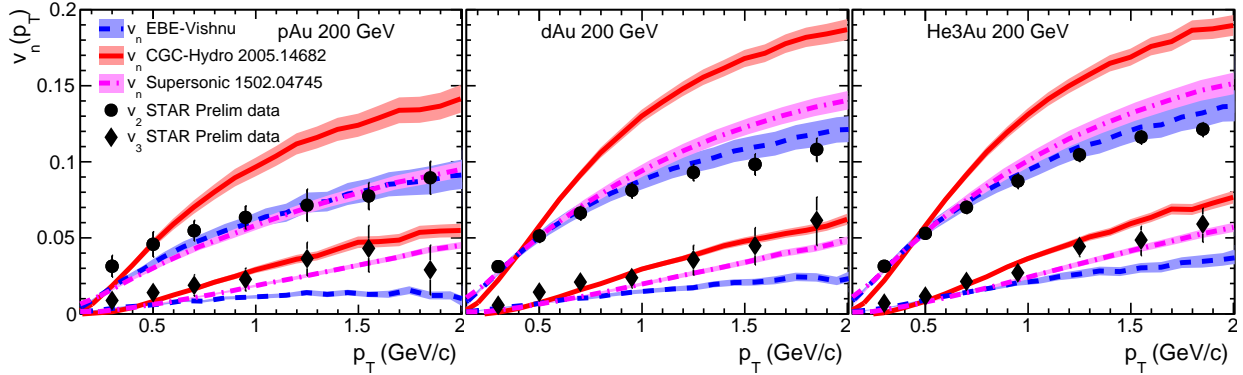


**Figure 39:** Comparison of  $v_2$  and  $v_3$  in  $p$ +Au,  $d$ +Au and  $^3\text{He}$ +Au collisions at  $\sqrt{s_{\text{NN}}}=200$  between STAR data and various model calculations. STAR data from Fig. 11.

1340 Such a small system scan program has been recently carried out at RHIC for a few  
 1341 asymmetric small systems including  $p$ +Au,  $d$ +Au and  $^3\text{He}$ +Au, where studies of elliptic  
 1342 flow ( $v_2$ ) and triangular flow ( $v_3$ ) have been performed [43, 146, 147]. In a Glauber model  
 1343 that only considers the fluctuations of nucleon positions [145],  $\varepsilon_2$  in  $d$ +Au and  $^3\text{He}$ +Au is  
 1344 expected to be larger than in  $p$ +Au, while  $\varepsilon_3$  in  $p$ +Au and  $d$ +Au are expected to be smaller  
 1345 than in  $^3\text{He}$ +Au. However, once the fluctuations at subnucleonic scales are included [144],  
 1346 the  $\varepsilon_3$  are expected to be similar among all three systems. Figure 39 compares the STAR  $v_2$   
 1347 and  $v_3$  results with three hydrodynamic models predictions with different assumptions about  
 1348 the initial state. Calculations [148, 149] that include both initial momentum anisotropy and  
 1349 hydrodynamic response to subnucleonic fluctuations indeed describe the STAR  $v_3$  data in all  
 1350 three systems, but one of the models [148] overestimates the  $v_2$  data. On the other hand, the  
 1351 hydrodynamic model based on fluctuations only at nucleonic level [150] fails to describe the  
 1352  $v_3$  data. This implies that the initial state in these asymmetric small collision systems are  
 1353 not well constrained, in particular in  $p$ +Au and  $d$ +Au system (there is reasonable consensus  
 1354 that the flow results in  $^3\text{He}$ +Au is dominated by FSM). The relative importance of FSM vs.  
 1355 ISM for the  $v_n$  data in small systems is an area of intense debate [151].

1356 **Physics case for a small A+A scan:** So far, both RHIC and the LHC carried out  
 1357 collisions for either relatively large systems (Pb+Pb, Au+Au, Xe+Xe, Cu+Cu, ...), which  
 1358 are well described by hydrodynamic models, or small asymmetric systems ( $p$ +Pb,  $p$ +Au,  
 1359  $d$ +Au, and  $^3\text{He}$ +Au), whose initial state are poorly constrained as discussed above. To  
 1360 quantitatively understand the initial momentum anisotropy and the role of subnucleonic  
 1361 fluctuations, collisions of small but symmetric systems, such as O+O, Al+Al and Ar+Ar  
 1362 will be necessary. They will also fill the gap between  $p$ + $p$  and Cu+Cu systems, which is  
 1363 a crucial unexplored frontier<sup>1</sup>, where a transition from ISM to FSM dominated collectivity  
 1364 may be observable. The list of key open questions related to collectivity in small systems  
 1365 includes:

- 1366 • How much do initial-state correlations vs. geometry-driven final-state interactions con-  
 1367 tribute to the observed collectivity? Can we unambiguously establish experimental  
 1368 evidence of initial-state correlations?
- 1369 • For final-state scenarios, to what extent does the collectivity arise from a hydrodynamic  
 1370 fluid-like QGP, as opposed to an off-equilibrium system with only a few scatterings per  
 1371 parton?
- 1372 • What is the role of subnucleonic fluctuations in determining the initial-state geometry?
- 1373 • Can we observe jet quenching in small systems?

1374 In principle, a scan of colliding ion species at RHIC by systematically varying the system size  
 1375 and geometry between  $p$ + $p$  and Cu+Cu collisions, will provide an unique lever-arm to dial  
 1376 contributions from various mechanisms and impose strong constraints on both ISM and FSM.  
 1377 Since the last RHIC  $p/d/\text{He}$ +Au scan, the STAR experiment has completed several detector  
 1378 upgrades that extend  $p_T$  and particle identification to  $|\eta| < 1.5$ , and provide centrality and  
 1379 event plane determination in  $2.1 < |\eta| < 5.1$  [17, 152, 153]. This extended detector capability  
 1380 will allow a full exploration of collectivity using all the observables and methods developed  
 1381 for large systems at RHIC/LHC. We will have better control of the non-flow systematics,  
 1382 leading to a better understanding of the multi-particle nature of the collectivity and the  
 1383 longitudinal correlations to constrain the full 3D initial conditions. As an illustration, model  
 1384 studies of  $v_2$  and  $v_3$  in a series of small systems including symmetric (C+C, O+O, Al+Al,  
 1385 Ar+Ar) and asymmetric ( $p$ +Au,  $d$ +Au,  $^4\text{He}$ +Au) collisions using the AMPT model are  
 1386 shown in Fig. 40. AMPT belongs to the category of final-state interaction models, where  
 1387  $v_n$  is largely driven by the geometry of initial nucleon distributions. The  $v_2$  values from  
 1388 asymmetric systems follow different trends from symmetric systems: the  $v_2$  in  $d/{}^4\text{He}$ +Au  
 1389 increases with  $N_{\text{ch}}$ , while it is relatively constant in  $p$ +Au. The  $v_3$  values show a similar  $N_{\text{ch}}$   
 1390 dependence as symmetric systems, except for  $d$ +Au which deviates from the common trend  
 1391 at large  $N_{\text{ch}}$ . This study demonstrates that, in a scenario driven by final-state interactions,  
 1392 a clear difference is expected between  $d/{}^4\text{He}$ +Au and A+A for  $v_2$ , while a relatively similar

---

<sup>1</sup>RHIC has no limitation on small A+A systems for the rate requested, based on private communication with Wolfram Fischer

1393 behavior should be observed for  $v_3$ . Contributions from other sources, especially ISM, are  
 1394 expected to follow a drastically different behavior; as the system size increases, the ISM  
 1395 contribution will gradually become subdominant. In this proposal, we shall focus on a short  
 1396 O+O run, which should already help us to address many of the points raised above.

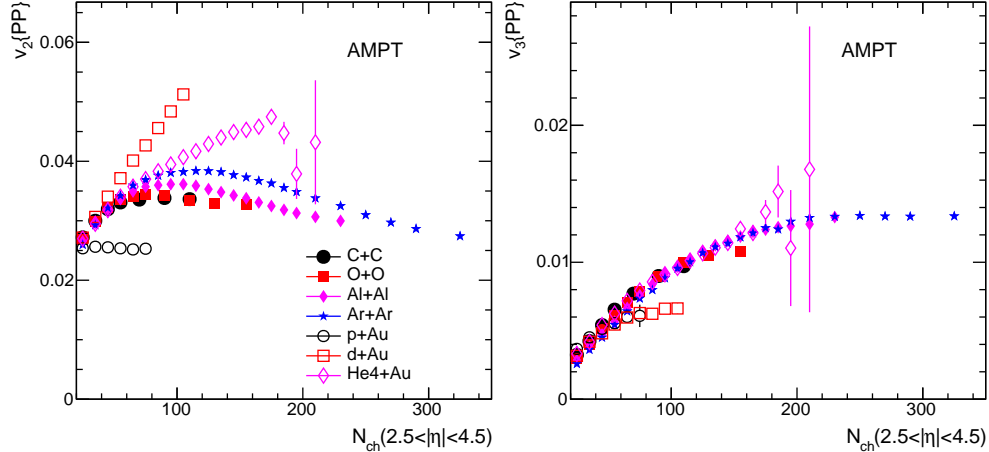
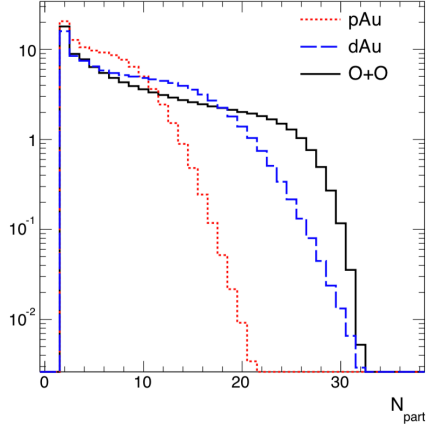


**Figure 40:** (Left) AMPT predictions for  $v_2$  and (Right)  $v_3$  as a function of  $N_{ch}$  in four symmetric and three asymmetric small collision systems. Figure from [154].

1397 **Arguments for a short O+O run in 2021:** In this BUR, we propose a O+O run at  
 1398  $\sqrt{s_{NN}} = 200$  GeV towards the end of the BES-II in 2021. The choice of O+O collisions  
 1399 as the starting point is motivated by the following reasons: 1) O+O has an  $N_{part}$  coverage  
 1400 comparable to  $p$ +Au and  $d$ +Au but with a much flatter distribution (see Fig. 41), which  
 1401 allows much better control of initial geometry and centrality bias, 2) Oxygen is a reasonably  
 1402 sized system for which the both the nucleonic and subnucleonic DOF are important, which  
 1403 together with  $p/d$ +Au data can be used disentangle these contributions, 3) a strong synergy  
 1404 with the proposed higher-energy O+O run at the LHC around 2023–2024 to enable a direct  
 1405 comparison of the same small-system collision species at drastically different energies. More  
 1406 details, including hydrodynamic model predictions, are presented and discussed below.

1407 The recent yellow report on the future LHC heavy-ion physics program discusses the  
 1408 possibility for smaller A+A collisions [155]. This includes a proposal of an O+O run at  
 1409  $\sqrt{s_{NN}} = 2.76$ –7 TeV in 2022<sup>2</sup>, and other light-ion species such as Ar+Ar beyond 2028. As  
 1410 mentioned earlier, one big advantage of the O+O system is that it allows a better control  
 1411 of  $N_{part}$  and  $\varepsilon_n$ , compared to peripheral Pb+Pb collisions [155]. An O+O run at RHIC  
 1412 right after the BES-II would provide a timely comparison of the same small system at very  
 1413 different collision energies (0.2 TeV vs. 2.76–7 TeV). This “RHIC-LHC energy scan” provides  
 1414 a unique opportunity to study systems with nearly identical initial nucleon geometry but  
 1415 very different subnucleonic fluctuations and different saturation scales [148]. The large lever-  
 1416 arm in collision energy should provide new insights on the onset behavior of collectivity,

<sup>2</sup>According to the latest schedule of the LHC run 3, O+O run will most likely be scheduled in 2023.



	pAu	dAu	<sup>16</sup> O+ <sup>16</sup> O
$\langle N_{\text{part}} \rangle$	5.8	8.8	9.5

**Figure 41:** The  $N_{\text{part}}$  distribution in O+O collisions compared with  $p$ +Au and  $d$ +Au collisions at  $\sqrt{s_{\text{NN}}} = 200$  GeV estimated from Glauber model. The table to the right shows the average  $N_{\text{part}}$  values in the three systems.

1417 jet quenching, energy dependence of initial state, or any other final-state effects in small  
 1418 systems: any model has to describe results at both energies, which naturally leads to a  
 1419 better understanding of results at each energy.

1420 Figure 42 compares the  $v_n(p_{\text{T}})$  data and hydrodynamic calculations for  $n = 2$  and 3 at  
 1421 two energies in large A+A systems (left) and in  $p$ +A systems (right). It is well-known that  
 1422  $v_n(p_{\text{T}})$  for charged hadrons in large systems has very little  $\sqrt{s_{\text{NN}}}$  dependence from RHIC  
 1423 to LHC [156], as well as from 39 to 200 GeV at RHIC [157, 158]. This is confirmed by the  
 1424 left panel which compares Pb+Pb [159] with Au+Au [160] data at 30–40% centrality, as  
 1425 well as calculations from the CGC-Hydro model. However, a comparison of  $v_n(p_{\text{T}})$  between  
 1426  $p$ +Pb [161] and  $p$ +Au [147] central data suggests a small difference in  $v_2$ , while the  $v_3$  data  
 1427 are nearly identical. In the FSM picture, this suggests that the contributions of subnucleonic  
 1428 fluctuations to the initial eccentricities are very different between the two collision energies.  
 1429 In the ISM picture, it may be the result of an energy dependence of initial momentum  
 1430 anisotropy. It would be exciting to see whether the  $\sqrt{s_{\text{NN}}}$  dependence for  $v_2$  and  $v_3$  in  $p$ +A  
 1431 collisions also persists in small A+A systems such as O+O collisions between RHIC and  
 1432 LHC. The CGC-Hydro model calculations of  $v_2$  and  $v_3$  in O+O collisions at RHIC and  
 1433 the LHC energies are shown in Fig. 42 (middle), where a split in both  $v_2$  and  $v_3$  between  
 1434 two energies is predicted. These rather non-trivial  $\sqrt{s}$  dependence across different collision  
 1435 systems reflects the rich physics mechanisms behind origin of collectivity.

1436 We propose a one-week O+O program in 2021 right after BES-II. Assuming a total  
 1437 interaction rate of  $\sim 10$ – $15$  kHz (based on recent isobar runs), the STAR DAQ rate of 2 kHz  
 1438 and the RHIC uptime of 50% (12 hour/day), tentative numbers of events we expect to record  
 1439 for different triggers are summarized in Table 8 for a one week run. Note that we do not  
 1440 have an estimation of minimum-bias trigger efficiency at this point, and assumed it to be  
 1441  $\sim 100\%$ .

1442 The event statistics listed in Table 8 should allow precision measurements of many types  
 1443 of two-particle correlations, including the  $N_{\text{ch}}$  dependence of integral  $v_n$ ,  $p_{\text{T}}$  dependence of  $v_n$

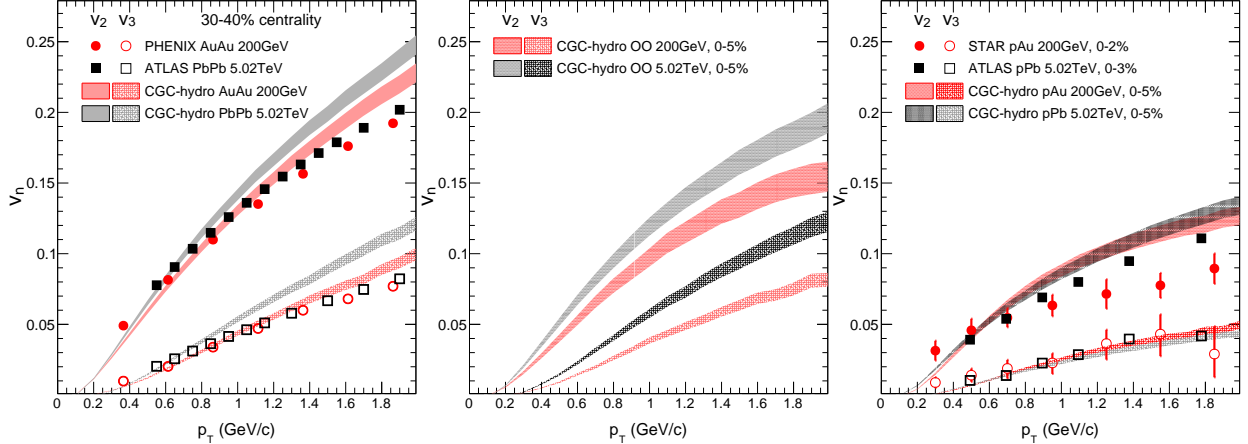


**Figure 42:** Comparison of measured  $v_2$  and  $v_3$  between Pb+Pb and Au+Au 30–40% centrality events (Left) and high-multiplicity  $p$ +Pb and  $p$ +Au data (Right) at RHIC and the LHC energies. The CGC-Hydro model calculations [148] are also shown for Au+Au and Pb+Pb (Left),  $p$ +Au and  $p$ +Pb (Right), and O+O as a prediction (Middle) at both energies.

**Table 8:** Number of events (in millions) needed in an O+O run at  $\sqrt{s_{NN}} = 200$  GeV for various triggers for one week running scenarios.

Triggers	Minimum bias	0–5% centrality
Events (1 week)	400 M	200 M

1444 in 0–5% for identified particles ( $\pi$ , K, p and  $\phi$ ) to test the NCQ-scaling. The non-flow effects  
 1445 for these observables can be studied in detail thanks to the large acceptance of iTPC and  
 1446 EPD. Based on a Glauber model estimation, the  $\langle N_{\text{part}} \rangle$  value is 9.5 and 26 for minimum-bias  
 1447 and 0–5% central O+O collisions, respectively.

1448 Figure 43 shows the projection of the statistical precision for the  $\phi$  meson  $v_2(p_T)$  in 0–5%  
 1449 centrality O+O collisions. Under the assumption that its  $v_2$  in O+O is similar to that of  
 1450 a charged hadron in  $p$ +Au around  $p_T \sim 2\text{--}3$  GeV/ $c$ , the estimation scales the  $\phi$   $v_2(p_T)$  in  
 1451 peripheral Au+Au collisions [162] to approximately match the charged hadron  $v_2$  in  $p$ +Au  
 1452 collisions in Fig. 42, accounting for differences in  $\langle N_{\text{part}} \rangle$ , event plane resolution, and event  
 1453 statistics. A decent measurement of  $\phi$  meson  $v_2$  can be achieved with one week of running.

1454 In fact, the statistics requirement in Table 8 is mainly driven by multi-particle correla-  
 1455 tions, for example four-particle cumulants for single harmonics  $c_2\{4\} = \langle v_n^4 \rangle - 2 \langle v_n^2 \rangle^2$ , four-  
 1456 particle symmetric cumulants  $SC(2, 3) = \langle v_2^2 v_3^2 \rangle - \langle v_2^2 \rangle \langle v_3^2 \rangle$  and three-particle asymmetric  
 1457 cumulants  $AC(2, 4) = \langle v_2^2 v_4 \cos 4(\Phi_2 - \Phi_4) \rangle$  ( $\Phi_n$  is the event plane). These observables are  
 1458 sensitive to event-by-event fluctuations of collectivity, and measurements of them at LHC in  
 1459  $p$ + $p$ ,  $p$ +Pb and Pb+Pb collisions have led to high impact results which provide evidence for  
 1460 geometry response in small systems [163–166].

1461 Figure 44 shows the projection of the statistical precision for the  $c_2\{4\}$  measurement.  
 1462 The projected precision should allow a measurement of  $c_2\{4\}$  signal, assuming a  $v_2\{4\}$  value

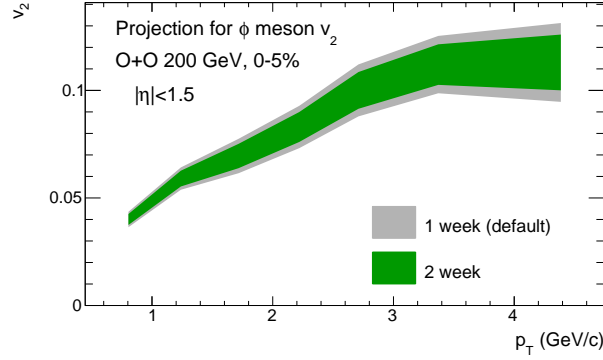


**Figure 43:** Projected statistical error on  $\phi$  meson  $v_2(p_T)$  in central O+O collisions within the TPC acceptance. The error bars for twice the statistics are shown for comparison.

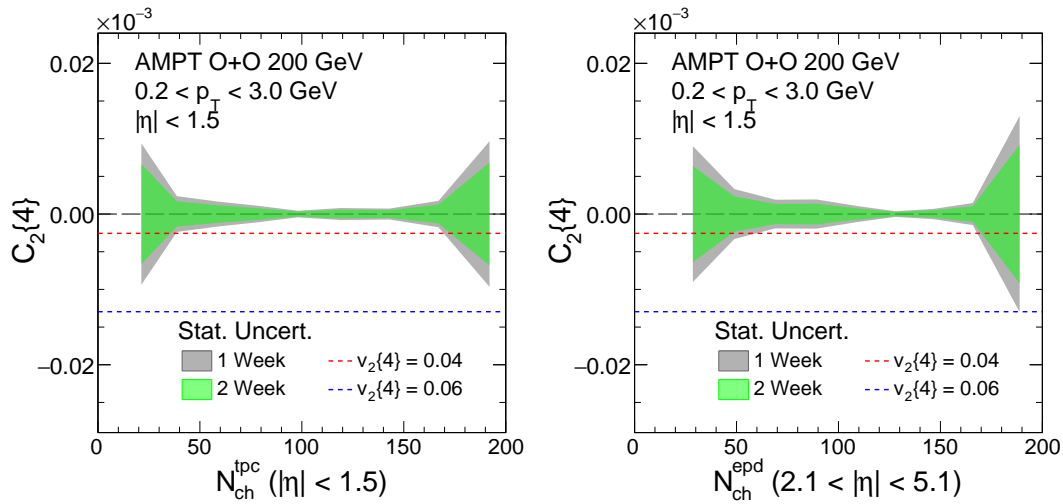


**Figure 44:** (Left) The projected statistical error bar on  $c_2\{4\}$  in 0.2-3 GeV/c in the TPC acceptance as a function of number of charged particles in TPC acceptance and (Right) EPD acceptance. The error bars for twice the statistics are shown for comparison.

1463 to be between 4–6% <sup>3</sup>.

1464 Figure 45 shows the projection of the statistical precision for the charged hadron  $R_{AA}$   
 1465 measurement for minimum bias O+O collisions (assume 400 Million). This calculation  
 1466 includes the state-of-art knowledge of nPDF effects and jet quenching modeling of Refs.  
 1467 [168, 169]. A significant suppression of  $R_{AA} = 0.85 - 0.9$  is expected which should be mea-  
 1468 surable with decent statistical uncertainty out to 15 GeV/c.

1469 **Answer to PAC questions from last year:** When this proposal was presented last year,  
 1470 we have received the following comments: "With regards to an O+O run, the case for this  
 1471 could become persuasive if, between now and next year, theorists with expertise in hydro-  
 1472 dynamics can provide some simulations that demonstrate what hydrodynamics predicts for

<sup>3</sup>The  $p_T$  integrated  $v_2\{4\}$  in  $d+Au$  from PHENIX [167] at forward rapidity is about 4%

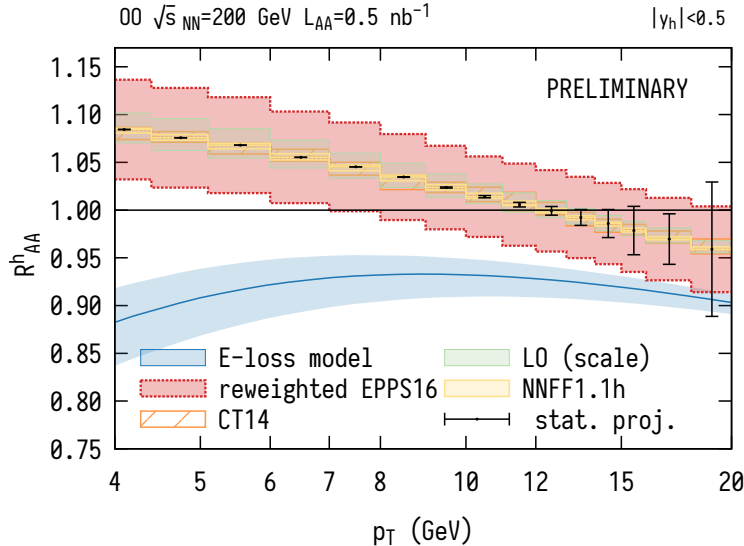


**Figure 45:** Prediction of minimum bias hadron nuclear modification factor for  $\sqrt{s_{NN}} = 200$  GeV O+O collisions following Refs. [168, 169] (the authors have graciously repeated the calculation for RHIC energy). A particular parton energy loss model predictions (blue line) is overlaid with the baseline in the absence of parton rescattering. The blue band represents model uncertainty only due to experimental uncertainties in  $\sqrt{s_{NN}} = 5.02$  TeV Pb+Pb collisions used to fit a free model parameter. The red band shows nPDF uncertainties reweighted with additional CMS  $p$ +Pb dijet data. Proton PDF (orange), leading order scale (green) and fragmentation function (yellow) uncertainties are fully correlated and cancel. Error bars illustrate statistical uncertainties for O+O mock data at 100% efficiency.

1473  $v_2$  and  $v_3$  behavior in O+O collisions, and how this compares to results from  $p$ +A, Cu+Cu,  
 1474 and Au+Au collisions. We also suggest that these calculations should be undertaken for  
 1475  $\alpha + \alpha$ , Be+Be, Al+Al and Ar+Ar collisions also, as well as for O+Au and other asymmetric  
 1476 small+large nuclear collision options, so as to be able to make the case that O+O is the  
 1477 optimal physics choice, most likely to yield new or substantially improved understanding of  
 1478 questions relating to how small droplets of QGP equilibrate and what is the smallest droplet  
 1479 of QGP that is possible to be formed in collisions at 200 GeV".

1480 We have prepared the following answers to these comments:

- 1481 • Why O+O? 1) O+O collisions cover similar  $N_{\text{part}}$  range as  $p$ +Au/ $d$ +Au (see Fig-  
 1482 ure 41) where the collectivity debate is ongoing, 2) O+O has similar  $N_{\text{part}}$  but different  
 1483 nucleon/sub-nucleon fluctuations, 3) leverage similar measurement at the LHC for new  
 1484 insight and precision.
- 1485 • Are there theoretical calculations? Many model studies on O+O exist by now, which re-  
 1486 flects the community interests: 1812.08096,1904.10415,1908.06212, 1910.09489, 2003.06747,  
 1487 2005.14682. Figure 42 shows the new prediction on O+O taken from 2005.14682,
- 1488 • Why not other collision systems? Analyzing power for  $2k$ -particle cumulants  $v_n\{2k\}$   
 1489 scales as  $N_{\text{events}} \times N_{\text{part}}^{2k}$ , system smaller than O+O, such as C+C require much longer

1490  
1491  
1492  
1493  
1494  
1495  
1496  
1497  
1498

running time and also difficult to setup the high-multiplicity triggers due to steeply falling  $N_{ch}$  distributions. Also these systems will not have compatible  $N_{part}$  coverage as  $p/d+Au$  systems. One may suggest to repeat the  $p/d+Au$ . But this will require long running time, since previous  $p+Au$  ( $d+Au$ ) data was taken over 5 (1.5) weeks period in Run-15 (Run-16).

- Why not larger small systems? We already have larger asymmetric systems, Cu+Au and  $^3\text{He}+Au$ . Results from both are consistent with final-state interpretation from both experiments and theory. Any system in between such as O+Au with  $\langle N_{part} \rangle = 60$  are expected to be dominated by final state effects.

1499 **2.2.2 Au+Au Collisions at  $\sqrt{s_{NN}} = 17.1$  GeV**

1500 **Net-proton kurtosis and light nuclei yield ratio from RHIC BES-I:** One of the  
1501 main goals of the RHIC Beam Energy Scan (BES) program is the search for the QCD critical  
1502 point (CP), which is a distinct singular feature of the QCD phase diagram. The experimental  
1503 confirmation of the existence of the CP would become a landmark in the exploration of the  
1504 phase structure of hot dense nuclear matter. The characteristic feature of the CP is the  
1505 divergence of the correlation length and density fluctuations. These critical phenomena  
1506 can be probed by measuring event-by-event fluctuations of conserved quantities, such as  
1507 baryon, electric charge, and strangeness numbers. The effect of the CP could show as a  
1508 non-monotonic energy dependence of higher order moments of these conserved quantities in  
close proximity of the critical point during a beam energy scan [122].

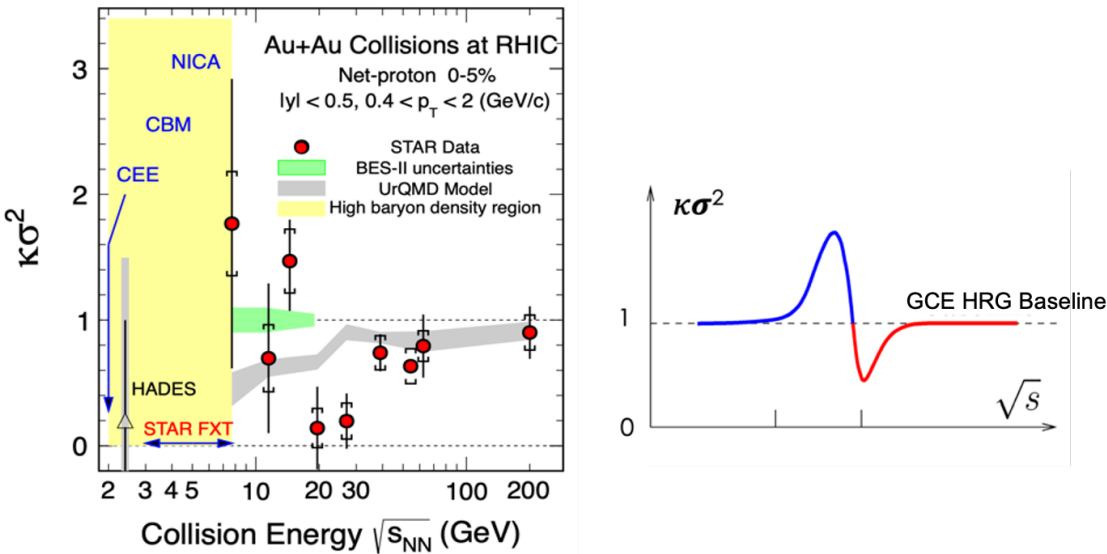


**Figure 46:** (Left) The fourth order net-proton fluctuations  $\kappa\sigma^2$  in most central (0-5%) Au+Au collisions as a function of collision energy from STAR BES-I measurements [123]. (Right) The characteristic signature predicted by the theoretical model for energy dependence of the fourth order fluctuations when the system passes through the critical region [122].

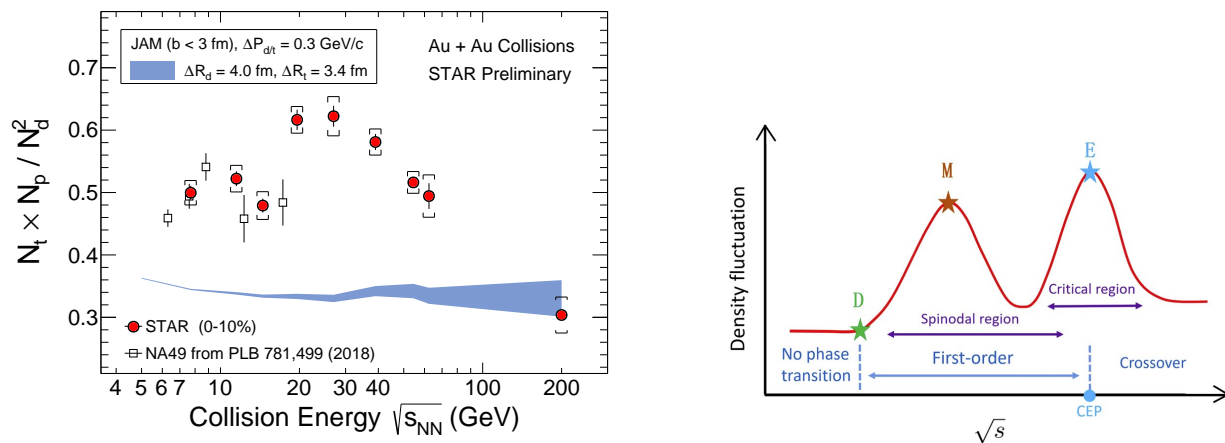


**Figure 47:** (Left) Collision energy dependence of the light nuclei yield ratio ( $N_t \times N_p / N_d^2$ ) in central Au+Au collisions. The open square data based on NA49 results in central Pb+Pb collisions at  $\sqrt{s_{NN}} = 6.3$  (0-7%), 7.6 (0-7%), 8.8 (0-7%), 12.3 (0-7%), and 17.3 (0-12%) GeV. (Right) Illustration of the density fluctuation as a function of collision energy in the critical region and the spinodal region [170].

1509 In the years 2010-2017 RHIC finished the BES-I after taking data in Au+Au collisions  
 1510 at  $\sqrt{s_{NN}} = 7.7, 11.5, 14.5, 19.6, 27, 39, 54.4, 62.4,$  and 200 GeV. With these experimental  
 1511 data STAR measured the higher order fluctuations of net-proton, net-charge, and net-kaon  
 1512 multiplicity distributions [123, 171–175]. One striking observation was the behavior of the  
 1513 fourth-order cumulants, or kurtosis, of the net-proton fluctuation  $\kappa\sigma^2$  in most central (0-  
 1514 5%) Au+Au collisions as a function of beam energy. As shown on the left of Fig. 46, the  
 1515 fourth order net-proton fluctuation is close to unity above 39 GeV but deviates significantly  
 1516 below unity at 19.6 and 27 GeV, then approaches or turns above unity at lower energies.  
 1517 This behavior may suggest that the created system skims close by the CP, and receive  
 1518 positive and/or negative contributions from critical fluctuations. The right of Fig. 46 shows  
 1519 the characteristic signature of the critical point for energy dependence of the fourth order  
 1520 fluctuations when the system passes through the critical region [122]. Along this argument,  
 1521 a peak structure above unity for net-proton kurtosis measurement at lower energies could be  
 1522 the signature of the CP. However, it is worth to point out that a first order phase transition  
 1523 could also cause a large increase of net-proton kurtosis [176]. When entering into the  
 1524 spinodal region (mixed phase), the double peak structure of  $\sigma$  field may cause the increase  
 1525 of the fourth order cumulants ( $C_4$ ).

In addition, STAR has measured light nuclei (deuteron and triton) production in Au+Au collisions at RHIC BES energies. The ratio of these yields are predicted to be sensitive to the neutron relative density fluctuations at kinetic freeze-out, which is expected to increase near the critical point and/or a first order phase transition [170]. The neutron density fluctuation

is defined as  $\Delta n = \langle(\delta n)^2\rangle/\langle n\rangle^2$ , which can be approximated from:

$$\Delta n = \frac{1}{g} \frac{N_t \times N_p}{N_d^2} - 1,$$

1526 where  $N_p$ ,  $N_d$  and  $N_t$  are the proton, deuteron and triton yields, respectively and  $g$  is a  
 1527 constant factor of 0.29 [170]. In the left panel of Fig. 47, we show the yield ratio  $N_t \times$   
 1528  $N_p/N_d^2$  in central Au+Au collisions as a function of collision energy. These light nuclei yield  
 1529 ratios are obtained by using the feed-down corrected proton yields, deuteron yield [177], and  
 1530 preliminary triton results [178]. The ratio as a function of energy exhibits a non-monotonic  
 1531 energy dependence with a peak around 19.6 GeV. The blue band showing a flat energy  
 1532 dependence represents the calculation of the light nuclei yield ratio in Au+Au collisions  
 1533 ( $b < 3$  fm) from a transport JAM model [179]. Furthermore, the yield ratio shown in Fig. 47  
 1534 seems to show a drop between 14.5 and 19.6 GeV. The experimental observation of non-  
 1535 monotonic energy dependence in yield ratio may suggest a double peak structure of the  
 1536 neutron density fluctuation, indicating that the system goes through the critical region and  
 1537 the first order spinodal region, as displayed in Fig. 47 right.

1538 At the end of Run-21, we propose to take one more energy point for Au+Au collisions at  
 1539 17.1 GeV based on the two observations discussed above and presented in Figs. 46 and 47:

- 1540 1. Net-p kurtosis and light nuclei yield ratio, which are both sensitive to the critical  
 1541 fluctuation, show dip and peak structures around 19.6 GeV. These may suggest that  
 1542 the system passed through the critical region around 19.6 GeV.
- 1543 2. We observe sudden changes between 19.6 and 14.5 GeV in the energy dependence of  
 1544 net-p kurtosis and light nuclei ratio measurements in the BES-I data measured by the  
 1545 STAR experiment. The neutron density fluctuations at low energies below 14.5 GeV  
 1546 are consistent with the results from NA49 experiment [170].

1547 These two observations indicate that the critical point may be close to 19.6 GeV. Since  
 1548 there are sudden changes in both observables between 19.6 (chemical freeze-out  $\mu_B =$   
 1549 205 MeV) and 14.5 GeV ( $\mu_B = 266$  MeV), it is important to conduct a finer beam en-  
 1550 ergy scan between these two energies. Therefore, we request a run with Au+Au collisions  
 1551 at  $\sqrt{s_{NN}} = 17.1$  GeV ( $\mu_B = 235$  MeV), which divides the range into approximately equal  $\mu_B$   
 1552 gaps.

1553 **Answer to PAC questions from last year:** When this proposal was presented last  
 1554 year, we have received the following comments: "To make the case for a  $\sqrt{s_{NN}} = 17.1$  GeV  
 1555 run, the key input will be results from measurements of fluctuation observables from Run-19  
 1556 data taken at  $\sqrt{s_{NN}} = 19.6$  and 14.6 GeV. If these measurements, with the smaller error  
 1557 bars that are anticipated, show evidence for a possible two-peaked structure in the plot of  
 1558 net proton kurtosis or other fluctuation observables as a function of  $\sqrt{s_{NN}}$ , this could at that  
 1559 time become a strong argument for a run at  $\sqrt{s_{NN}} = 17.1$  GeV."

1560 To reply the comments from PAC last year, we have analyzed the net-proton fluctuation  
 1561 and light nuclei production from the Run-19 fast-offline data of Au+Au collisions at  $\sqrt{s_{NN}}$

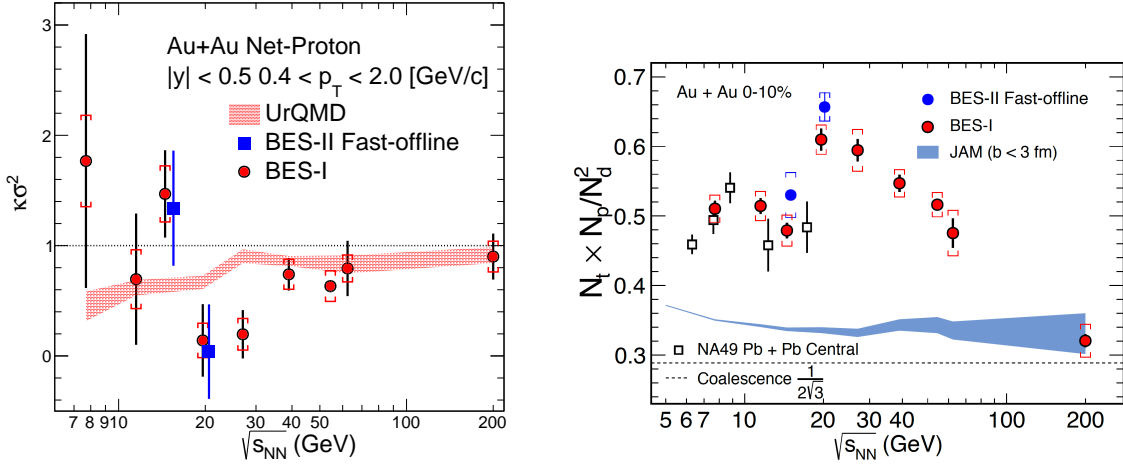


**Figure 48:** The red solid markers are the results from RHIC BES-I and the blue square represents the results of Run19 fast-offline data. (Left) The fourth order net-proton fluctuations  $\kappa\sigma^2$  in most central (0-5%) Au+Au collisions as a function of collision energy. (Right) Collision energy dependence of the light nuclei yield ratio ( $N_t \times N_p / N_d^2$ ) in central Au+Au collisions. The open square data based on NA49 results in central Pb+Pb collisions at  $\sqrt{s_{NN}} = 6.3$  (0-7%), 7.6 (0-7%), 8.8 (0-7%), 12.3 (0-7%), and 17.3 (0-12%) GeV.

1562 = 14.6 and 19.6 GeV. The statistics of the Run-19 fast-offline data of 0-5% Au+Au collisions  
 1563 shown in Fig. 48 are about 580k and 750k events for 14.6 and 19.6 GeV, respectively, which  
 1564 are roughly about 5% of the full min-bias statistics of these two data sets. It is found  
 1565 that both net-proton fluctuation and light nuclei yield ratios in 0-5% most central Au+Au  
 1566 collisions from BES-I are consistent with the results from Run-19 fast-offline data of 14.6  
 1567 and 19.6 GeV. For clarity in Fig. 48, the X-axis positions of Run-19 fast-offline data are  
 1568 slightly shifted.

**Table 9:** Event statistics (in millions) needed in a Au+Au run at  $\sqrt{s_{NN}} = 17.1$  GeV for fourth order net-proton fluctuations ( $\kappa\sigma^2$ ) and light nuclei yield ratio ( $N_t \times N_p / N_d^2$ ) measurements.

Triggers	Minimum Bias	net-p $\kappa\sigma^2$ (0-5%)	$N_t \times N_p / N_d^2$ (0-10%)
Number of events	250 M	6% error level	3.6% error level

1569 **Required number of minimum bias events and statistical uncertainty level:** Ac-  
 1570 cording to the previous estimation of the required event statistics for BES-II energies pre-  
 1571 sented in Table 6, we need about 250 million minimum-bias events for the net-proton kurtosis  
 1572 measurement at 17.1 GeV, which requires 2.5 weeks data taking. It gives us about 12.5  
 1573 million events (250/20) in 0-5% most central collisions. This will ensure that the relative  
 1574 statistical error of net-proton  $\kappa\sigma^2$  in 0-5% most central Au+Au collisions will reach the 6%

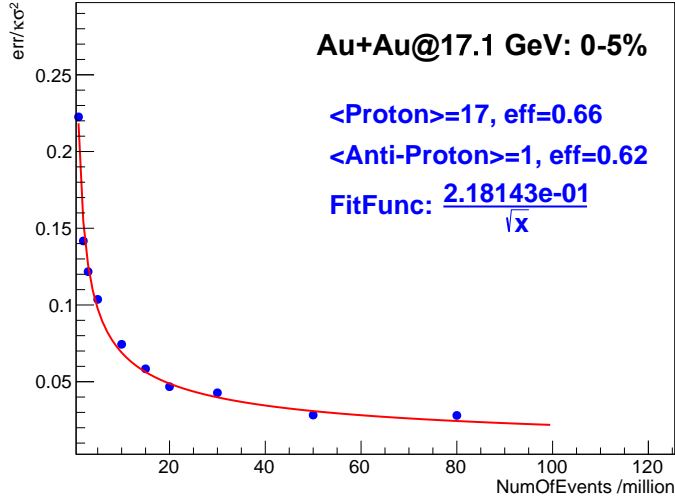


**Figure 49:** Monte Carlo simulation for the relative statistical errors of net-proton  $\kappa\sigma^2$  in 0-5% most central Au+Au collisions at 17.1 GeV. A Skellam distribution for net-proton is assumed; the mean value for protons and anti-protons are 17 and 1, respectively. The average efficiencies for proton and anti-proton are 0.66 and 0.62, respectively.

1575 level (shown in Fig. 49). These event statistics will also ensure that the relative statistical  
 1576 error of the light nuclei ratio will reach about 3.6% level in 0-10% central Au+Au collisions.  
 1577 In addition to the improved statistics, utilizing the iTPC will enable the measurement of  
 1578 lower  $p_T$  light nuclei and will reduce the systematic uncertainties associated with the low  $p_T$   
 1579 yield extrapolation.

1580 If nature puts the critical point in the QCD phase diagram between 14.5 and 19.6 GeV  
 1581 (with  $\mu_B$  around 200–270 MeV), RHIC has the best chance to discover it!

### 1582 **2.2.3 Au+Au Collisions in FXT Mode at $\sqrt{s_{NN}} = 3.0$ GeV - II: 2 Billion Goal**

1583 In the previous section, we have discussed the great physics interests for low energy heavy-ion  
 1584 collisions utilizing the FXT setup at the STAR experiment. We have made our arguments  
 1585 for taking a minimum of 300 million Au+Au FXT events at  $\sqrt{s_{NN}} = 3.0$  GeV. With further  
 1586 available beam time, we would like to request to collect up to 2 billion events with the same  
 1587 setup for the following physics measurements.

1588 Proton correlations higher than 4-th order are useful to study the possible contributions  
 1589 of protons from hadronic phase or QGP phase [176]. The requested 2 billion events statistics  
 1590 will enable us to perform the analyses of proton moments and cumulants up to 5-th and 6-th  
 1591 orders. Measurements of 5-th and 6-th order moments and cumulants have been proposed  
 1592 to be sensitive to the search for the phase boundary in the high baryon density region [176].

1593 A much larger data sample (2 billion events) will enable us to further investigate the  
 1594 centrality dependence of  $\phi$  meson production. The Run-18 data analysis in 40-60% centrality

1595 bin yields  $\sim 13\%$  relative uncertainty in the  $\phi$  production yield. A two-billion dataset will  
 1596 reduce the statistical uncertainty to be  $< 5\%$ . This will allow us to study the system size  
 1597 dependence of  $\phi$  meson production to quantitatively understand the canonical suppression  
 1598 for strangeness. The large statistics will also offer the opportunity to further measure  $\phi$   
 1599 meson directed and elliptic flow behavior in these collisions.

1600 While there have been tens of hypernuclei measured so far, there are only very few double- $\Lambda$   
 1601  $\Lambda$  hypernuclei candidates reported from emulsion experiments [180–184]. Their properties  
 1602 are directly related to the  $\Lambda\Lambda$  interaction. Low energy heavy-ion collisions can be a unique  
 1603 environment to copiously produce these light double- $\Lambda$  hypernuclei. For instance, according  
 1604 to the thermal model prediction, the  ${}^5_{\Lambda\Lambda}\text{H}$  production yield increases by more than 3 orders  
 1605 of magnitude at the low energies compared to that at top RHIC and LHC energies [134].

1606 We performed a Monte Carlo simulation study for the decay chain  ${}^5_{\Lambda\Lambda}\text{H} \rightarrow {}^5_{\Lambda}\text{He} + \pi^-$ , and  
 1607  ${}^5_{\Lambda}\text{He} \rightarrow {}^4\text{He} + p + \pi^-$  within the STAR detector acceptance. Assuming the production yield  
 1608 based on the thermal model prediction [134], with 2 billion Au+Au FXT data at  $\sqrt{s_{\text{NN}}} = 3.0$  GeV  
 1609 and with the iTPC and eTOF detector, we will have a chance to observe  $\sim 27$   
 1610 signal counts. This will be an unprecedented sample that allows us to study double- $\Lambda$   
 1611 hypernuclei properties and their production mechanism, providing new insights towards the  
 1612 understanding of the  $\Lambda\Lambda$  interaction.

## 1613 2.3 Future Possibilities

### 1614 2.3.1 Exploring the Nuclear Equation-of-State (EoS) with Heavy Ion Collisions

1615 In the interior of the fireball created in HI collisions, nuclear densities of up to  $10 \rho_0$  can be  
 1616 achieved depending on the energy of the colliding nuclei [185]. Similar densities are predicted  
 1617 to be present in the core of neutron stars (NS). However, the composition and maximal mass  
 1618 of NS is highly dependent on the nuclear equation-of-state (EoS) which is close related to  
 1619 the compressibility of nuclear matter. Therefor HI collisions are considered as an ideal tool  
 1620 to study the EoS at high nuclear densities and establish a bridge between astrophysics and  
 1621 nuclear physics.

1622 Already in the early 80s several observables probing the EoS (i.e. which are sensitive  
 1623 on the density and pressure of the system) like particle production [186, 187], transverse  
 1624 momentum analysis [188], and directed and elliptic flow [189, 190] were proposed. At low  
 1625 energies and densities up to about  $2.5 \rho_0$  elliptic flow analyses favor a soft EoS [191] while at  
 1626 AGS energies (between  $2.5$  and  $4.5 \rho_0$ ) no clear picture has been established yet. Transverse  
 1627 flow measurements hint to a soft ( $K \leq 210$ ) EoS, while elliptic flow measurements indicate a  
 1628 stiff ( $K \approx 300$ ) EoS [190]. Another method to probe the equation-of-state of nuclear matter  
 1629 was proposed already in 1985 by Aichelin and Ko [192] by measuring the sub-threshold  
 1630 production of strange particles which are created in the dense medium early in the reaction.  
 1631 Especially the multi-strange particle production at sub-threshold energies should be highly  
 1632 sensitive to the density of the medium since multiple-collision processes are required. Hence  
 1633 information on the EoS is stored in the yield and slope of the excitation function of the sub-  
 1634 threshold produced particles which can be compared to various theoretical models. It is also

1635 clear that the abundance of produced particles is highest at heavy systems like Au+Au since  
 1636 the reaction volume is big. Therefore comparison measurements with light system like C+C  
 1637 can be used as a reference where the influence of the EoS is small. In addition, systematic  
 1638 errors both in experiment and theory cancel out to a large extent by taking the yield ratio  
 1639 of produced (multi-) strange particles at both systems.

1640 Figure 50 shows the normalized yield ratio  $((M_{K^+}/A)_{Au+Au}/(M_{K^+}/A)_{C+C})$  of sub-threshold  
 1641 produced  $K^+$  as a function of 4 different beam energies [193]. Comparison to different mod-  
 1642 els [194, 195] predicts a soft EoS at low bombarding energies around  $E_{beam} \approx 1.5 \text{ GeV}$ . On  
 1643 the other hand, the finding of neutron stars with masses above 2 solar masses can only  
 1644 be explained by a stiff EoS [196] which should be measurable in flow observable at higher  
 incident energies.

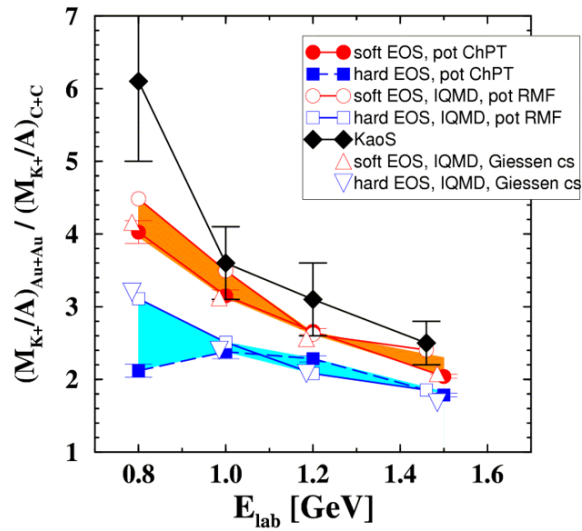


**Figure 50:** Excitation function of the ratio of  $K^+$  multiplicity obtained in Au+Au over C+C reactions [193] together with model calculations [194, 195] indicating a soft EoS at these bombarding energies.

1645  
 1646 Independent observables at these higher energies are the production rates of multi-strange  
 1647 baryons, of which several have their NN production threshold in the reach of BES-II:  $\Xi^-$   
 1648 (production threshold  $\sqrt{s_{NN}} = 3.247 \text{ GeV}$ ),  $\Omega^-$  (production threshold  $\sqrt{s_{NN}} = 4.092 \text{ GeV}$ ),  $\Xi^+$   
 1649 (over  $\Xi^+\Xi^-$ -channel, production threshold  $\sqrt{s_{NN}} = 4.520 \text{ GeV}$ ) and  $\Omega^+$  (over  $\Omega^+\Omega^-$ -channel,  
 1650 production threshold  $\sqrt{s_{NN}} = 5.222 \text{ GeV}$ ). A beam energy scan in small steps (with 3 to 4  
 1651 points with distance of about 200 to 300 MeV) below the production threshold energy for the  
 1652 various particles species for Au+Au collisions could give access to the properties of the EoS  
 1653 as function of colliding energy and density. In fact a big fraction of the measurements were  
 1654 already finished during the BES-II campaign and only a few additional fixed target points  
 1655 have to be performed which depends on the number of investigated particles used as probes.  
 1656 Measurement of the pressure as function of energy in small steps could even allow for the

1657 discovery of a 1<sup>st</sup> order phase transition in the covered energy range [197]. Measurements in  
 1658 the heavy system could be accompanied by a reference measurement of a light system (e.g.  
 1659 C+C) for at least one particle species and extrapolated to the others. However, since the  
 1660 production yield scales with the number of participants the time needed for the light system  
 1661 is significantly longer (few weeks) as for the heavy system which needs typically btw. 12 h  
 1662 and a day.

1663 Nevertheless the proposed measurements have a high discovery potential and could be  
 1664 an opportunity for a future fixed target HI program at STAR.

## 1665 2.4 Exploring the Microstructure of the QGP (Run-23 and Run-25 1666 Au+Au)

1667 The completion of the RHIC's scientific mission involves the two central goals [198] of (i)  
 1668 mapping out the phase diagram of the QCD, and (ii) probing the inner workings of the QGP  
 1669 by resolving its properties at short length scales. The complementarity of the RHIC and LHC  
 1670 facilities to study the latter is scientifically as essential as having more than one experiment  
 1671 independently study the microstructure of the QGP. With several years of operating the  
 1672 recently installed iTPC upgrade and the soon-to-be installation and operation of STAR's  
 1673 forward detectors, the STAR collaboration will be in an excellent position to take advantage  
 1674 of its vastly improved detection capabilities. Combine this with the prospect of a substantial  
 1675 increase in beam luminosities and RHIC will be uniquely positioned to fully engage in a  
 1676 detailed exploration of the QGP's microstructure. Through careful discussions in its physics  
 1677 working groups, the STAR collaboration has identified a number of topics that together  
 1678 make a compelling case to take data during Runs 23-25 alongside sPHENIX, and successfully  
 1679 complete RHIC's scientific mission. In this section, we present a selection of those topics  
 1680 that will take full advantage of both STAR and RHIC's unique capabilities and address the  
 1681 following important questions about the inner workings of the QGP.

- 1682 • What is the precise temperature dependence of the shear  $\eta/s$ , and bulk  $\zeta/s$  viscosity?
- 1683 • What is the nature of the 3-dimensional initial state at RHIC energies? How does  
 1684 a twist of the event shape break longitudinal boost invariance and decorrelate the  
 1685 direction of an event plane?
- 1686 • How is global vorticity transferred to the spin angular momentum of particles on such  
 1687 short time scales? And, how can the global polarization of hyperons be reconciled with  
 1688 the spin alignment of vector mesons?
- 1689 • What is the precise nature of the transition near  $\mu_B = 0$ , and where does the sign-  
 1690 change of the susceptibility ratio  $\chi_6^B/\chi_2^B$  take place?
- 1691 • What is the electrical conductivity, and what are the chiral properties of the medium?
- 1692 • What can we learn about confinement and thermalization in a QGP from charmonium  
 1693 measurements?

1694  
1695  
1696

- What are the underlying mechanisms of jet quenching at RHIC energies? What do jet probes tell us about the microscopic structure of the QGP as a function of resolution scale?

1697  
1698  
1699  
1700  
1701  
1702  
1703  
1704  
1705  
1706  
1707  
1708  
1709  
1710  
1711  
1712  
1713

The event statistics projections that are used in this section will rely on the CAD’s recently update 2023E and 2025E Au+Au luminosities [199] and are listed in Table 10. For each year we presume 24 weeks of RHIC operations, and based on past run operations an overall average of 85% × 60% (STAR×RHIC) uptime, respectively. The minimum-bias rates assume a conservative 1.5 kHz DAQ rates which will allow sufficient bandwidth for specialized triggers which are listed as integral luminosities. In order to achieve the projected luminosities, the collaboration will look into optimizing the interaction rates at STAR by allocating low and high luminosities periods within fills. Such periods, in which low interaction rates are sampled in the early part of a fill and high interaction rates typically in the later part, will allow us to collect clean, low pile-up, minimum bias events, while at the same time not burn beam luminosities that could affect interaction rates for sPHENIX. Clean minimum bias events will improve tracking efficiencies which in turn are expected to benefit many of the proposed correlation analyses. Optimization of the available bandwidth for high- $p_T$  triggers would allow us to push for lower  $p_T$  thresholds, thus further reducing biases. The impact of such an optimization will lead to some reduction in the projected rates, while still enabling a significant improvement in the precision and kinematic reach of current STAR measurements, and making important measurements that are yet more differential possible.

year	minimum bias [×10 <sup>9</sup> events]	high- $p_T$ int. luminosity [nb <sup>-1</sup> ]		
		all vz	vz <70cm	vz <30cm
2014	2	26.5	19.1	15.7
2016				
2023	10	43	38	32
2025	10	58	52	43

**Table 10:** STAR minimum bias event statistics and high- $p_T$  luminosity projections for the 2023 and 2025 Au+Au runs. For comparison the 2014/2016 event statistics and luminosities are listed as well.

1714  
1715  
1716  
1717  
1718  
1719  
1720  
1721  
1722  
1723  
1724

At RHIC it is possible to build detectors that can span from mid-rapidity to beam rapidity – with the two recent upgrades STAR is able to achieve this unique capability. STAR’s BES-II upgrade sub-systems comprised of the inner Time Projection Chamber (iTPC,  $1.0 < |\eta| < 1.5$ ), endcap Time Of Flight (eTOF,  $1 < \eta < 1.5$ ) and Event Plane Detector (EPDs,  $2.1 < |\eta| < 5.1$ ), that are all commissioned and fully operational since the beginning of 2019 [16–18]. As will be discussed in Sect. 4, the STAR collaboration is constructing a forward rapidity ( $2.5 < \eta < 4$ ) upgrade that will include charged particle tracking and electromagnetic/hadronic calorimetry [200]. For charge particle tracking the aim is to construct a combination of silicon detectors and small strip thin gap chamber detectors. The combination of these two tracking detectors will be referred to as the forward tracking system (FTS). The FTS will be capable of discriminating the hadron charge sign. It should be able to measure transverse

1725 momentum of charged particles in the range of  $0.2 < p_T < 2$  GeV/ $c$  with 20–30% momentum  
 1726 resolution. In what follows, we will refer to the combination of the existing TPC ( $|\eta| < 1$ )  
 1727 and the iTPC upgrade as iTPC ( $|\eta| < 1.5$ ) for simplicity.

1728 The impetus for running STAR during the year of 2023-2025 in terms of bulk correlation  
 1729 measurements in Au+Au 200 GeV collisions comes from gains via: i) extended acceptance  
 1730 and ii) enhanced statistics. In the first subsections, we briefly describe how these two op-  
 1731 portunities can be exploited to perform correlations measurements that are unique to the  
 1732 physics goals of the RHIC heavy-ion program.

1733 Next, thanks to a reduced material budget between the beam and the iTPC, STAR will  
 1734 be uniquely positioned to perform dielectron measurements with which we propose to probe  
 1735 degrees of freedom of the medium and its transport properties. For that we will use the  
 1736 high precision dilepton excess yield, i.e.  $l^+l^-$  invariant mass distribution after subtraction  
 1737 of dilepton sources produced after freeze-out, and contributions from the initial collisions  
 1738 such as Drell-Yan and correlated charm-anticharm pairs. Furthermore, we propose to study  
 1739 the virtuality, Wigner function and final-state magnetic field in the QGP. For the latter  
 1740 photon-photon collisions in ultra-peripheral, peripheral, and midcentral reactions and  $p+A$   
 1741 (all centralities) in both channels  $e^+e^-$ ,  $\mu^+\mu^-$  will be measured with high accuracy.

1742 In the last subsections, we address our proposed charmonium measurements and motivate  
 1743 the importance of STAR's proposed program of precise jet measurements to explore the  
 1744 micro-structure of the QGP.

#### 1745 **2.4.1 Correlation Measurements Utilizing Extended Acceptance**

1746 Figure 51 demonstrates how STAR with the BES-II and forward upgrades will extend the  
 1747 two-particle phase-space (in terms of  $\eta_1$  and  $\eta_2$  with respect to beam rapidity) many times  
 1748 enabling us to perform correlation measurements over a wide window of relative pseudorapidity.  
 1749 Since many of the important correlation measures are based on two-particle correlations,  
 1750 this enhanced phase-space will provide STAR with many advantages: 1) increase the number  
 1751 of pairs to bring better precision, 2) a reduction in different sources of the non-flow  
 1752 background by increasing the pseudorapidity separation. Many multi-particle correlations  
 1753 will also benefit from the increase in triplets, quadruplets and so on due to the overall in-  
 1754 crease in acceptance. With this unique extended pseudorapidity reach our goal is to perform  
 1755 correlation measurements to enable a deeper understanding of the largely unexplored three-  
 1756 dimensional structure of the initial state, and temperature dependent transport properties  
 1757 of the subsequent fluid-like medium produced in heavy ion and small system collisions at  
 1758 RHIC.

1759 Two key sets of measurements are of interests: 1) pseudorapidity dependence of azimuthal  
 1760 correlations, 2) pseudorapidity dependence of global hyperon polarization.

1761 **Pseudorapidity-dependent azimuthal correlation to tightly constrain tempera-**  
 1762 **ture dependence of viscosity:** The idea of tightly constraining the temperature viscos-  
 1763 ity of the QGP was envisioned in the 2015 Long Range Plan for Nuclear Science [198]. The  
 1764 QCD matter formed at RHIC shows nearly perfect fluidity characterized by the smallest

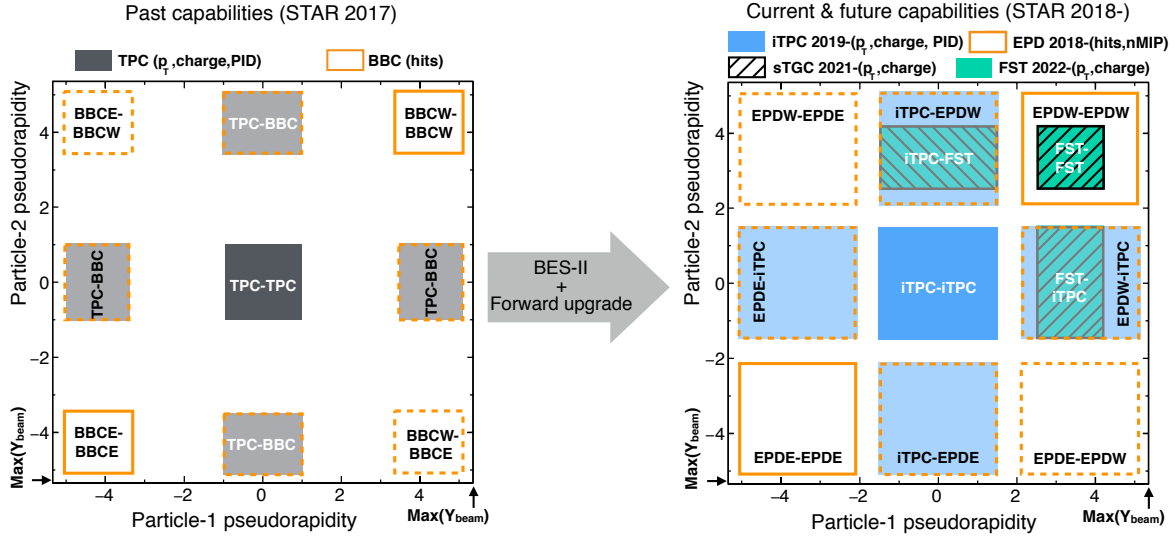


**Figure 51:** A visual representation of two-particle phase space in pseudorapidity covered by STAR detectors with respect to the region allowed by maximum beam rapidity ( $Y_{beam}=5.36$  at 200 GeV Au+Au collisions) of RHIC. Left and right panels show the capabilities before and after BES-II and forward upgrades of the STAR detector, respectively.. Note that in addition to a larger pair acceptance, the EPD granularity is over an order of magnitude larger than that of the BBC, and individual EPD tiles are shown to be separable into 1, 2, 3 MIP responses.

1765 viscosity to entropy ratio  $\eta/s$  known in nature. The temperature dependence of  $\eta/s$  and  
 1766 other transport parameters has not been fully constrained. One major aim is to perform  
 1767 precision measurements to contain the temperature dependence of shear  $\eta/s$  (T) and bulk  
 1768  $\zeta/s$  (T) viscosity. Hydrodynamic simulations have demonstrated that since the temperature  
 1769 of the produced fireball in HICs vary with the rapidity, the measurement of the rapidity  
 1770 dependence of flow harmonics has the potential to constrain  $\eta/s$  (T) and  $\zeta/s$  (T) [201]. For  
 1771 this, RHIC measurements have advantage over the LHC since the smaller beam rapidity at  
 1772 RHIC provides stronger variations of the temperature with rapidity. The beam energy scan  
 1773 at RHIC provides an additional handle on temperature to map  $\eta/s$  (T), and  $\zeta/s$  (T) over  
 1774 a wide range of temperature. Indeed, the hydrodynamic simulation of Ref. [201] indicates  
 1775 that  $\eta/s$  (T) at lower temperatures, near its possible minimum ( $T = T_c$ ), can be better  
 1776 constrained by RHIC measurements. Results from such simulations are shown in Fig. 52. In  
 1777 this simulation, a number of QCD-motivated parameterizations of the temperature dependence  
 1778 of the shear viscosity were assumed, as shown in Fig. 52 (left). Existing data from  
 1779 the PHOBOS collaboration suffer from large uncertainties, therefore only limited constraints  
 1780 on the temperature dependence of the transport parameters can be achieved. The BES-II  
 1781 and the forward upgrade of STAR will provide precise estimations of different azimuthal  
 1782 correlation observables:  $v_n(\eta)$  and other higher-order ( $n > 2$ ) flow coefficients  $v_n(\eta)$ , its fluctuations  
 1783  $\sigma(v_n)/v_n$ , that have never been measured at forward rapidity, are essential in terms

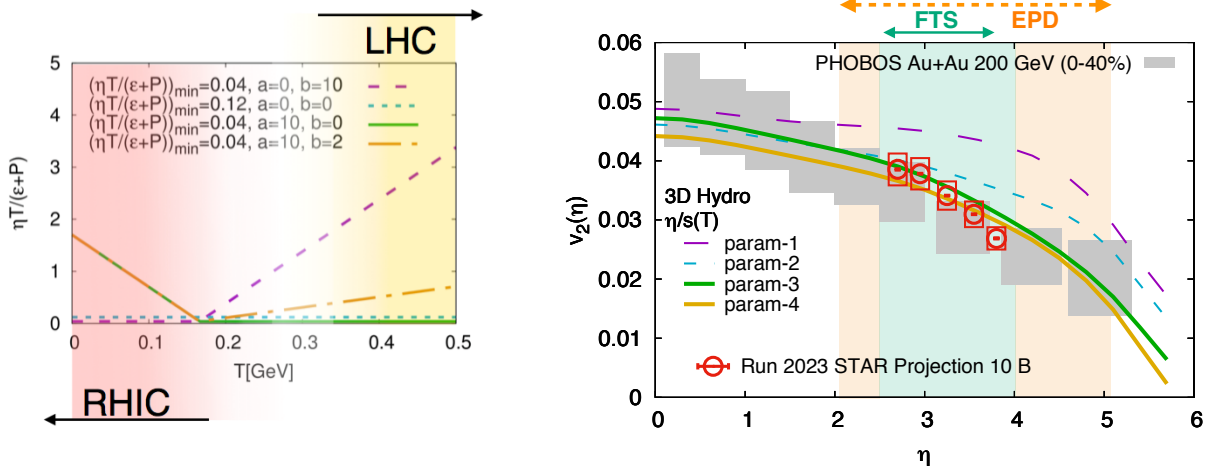


**Figure 52:** (Left) Different parameterizations of the temperature dependence of the shear viscosity to entropy  $\eta/s$  ( $T$ ) (at zero chemical potential) used in the hydrodynamical simulation of Ref. [201]. Interestingly, it has been demonstrated in Ref. [202] that the region of lowest  $\eta/s$  is the one that can be probed at RHIC. (Right) Effects on the elliptic flow co-efficient  $v_2$  due to different parameterizations of the viscosity parameter, indicating better constraints on  $\eta/s$  ( $T$ ) can only be performed by measurements at forward rapidities at RHIC. The interpretation of the existing PHOBOS data is limited by the large uncertainties. The projection for STAR measurements are shown on the same plot.

1784 of constraining  $\eta/s$  ( $T$ ) near its possible minimum. While transverse momentum integrated  
 1785 quantities can already constrain the shear viscosity, additional information about the  $p_T$  is  
 1786 essential to constrain the bulk viscosity  $\zeta/s$  – in particular the information of  $\langle p_T \rangle$  is needed  
 1787 to constrain  $\zeta/s(T)$ . With the forward tracking systems it will be possible to measure the  
 1788  $p_T$  dependence of  $v_n$  in A+A collisions in 2023.

1789 **Pseudorapidity-dependent azimuthal correlations to constrain the longitudinal**  
 1790 **structure of the initial state:** Initial-state longitudinal fluctuations and the fluid dy-  
 1791 namical response of the medium formed in heavy ion collisions can lead to de-correlations  
 1792 of the direction of the reaction planes  $\Psi_n$  (which determines the orientation of the har-  
 1793 monic anisotropies) with pseudorapidity (see Fig. 53). Such effects are often referred to as  
 1794 torque or twist of the event shape [205–207] that eventually leads to a breaking of longitu-  
 1795 dinal/boost/rapidity invariance. The magnitude of the de-correlation is determined by the  
 1796 details of the dynamics of initial state, and the distribution of nucleons and partons inside  
 1797 the colliding nuclei. Several promising observables have been proposed to study this effect,  
 1798 Fig. 53 shows one which can be expressed as  $r_n(\eta_a, \eta_b) = V_{n\Delta}(-\eta_a, \eta_b)/V_{n\Delta}(\eta_a, \eta_b)$ , where  
 1799  $V_{n\Delta}(\eta_a, \eta_b)$  is the Fourier coefficient calculated with pairs of particles taken from three differ-  
 1800 ent pseudorapidity regions  $-\eta_a, \eta_a$  and  $\eta_b$ . The observable  $r_n(\eta_a, \eta_b)$  was originally introduced  
 1801 and measured by CMS collaboration in Ref. [208] and also been measured by the ATLAS  
 1802 collaboration in [209]. An observable using three-particle correlations that is sensitive to

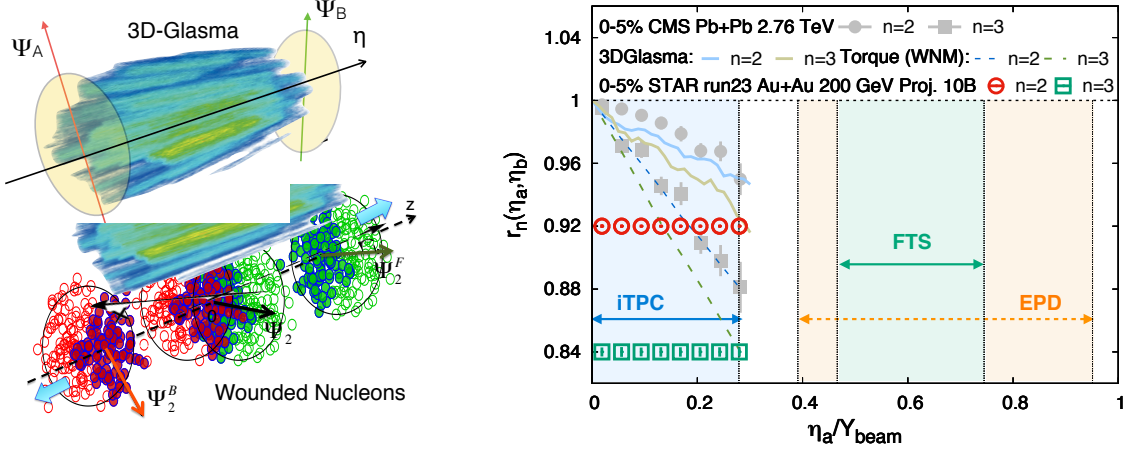


**Figure 53:** (Left) Cartoon to demonstrate the de-correlation of event planes in the longitudinal direction of a collision from a gluon saturation based 3D-Glasma model [203] and a wounded nucleon model (WNM) [204, 205]. (Right) The longitudinal de-correlation of elliptic anisotropy plane as a function of the pseudorapidity in units of beam rapidity. CMS results are compared predictions from two models in the left with STAR projection for Run-23 (using preliminary Run-19 results) for anticipated 10 B min-bias events. The colored regions show that the current and future capabilities at STAR (with iTPC+EPD+FTS) can extend such measurements with good precision by covering a large fraction of the beam rapidity at 200 GeV – this demonstrates the unique strength to STAR to study the physics of 3D initial state.

1803 this effect is [210] the relative pseudorapidity dependence of the three-particle correlator  
 1804  $C_{m,n,m+n}(\eta_a, \eta_b, \eta_c) = \langle \cos(m\phi_1(\eta_a) + n\phi_2(\eta_b) - (m+n)\phi_3(\eta_c)) \rangle$ . Also, another very similar  
 1805 to  $r_n$  in term of design but involving four-particle correlations is:  $R_{n,n|n,n}(\eta_a, \eta_b)$  [211]. As  
 1806 shown in Fig. 53 CMS measurements of  $r_n$  show the strongest de-correlation ( $\sim 16\%$  for  
 1807  $n=3$ ,  $\sim 8\%$  for  $n=2$ ) in central events within the range of their acceptance. The initial state,  
 1808 described by gluon saturation, as simulated by the 3D-Glasma model, breaking of boost  
 1809 invariance is determined by the QCD equations which predict the evolution of gluons in the  
 1810 saturation regime with Bjorken-x. At the LHC such models predict weaker de-correlation as  
 1811 compared to initial state described by wounded nucleon models and do a good job in explain-  
 1812 ing the  $r_2$  data from CMS collaboration [203] but over-predicts  $r_3$  results. One expects the  
 1813 nature of the initial state to change from LHC to RHIC, in particular the region of Bjorken-x  
 1814 probed is very different. It is therefore extremely important to utilize the enhanced accep-  
 1815 tance of the STAR detector with the Au+Au 200 GeV run to study this effect. In Fig. 53  
 1816 STAR's projections using preliminary Run-19 results for 10 B events are shown for the mea-  
 1817 surement of  $r_n$  within the acceptance  $|\eta| < 1.5$ . The colored regions show that the current  
 1818 and future capabilities at STAR (with iTPC+EPD+FTS) can extend such measurements  
 1819 using observables  $r_n, C_{m,n,m+n}, R_{n,n|n,n}$  with good precision by covering either equal (iTPC  
 1820 only) or larger (iTPC+FTS+EPDs) fraction of the beam rapidity at 200 GeV compared to  
 1821 the LHC measurements. This unique measurement capability will help pin down the nature  
 1822 of the 3-D initial state of heavy ion collisions. It will also help constrain different models

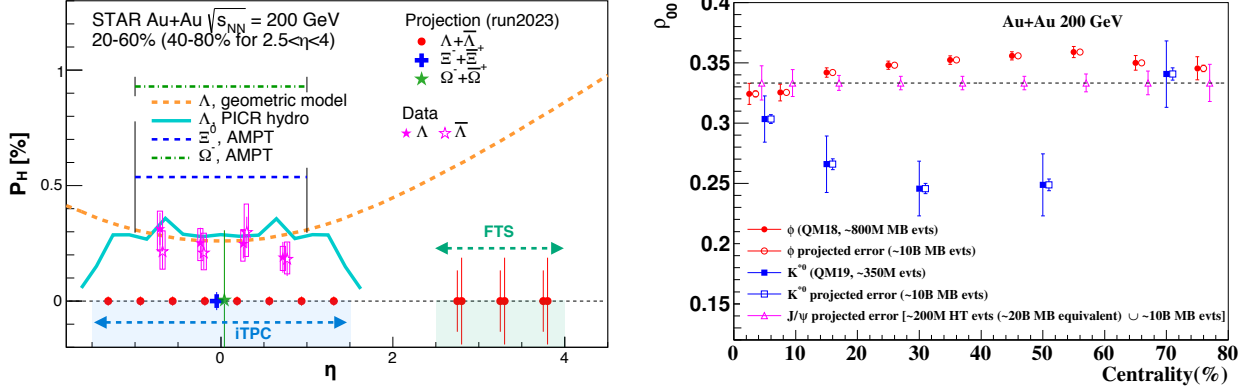


**Figure 54:** (Left) Projections (along with preliminary data) for differential measurements of  $\Lambda(\bar{\Lambda})$  polarization over the extend range of pseudorapidity with the iTPC and FTS detectors of STAR that will help resolve tension between different theoretical model predictions (shown by curves) of polarization with  $\eta$ . In addition, projections for the measurements of spin-1/2  $\Xi$  and spin-3/2  $\Omega$  particles are also shown. (Right) Spin alignment co-efficient  $\rho_{00}$  as a function of centrality, with projected errors based on  $\sim 10$  billion events. The enhanced statistics Run-23, combined with the excellent dilepton capabilities of STAR, will enable us to measure  $J/\psi$  alignment along with increasing the significance of the  $\phi$  and  $K^{*0}$  measurements.

1823 of QCD that predict the rapidity (or Bjorken-x) dependence of valance quark and gluon  
 1824 distributions inside colliding nuclei that has been demonstrated by theoretical calculations  
 1825 in Ref. [203, 212].

1826 **Pseudorapidity dependence of global hyperon polarization:** The global polariza-  
 1827 tion of hyperons produced in Au+Au collisions has been observed by STAR [20]. The origin  
 1828 of such a phenomenon has hitherto been not fully understood. Several outstanding questions  
 1829 remain. How exactly is the global vorticity dynamically transferred to the fluid-like medium  
 1830 on the rapid time scales of collisions? Then, how does the local thermal vorticity of the  
 1831 fluid gets transferred to the spin angular momentum of the produced particles during the  
 1832 process of hadronization and decay? In order to address these questions one may consider  
 1833 measurement of the polarization of different particles that are produced in different spatial  
 1834 parts of the system, or at different times. A concrete proposal is to: 1) measure the  $\Lambda(\bar{\Lambda})$   
 1835 polarization as a function of pseudorapidity and 2) measure it for different particles such  
 1836 as  $\Omega$  and  $\Xi$ . Both are limited by the current acceptance and statistics available. However,  
 1837 as shown in Fig. 54 with the addition of the iTPC and FTS, and with high statistics data  
 1838 from Run-23 it will be possible to perform such measurements with a reasonable significance.  
 1839 iTPC (+TPC) has excellent PID capability to measure all these hyperons. Although the  
 1840 FTS has no PID capability we can do combinatorial reconstruction of  $\Lambda(\bar{\Lambda})$  candidates via  
 1841 displaced vertices. A similar analysis was performed and published by STAR using the pre-  
 1842 vious FTPC [213]. In order to make a conservative projection we assume similar momentum  
 1843 resolution of 10 – 20% for single charged tracks, similar overall tracking efficiency, charge

1844 state identification capability for the FTS and FTPC (see the forward upgrade section for  
1845 exact numbers). We also assume the FTS, with its novel-tracking framework, will be able  
1846 to measure a minimum separation of 20 cm between the all pairs of one positive and one  
1847 negative track (a possible decay vertex) from the main vertex of the event. This will give rise  
1848 to about 5% efficiency of  $\Lambda(\bar{\Lambda})$  reconstruction with about 15 – 20% background contribution  
1849 from  $K_S^0 \rightarrow \pi^+ + \pi^-$  [213]. With this we can make projections for a polarization measure-  
1850 ment in Au+Au 200 GeV 40 – 80% assuming 10 Billion minimum-bias events as shown in  
1851 Fig. 54. The two different error bars correspond to lower and upper limits considering cur-  
1852 rent uncertainties on the efficiency of charged track reconstruction and the final efficiency of  
1853  $\Lambda$  reconstruction. Currently theoretical models predict contradictory trends for the pseudo-  
1854 rapidity dependence of  $\Lambda$  polarization. If the initial local orbital angular momentum driven  
1855 by collision geometry [214] plays a dominant role it will lead to increases of polarization with  
1856 pseudorapidity. On the other hand if the local thermal vorticity and hydrodynamic evolu-  
1857 tion [215] play a dominant role it will predict decreasing trend or weak dependence with  
1858 pseudorapidity. Such tensions can be easily resolved with the future proposed measurement  
1859 during Run-23.

#### 1860 2.4.2 Correlation Measurements Utilizing the Enhanced Statistics

1861 Over the past years the STAR collaboration has pursued dedicated measurements at Au+Au  
1862 collisions at  $\sqrt{s_{NN}} = 200$  GeV that have major discovery potential but are intrinsically statis-  
1863 tics hungry. In the past, attempts have been made to combine datasets from several years  
1864 to increase the significance of such measurements. This results in additional uncorrectable  
1865 systematic uncertainties in the measurements, mostly due to run-to-run variation of detector  
1866 response and collision conditions. A single stable long run with similar detector conditions,  
1867 as anticipated during Run-23, will not only reduce the statistical uncertainty but will also  
1868 bring the systematics under control. In the following section, and also in section 1.2.6, we  
1869 propose correlation measurements that will utilize the enhanced statistics from Run-23 and  
1870 can lead to high-impact results. To start with we assume STAR will collect data at the rate of  
1871 1.5 kHz and a combined RHIC×STAR uptime of 50% (12 hour/day) for 24 weeks of running  
1872 during Run-23. This will lead to the accumulation of about  $24 \times 7 \times 86400 \times 0.5 \times 1500 \approx 10$   
1873 billion events.

1874 **Global spin alignment of  $J/\psi$ :** Surprisingly large signals of global spin alignment of  
1875 vector mesons such as  $\phi(1020)$  and  $K^{*0}(892)$  have been measured via the angular distri-  
1876 bution of one of their decay products. These experimental observations of vector meson  
1877 spin alignment have yet to be interpreted satisfactorily by theory calculations. It has been  
1878 realized that the mechanism driving the global polarization of hyperons can have its im-  
1879 print on vector meson spin alignments albeit the observed strength of signals for the two  
1880 measurements cannot be reconciled. In fact the large quantitative difference between the  
1881 measurements of  $\phi(1020)$  and  $K^{*0}(892)$  spin alignment as shown in Fig. 54 (right) cannot  
1882 be simultaneously explained by conventional mechanisms of spin-orbit coupling, driven by  
1883 angular momentum, without invoking strong force fields. It is argued that the strong force

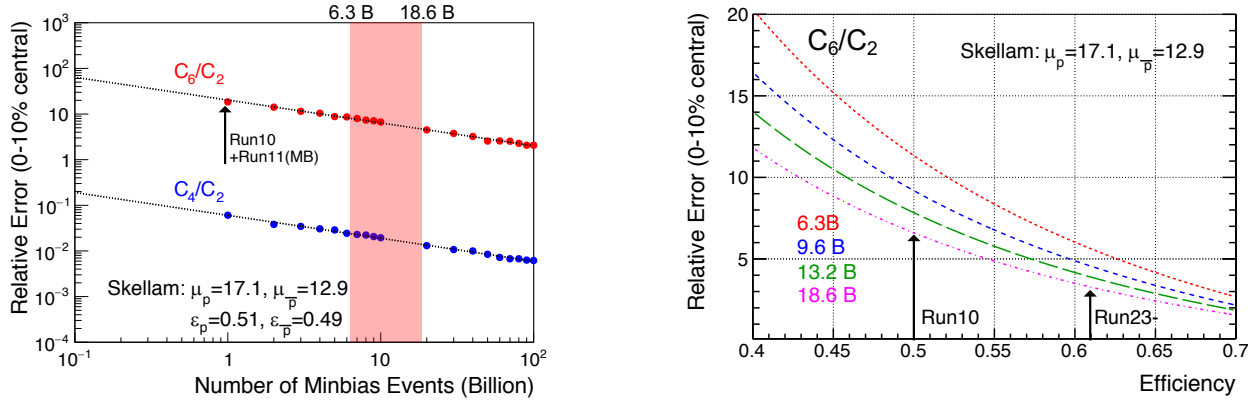


**Figure 55:** Projection for measurement of ratio of sixth order over second order cumulants of net-proton distribution.

1884 field makes a dominant contribution to the spin-alignment coefficient  $\rho_{00}$  of  $\phi$ , while for  $K^{*0}$ ,  
 1885 the contribution is diminished due to the mixing of quark flavors (averaging-out of different  
 1886 meson fields) [216, 217]. Therefore, the current preliminary experimental data from STAR  
 1887 (Fig. 54, showing  $\rho_{00}(\phi) > \rho_{00}(K^{*0})$ ) support the role of strong force field as a key mechanism  
 1888 that leads to global spin alignment. However, a stringent test of such a prediction can be  
 1889 performed by measuring the spin alignment of  $J/\psi$ . This is because similar arguments apply  
 1890 for both  $\phi$  and  $J/\psi$ , i.e. like  $s$  and  $\bar{s}$ , the strong field component also couples to  $c$  and  $\bar{c}$  quarks  
 1891 leading to larger  $\rho_{00}$  for  $J/\psi$ . In Fig. 54(right) we present the projected uncertainties for  $\rho_{00}$   
 1892 of  $J/\psi$  estimated for various centralities assuming: 1) 10 billion min-bias events for low  $p_T$   
 1893  $J/\psi$  measurements and, 2) 200 million events implementing High Tower (HT) triggers with  
 1894 the Barrel Electromagnetic Calorimeter for the high  $p_T$   $J/\psi$ . Both assume 24 weeks running  
 1895 anticipated in Run-23. It is worth to mention that apart from  $J/\psi$  spin alignment, such a  
 1896 large statistics data set will also allow addition differential study of global spin alignment of  
 1897  $\phi$  and  $K^{*0}$  and help to further elucidate the mechanism behind vector meson spin alignment.

1898 **Sixth order cumulant of net-proton distributions:** LQCD calculations [218, 219] pre-  
 1899 dict a sign change of the susceptibility ratio  $\chi_6^B/\chi_2^B$  with temperature ( $T$  at  $\mu_B = 0$ ) taking  
 1900 place in the range of 145-165 MeV. The observation of this ratio going from positive to neg-  
 1901 ative values is considered to be a signature of a crossover transition. As described in the  
 1902 previous section 1.1.2, the cumulants of net-proton distribution are sensitive to the chiral  
 1903 crossover transition at vanishing baryon chemical potential. Interestingly, as reported in the  
 1904 last BUR and in the recent Quark Matter 2019, the preliminary results from STAR [220] ob-  
 1905 served  $C_6/C_2 > 0$  in 54.4 GeV while  $C_6/C_2 < 0$  in 200 GeV in central Au+Au collisions. The  
 1906 observation of positive  $C_6/C_2$  at lower energies can be further confirmed by higher statistics  
 1907 data sets from the BES-II program over the energy range of 7.7-19.6 GeV, which also include  
 1908 the increased acceptance iTPC. The observation of negative  $C_6/C_2$  is intriguing and by far  
 1909 only seen at 200 GeV and based on the current STAR data has less than  $2.5\sigma$  significance  
 1910 in terms of statistical uncertainties. The current systematic uncertainty is of similar order

1911 as statistical uncertainty mainly due to combining data sets from Run-10 and Run-11. As  
 1912 shown in the projection plot of Fig. 55 it is possible to establish definitive observation of  
 1913 negative  $C_6/C_2$  at 200 GeV with nearly 10 billion minimum-bias events collected during the  
 1914 Run-23 with 15% increase in the reconstruction efficiency and enhanced acceptance of the  
 1915 iTPC detector upgrade. A similar measurement can be performed at the LHC ,however only  
 1916 STAR measurements can pinpoint the region of  $T$  and  $\mu_B$  where this phenomenon occurs.  
 1917 In other words it can establish if that the sign change occurs somewhere between 54.4 GeV  
 1918 and 200 GeV. Such a measurement has the potential to establish the first experimental  
 1919 observation of QCD chiral crossover transition.

### 1920 2.4.3 Electromagnetic Probes

1921 **Probing the degrees of freedom of the medium and its transport properties:** As  
 1922 discussed in Sect. 1.1.3, at  $\mu_B \sim 0$  Lattice QCD works and can be directly tested against  
 1923 experimental results. This will help to disentangle  $\rho$  melting from other explanations such  
 1924 as collision broadening. In case the measured in-medium spectral function merges into the  
 1925 QGP description this would indicate a transition from hadrons into a structure-less quark-  
 1926 antiquark continuum, thus providing the manifestation of chiral symmetry restoration. We  
 1927 will continue to search for a direct signature of chiral symmetry restoration via chiral  $\rho$ - $a_1$   
 1928 mixing. The signal is predicted to be detectable in the dilepton intermediate mass range.  
 1929 Difficulties are related to the fact that correlated charm-anticharm and QGP saturate the  
 1930 invariant mass region of 1.1 — 1.3 GeV/ $c^2$ . Therefore an accurate measurement of the  
 1931 excess dilepton yield, i.e. dilepton yield after subtraction of the cocktail of contributions from  
 1932 final-state decays, Drell-Yan and those from correlated heavy-flavor decays, up to invariant  
 1933 mass of 2.5 GeV/ $c^2$  is required. The challenging analysis on charmed-decayed dielectron  
 1934 is ongoing from the data sets taken with the Heavy Flavor Tracker at STAR [221]. Thus  
 1935 deeper understanding of origin of thermal radiation in Au+Au collisions at  $\sqrt{s_{NN}} = 200$  GeV  
 1936 from  $\sim$ zero mass up to 2.5 GeV/ $c^2$  will become possible with rigorous theoretical efforts and  
 1937 improved dielectron measurements. Figure 56 shows the expected statistical and systematic  
 1938 uncertainties of the dielectron excess mass spectrum with all the detector upgrades and for  
 1939 the anticipated total Run-23/Run-25 statistics of  $20 \times 10^9$  events.

1940 Another application of dileptons is to use them to measure transport coefficients. The  
 1941 electrical conductivity can be directly obtained as the low-energy limit of the EM spectral  
 1942 function. We aim to extract such information by studying excess dielectron yields at the low-  
 1943 energy regime of the dilepton spectra and the conductivity peak at small invariant masses,  
 1944 i.e. at low invariant mass and low  $p_T^{ee}$ . Low field run could be profitable, however already  
 1945 now dileptons with pair  $p_T^{ee}$  down to 60 MeV/ $c$  could be measured. Measurement of Drell-Yan  
 1946 in  $p$ +A collisions at low  $p_T$  would provide an important reference to constrain the dilepton  
 1947 cocktail.

1948 To gain a deeper understanding of the microscopic origin of the excess radiation, we will

- 1949 • separate early from later time radiation by measuring dilepton elliptic flow ( $v_2$ ) as a
- 1950 function of dilepton mass;

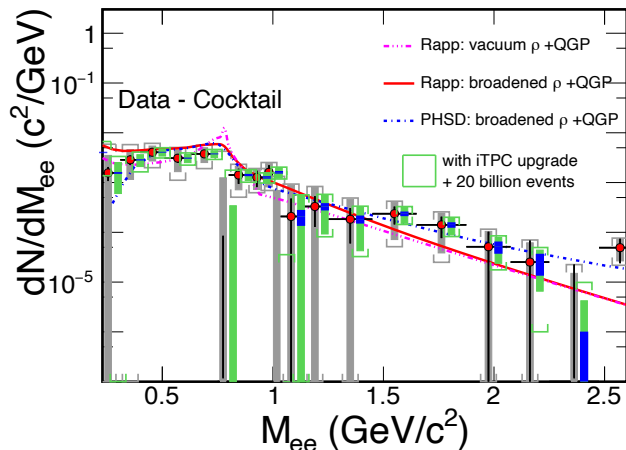


**Figure 56:** The expected statistical and systematic uncertainties on the dielectron excess mass spectrum with the iTPC upgrade compared to the current TPC case. The data are from our measurements in  $\sqrt{s_{NN}} = 200$  GeV Au+Au collisions [58]. Model comparisons are also shown. The boxes represent systematic uncertainties from data and the brackets represent the total systematic uncertainties including those from cocktails. The grey ones are for the current case while the green ones are for the Run-23+Run-25 case. The blue bands represent statistical uncertainties from 20 billion minimum-bias events with the iTPC upgrade.

- 1951 • identify the source of dilepton radiation by studying dilepton polarization versus in-  
1952 variant mass (helicity angle);
- 1953 • measure precisely the lifetime of the interacting fireball. As an observable we will use  
1954 integrated low-mass yield but also compare explicit model calculations with various  
1955  $\mathcal{T}_{fireball}$ ;
- 1956 • extract an average radiating source temperature from the fit of a Boltzmann distribu-  
1957 tion to the invariant mass slope in the range 1.1 - 2.5 GeV/ $c^2$  spectrum. The higher  
1958 the invariant mass, the stronger the QGP contribution to the spectrum, the higher the  
1959 chance to measure temperature of the QGP.

1960 Last, but not least, concerning direct-photon emission, the existing difference, on the  
1961 order of a factor of two, between the low momentum spectra from PHENIX and STAR in  
1962 200 GeV Au+Au collisions, has to be resolved. In order to clarify the direct photon puzzle  
1963 we will measure the direct virtual photon yield as well as its elliptic flow coefficient. We will  
1964 particularly focus on low  $p_T$   $\eta$  measurement which might be instrumental in clarifying this  
1965 long standing question.

1966 **Studying the photon Wigner function and final-state magnetic fields in the QGP:**  
1967 The unsuccessful description of STAR data by the STARLight model led to the attribution  
1968 of the broadening to the possible residual magnetic field trapped in an electrically conducting  
1969 QGP; which is key information to the study of the chiral magnetic effect. Similarly, ATLAS  
1970 qualified the effect via the acoplanarity of lepton pairs in contrast to the measurements in

1971 UPC and explained the additional broadening by multiple electromagnetic scatterings in  
 1972 the hot and dense medium, which is analogous to the medium  $P_{\perp}$ -broadening effects for  
 1973 jet quenching. These descriptions of the broadening in hadronic collisions are based on  
 1974 the assumption that there is no impact parameter dependence of the transverse momentum  
 1975 distribution for the electromagnetic production. Recent lowest-order QED calculation, in  
 1976 which the impact parameter dependence is recovered, could reasonably describe the broad-  
 1977 ening observed by STAR and ATLAS without any in-medium effect. To solve the puzzle, we  
 1978 propose to precisely study the initial  $P_{\perp}$ -broadening for the dilepton pair in ultra-peripheral  
 1979 collisions. Different neutron emission tags serve as the centrality definition, and will allow us  
 1980 to explore the broadening baseline variation with impact parameter. Furthermore, the differ-  
 1981 ential spectrum as a function of pair  $P_{\perp}$ , rapidity, and mass enable us to study the Wigner  
 1982 function of the initial electromagnetic field, which provide the information to extract the  
 1983 momentum and space correlation of EM field.

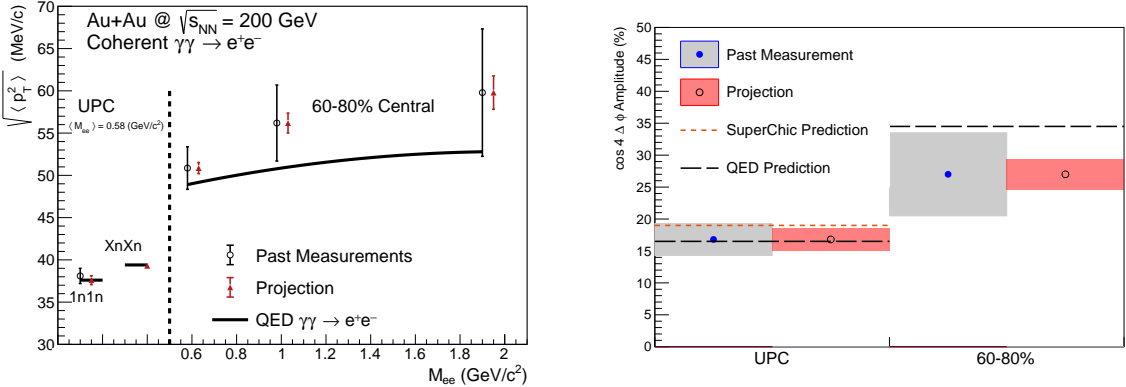


**Figure 57:** (Color online) Projections for measurements of the  $\gamma\gamma \rightarrow e^+e^-$  process in peripheral and ultra-peripheral collisions. Left: The  $\sqrt{\langle p_T^2 \rangle}$  of di-electron pairs within the fiducial acceptance as a function of pair mass,  $M_{ee}$ , for 60–80% central and ultra-peripheral Au+Au collisions at  $\sqrt{s_{NN}} = 200$  GeV. Right: The projection of the  $\cos 4\Delta\phi$  measurement for both peripheral (60–80%) and ultra-peripheral collisions.

1984 As shown in Fig. 57, comparing with the latest QED calculation, there still exists addi-  
 1985 tional broadening in peripheral collisions, although the significance is only about  $1\sigma$ , which  
 1986 still leave room for the medium effect. In Run-23 and Run-25, as projected in the figure, we  
 1987 could judge the existence of additional broadening with much higher precision and further  
 1988 constrain the strength of final-state magnetic field in the QGP.

1989 Precision measurement of the amplitude of the recently observed  $\cos 4\Delta\phi$  modulation of  
 1990 the  $\gamma\gamma \rightarrow e^+e^-$  process will allow precision mapping of the photon Wigner function and  
 1991 provide additional constraints on possible final-state effects, thereby complementing the  $P_{\perp}$   
 1992 broadening measurement. Figure 57 right panel shows the projected precision for a mea-  
 1993 surement of the  $\cos 4\Delta\phi$  modulation in Run-23+25. The modulation is a direct result of  
 1994 the mismatch in initial and final spin configuration of the  $\gamma\gamma \rightarrow e^+e^-$  process. Any final-

1995 state effect that modifies the  $P_{\perp}$  will necessarily reduce the amplitude of the modulation.  
 1996 Assuming the same central value as previously measured, evidence for suppression of the  
 1997  $\cos 4\Delta\phi$  modulation will be visible at the  $> 3\sigma$  level (stat. & syst. uncertainty). Preci-  
 1998 sion measurement of the  $\cos 4\Delta\phi$  modulation in Run-23+25 may also allow a first direct  
 1999 experimental measurement of the impact parameter dependence of this new observable (by  
 2000 comparing UPC and 60 – 80%). Assuming the same central values as previously measured,  
 2001 the improved precision will provide evidence for impact parameter dependence at the  $> 3\sigma$   
 2002 level (stat. & syst. uncertainty). Assuming the central value predicted by QED would lead  
 2003 to a  $> 5\sigma$  difference between the UPC case and the 60 – 80% case.

2004 **Ultra-peripheral Au+Au collisions: probe gluon distribution inside nucleus:**  
 2005 STAR recently observed a significant  $\cos 2\Delta\phi$  azimuthal modulation in  $\pi^+\pi^-$  pairs from  
 2006 photonuclear  $\rho^0$  and continuum production. The structure of the observed modulation as  
 2007 a function of the  $\pi^+\pi^-$  pair transverse momentum,  $P_{\perp}$ , appears related to the diffractive  
 2008 pattern. Recent theoretical calculations [222], which implemented linearly polarized pho-  
 2009 tons interacting with the saturated gluons inside a nucleus, have successfully described the  
 2010 qualitative features of the observed modulation (see Fig. 58), and indicate that the detailed  
 2011 structure of the  $\cos 2\Delta\phi$  modulation vs.  $P_{\perp}$  is sensitive to the nuclear geometry and gluon  
 2012 distribution. Data from Run-23+25 would allow the additional statistical reach needed to  
 2013 perform multi-differential analysis, providing stronger theoretical constraints. Specifically,  
 2014 multi-differential analysis of the  $\cos 2\Delta\phi$  modulation with respect to pair rapidity and pair  
 2015 mass are needed. Multi-differential analysis with respect pair mass is needed to separate  
 2016 the  $\rho^0$  production from the continuum Drell-Soding production. Multi-differential analysis  
 2017 with respect to the pair rapidity is needed to quantitatively investigate how the double-slit  
 2018 interference mechanism effects the structure of the observed azimuthal modulation. Addi-  
 2019 tional statistical precision is also needed for measurement of the higher harmonics. Similar  
 2020 measurements with  $J/\Psi \rightarrow e^+e^-$  can be performed and such measurements at higher mass  
 2021 provide better comparison with more reliable QCD calculation.

2022 Ultraperipheral A+A collisions, where photons generated by the Lorentz-boosted electro-  
 2023 magnetic field of one nucleus interact with the gluons inside the other nucleus, can provide  
 2024 certain 3D gluonic tomography measurements of heavy ions, even before the operation of  
 2025 the future EIC. STAR has performed experimental measurements of the photoproduction  
 2026 of  $J/\psi$  at low transverse momentum in non-UPC heavy-ion collisions [223], accompanying  
 2027 the violent hadronic collisions. A detailed study with  $p_{\text{T}}$  distributions has shown that the  
 2028  $|t|$  distribution in peripheral collisions is more consistent with the coherent diffractive pro-  
 2029 cess than the incoherent process. Although models [224, 225] incorporating different partial  
 2030 coherent photon and nuclear interactions could explain the yields, it remains unclear how  
 2031 the coherent process happens and whether final-state effects play any role [226]. Resolving  
 2032 this puzzle with high statistical data and detailed  $|t|$  distributions at different centralities  
 2033 at RHIC as projected for Run-23+25 in Fig. 58 may be important for understanding what  
 2034 defines the coherentness of the photoproduction, how vector mesons are formed in the pro-  
 2035 cess and how exclusive the similar process has to be in future EIC experiments with forward

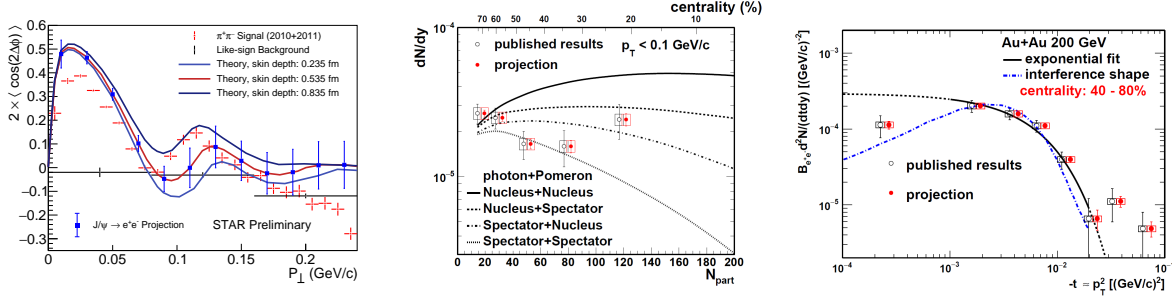


**Figure 58:** Left: Measurement of the  $\cos 2\Delta\phi$  modulation of  $\pi^+\pi^-$  pairs from photonuclear  $\rho^0$  and continuum production compared to theoretical predictions [222]. Projections are shown for a similar measurement of the azimuthal modulation of  $e^+e^-$  pairs from photonuclear production of the  $J/\psi$ . Center: Projection of the  $dN/dy$  of photoproduced  $J/\psi$  in non-UPC events vs. the event centrality ( $N_{\text{part}}$ ) compared to various theoretical production scenarios. Right: Projection of the  $t$  spectra of photoproduced  $J/\psi$  in 40 – 80% central collisions.

2036 neutron veto/tagging.

#### 2037 2.4.4 Deconfinement and Thermalization With Charmonia Measurements

2038 Measurements of charmonia in heavy-ion collisions provide important information about the  
 2039 thermodynamic properties of the created medium. Production of  $J/\psi$  mesons in Au+Au  
 2040 collisions at RHIC was found to be suppressed compared to the production in  $p+p$  collisions.  
 2041 The suppression of charmonium states is due to a screening of the  $c\bar{c}$  potential by the  
 2042 medium color charges. In addition,  $J/\psi$  production can be affected by recombination of  
 2043 charm quarks in a later stage of the collision evolution. The regeneration mechanism is  
 2044 expected to contribute mostly at the low  $J/\psi$  transverse momentum range.

2045 In particular, STAR proposes to utilize the Run-23+25 RHIC heavy-ion runs to measure:  
 2046 (i) low transverse momentum  $J/\psi$  elliptic flow ( $v_2$ ) in order to study in more detail the  
 2047 recombination mechanism (ii)  $J/\psi$  directed flow ( $v_1$ ) that will allow us to study the initial  
 2048 tilt of the bulk medium (iii) suppression of the loosely bounded  $\psi(2S)$  state to explore the  
 2049 temperature profile of the medium.

2050 An important observable for studying the properties of the deconfined medium is the  
 2051 second order flow harmonic of the Fourier expansion of the azimuthal distribution of the  
 2052 produced hadrons, the elliptic flow coefficient  $v_2$ . As in the case of light hadrons, a positive  $v_2$   
 2053 of  $D$ -mesons and electrons from heavy-flavor hadron decays was observed at RHIC energies  
 2054 of 54.4 and 200 GeV. Which suggests that charm quarks may (partially) thermalize and  
 2055 participate in the bulk medium collective evolution. On the other hand, the  $v_2$  of heavier  
 2056  $J/\psi$  reported by STAR based on the 2010 Au+Au 200 GeV data sample was found to be  
 2057 consistent with zero, albeit within large statistical uncertainties and systematic uncertainties  
 2058 due to non-flow effects. The precision of the measurement was also not enough to distinguish  
 2059 between theoretical model calculations that assume only primordial  $J/\psi$  production and ones  
 2060 that include additional  $J/\psi$  production via the recombination. This calls for a larger sample

2061 of heavy-ion data at 200 GeV, as will be provided by RHIC in 2023 and 2025, in order to  
 2062 observe a possible non-zero  $J/\psi$   $v_2$  at RHIC energies and put more constraints on the  $J/\psi$   
 2063 production models especially regarding its regeneration. Particularly important for these  
 2064 studies is STAR's potential to measure low transverse momentum  $J/\psi$  with a very good  
 2065 precision. This excellent low- $p_T$  performance at STAR can be achieved thanks to its low  
 2066 material budget and great particle identification capabilities.

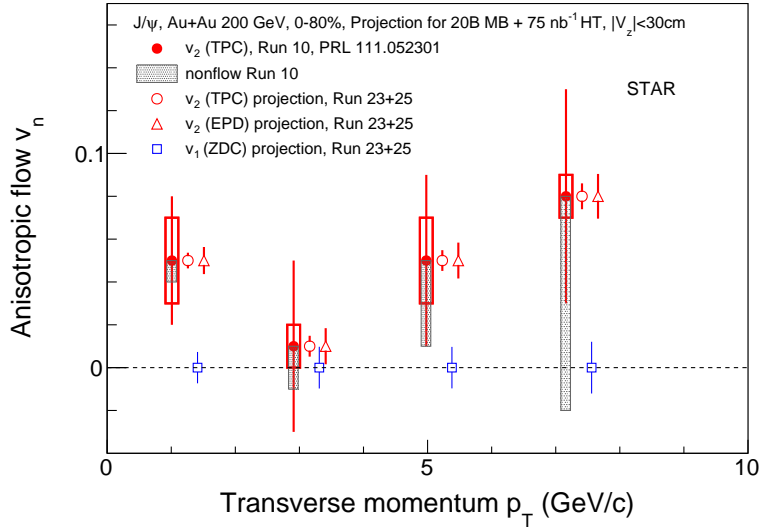


**Figure 59:** Projections for the  $J/\psi$  ( $J/\psi \rightarrow e^+e^-$ ) directed ( $v_1$ ) and elliptic ( $v_2$ ) flow vs  $J/\psi$   $p_T$  in 0-80% Au+Au collisions at 200 GeV, assuming 20 B MB events and HT triggered events corresponding to an integrated luminosity of  $75 \text{ nb}^{-1}$  with  $|V_Z| < 30 \text{ cm}$ .

2067 Moreover, the second order Event Plane (EP) can be reconstructed using the new Event  
 2068 Plane Detectors (EPD) installed before Run-18. It is expected that using the forward EPD  
 2069 will significantly decrease the contribution from the non-flow effects and consequently the  
 2070 measurement's systematic uncertainties. Also, an inverse of the EP resolution enters di-  
 2071 rectly the  $J/\psi$   $v_2$  uncertainty calculation. Thanks to the EPD, the resolution of the EP  
 2072 reconstruction at forward rapidity for the  $J/\psi$   $v_2$  measurement at STAR will improve. Fig-  
 2073 ure 59 presents statistical projections for the  $J/\psi$   $v_2$  measurement in 0-80% central Au+Au  
 2074 collisions assuming 20 B MB events and HT triggered events corresponding to an integrated  
 2075 luminosity of  $75 \text{ nb}^{-1}$ . Both cases of the second order EP reconstruction, using the for-  
 2076 ward EPD and mid-rapidity TPC detectors, are considered and shown. A clear significant  
 2077 improvement in the precision of the  $J/\psi$   $v_2$  can be seen across the whole experimentally  
 2078 accessible  $J/\psi$   $p_T$  coverage of the previous measurement. In addition, the new larger dataset  
 2079 would allow to extend the measured  $p_T$  range beyond 10 GeV/c.

2080 Studies of the directed flow,  $v_1$ , as a function of rapidity provide crucial information to  
 2081 understand the initial tilt of the medium produced in heavy-ion collision. Heavy quarks are  
 2082 produced in the early stage of a heavy-ion collision and thus are of a particular interest for  
 2083 the medium initial asymmetry studies. STAR recently reported the first measurement of D-

2084 meson  $v_1$  in Au+Au collisions at 200 GeV where the magnitude of the heavy-flavor meson  $v_1$   
 2085 is about 25 times larger than the  $v_1$  for charged kaons. With the 2023-2025 data, STAR would  
 2086 have a unique opportunity to also study the  $v_1$  of a bound  $c\bar{c}$  state, the  $J/\psi$  mesons, for which  
 2087 even larger directed flow can be expected [227]. In addition to STAR's excellent capability  
 2088 to reconstruct low- $p_T$   $J/\psi$ , as discussed above, the iTPC detector completed in 2018 will  
 2089 improve the momentum resolution and extend the pseudorapidity coverage. This will provide  
 2090 better precision for the slope extraction of the  $v_1$  vs  $y$  measurement, that quantifies the  
 2091 strength of directed flow. The expected precision of a  $J/\psi$   $v_1$  measurement vs  $p_T$  at STAR in  
 2092 2023-2025, assuming 20 B MB events and HT triggered events corresponding to an integrated  
 2093 luminosity of  $75 \text{ nb}^{-1}$ , in 0-80% central Au+Au collisions at 200 GeV is shown in Fig. 59.  
 2094 Together with the  $J/\psi$   $v_2$  measurements,  $v_1$  would provide a more complete picture of the  
 2095  $J/\psi$  production mechanism as well as the medium properties in heavy-ion collisions at RHIC.

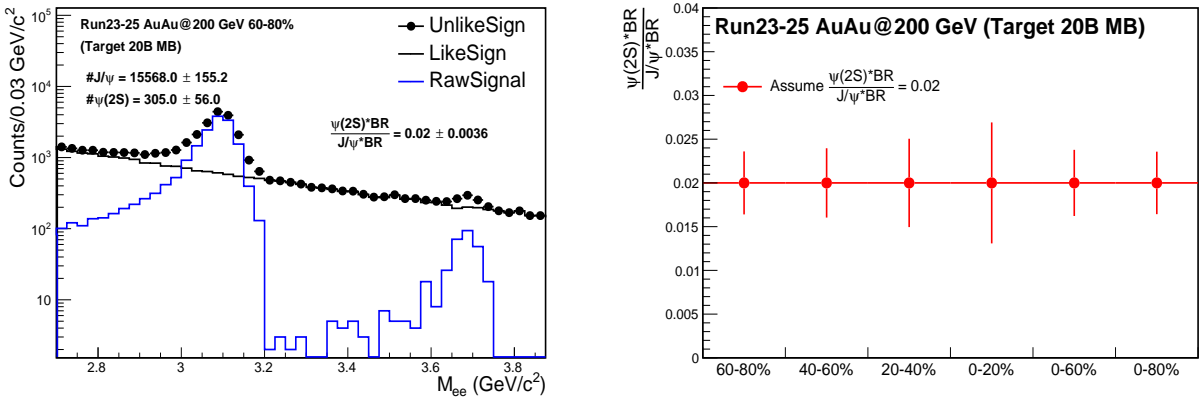


**Figure 60:** Projections for the  $J/\psi$  and  $\psi(2S)$  signals in 60-80% Au+Au collisions at 200 GeV and the yield ratio in various centrality bins. The improvement of momentum and  $dE/dx$  resolution thanks to the iTPC upgrade have not been taken into account.

2096  $\psi(2S)$  is the most loosely bounded quarkonium state accessible in the heavy-ion collision  
 2097 experiments. Its dissociation temperature is predicted to be around or below the critical  
 2098 temperature and is much less than that of  $J/\psi$  and  $\Upsilon$  states. It is more likely to be dis-  
 2099 sociated in the early stage and in the core of the fireball and the  $\psi(2S)$  survived may have  
 2100 significant contribution from the regeneration at later stage in the evolution of the fireball.  
 2101 The relative suppression of  $\psi(2S)$  and  $J/\psi$  is sensitive to the the temperature profile of the  
 2102 fireball produced in heavy-ion collisions and its space-time evolution. It is also argued that  
 2103 the charmonium formation process from a  $c\bar{c}$  pair may be affected by the QGP or the ini-  
 2104 tial strong external magnetic field, altering the relative yields among different charmonium  
 2105 states [228, 229]. The measurement of  $\psi(2S)$  is much more difficult than that of  $J/\psi$  due to  
 2106 a much smaller production cross-section and dilepton decay branching ratio, resulting in a  
 2107 very low signal-to-background ratio. The ALICE Collaboration successfully measured the  
 2108 relative suppression of  $\psi(2S)$  and  $J/\psi$  in Pb+Pb collisions at forward rapidity [230], and the  
 2109 ATLAS and CMS Collaborations published the relative suppression in Pb+Pb collisions at

2110 mid-rapidity and high  $p_T$  [231, 232]. Attempts to measure  $\psi(2S)$  suppression in heavy-ion  
 2111 collisions at RHIC have not been successful to date. The low material budget and excellent  
 2112 particle identification capability of STAR together with the combined large data sample in  
 2113 2023 and 2025 will provide a unique opportunity to measure the suppression of  $\psi(2S)$  at low  
 2114  $p_T$  and mid-rapidity in heavy-ion collisions. Figure 60 shows the projections of  $\psi(2S)$  signal  
 2115 and the yield ratio of  $\psi(2S)$  and  $J/\psi$  in Au+Au collisions assuming 20 B MB events. The  
 2116 improvement of momentum and  $dE/dx$  resolution thanks to the STAR iTPC upgrade will  
 2117 further enhance the signal-to-background ratio and the significance of  $\psi(2S)$  signal.

#### 2118 2.4.5 Jet Probes

2119 Precise jet quenching measurements with reconstructed jets over a broad kinematic range  
 2120 at RHIC are essential to meet the goal of the NSAC 2015 Long Range Plan, to “probe the  
 2121 inner workings of the QGP” [198]. For example, the dependence of jet energy loss on the jet  
 2122  $p_T$  and the resolution or angular scale tagged by jet substructure observables are key tools  
 2123 to discriminate jet quenching mechanisms [233–236]. In addition, the measurement of jet  
 2124 acoplanarity as a probe of in-medium jet scattering is most sensitive at low jet  $p_T$  to a given  
 2125 momentum transfer and to medium-induced radiative effects [237], and is least affected by  
 2126 background due to vacuum Sudakov radiation [238].

2127 The highest-statistics STAR Au+Au collision datasets currently available were recorded  
 2128 in 2014 and 2016, with the integrated luminosity sampled by STAR BEMC triggers shown  
 2129 in Table 10. Preliminary jet analyses using the 2014 dataset are discussed in section 1.1.1  
 2130 and are moving towards publication. STAR will continue to exploit these rich datasets to  
 2131 carry out high-precision measurements with fully reconstructed jets over the full RHIC phase  
 2132 space.

2133 The 2023 and 2025 runs will generate another significant increase in sampled integrated  
 2134 luminosity, enabling a third generation of STAR heavy-ion jet measurements that are yet  
 2135 more differential and precise. STAR’s open geometry near the beam pipe allows it to utilize  
 2136 a wide range in the vertex position along the beam direction ( $vz$ ) for jet analyses, thereby  
 2137 utilizing the RHIC luminosity efficiently. Optimization of the  $vz$  range used in an analysis  
 2138 entails a balance between statistical precision and complexity of corrections, with the latter  
 2139 influencing the systematic uncertainty of the measurement. Recent STAR jet measurements  
 2140 in Au+Au collisions have employ two different  $z$ -vertex cuts: the inclusive charged-particle  
 2141 jet analysis [7] utilizes  $|vz| < 30$  cm, whereas the  $\gamma_{\text{dir}} + \text{jet}$  analysis [10] utilizes  $|vz| < 70$   
 2142 cm. With the success of the  $\gamma_{\text{dir}} + \text{jet}$  analysis in analyzing this broad  $vz$  range with good  
 2143 systematic precision, we will re-examine this cut for future jet measurements, including the  
 2144 inclusive jet analysis. In section 2.4 we present the sampled integrated luminosity in 2023 and  
 2145 2025 for both the 30 cm and 70 cm  $vz$  cuts. The following physics performance projections  
 2146 are based on the 70 cm cut, using the cumulative sampled integrated luminosity for Run-14,  
 2147 Run-16, and 2023 and 2025 together. For  $|vz| < 70$  cm, this total is  $110 \text{ nb}^{-1}$ , which is a  
 2148 factor 11 increase in trigger statistics relative to the current analyses based on Run-14 data.

2149 To quantify the effect of this marked increase in integrated luminosity, we utilize two  
 2150 mature jet measurements currently in progress and discuss their expected improvement

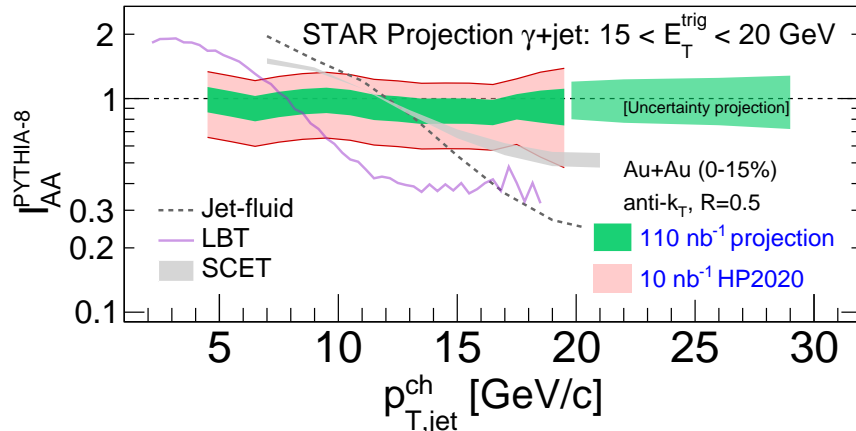


**Figure 61:** Ratio of semi-inclusive distributions of charged-particle jets (anti- $k_T$ ,  $R = 0.5$ ) recoiling from a direct-photon trigger with  $15 < E_T < 20$  GeV for central Au+Au collisions at  $\sqrt{s_{NN}} = 200$  GeV measured by STAR (numerator) and  $p+p$  collisions simulated by PYTHIA (denominator). The pink band shows the cumulative uncertainty for the current analysis based on  $10 \text{ nb}^{-1}$  [10], while the green band shows the projected uncertainty for  $110 \text{ nb}^{-1}$ . Theory calculations are discussed in [10].

2151 with enhanced integrated luminosity. These analyses are the semi-inclusive distribution  
 2152 of charged-particle jets recoiling from a high- $E_T$  direct-photon trigger ( $\gamma_{\text{dir}} + \text{jet}$ ); and the  
 2153 differential measurement of energy loss for jet populations selected by varying a substructure  
 2154 metric. Since these analyses are mature, their analysis methodologies and correction  
 2155 schemes are optimized, so that their projections based on increased statistics are meaningful.  
 2156 We do not imply that these will be the only flagship measurements that STAR will make  
 2157 with the 2023/2025 datasets; we will additionally continue to focus, for instance, on fully  
 2158 reconstructed jets and utilizing substructure observables, including those not yet developed.  
 2159 However, these analyses are most mature at present, and therefore provide the most accurate  
 2160 projections of gain in precision.

2161 **Semi-inclusive  $\gamma_{\text{dir}} + \text{jet}$  measurement:** Figure 61 shows  $I_{AA}$  for fully-corrected semi-  
 2162 inclusive distributions of charged-particle jets (anti- $k_T$ ,  $R = 0.5$ ) recoiling from a direct-  
 2163 photon trigger with  $15 < E_T < 20$  GeV in central Au+Au collisions at  $\sqrt{s_{NN}} = 200$  GeV, for  
 2164 the current analysis based on  $10 \text{ nb}^{-1}$  [10] within  $|vz| < 70$  cm, and projected for  $110 \text{ nb}^{-1}$ .  
 2165 Significant reduction in the uncertainty band is seen to result from the increase in integrated  
 2166 luminosity, together with significant increase in kinematic reach.

2167 Note that the projection to  $110 \text{ nb}^{-1}$  only takes into account the increase in statistical  
 2168 precision, and assumes that the systematic uncertainty remains the same. The reduction in  
 2169 width of the uncertainty band is therefore less than the factor  $1/\sqrt{11}$  expected from statistical  
 2170 considerations alone, indicating the magnitude of the systematic component. Experience  
 2171 shows that systematic uncertainty can also be improved by an increase in statistical precision,  
 2172 since additional and more differential systematic studies can be carried out. However, it is

2173 not possible to project that improvement with confidence at present; thus Fig. 61 should  
 2174 be regarded as a conservative estimate of the improvement in precision of this measurement  
 2175 channel with the projected integrated luminosity increase.

2176 Broadening of the back-to-back di-jet angular distribution due to jet scattering from con-  
 2177 stituents of the QGP (medium-induced acoplanarity) was proposed over three decades ago  
 2178 as a diagnostic probe of the QGP [239, 240]. While the physical picture of this process is  
 2179 intuitive and compelling, such measurements are extremely challenging, because of both the  
 2180 large jet backgrounds in heavy-ion collisions, and the large contribution of vacuum QCD pro-  
 2181 cesses (Sudakov radiation) to the di-jet angular distribution [238]. In addition, minimization  
 2182 of these two effects nominally drives the experimentalist in opposite directions: minimization  
 2183 of background effects prefers larger  $p_{T,\text{jet}}$ , whereas minimization of Sudakov broadening and  
 2184 higher sensitivity to medium-induced momentum transfer prefers lower  $p_{T,\text{jet}}$  [238]. These  
 2185 contradictory requirements were resolved only with the development of absolutely normalized  
 2186 semi-inclusive jet measurements in heavy-ion collisions, with statistically-based background  
 2187 corrections that enable measurements at low  $p_{T,\text{jet}}$  and large  $R$  [1, 241].

2188 The first generation searches for medium-induced acoplanarity using this approach did  
 2189 not exhibit a significant signal above background [1, 241], though with limited statistical  
 2190 precision. Higher-precision measurements of medium-induced acoplanarity over a broad  $p_{T,\text{jet}}$   
 2191 range – including low  $p_{T,\text{jet}}$  – are clearly of great interest at both RHIC and the LHC. Such  
 2192 measurements may provide a direct probe of  $\hat{q}$  [238], or evidence of large-angle jet scattering  
 2193 off of quasi-particles in the QGP [242]. Consideration of higher-order processes suggests that  
 2194 the contribution of radiative corrections to this distribution may be negative [237], thereby  
 2195 narrowing rather than broadening the recoil jet azimuthal distribution; a recent preliminary  
 2196 measurement by ALICE may indeed have observed such an effect [243]. Complementary  
 2197 measurements of medium-induced acoplanarity over wide phase space by STAR at RHIC and  
 2198 ALICE at the LHC, using similar instrumentation and similar analysis techniques, promise to  
 2199 provide strong constraints on theoretical descriptions of this fundamental process, providing  
 2200 new insight into the inner workings of the QGP [198].

2201 Figure 62 shows the semi-inclusive distribution of the azimuthal separation between a  
 2202 direct-photon trigger with  $15 < E_T < 20$  GeV and a charged-particle jet (anti- $k_T$ ,  $R = 0.5$ )  
 2203 with  $10 < p_{T,\text{jet}}^{\text{ch}} < 15$  GeV/ $c$ , in central Au+Au collisions at  $\sqrt{s_{\text{NN}}} = 200$  GeV with only  
 2204 statistical error bars, based on the analysis described in [10]. Azimuthal smearing of this  
 2205 observable due to uncorrelated background is small, and such acoplanarity measurements  
 2206 are therefore strongly statistics-dominated [1, 241]. The grey points are from the current  
 2207 analysis based on  $10 \text{ nb}^{-1}$  [10], whereas the red points correspond to  $110 \text{ nb}^{-1}$ . A marked  
 2208 increase in measurement precision is projected, with corresponding qualitative increase in  
 2209 physics impact. Similar improvements in precision for this observable are expected at the  
 2210 LHC in Run 3, due to detector upgrades and enhanced machine luminosity [155].

2211 **Jet measurement with a varying substructure metric:** An important facet of the  
 2212 third generation of STAR jet measurements is a systematic exploration of parton energy loss  
 2213 based on controlled variation of the jet shower topology. Jet evolution produces a unique

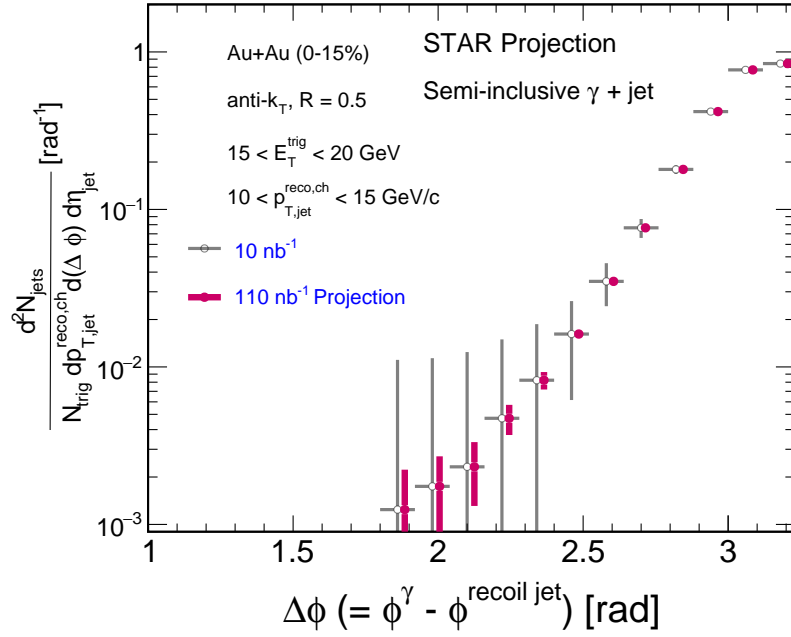


**Figure 62:** Semi-inclusive azimuthal distribution of charged jets (anti- $k_T$ ,  $R=0.5$ ) with  $10 < p_{T,\text{jet}}^{\text{ch}} < 15$  GeV/ $c$  recoiling from a direct photon trigger with  $15 < E_T^{\text{trig}} < 20$  GeV, in central Au+Au collisions at  $\sqrt{s_{\text{NN}}} = 200$  GeV. Grey points: current analysis with  $10 \text{ nb}^{-1}$  [10]; red points: projection for  $110 \text{ nb}^{-1}$ . Error bars are statistical only.

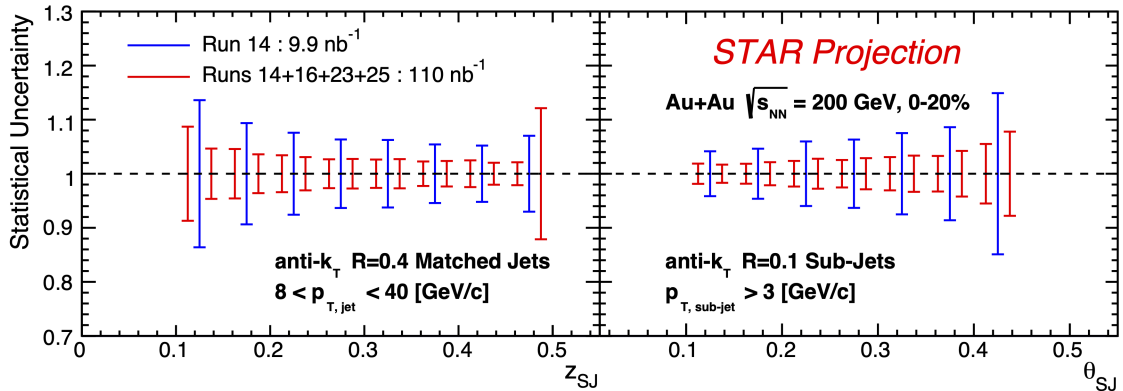


**Figure 63:** Two-panel figure showing statistical uncertainty for the two-subject observables in 0-20% central Au+Au collisions for  $10 \text{ nb}^{-1}$  in blue and projection for  $110 \text{ nb}^{-1}$  in red.

2214 pattern of radiation in both angle and momentum, and jet substructure observables are a  
 2215 broad class of measurements of combinations of the jet constituents' angle and/or momentum  
 2216 via algorithms or correlations. As the jet undergoes interactions with the medium, jet  
 2217 substructure modification for a given jet energy (e.g. comparing the heavy-ion results to  
 2218 those in  $p+p$  collisions) has been used as a way to access the microscopic properties of the  
 2219 medium. By selecting on jets based on their substructure, we can study how a particular  
 2220 class of jets interacts with the medium to determine the effects of e.g. color coherence, dead  
 2221 cone, etc. on parton-medium interactions. In other words, the STAR jet program for Run-  
 2222 23+Run-25 will focus on jet substructure as a jet-tagger.

2223 Recent theory calculations have shown significant differences between energy loss signa-  
 2224 tures for jets that are perceived by the medium as a single or multiple color charges [235].  
 2225 Algorithms such as SoftDrop and sub-jets [244, 245] provide observables that correspond to  
 2226 the splitting within jets via momentum fractions and an inherent angular scale which then  
 2227 serve as a proxy for the resolution scale in the medium. This is often referred to as coher-  
 2228 ent vs. de-coherent energy loss where the coherent length of the medium is related to its  
 2229 temperature and  $\hat{q}$  [246]. By isolating population of jets based on their substructure, one  
 2230 can directly probe energy loss for varying resolution scales. The integrated luminosity from  
 2231 the Run-23+Run-25 datasets will not only provide a substantial increase in statistics in the  
 2232 current measurements of jet substructure, they also make the phase space available for rare  
 2233 processes such as wide angle emissions from high- $p_T$  jets. This enables STAR to extend our  
 2234 current measurements of differential energy loss [2] to fine binning in the opening angles and  
 2235 momentum fractions, as shown in Fig. 63. The current resolution of  $\delta\theta_{\text{SJ}} = 0.1$  [2] is predom-  
 2236 inantly due to statistical limitations in our older dataset sample. The significant increase in  
 2237 integrated luminosity for Run-23+Run-25, coupled with excellent tracking resolution of the  
 2238 STAR TPC will reduce the opening angles resolution to 0.025 and have a significant popula-  
 2239 tion of jets where we can further identify and select jet topologies in both  $z$  and  $\theta$  and study  
 2240 energy loss in a three-dimensional fashion. By extending to high energy splittings within

2241 jets, at varied opening angles, we can probe earlier formation times whereby vacuum-like  
2242 emissions and medium induced radiations are expected to occur.

2243 STAR is uniquely situated to perform high impact differential measurements of parton  
2244 energy loss starting from the unbiased, semi-inclusive jet population, to a topologically spe-  
2245 cial population of jets, selected via jet substructure observables.

2246 Given the unique nature of jet-medium interactions at RHIC, with the jet and sub-jet  
2247 scales sufficiently closer to the medium scale, the aforementioned measurements bolster the  
2248 importance of the STAR jet program with the goal of extracting the microscopic properties  
2249 of the QGP as outlined in the 2015 LRP.

### 3 Cold QCD Physics with $p^\uparrow+p^\uparrow$ and $p^\uparrow+A$ Collisions at 510 and 200 GeV

The exploration of the fundamental structure of strongly interacting matter has always thrived on the complementarity of lepton scattering and purely hadronic probes. As the community eagerly anticipates the future Electron Ion Collider, an outstanding scientific opportunity remains to complete “must-do” measurements in  $p+p$  and  $p+A$  physics during the final years of RHIC. These measurements will be essential if we are fully to realize the scientific promise of the EIC, by providing a comprehensive set of measurements in hadronic collisions that, when combined with future data from the EIC, will establish the validity and limits of factorization and universality. Much of the Run-22 and Run-24 physics program outlined here is, on the one hand, unique to proton-proton and proton-nucleus collisions and offers discovery potential on its own. On the hand, these studies will lay the groundwork for the EIC, both scientifically and in terms of refining the experimental requirements of the physics program, and thus are the natural next steps on the path to the EIC. When combined with data from the EIC these STAR results will provide a broad foundation to a deeper understanding of fundamental QCD.

The separation between the intrinsic properties of hadrons and interaction-dependent dynamics, formalized by the concept of factorization, is a cornerstone of QCD and largely responsible for the predictive power of the theory in many contexts. While this concept and the associated notion of universality of the quantities that describe hadron structure have been successfully tested for unpolarized and, to a lesser extent, longitudinally polarized parton densities, its experimental validation remains an unfinished task for much of what the EIC is designed to study – the three-dimensional structure of the proton and the physics of dense partonic systems in heavy nuclei. To establish the validity and limits of factorization and universality, it is essential to have data from *both* lepton-ion and proton-ion collisions, with experimental accuracy that makes quantitative comparisons meaningful.

Beginning in Run-22, STAR will be in a unique position to provide this essential  $p+p$  and  $p+A$  data. A full suite of forward detectors will be installed, providing excellent charged-particle tracking at high pseudorapidity ( $2.5 < \eta < 4$ ) for the first time, coupled with both electromagnetic and hadronic calorimetry. This will enable STAR to explore the interesting regimes of high- $x$  (largely valence quark) and low- $x$  (primarily gluon) partonic physics with unparalleled precision. In addition, mid-rapidity detector upgrades motivated primarily by the BES-II program – the iTPC, eTOF, and EPD systems – will substantially extend STAR’s already excellent kinematic reach and particle identification capabilities beyond those that existed during previous  $p+p$  and  $p+A$  runs.

For the case of  $p+p$  spin physics, it’s important to recognize the complementary roles that will be played by Run-22 at 510 GeV and Run-24 at 200 GeV. The combination of 510 GeV  $p+p$  collisions and the STAR Forward Upgrade will provide access to forward jet physics at perturbative scales, thereby enabling measurements at the highest and lowest  $x$  values. In parallel, mid-rapidity measurements at 510 and, especially, 200 GeV will interpolate between the high and low  $x$  values, with significant overlaps to probe evolution effects

2291 and provide cross-checks. Together, the two runs will allow STAR to measure fundamental  
2292 proton properties, such as the Sivers and transversity distributions, over nearly the entire  
2293 range  $0.005 < x < 0.5$ .

2294 Run-24 will also provide outstanding opportunities to probe fundamental questions re-  
2295 garding QCD in cold nuclear matter. The STAR Forward Upgrade will enable an extensive  
2296 suite of measurements probing the quark-gluon structure of heavy nuclei and the regime of  
2297 low- $x$  non-linear gluon dynamics, as predicted by saturation models. STAR will also ex-  
2298 plore how a nucleus, serving as a color filter, modifies the propagation, attenuation, and  
2299 hadronization of colored quarks and gluons.

2300 For these reasons, STAR requests at least 16 weeks of polarized  $p+p$  data-taking at  $\sqrt{s} =$   
2301 510 GeV in Run-22. All data taking will involve proton beams polarized transversely relative  
2302 to their momentum direction in order to focus on those observables where factorization,  
2303 universonality, and/or evolution remain open questions, with spins aligned either vertically or  
2304 radially at the STAR IR (still to be determined through more detailed simulation studies).  
2305 Based on the latest guidance from CAD, and mindful of ‘lessons learned’ in previous  $p+p$   
2306 runs at full energy, we will ask for luminosity-leveling of the collision rate to maximize the  
2307 efficiency of our main tracking detectors. Assuming we will have running conditions similar to  
2308 those achieved in Run-17, we expect to sample at least  $400 \text{ pb}^{-1}$  for our rare / non-prescaled  
2309 triggers.

2310 STAR also requests at least 11 weeks of polarized  $p+p$  data-taking at  $\sqrt{s} = 200 \text{ GeV}$   
2311 and 11 weeks of polarized  $p+\text{Au}$  data-taking at  $\sqrt{s_{NN}} = 200 \text{ GeV}$  during Run-24. Similar  
2312 to Run-22, all of the running will involve transversely polarized protons, with the choice  
2313 between vertical or radial polarization to be determined during the coming year. Based on  
2314 recent (08-21-20) CAD guidance, we expect to sample at least  $235 \text{ pb}^{-1}$  of  $p+p$  collisions  
2315 and  $1.3 \text{ pb}^{-1}$  of  $p+\text{Au}$  collisions. These totals represent 4.5 times the luminosity that STAR  
2316 sampled during transversely polarized  $p+p$  collisions in Run-15, and 3 times the luminosity  
2317 that STAR sampled during transversely polarized  $p+\text{Au}$  collisions in Run-15.

## 2318 **3.1 Run-22 Request for $p^\uparrow+p^\uparrow$ Collisions at 510 GeV**

### 2319 **3.1.1 Inclusive transverse spin asymmetries at forward rapidities**

2320 The experimental study of spin phenomena in nuclear and particle physics has a long history  
2321 of producing important, and often surprising, results. Attempts to understand such data  
2322 have pushed the field forward, forcing the development of both new theoretical frameworks  
2323 and new experimental techniques. Recent and ongoing detector upgrades at STAR, at mid-  
2324 and forward-rapidity, coupled with the versatility of RHIC, will allow us to gain new insights  
2325 into long-standing puzzles, and to probe more deeply the complexities of emergent behavior  
2326 in QCD.

2327 Results from PHENIX and STAR have shown that large transverse single-spin asym-  
2328 metries (TSSA) for inclusive hadron production, first seen in  $p+p$  collisions at fixed-target  
2329 energies and modest  $p_T$ , extend to the highest RHIC center-of-mass energies,  $\sqrt{s} = 500 \text{ GeV}$ ,  
2330 and surprisingly large  $p_T$ . Figure 64 summarizes the world data for the inclusive pion asym-

2331 metries  $A_N$  as a function of Feynman- $x$ . The asymmetries are seen to be nearly independent  
 2332 of  $\sqrt{s}$  over the very wide range of roughly 5 to 500 GeV.

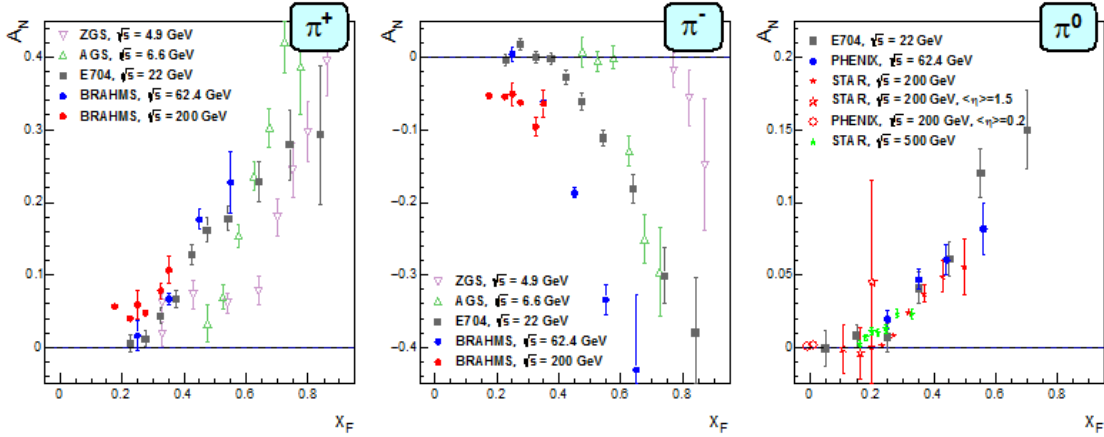


**Figure 64:** Transverse single-spin asymmetry  $A_N$  measurements for charged and neutral pions at different center-of-mass energies as a function of Feynman- $x$ .

2333 To understand the observed TSSAs, one needs to go beyond the conventional leading-  
 2334 twist (twist-2) collinear parton picture for the hard-scattering processes. Two theoretical  
 2335 formalisms have been developed to try to explain these sizable asymmetries in the QCD  
 2336 framework: transverse-momentum-dependent (TMD) parton distribution and fragmentation  
 2337 functions, such as the Sivers and Collins functions; and transverse-momentum-integrated  
 2338 (collinear) quark-gluon-quark correlations, which are twist-3 distributions in the initial state  
 2339 proton or in the fragmentation process. For many of the experimentally accessible spin  
 2340 asymmetries, several of these functions can contribute, and need to be disentangled in order  
 2341 to understand the experimental data in detail, in particular the observed  $p_T$  dependence.  
 2342 These functions manifest their spin dependence either in the initial state—for example, the  
 2343 Sivers distribution and its twist-3 analog, the Efremov-Teryaev-Qiu-Sterman (ETQS) func-  
 2344 tion [247]—or in the final state via the fragmentation of polarized quarks, such as in the  
 2345 Collins function and related twist three function  $\hat{H}_{FU}(z, z_z)$ .

2346 Incorporating the fragmentation term within the collinear twist-3 approach demonstrated  
 2347 the ability of this formalism to describe the large values of  $A_N$  for  $\pi^0$  production observed at  
 2348 RHIC [248]. In this work, the relevant (non-pole) 3-parton collinear fragmentation function  
 2349  $\hat{H}_{FU}(z, z_z)$  was fit to the RHIC data. The so-called soft-gluon pole term, involving the ETQS  
 2350 function  $T_{q,F}(x_1, x_2)$ , was also included by fixing  $T_{q,F}$  through its well-known relation to the  
 2351 TMD Sivers function  $f_{1T}^\perp$ . The authors obtained a very good description of the data due to  
 2352 the inclusion of the non-pole fragmentation function and based on this work they were able  
 2353 to make predictions for  $\pi^+$  and  $\pi^-$  production asymmetries  $A_N$  at the forward rapidities  
 2354 covered by the STAR upgrades,  $2.5 < \eta < 4$ . The results are shown in Fig. 65 for  $\sqrt{s} = 200$   
 2355 and 500 GeV for two rapidity ranges,  $2 < \eta < 3$  and  $3 < \eta < 4$ .

2356 In Run-22, with the full suite of forward tracking detectors and calorimetry installed,  
 2357 STAR will for the first time be able to map out inclusive charged-hadron asymmetries up to

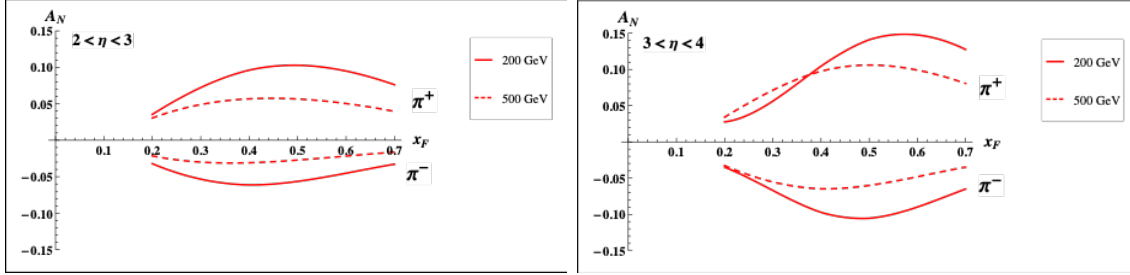


**Figure 65:** Predictions for  $A_N$  for  $\pi^+$  and  $\pi^-$  production over the ranges  $2 < \eta < 3$  (left) and  $3 < \eta < 4$  (right) at  $\sqrt{s} = 200$  GeV (solid lines) and 500 GeV (dashed lines). The  $\sqrt{s} = 200$  GeV BRAHMS  $A_N$  data for charged pions cover up to  $x_F$  of 0.3.

2358 the highest energies achievable at RHIC and at these forward rapidities. It would be very  
 2359 interesting to confirm that these asymmetries are indeed largely independent of center-of-  
 2360 mass energy. The measurements of  $A_N$  for charged hadrons, together with analogous data  
 2361 (from Run-22 as well as previous STAR runs) on  $A_N$  for direct photons and neutral pions,  
 2362 should provide the best data set in the world to constrain the evolution and flavor dependence  
 2363 of the twist-3 ETQS distributions and to determine if the 3-parton collinear fragmentation  
 2364 function  $H_{FU}$  is the main driver of the large forward inclusive asymmetries.

### 2365 3.1.2 Sivers and Efremov-Teryaev-Qiu-Sterman Function

2366 There is great theoretical interest in testing the relation between the ETQS correlation  
 2367 functions and the Sivers function. As discussed above, both the Sivers and the ETQS  
 2368 functions encapsulate partonic spin correlations within the proton, but they are formally  
 2369 defined in different frameworks. While the Sivers function is a TMD quantity that depends  
 2370 explicitly on spin-dependent transverse partonic motion  $k_T$ , the ETQS function is a twist-3  
 2371 collinear distribution, in which SSAs are generated through soft collinear gluon radiation

2372 Measurements of forward jet production from the ANDY collaboration [249] indicated  
 2373 rather small asymmetries. This was argued to be consistent with the idea that the twist-3  
 2374 parton correlation functions for up and down valence quarks should cancel, because their  
 2375 behavior reflects the Sivers functions extracted from fits to the SIDIS data that demonstrate  
 2376 opposite sign, but equal magnitude, up and down quark Sivers functions. Preliminary STAR  
 2377 results on charge-tagged dijets at mid-rapidity (see Fig. 29) support this interpretation, with  
 2378 the caveat that the measured observable (a spin-dependent  $\langle k_T \rangle$ ) is defined in the TMD, and  
 2379 not the twist-3, framework.

2380 To better test quantitatively the relation between the two regimes, one can measure spin  
 2381 asymmetries for jets which are *intentionally* biased towards up or down quark jets via detec-  
 2382 tion of a high- $z$  charged hadron within the jet. Higher-twist calculations of jet asymmetries  
 2383 based on the Sivers function predict sizeable effects for these flavor-enhanced jets. With the  
 2384 suite of new forward detectors installed at STAR, full jet reconstruction, along with iden-  
 2385 tification of a high- $z$  hadron of known charge sign, will be possible at high pseudorapidity.  
 2386 Using realistic jet smearing in a forward calorimeter and tracking system, and requiring a

2387 charged hadron with  $z > 0.5$ , the asymmetries can be separated and compared to the pre-  
 2388 dictions for the Sivers function based on current SIDIS data. The expected uncertainties,  
 2389 plotted at the predicted values, can be seen in Fig. 66. Dilutions by underlying event and  
 2390 beam remnants were taken into account. The simulations have assumed only an integrated  
 2391 luminosity of  $100 \text{ pb}^{-1}$  at  $\sqrt{s} = 200 \text{ GeV}$ , which is significantly lower than what is currently  
 2392 expected for the Run-24 200 GeV polarized  $p+p$  run. The same measurement is possible at  
 2393 500 GeV.

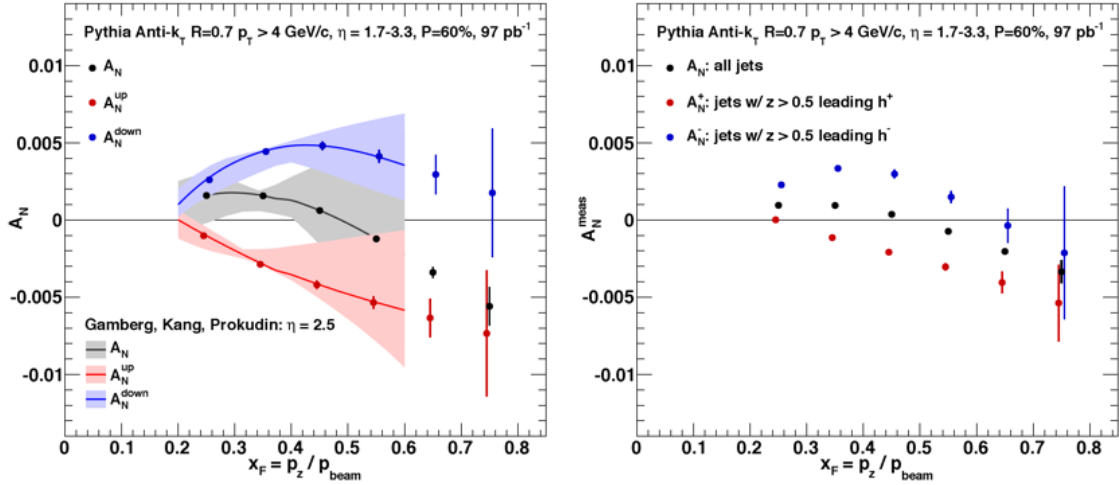


**Figure 66:** Left: up quark (red points), down quark (blue points) and all jet (black points) single spin asymmetries as a function of  $x_F$  as calculated by the ETQS based on the SIDIS Sivers functions. Right: Expected experimental sensitivities for jet asymmetries tagging in addition a positive hadron with  $z$  above 0.5 (red points), a negative hadron with  $z$  above 0.5 (blue points) or all jets (black) as a function of  $x_F$ . Note: these figures are for 200 GeV center-of-mass energy proton collisions – the 500 GeV results are expected to be qualitatively similar.

2394 In a TMD framework, the Sivers effect manifests itself as a correlation (a triple product)  
 2395 between the transverse momentum of a parton ( $\vec{k}_T$ ) with momentum fraction  $x$ , and the  
 2396 transverse spin ( $\vec{S}$ ) of a polarized proton moving in the longitudinal ( $\vec{p}$ ) direction. Thus,  
 2397 for transversely polarized protons, the Sivers effect probes whether the  $k_T$  of the constituent  
 2398 quarks is preferentially oriented in a direction perpendicular to both the proton momentum  
 2399 and its spin. Momentum conservation then implies that the two jets in the final state will  
 2400 not emerge back-to-back on average, but instead will ‘tilt’ in the direction of the summed  
 2401  $k_T$  of the initial state partons. Moreover, the (average) tilt of interest will reverse direction  
 2402 under a ‘flip’ of the proton spin; a spin-dependent  $\langle k_T \rangle$  can then be extracted by associating  
 2403 the azimuthal opening angle of the jet pair with this tilt.

2404 STAR carried out an earlier measurement of this transverse single-spin asymmetry using  
 2405 a dijet dataset with  $\sim 1 \text{ pb}^{-1}$  of integrated luminosity [113], and found it to be consistent with  
 2406 zero within  $2\sigma$ . An ongoing and much improved analysis has been described in Sect. 1.3.3.  
 2407 Perhaps most significantly, the jets were sorted according to their net charge  $Q$ , calculated  
 2408 by summing the signed momentum of all particle tracks with  $p > 0.8 \text{ GeV}$ , to minimize

2409 underlying event contributions, yielding jet samples with enhanced contributions from  $u$   
 2410 quarks (positive  $Q$ ) and  $d$  quarks (negative  $Q$ ), with a large set near  $Q = 0$  dominated by  
 2411 gluons. Simple kinematics allow for conversion from the spin-dependent ‘tilt’ of the dijet  
 2412 pair to a value of  $k_T$  on an event-by-event basis; these are then sorted by the  $Q$  of the jet  
 2413 and binned by the summed pseudorapidities of the outgoing jets,  $\eta^{\text{total}} \equiv \eta_3 + \eta_4$ . Because  
 2414 the contributions of different partons ( $u$ ,  $d$ , all else) to  $\langle k_T \rangle$  vary with both  $Q$  and also  $\eta^{\text{total}}$ ,  
 2415 in a way that can be estimated robustly using simulation, the data can be inverted to yield  
 2416 values of  $\langle k_T \rangle$  for the individual partons, though with coarser binning in  $\eta^{\text{total}}$ .

2417 With the new forward detectors in place, along with the enhanced reach in  $\eta$  afforded by  
 2418 the iTPC, this technique can be expanded in Run-22 to cover pseudorapidities at STAR from  
 2419 roughly -1 to +4, though with a gap at  $1.5 < \eta < 2.5$ . Despite this gap, values of  $\langle k_T \rangle$  can be  
 2420 extracted for  $u$  and  $d$  quarks for  $\eta^{\text{total}}$  ranging from  $\sim -1.5$  to as high as 7 with reasonable  
 2421 statistics. This latter regime will probe  $2 \rightarrow 2$  hard scattering events in which  $x_1 \gg x_2$ ,  
 2422 *i.e.*, a sample enriched in valence quarks interacting with low- $x$  gluons. Such measurements,  
 2423 exploiting the full kinematic reach of STAR, will not only allow precise determinations of  
 2424 the average transverse partonic motion,  $\langle k_T \rangle$ , exhibited by individual partonic species in  
 2425 the initial state, but will provide important information on the  $x$  dependence of the proton  
 2426 Sivers functions.

2427 Collisions at  $\sqrt{s} = 510$  GeV will also allow STAR to continue our successful program  
 2428 to study the evolution and sign change of the Sivers function. By focusing on interactions  
 2429 in which the final state involves only weakly interacting particles, and hence the transverse  
 2430 partonic motion (in a TMD framework) or the collinear gluon radiation (in twist-3) must be  
 2431 in the initial state, one can test for the predicted sign change in  $A_N$  relative to interactions  
 2432 in which these terms must appear in the final state, such as SIDIS measurements. The  
 2433 improved tracking capabilities provided by the iTPC upgrade will allow us to push our mid-  
 2434 rapidity  $W^\pm$  and  $Z^0$  measurements to larger rapidity  $y_{W/Z}$ , a regime where the asymmetries  
 2435 are expected to increase in magnitude and the anti-quark Sivers’ functions remain largely  
 2436 unconstrained. Figure 67 demonstrates the expected precision of asymmetry measurements  
 2437 after data from the Run-17 has been fully analyzed. In addition to the noted extension of  
 2438 our kinematic reach, an additional 16 or more weeks of beam time at  $\sqrt{s} = 510$  GeV in  
 2439 Run-22 would increase our data set by more than a factor of 2. This experimental accuracy  
 2440 would significantly enhance the quantitative reach of testing the limits of factorization and  
 2441 universality in lepton-proton and proton-proton collisions.

### 2442 3.1.3 Transversity, Collins Function and Interference Fragmentation Function

2443 A complete picture of nucleon spin structure at leading twist must include contributions  
 2444 from the unpolarized and helicity distributions, as well as those involving transverse po-  
 2445 larization, such as the transversity distribution [252–254]. The transversity distribution  
 2446 can be interpreted as the net transverse polarization of quarks within a transversely polar-  
 2447 ized proton. The difference between the helicity and transversity distributions for quarks  
 2448 and antiquarks provides a direct,  $x$ -dependent connection to nonzero orbital angular mo-  
 2449 mentum components in the wave function of the proton [255]. Recently, the first lattice

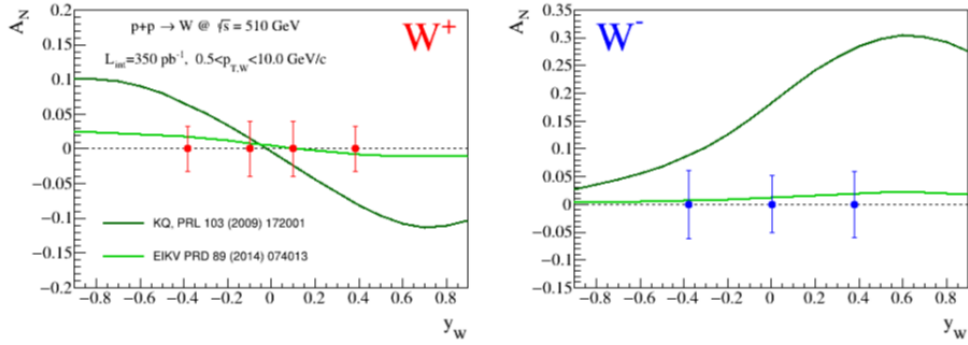


**Figure 67:** Projected uncertainties for transverse single-spin asymmetries of  $W^\pm$  bosons as functions of their rapidity for a delivered integrated luminosity of  $350 \text{ pb}^{-1}$  and an average beam polarization of 55%. The dark and light green lines are theoretical predictions from the KQ [250] and EIKV [251] groups, respectively, folding in data on the sea-quark Sivers functions.

2450 QCD calculation of the transversity distribution has been performed [256]. In addition,  
 2451 the measurement of transversity has received substantial interest as a means to access the  
 2452 tensor charge of the nucleon, defined as the integral over the valence quark transversity:  
 2453  $\delta q^a = \int_0^1 [\delta q^a(x) - \delta \bar{q}^a(x)] dx$  [253, 257]. Measuring the tensor charge is very important for  
 2454 several reasons. First, it is an essential and fundamental quantity to our understanding of  
 2455 the spin structure of the nucleon. Also, the tensor charge can be calculated on the lattice  
 2456 with comparatively high precision, due to the valence nature of transversity, and hence is  
 2457 one of the few quantities that allow us to compare experimental results on the spin structure  
 2458 of the nucleon directly to *ab initio* QCD calculations. Finally, the tensor charge describes  
 2459 the sensitivity of observables in low-energy hadronic reactions to beyond the standard model  
 2460 physics processes with tensor couplings to hadrons. Examples are experiments with ultra-  
 2461 cold neutrons and nuclei.

2462 Transversity is difficult to access due to its chiral-odd nature, requiring the coupling of  
 2463 this distribution to another chiral-odd distribution. Semi-inclusive deep-inelastic scattering  
 2464 (SIDIS) experiments have successfully probed transversity through two channels: asym-  
 2465 metric distributions of single pions, convoluting the TMD transversity distribution with  
 2466 the TMD Collins fragmentation function, and azimuthally asymmetric distributions of di-  
 2467 hadrons, coupling transversity to the so-called “interference fragmentation function” (IFF)  
 2468 in the framework of collinear factorization. Yet in spite of a wealth of lepton-scattering  
 2469 data, the kinematic reach of existing SIDIS experiments limits the precision with which the  
 2470 proton’s transversity can be extracted, as the range of Bjorken- $x$  values that can be accessed  
 2471 does not extend above  $x \sim 0.3$

2472 In hadronic collisions, the  $k_T$  integrated quark transversity distribution may be accessed  
 2473 via two channels. The first is the single spin asymmetry of the azimuthal distribution of  
 2474 hadrons in high energy jets [109]. In the jet+hadron channel, the collinear transversity  
 2475 distribution couples to the TMD Collins function [109, 110]. This makes  $p+p$  collisions a  
 2476 more direct probe of the Collins fragmentation function than Collins asymmetries in SIDIS

2477 [109], where a convolution with the TMD transversity distribution enters. This also makes  
 2478 the Collins asymmetry in  $p+p$  collisions an ideal tool to explore the fundamental QCD  
 2479 questions of TMD factorization, universality, and evolution. The second channel is the  
 2480 single spin asymmetry of pion pairs, where transversity couples to the collinear interference  
 2481 fragmentation function [258]. STAR mid-rapidity IFF data [259] have been included in the  
 2482 first extraction of transversity from SIDIS and proton-proton IFF asymmetries [260].

2483 The universality of TMD PDFs and fragmentation functions in  $p+p$  collisions has been an  
 2484 open question. General arguments [261, 262] have shown that factorization can be violated  
 2485 in hadron-hadron collisions for TMD PDFs like the Sivers function, though very recent  
 2486 calculations indicate the violations might be quite small [263, 264]. In contrast, while there  
 2487 is no general proof that the Collins effect in  $p+p$  collisions is universal to all orders, explicit  
 2488 calculations [109, 110, 265, 266] have shown that diagrams like those that violate factorization  
 2489 of the Sivers function make no contribution to the Collins effect at the one- or two-gluon  
 2490 exchange level, thereby preserving its universality at least to that level.

2491 Comparisons of the transversity distributions extracted from the Collins and IFF channels  
 2492 will allow STAR to study the size and nature of any factorization breaking effects for TMD  
 2493 observables in hadronic collisions. Likewise, comparisons with the transversity, Collins and  
 2494 IFF distributions extracted from SIDIS collisions will shed light on universality and constrain  
 2495 evolution effects. The measurement of evolution effects in TMD distributions is particularly  
 2496 important because, unlike the collinear case, TMD evolution contains a non-perturbative  
 2497 component that cannot be calculated directly. Measurements at  $\sqrt{s}$  of 200 and 510 GeV will  
 2498 provide additional experimental constraints on evolution effects and provide insights into the  
 2499 size and nature of TMD observables at the future Electron-Ion Collider.

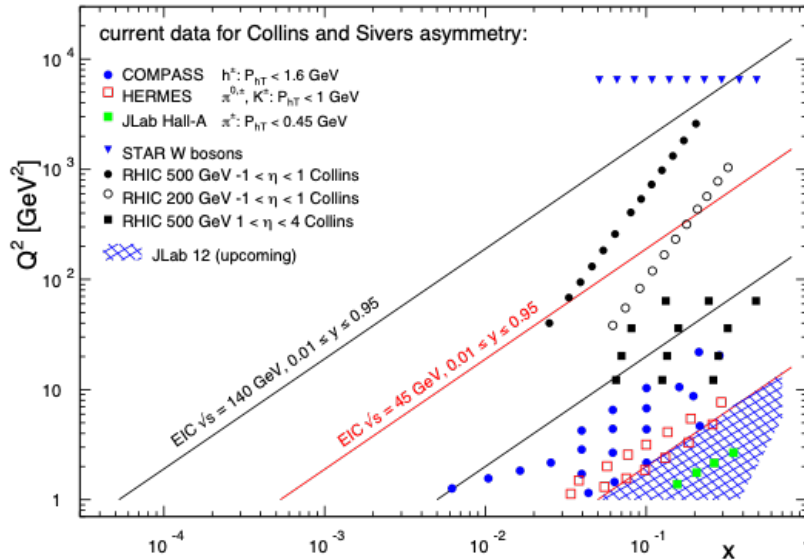


**Figure 68:**  $x - Q^2$  coverage of RHIC measurements compared to existing Collins and Sivers effect measurements in SIDIS and the future coverage of the EIC.

2500 Extending measurements of di-hadron and Collins asymmetries to the forward direction

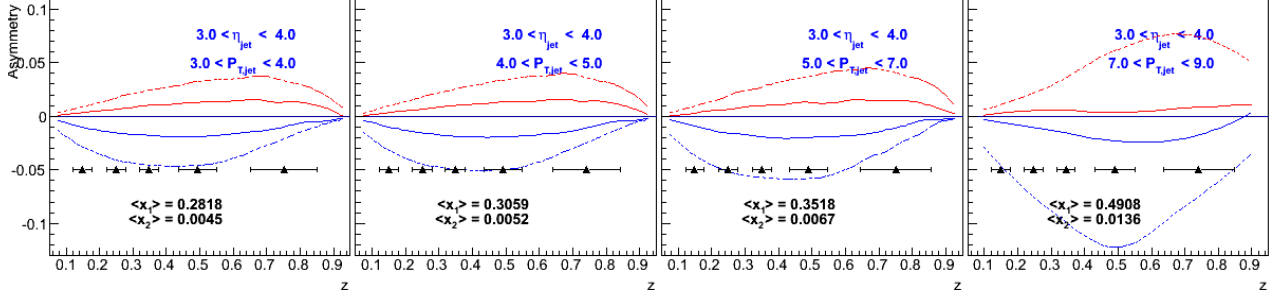


**Figure 69:** Expected  $h^-$  Collins asymmetry uncertainties at  $3 < \eta < 4$  (black points) from a sampled luminosity of  $268 \text{ pb}^{-1}$  at  $\sqrt{s} = 510 \text{ GeV}$ , compared to positive (red) and negative (blue) pion asymmetries based on the Torino extraction (full lines) and the Soffer bound (dashed lines) as a function of hadron  $z$  for bins in jet  $p_T$ . Most uncertainties are smaller than the height of the triangles.

2501 during Run-22 will allow access to transversity in the region  $x > 0.3$ . This valence quark  
 2502 region is not currently probed by any experiments and is essential for the determination of  
 2503 the tensor charge, which receives 70% of its contributions from  $0.1 < x < 1.0$ . In addition,  
 2504 probing transversity in  $p+p$  collisions also provides better access to the  $d$ -quark transversity  
 2505 than is available in SIDIS, due to the fact that there is no charge weighting in the hard  
 2506 scattering QCD  $2 \rightarrow 2$  process in  $p+p$  collisions. This is a fundamental advantage of  $p+p$   
 2507 collisions, as any SIDIS measurement of the  $d$ -quark transversity has to be on a bound  
 2508 system, *e.g.* He-3, which ultimately requires nuclear corrections to extract distributions.  
 2509 The high scale we can reach in 500 GeV collisions at RHIC has allowed STAR [267] to  
 2510 demonstrate, for the first time, that previous SIDIS measurements at low scales are in fact  
 2511 accessing the nucleon at leading twist. Figure 68 shows the  $x - Q^2$  coverage spanned by  
 2512 the RHIC measurements compared to the future EIC, JLab-12, and the current SIDIS world  
 2513 data.

2514 Another fundamental advantage of  $p+p$  collisions is the ability to access gluons di-  
 2515 rectly. While gluons cannot be transversely polarized in a transversely polarized spin 1/2  
 2516 hadron, they can be linearly polarized. Similarly, there exists an equivalent of the Collins  
 2517 fragmentation function for the fragmentation of linearly polarized gluons into unpolarized  
 2518 hadrons [268]. The linear polarization of gluons is a largely unexplored phenomenon, but it  
 2519 has been a focus of recent theoretical work, in particular due to the relevance of linearly po-  
 2520 larized gluons in unpolarized hadrons for the  $p_T$  spectrum of the Higgs boson measured at the  
 2521 LHC. Polarized proton collisions with  $\sqrt{s} = 510 \text{ GeV}$  at RHIC, in particular for asymmetric  
 2522 parton scattering if jets are detected in the backward direction, are an ideal place to study  
 2523 the linearly polarized gluon distribution in polarized protons. (Note that the distributions of  
 2524 linearly polarized gluons inside an unpolarized and a polarized proton provide independent  
 2525 information). A first measurement of the ‘‘Collins-like’’ effect for linearly polarized gluons  
 2526 has been done by STAR with data from Run-11 [267], providing constraints on this function  
 2527 for the first time.

2528 Figure 69 shows projected uncertainties for Collins asymmetries at 510 GeV with the

2529 Forward Upgrade during Run-22. As indicated on the figure, jets with  $3 < \eta < 4$  and  
 2530  $3 < p_T < 9$  GeV/ $c$  will explore transversity in the important region  $0.3 < x < 0.5$  that  
 2531 has not yet been probed in SIDIS. A realistic momentum smearing of final state hadrons as  
 2532 well as jets in this rapidity range was assumed and dilutions due to beam remnants (which  
 2533 become substantial at rapidities close to the beam) and underlying event contributions have  
 2534 been taken into account. As no dedicated particle identification at forward rapidities will be  
 2535 available for these measurements, only charged hadrons were considered. This mostly reduces  
 2536 the expected asymmetries due to dilution by protons (10-14%) and a moderate amount of  
 2537 kaons (12-13%). As anti-protons are suppressed compared to protons in the beam remnants,  
 2538 especially the negative hadrons can be considered a good proxy for negative pions ( $\sim 78\%$   
 2539 purity according to PYTHIA6). Given their sensitivity to the down quark transversity via  
 2540 favored fragmentation, they are particularly important since SIDIS measurements, due to  
 2541 their electromagnetic interaction, are naturally dominated by up-quarks. We have estimated  
 2542 our statistical uncertainties based on an accumulated luminosity of  $268 \text{ pb}^{-1}$ , which leaves  
 2543 nearly invisible uncertainties after smearing. These expected uncertainties are compared to  
 2544 the asymmetries obtained from the transversity extractions based on SIDIS and Belle data  
 2545 [269] as well as from using the Soffer positivity bound for the transversity PDF [270]. More  
 2546 recent global fits have slightly different central up and down quark transversity distributions.  
 2547 But due to the lack of any SIDIS data for  $x > 0.3$ , the upper uncertainties are compatible  
 2548 with the Soffer bounds. This high- $x$  coverage will give important insights into the tensor  
 2549 charge, which is essential to understand the nucleon structure at leading twist.

2550 Although the studies presented here are for the Collins asymmetries, the resulting sta-  
 2551 tistical uncertainties will be similar for other measurements using azimuthal correlations of  
 2552 hadrons in jets. One important example is the measurement of “Collins-like” asymmetries to  
 2553 access the distribution of linearly polarized gluons. As described earlier, the best kinematic  
 2554 region to access this distribution is at backward angles with respect to the polarized proton  
 2555 and at small jet  $p_T$ . Figure 69 shows that a high precision measurement of the distribution  
 2556 of linearly polarized gluons down to  $x \sim 0.005$  will be performed concurrently.

2557 It is also important to recognize that these hadron-in-jet measurements with the STAR  
 2558 Forward Upgrade will provide very valuable experience detecting jets close to beam rapidity  
 2559 that will inform the planning for future jet measurements in similar kinematics at the EIC.

2560 While the STAR Forward Upgrade will provide sensitivity to transversity to the highest  
 2561  $x$ , concurrent mid-rapidity measurements (see Fig. 68) will provide the most precise informa-  
 2562 tion as a function of  $x$ ,  $z$ ,  $j_T$ , and  $Q^2$  to probe questions of TMD factorization, universality,  
 2563 and evolution. The left panel of Fig. 70 shows published STAR measurements of the Collins  
 2564 asymmetry vs. pion  $z$  in 500 GeV p+p collisions from 2011 [267]. The results, which repre-  
 2565 sented the first ever observation of the Collins effect in p+p collisions, are consistent at the  
 2566 2-sigma level with model predictions, with and without TMD evolution, derived from fits to  
 2567  $e^+e^-$  and SIDIS data [109,271]. However, greater precision is clearly necessary for a detailed  
 2568 universality test, as well as to set the stage for the EIC.

2569 In 2017, STAR sampled about 14 times the luminosity that we recorded in 2011. In Run-  
 2570 22, we propose to record another data set equivalent to 16 times the sampled luminosity from



2589 • What is the role of orbital motion of sea quarks and gluons in building the nucleon  
2590 spin?

2591 • Saturation in nuclei.

2592 **Diffraction:** The essential characteristics of diffraction in QCD are summarized by two  
2593 facts:

2594 • The event is still called diffractive if there is a rapidity gap. Due to the presence  
2595 of a rapidity gap, the diffractive cross-section can be thought of as arising from an  
2596 exchange of several partons with zero net color between the target and the projectile.  
2597 In high-energy scattering, which is dominated by gluons, this color neutral exchange  
2598 (at the lowest order) consists of at least two exchanged gluons. This color singlet  
2599 exchange has historically been called the pomeron, which had a specific interpretation  
2600 in Regge theory. A crucial question in diffraction is the nature of the color neutral  
2601 exchange between the protons. This interaction probes, in a novel fashion, the nature  
2602 of confining interactions within hadrons.

2603 • The proton/nuclear target is not always an opaque “black disk” obstacle of geometric  
2604 optics. A projectile that interacts more weakly due to color-screening and asymptotic  
2605 freedom is likely to produce a different diffractive pattern from a larger, more strongly  
2606 interacting, projectile.

2607 HERA discovered that 15% of the total ep cross-section is given by diffractive events  
2608 (for details see [272] and references therein), basically independent of kinematics. At RHIC  
2609 center-of-mass energies diffractive scattering events constitute  $\sim 25\%$  of the total inelastic  
2610  $p+p$  cross-section [273]. As described above diffraction is defined as an interaction that  
2611 is mediated by the exchange of the quantum numbers of the vacuum, as shown in Fig. 71.  
2612 Experimentally these events can be characterized by the detection of a very forward scattered  
2613 proton and jet (singly diffractive) or two jets (doubly diffractive) separated by a large rapidity  
2614 gap. Central diffraction, where two protons, separated by rapidity gaps, are reconstructed  
2615 along with a jet at mid-rapidity, is also present, but suppressed compared to singly and  
2616 doubly diffractive events. To date, there have been no data in  $p+p$  collisions studying spin  
2617 effects in diffractive events at high  $\sqrt{s}$  apart from measuring single spin asymmetries in  
2618 elastic  $p+p$  scattering [274–277].

2619 A discovery of large transverse single spin asymmetries in diffractive processes would  
2620 open a new avenue to study the properties and understand the nature of the diffractive  
2621 exchange in  $p+p$  collisions. One of the primary observables of STAR to access transverse  
2622 spin phenomena has been forward neutral pion production in transversely polarized  $p+p$   
2623 collisions at both  $\sqrt{s} = 200$  and 500 GeV. Figure 31 shows the isolated and non-isolated  
2624 transverse single spin asymmetries  $A_N$  for  $\pi^0$  detected in the STAR FMS at  $2.5 < \eta < 4.0$   
2625 as a function of  $x_F$ .

2626 All these observations might indicate that the underlying subprocess causing a significant  
2627 fraction of the large transverse single spin asymmetries in the forward direction are not

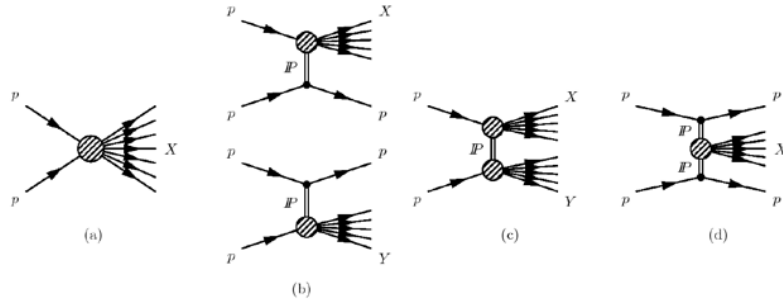


**Figure 71:** Schematic diagrams of (a) nondiffractive,  $pp \rightarrow X$ , (b) singly diffractive,  $pp \rightarrow Xp$  or  $pp \rightarrow pY$ , (c) doubly diffractive,  $pp \rightarrow XY$ , and (d) centrally diffracted,  $pp \rightarrow pXp$ , events.

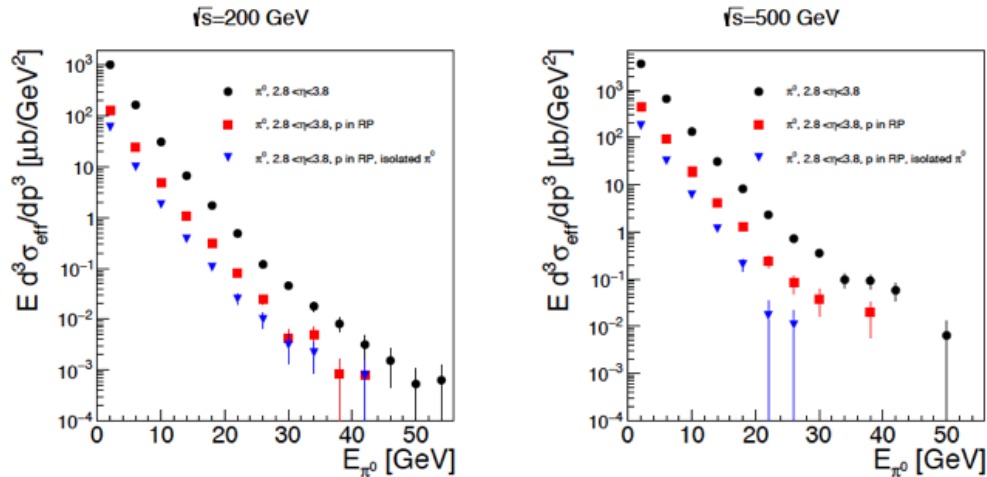


**Figure 72:** Estimate of the cross-section for hard diffractive processes at  $\sqrt{s} = 200$  GeV and 500 GeV using PYTHIA 8. The different points reflect different analysis cuts applied:  $\pi^0$  in rapidity  $2.8 < \eta < 3.8$  (black), one proton is required to be detected in the STAR Roman Pot acceptance (red) and an isolation cut of 35 mrad around the  $\pi^0$  (blue).

2628 of  $2 \rightarrow 2$  parton scattering processes but of diffractive nature. PYTHIA-8 [11] was used  
 2629 to evaluate the fraction of hard diffractive events [278] contributing to the inclusive  $\pi^0$   
 2630 cross-section at forward rapidities. Figure 72 shows the hard diffractive cross-section for  
 2631  $\pi^0$  production at  $\sqrt{s} = 200$  GeV and 500 GeV for a rapidity range of  $2.5 < \eta < 4.0$  with  
 2632 and without applying several experimental cuts, i.e. the proton in the STAR Roman Pot  
 2633 acceptance. The prediction from this PYTHIA-8 simulation is that 20% of the total inclusive  
 2634 cross-section at forward rapidities is of diffractive nature. This result is in agreement with  
 2635 measurements done over a wide range of  $\sqrt{s}$  (see Fig. 12 in Ref. [272]).

2636 In 2015 STAR collected data in  $\sqrt{s} = 200$  GeV transversely polarized  $p+p$  collisions,  
 2637 where an isolated  $\pi^0$  is detected in the forward pseudorapidity range along with the forward-  
 2638 going proton  $p$ , which scatters with a near-beam forward pseudorapidity into Roman Pot  
 2639 detectors. The sum of the  $\pi^0$  and the scattered proton energies is consistent with the incident  
 2640 proton energy of 100 GeV, indicating that no further particles are produced in this direction.  
 2641 Correlations between the  $\pi^0$  and scattered proton have been presented [279], along with  
 2642 single-spin asymmetries which depend on the azimuthal angles of both the pion and the

2643 proton. This is the first time that spin asymmetries have been explored for this process, and  
2644 a model to explain their azimuthal dependence is needed.

2645 The STAR Forward Upgrade will be a game changer for diffractive measurements at  
2646 RHIC. It will allow the reconstruction of full jets both at  $\sqrt{s} = 200$  GeV and 510 GeV.  
2647 As at HERA we will be able to reconstruct jets produced with the scattered proton tagged  
2648 in Roman Pots and/or requiring rapidity gaps. Measuring spin asymmetries for diffractive  
2649 events as function of  $\sqrt{s}$  might reveal surprises, which will inspire new physics opportunities  
2650 for EIC, i.e SSA in polarized eA collisions.

## 2651 **3.2 Run-24 Request for Polarized $p+p$ and $p+A$ Collisions at 200** 2652 **GeV**

2653 Run-24, with polarized  $p+p$  and  $p+Au$  collisions at  $\sqrt{s_{NN}} = 200$  GeV, will likely be the last  
2654 RHIC spin/cold QCD run. This run will provide STAR with the unique opportunity to in-  
2655 vestigate these 200 GeV collision systems with the Forward Upgrade providing full tracking  
2656 and calorimetry coverage over the region  $2.5 < \eta < 4$  and the iTPC providing enhanced  
2657 particle identification and expanded pseudorapidity coverage at mid-rapidity. These power-  
2658 ful detection capabilities, when combined with substantially increased sampled luminosity  
2659 compared to Run-15, will enable critical measurements to probe universality and factoriza-  
2660 tion in transverse spin phenomena and nuclear PDFs and fragmentation functions, as well as  
2661 low- $x$  non-linear gluon dynamics characteristic of the onset of saturation. This will provide  
2662 unique insights into fundamental QCD questions in the near term, and essential baseline  
2663 information for precision universality tests when combined with measurements from the EIC  
2664 in the future.

2665 We therefore request at least 11 weeks of polarized  $p+p$  data-taking at  $\sqrt{s} = 200$  GeV  
2666 and 11 weeks of polarized  $p+Au$  data-taking at  $\sqrt{s_{NN}} = 200$  GeV during Run-24. All of  
2667 the running will involve transversely polarized protons, with the choice between vertical  
2668 or radial polarization to be determined during the coming year. Based on recent (08-21-  
2669 20) C-AD guidance, we expect to sample at least  $235 \text{ pb}^{-1}$  of  $p+p$  collisions and  $1.3 \text{ pb}^{-1}$   
2670 of  $p+Au$  collisions. These totals represent 4.5 times the luminosity that STAR sampled  
2671 during transversely polarized  $p+p$  collisions in Run-15 and 3 times the luminosity that STAR  
2672 sampled during transversely polarized  $p+Au$  collisions in Run-15.

### 2673 **3.2.1 Spin Physics with Polarized $p+p$ and $p+Au$ Collisions at 200 GeV**

2674 Section 1.3.3 described several very mature STAR analyses that are based on the transversely  
2675 polarized  $p+p$  and  $p+Au$  data sets that we recorded during 2015. Run-24 will enable STAR  
2676 to probe these questions with a far more capable detector and much larger data sets than were  
2677 available during Run-15, thereby allowing us to set the stage for related future measurements  
2678 at the EIC. Here we give brief descriptions of several of the opportunities presented by Run-  
2679 24.

2680 **Forward transverse spin asymmetries:** Section 1.3.3 presents a small subset of the  
 2681 results that STAR will publish very soon in a pair of papers discussing forward transverse  
 2682 spin asymmetries in  $p+p$ ,  $p+Al$ , and  $p+Au$  collisions measured with the Forward Meson  
 2683 Spectrometer (FMS). One paper focuses on the dynamics that underlie the large asymmetries  
 2684 that have been seen to date. Figure 31 shows that  $A_N$  for forward  $\pi^0$  production in  $p+p$   
 2685 collisions at 200 and 500 GeV is substantially larger when the  $\pi^0$  is isolated than when it  
 2686 is accompanied by additional nearby photons. The same analysis also shows that  $A_N$  for  
 2687 inclusive electromagnetic jets (EM-jets) in 200 and 500 GeV collisions is substantially larger  
 2688 than that for EM-jets that contain three or more photons and that the Collins asymmetry  
 2689 for  $\pi^0$  in EM-jets is very small. The other paper focuses on the nuclear dependence of  $A_N$   
 2690 for  $\pi^0$  in  $\sqrt{s_{NN}} = 200$  GeV collisions. It presents a detailed mapping of  $A_N$  as functions of  
 2691  $x_F$  and  $p_T$  for all three collision systems. Figure 30 shows the observed nuclear dependence  
 2692 is very weak. The same analysis shows that isolated *vs.* non-isolated  $\pi^0$  behave similarly in  
 2693  $p+Al$  and  $p+Au$  collisions as they do in  $p+p$  collisions.

2694 These two papers will provide a wealth of new data to inform the ongoing discussion  
 2695 regarding the origin of the large inclusive hadron transverse spin asymmetries that have  
 2696 been seen in  $p+p$  collisions at forward rapidity over a very broad range of collision energies.  
 2697 Nonetheless, the STAR Forward Upgrade will be a game changer for such investigations.  
 2698 It will enable measurements of  $A_N$  for  $h^{+/-}$ , in addition to  $\pi^0$ . It will enable isolation  
 2699 criteria to be applied to the  $h^{+/-}$  and  $\pi^0$  that account for nearby charged, as well as neutral,  
 2700 fragments. It will enable full jet asymmetry and Collins effect measurements, again for  
 2701  $h^{+/-}$  in addition to  $\pi^0$ , rather than just EM-jet measurements. It will permit all of these  
 2702 measurements to be performed at both 510 GeV, as discussed in Sects. 3.1.1 and 3.1.2, and  
 2703 at 200 GeV. In addition, all of these observables can be tagged by forward protons detected  
 2704 in the STAR Roman pots to identify the diffractive component of the observed transverse  
 2705 spin asymmetries. For  $p+p$  there will be considerable overlap between the kinematics at  
 2706 the two energies, but the 510 GeV measurements will access higher  $p_T$ , while the 200 GeV  
 2707 measurements will access higher  $x_F$ . Meanwhile, at 200 GeV we will also perform the full  
 2708 suite of measurements in  $p+Au$  to identify any nuclear effects. Figure 65 shows one set  
 2709 of predictions for the inclusive  $\pi^{+/-}$   $A_N$  in 200 and 500 GeV  $p+p$  collisions, while Fig. 66  
 2710 shows the estimated sensitivity of one hadron-in-jet measurement that will help to isolate  
 2711 the Sivers effect contribution at 200 GeV.

2712 **Sivers effect:** Sections 1.3.3 and 3.1.2 describe the first ever observation of the Sivers  
 2713 effect in dijet production. Such measurements are crucial to explore questions regarding  
 2714 factorization of the Sivers function in dijet hadroproduction [261–264]. Those results were  
 2715 derived from 200 GeV transverse spin data that STAR recorded in 2012 and 2015 (total  
 2716 sampled luminosity  $\sim 75$  pb $^{-1}$  for the two years combined). Nonetheless, the uncertainties  
 2717 remain large, as can be seen in Fig. 29. Run-24 data will reduce the uncertainties for  
 2718  $|\eta_3 + \eta_4| < 1$  by a factor of two. The increased acceptance from the iTPC will reduce the  
 2719 uncertainties at  $|\eta_3 + \eta_4| \approx 2.5$  by a much larger factor, while the Forward Upgrade will  
 2720 enable the measurements to be extended to even larger values of  $|\eta_3 + \eta_4|$ . When combined

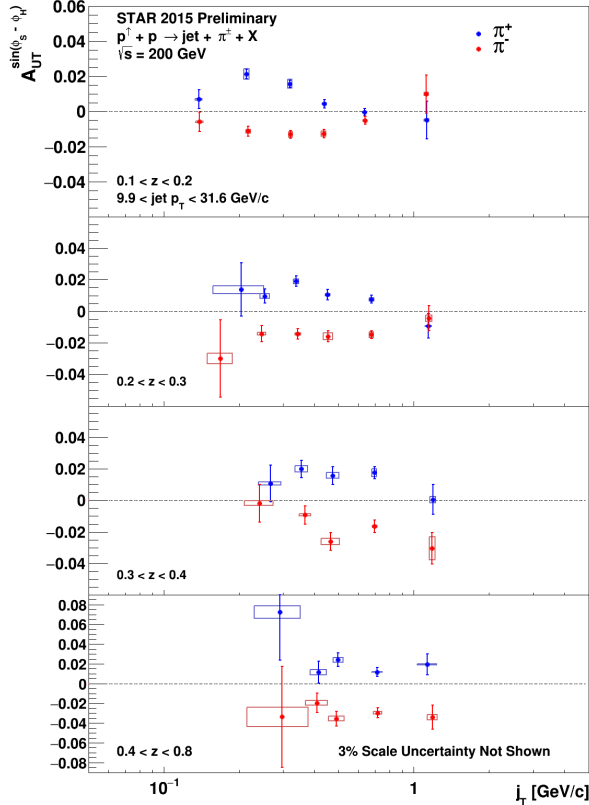


**Figure 73:** Preliminary 2015 results for the Collins asymmetry for charged pions in 200 GeV  $p+p$  collisions as a function of  $z$  and  $j_T$ , integrated over  $9.9 < p_T < 31.6$  GeV/ $c$  and  $0 < \eta < 0.9$ .

2721 with the 510 GeV data from 2017 and 2022 (see Sect. 3.1.2), the results will provide a detailed  
 2722 mapping *vs.*  $x$  for comparison to results for Sivers functions extracted from SIDIS, Drell-Yan,  
 2723 and vector boson production.

2724 **Transversity and related quantities:** As described in Sect. 3.1.3, measurements of the  
 2725 Collins asymmetry and IFF in  $p+p$  collisions at RHIC probe fundamental questions regarding  
 2726 TMD factorization, universality, and evolution. Data from 200 GeV  $p+p$  collisions will play  
 2727 an essential role toward answering these questions. Figure 68 shows that 200 GeV  $p+p$   
 2728 collisions interpolate between the coverage that we will achieve during Run-22 at high- $x$   
 2729 with the Forward Upgrade and at low- $x$  with the STAR mid-rapidity detectors. They will  
 2730 also provide a significant overlapping region of  $x$  coverage, but at  $Q^2$  values that differ by a  
 2731 factor of 6. This will provide valuable information about evolution effects, as well as cross-  
 2732 checks between the two measurements. Furthermore, for most of the overlapping  $x$  region,  
 2733 200 GeV  $p+p$  collisions will also provide the greatest statistical precision (see for example  
 2734 Fig. 70), thereby establishing the most precise benchmark for future comparisons to  $ep$  data  
 2735 from the EIC.

2736 The high statistical precision of the Run-24 data will enable detailed multi-dimensional  
 2737 binning for the Collins asymmetry results. This is particularly valuable because, as empha-  
 2738 sized in [109, 110], hadron-in-jet measurements in  $p+p$  collisions provide a direct probe of  
 2739 the Collins fragmentation function since they combine it with the *collinear* transversity dis-

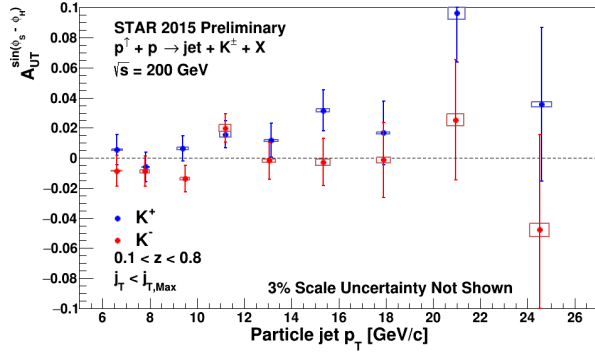


**Figure 74:** Preliminary 2015 results for the  $K^{+/-}$  Collins asymmetries *vs.* jet  $p_T$  for  $0 < \eta < 0.9$  in 200 GeV  $p+p$  collisions.

2740 tribution. In general, the observed asymmetries are functions of jet ( $p_T, \eta$ ), hadron ( $z, j_T$ ),  
 2741 and  $Q^2$ . However, the physics interpretations associated with these variables separate, with  
 2742  $p_T$  and  $\eta$  primarily coupling to the incident quark  $x$  and the polarization transfer in the  
 2743 hard scattering, while  $z$  and  $j_T$  characterize the fragmentation kinematics. Thus,  $A_{UT}$  *vs.*  
 2744  $p_T$ , as shown in Fig. 28 for the preliminary 2015 analysis, provides information about the  
 2745 transversity distribution. In parallel, the  $(z, j_T)$  dependence, integrated over a wide range of  
 2746 jet  $p_T$ , as shown in Fig. 73 for the preliminary 2015 results, provides a detailed look at the  
 2747 Collins fragmentation function. Note that STAR finds the maximum value of  $A_{UT}$  shifts to  
 2748 higher  $j_T$  as  $z$  increases. The statistical uncertainties in Figs. 28 and 73 will be reduced by  
 2749 a factor of 2.5 when Run-15 and Run-24 data are combined together.

2750 The 2015 Collins analysis has also, for the first time, measured the Collins effect for  
 2751 charged kaons in  $p+p$  collisions, as shown in Fig. 74. The asymmetries for  $K^+$ , which  
 2752 like  $\pi^+$  have a contribution from favored fragmentation of  $u$  quarks, are about 1.5-sigma  
 2753 larger than those for  $\pi^+$  in Fig. 28, while those for  $K^-$ , which can only come from unfavored  
 2754 fragmentation, are consistent with zero at the 1-sigma level. These trends are similar to those  
 2755 found in SIDIS by HERMES [280] and COMPASS [281], and provide additional insight into  
 2756 the Collins fragmentation function. This same analysis with Run-24 data will yield statistical  
 2757 uncertainties a factor of 3 smaller than those in Fig. 74. This is a much greater improvement  
 2758 than would be expected from the increase in sampled luminosity thanks to the improved  
 2759  $dE/dx$  resolution provided by the iTPC. In addition, the iTPC will enable the measurements  
 2760 in Figs. 28, 73, and 74 to be extended to an additional higher  $\eta$  bin ( $0.9 < \eta < 1.3$ ).

2761 RHIC has the unique opportunity to extend the Collins effect measurements to nuclei.  
 2762 This will provide an alternative look at the universality of the Collins effect in hadro-  
 2763 production by dramatically increasing the color flow options of the sort that have been  
 2764 predicted to break factorization for TMD PDFs like the Sivers effect [261, 262]. This will  
 2765 also explore the spin dependence of the hadronization process in cold nuclear matter. STAR  
 2766 collected a proof-of-principle data set during the 2015  $p+Au$  run that is currently under  
 2767 analysis. Those data will provide a first estimate of medium-induced effects. However, the  
 2768 small nuclear effects seen by STAR for forward inclusive  $\pi^0 A_N$  (see Fig. 30) indicate that  
 2769 greater precision will likely be needed. Figure 70 shows the projected 2015+'24 statistical  
 2770 uncertainties for the  $p+Au$  Collins asymmetry measurement at  $\sqrt{s_{NN}} = 200$  GeV, compared

2771 to those for the  $p+p$  at the same energy.

2772 **Ultra-peripheral collisions:** The formalism of generalized parton distributions (GPDs)  
 2773 provides a theoretical framework which addresses some of the above questions [282–285].  
 2774 Constraints on GPDs have mainly been provided by exclusive reactions in DIS, e.g. deeply  
 2775 virtual Compton scattering. RHIC, with its unique capability to collide transversely polar-  
 2776 ized protons at high energies, has the opportunity to measure  $A_N$  for exclusive  $J/\Psi$  produc-  
 2777 tion in ultra-peripheral collisions (UPCs) [286]. In such a UPC process, a photon emitted by  
 2778 the opposing beam particle (p or A) collides with the polarized proton. The measurement is  
 2779 at a fixed  $Q^2 \sim M_{J/\psi}^2 \approx 10 \text{ GeV}^2$  and  $10^{-4} < x < 10^{-1}$ . A nonzero asymmetry would be the  
 2780 first signature of a nonzero GPD  $E_g$  for gluons, which is sensitive to spin-orbit correlations  
 2781 and is intimately connected with the orbital angular momentum carried by partons in the  
 2782 nucleon and thus with the proton spin puzzle.

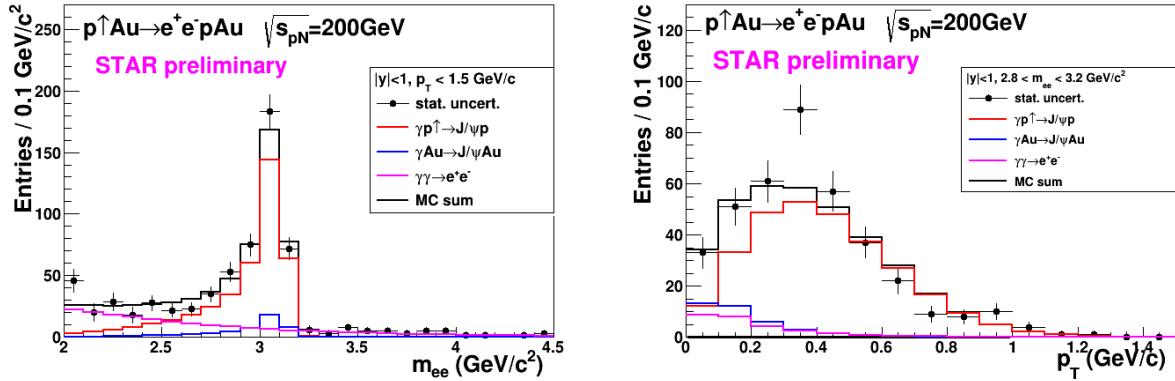


**Figure 75:** Mass distribution of selected  $e^+e^-$  pairs (left), and  $p_T$  distribution of the  $J/\psi$  mass peak (right). The colored histograms are the indicated processes modelled by STARlight and the sum fit to the data.

2783 The 2015  $p^\uparrow$ +Au data allowed a proof-of-principle of such a measurement. A trigger  
 2784 requiring back-to-back energy deposits in the Barrel Electromagnetic Calorimeter selected  
 2785  $J/\Psi$  candidates. The  $e^+e^-$  mass distribution after selection cuts is shown in the left of  
 2786 Fig. 75, and the pair  $p_T$  distribution of the  $J/\psi$  mass peak is shown on the right of the  
 2787 figure. The data are well described by the STARlight model [287] (colored histograms in  
 2788 the figure), including the dominant  $\gamma+p^\uparrow\rightarrow J/\psi$  signal process and the  $\gamma+Au\rightarrow J/\psi$  and  
 2789  $\gamma+\gamma\rightarrow e^+e^-$  background processes. The left of Fig. 76 shows the transverse asymmetry  $A_N^\gamma$   
 2790 for the signal  $J/\psi$ , which have a mean photon-proton center-of-mass energy  $W_{\gamma p} \approx 24 \text{ GeV}$ .  
 2791 The result is consistent with zero. Also shown is a prediction based on a parameterization  
 2792 of  $E_g$  [288]; the present data provide no discrimination of this prediction.

2793 This measurement can be greatly improved with a high statistics transversely polarized  
 2794  $p^\uparrow$ +Au run in 2024. The integrated luminosity for the 2015 measurement was  $140 \text{ nb}^{-1}$ ; the  
 2795 2024 run will provide  $1.3 \text{ pb}^{-1}$ , allowing a sizeable reduction of statistical uncertainty in the

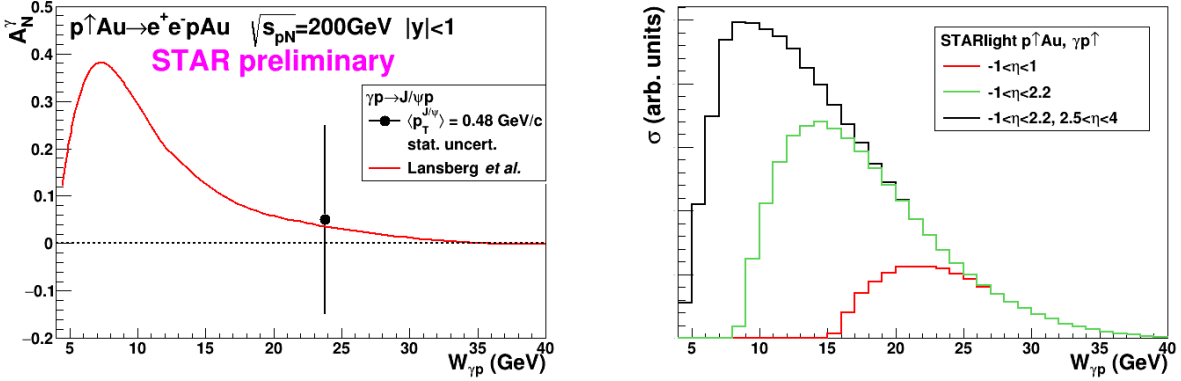


**Figure 76:** Left: The measured  $J/\psi$  transverse asymmetry  $A_N^\gamma$  and a prediction based on a parameterization of  $E_g$ . Right: The accepted cross section for  $\gamma+p^\dagger \rightarrow J/\psi$  for various detector pseudorapidity  $\eta$  ranges; the black curve shows the result for the full STAR detector with the Forward Upgrade and the iTPC.

2796 same  $W_{\gamma p}$  range. However, the Forward Upgrade and iTPC will also provide a significant  
 2797 extension of the  $W_{\gamma p}$  range of the measurement. The right panel of Fig. 76 shows the  
 2798 accepted cross section for  $\gamma+p^\dagger \rightarrow J/\psi$  for various detector pseudorapidity ranges. With the  
 2799 full detector, the sensitive cross section is a factor of five times the central barrel alone and  
 2800 the expected asymmetry is substantially larger. The statistical uncertainty on  $A_N^\gamma$  as shown  
 2801 in the left of Fig. 76 will be  $\approx 0.02$ , offering a powerful test of a non-vanishing  $E_g$ . Also, the  
 2802 accepted region has a lower mean  $W_{\gamma p} \approx 14$  GeV. Predictions based on  $E_g$  parameterizations  
 2803 such as shown in the figure have a larger asymmetry at lower  $W_{\gamma p}$ , with increased possibility  
 2804 of a nonzero result. Alternatively, the increased statistics will allow a measurement of  $A_N^\gamma$   
 2805 in bins of  $W_{\gamma p}$ .

2806 Similar measurements are also possible with future  $p^\dagger+p^\dagger$  runs at  $\sqrt{s} = 200$  and 510  
 2807 GeV. However, the UPC cross section scales with  $Z^2$  of the the nucleus emitting the photon;  
 2808 for protons this is  $1/79^2$  relative to Au nuclei, which makes analogous measurements in  $p+p$   
 2809 collisions extremely luminosity hungry.

### 2810 3.2.2 Physics Opportunities with Unpolarized proton-Nucleus Collisions

2811 Our quest to understand QCD processes in Cold Nuclear Matter (CNM) centers on the  
 2812 following fundamental questions:

- 2813 • Can we experimentally find evidence of a novel universal regime of non-linear QCD  
 2814 dynamics in nuclei?
- 2815 • What is the role of saturated strong gluon fields, and what are the degrees of freedom  
 2816 in this high gluon density regime?
- 2817 • What is the fundamental quark-gluon structure of light and heavy nuclei?

- Can a nucleus, serving as a color filter, provide novel insight into the propagation, attenuation and hadronization of colored quarks and gluons?

Various aspects of these questions have been addressed by numerous experiments and facilities around the world, most of them at significantly lower center-of-mass energies and kinematic reach than RHIC. Deep inelastic scattering on nuclei addresses some of these questions with results from, for instance, HERMES at DESY [289–291], CLAS at JLab [292], and in the future at the JLab 12 GeV. This program is complemented by hadron-nucleus reactions in fixed target  $p+A$  at Fermilab (E772, E886, and E906) [293] and at the CERN-SPS.

In the following we propose a measurement program unique to RHIC to constrain the initial state effects in strong interactions in the nuclear environment. We also highlight the complementarity to the LHC  $p+Pb$  program and stress why RHIC data are essential and unique in the quest to further our understanding of nuclei. The uniqueness of the RHIC program is based on the flexibility of the RHIC accelerator to run collisions of different particle species at very different center-of-mass energies. This in combination with the enhanced STAR detector capabilities in Run-24 allows to disentangle nuclear effects in the initial and final state as well as leading twist shadowing from saturation effects in a kinematic regime where all these effects are predicted to be large. Most of the discussed measurements critically rely on the Forward Upgrade.

### The initial state of nuclear collisions:

**Nuclear parton distribution functions:** A main emphasis of the 2015 and later  $p+A$  runs is to determine the initial conditions of the heavy ion nucleus before the collision to support the theoretical understanding of the A+A program both at RHIC and the LHC. In the following, the current status of nPDFs will be discussed, including where the unique contributions of RHIC lie, in comparison to the LHC and the future EIC.

Our current understanding of nuclear parton distribution functions (nPDFs) is still very limited, in particular, when compared with the rather precise knowledge of PDFs for free protons collected over the past 30 years. Figure 77 shows an extraction of nPDFs from available data, along with estimates of uncertainties. All results are shown in terms of the nuclear modification ratios, i.e., scaled by the respective PDF of the free proton. The yellow bands indicate regions in  $x$  where the fits are not constrained by data [294] and merely reflect the freedom in the functional form *assumed* in the different fits. Clearly, high precision data at small  $x$  and for various different values of  $Q^2$  are urgently needed better to constrain the magnitude of suppression in the  $x$  region where non-linear effects in the scale evolution are expected. In addition, such data are needed for several different nuclei, as the A-dependence of nPDFs cannot be predicted from first principles in pQCD and, again, currently relies on assumptions. Note that the difference between DSSZ [295] and EPS09 for the gluon modification arise from the different treatment of the PHENIX midrapidity  $\pi^0 R_{dAu}$  data [296], which in the EPS09 [297] fit are included with an extra weight of 20. The  $\pi^0 R_{dAu}$  data are the only data, which can probe the gluon in the nucleus directly, but these

2858 data also suffer from unknown nuclear effects in the final state (see [298]). Therefore, it is  
 2859 absolutely critical to have high precision data only sensitive to nuclear modification in the  
 2860 initial state over a wide range in  $x$  and intermediate values of  $Q^2$  (away from the saturation  
 2861 regime) to establish the nuclear modification of gluons in this kinematic range.

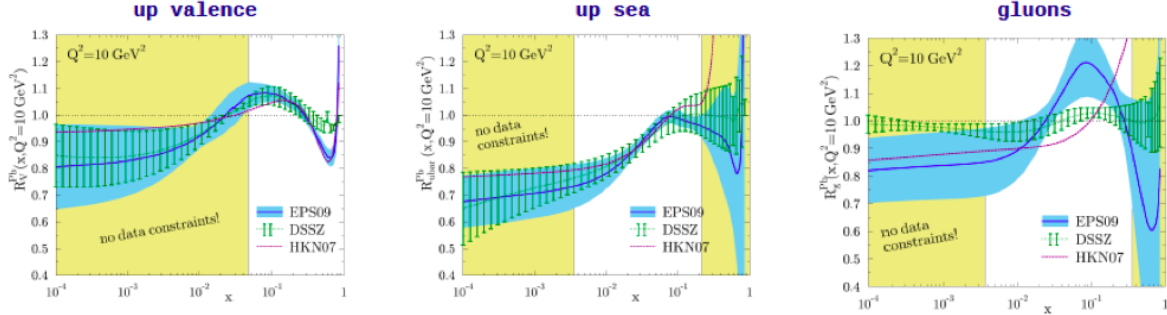


**Figure 77:** Summary of the most recent sets of nPDFs. The central values and their uncertainty estimates are given for the up valence quark, up sea quark, and the gluon. The yellow bands indicate regions in  $x$  where the fits are not constrained by any data (taken from Ref. [294]).

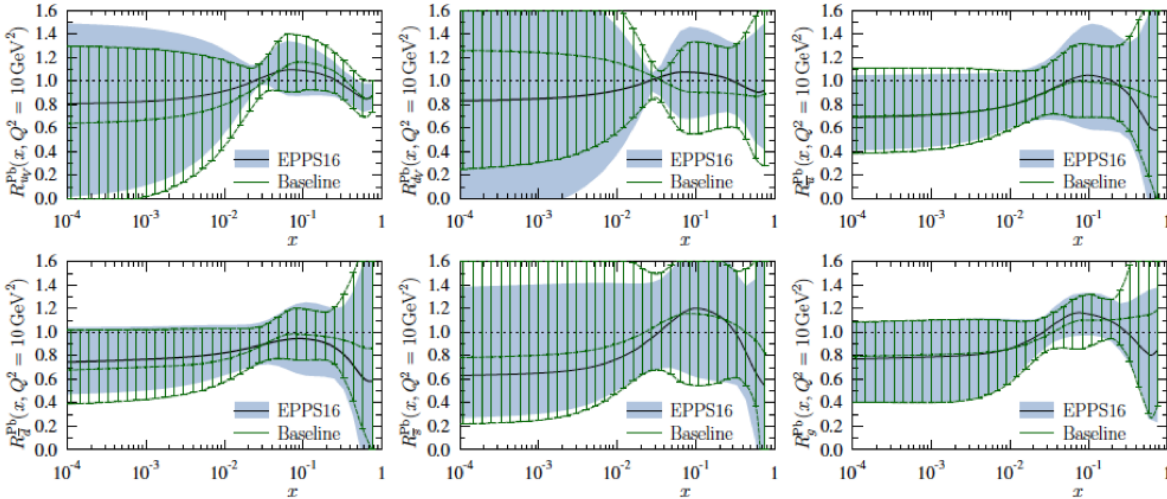


**Figure 78:** The nuclear modifications at  $Q^2=10\text{GeV}^2$  from the EPPS-16 fit (black central line and light-blue bands) compared with the Baseline fit (green curves with hatching) which uses only the data included in the EPS09 fit.

2862 It is important to realize that the measurements from RHIC are compelling and essential  
 2863 even when compared to what can be achieved in  $p+\text{Pb}$  collisions at the LHC. Due to the  
 2864 higher center-of-mass system energy most of the LHC data have very high  $Q^2$ , where the  
 2865 nuclear effects are already reduced significantly by evolution and are therefore very difficult to  
 2866 constrain. Two recent articles [299,300] assessed the impact of the available LHC Run-I  $p+\text{Pb}$   
 2867 data on determinations of nPDFs. The rather moderate impact of these data is illustrated

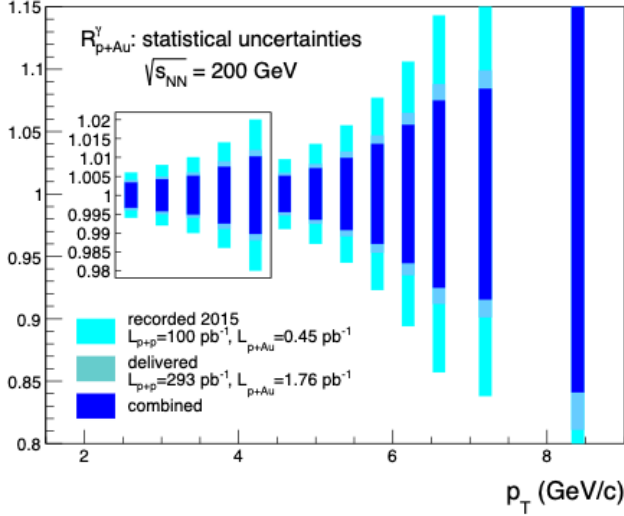


**Figure 79:** Projected statistical uncertainties for  $R_{pA}$  for direct photons in Run-15 (light blue) and a run in 2024 (blue) and the sum of both (dark blue). The recorded luminosity for Run-15 was  $L_{pAu} = 450 \text{ nb}^{-1}$  and  $L_{pp} = 100 \text{ pb}^{-1}$ . The delivered luminosity for Run-24 is assumed to be  $L_{pAu} = 1.8 \text{ pb}^{-1}$  and  $L_{pp} = 300 \text{ pb}^{-1}$ .

2868 in Figure 78. Note that the extra weight factor of 20 for the PHENIX midrapidity  $\pi^0 R_{dAu}$   
 2869 data [296] in the original EPS09 [297] fit was removed in all of the new fits, leading to a  
 2870 much smaller nuclear modification factor for gluons, especially at medium to high  $x$ .

2871 RHIC has the *unique* capability to provide data in a kinematic regime (moderate  $Q^2$  and  
 2872 medium-to-low  $x$ ) where the nuclear modification of the sea quark and the gluon is expected  
 2873 to be sizable and currently completely unconstrained. In addition, and unlike the LHC,  
 2874 RHIC has the potential to vary the nucleus in  $p+A$  collisions and as such also constrain the  
 2875  $A$ -dependence of nPDFs.

2876 Extraction of this information is less ambiguous if one uses processes in which strong  
 2877 (QCD) final-state interactions can be neglected or reduced. Such golden channels would  
 2878 include: a measurement of  $R_{pA}$  for Drell-Yan production at forward pseudo-rapidities with  
 2879 respect to the proton direction ( $2.5 < \eta < 4.$ ) to constrain the nuclear modifications of sea-  
 2880 quarks; and of  $R_{pA}$  for direct photon production in the same kinematic regime to constrain  
 2881 the nuclear gluon distribution. Data for the first measurement of  $R_{pA}$  for direct photon  
 2882 production have already been taken during the  $p+Au$  and  $p+Al$  runs in 2015, with recorded  
 2883 luminosities by STAR of  $L_{pAu} = 0.45 \text{ pb}^{-1}$  and  $L_{pAl} = 1 \text{ pb}^{-1}$ , respectively. The anticipated  
 2884 statistical precision for  $p+Au$  runs in 2015 and projections for the run in 2024 are shown in  
 2885 Fig. 79. The Forward Upgrade with its tracking at forward rapidities will also provide the  
 2886 possibility to measure  $R_{pA}$  for positive and negatively charged hadrons.

2887 Figure 80(left) shows the significant impact of the Run-15 and Run-24  $R_{pA}$  for direct  
 2888 photon production on the corresponding theoretical expectations and their uncertainties  
 2889 obtained with the EPPS-16 set of nPDFs. The uncertainty bands are obtained through a  
 2890 re-weighting procedure [301] by using the projected data shown in Fig. 79 and randomizing  
 2891 them according to their expected statistical uncertainties around the central values obtained  
 2892 with the current set of EPPS-16 nPDFs. Figure 80(right) shows how these measurements  
 2893 will help significantly in further constraining the nuclear gluon distribution in a broad range  
 2894 of  $x$  that is roughly correlated with accessible transverse momenta of the photon, i.e., few

2895 times  $10^{-3} < x < \text{few times } 10^{-2}$ . The relevant scale  $Q^2$  is set be  $\sim p_T^2$  and ranges from 6  
 2896  $\text{GeV}^2$  to about  $40 \text{ GeV}^2$ . Like all other inclusive probes in  $p+p$  and  $p+A$  collisions, e.g., jets,  
 2897 no access to the exact parton kinematics can be provided event-by-event but global QCD  
 2898 analyses easily account for that. After the  $p+Au$  run in 2024, the statistical precision of the  
 2899 prompt photon data will be sufficient to contribute to a stringent test of the universality  
 2900 of nuclear PDFs when combined with the expected data from the EIC (see Figure 2.22 and  
 2901 2.23 in Ref [302]).

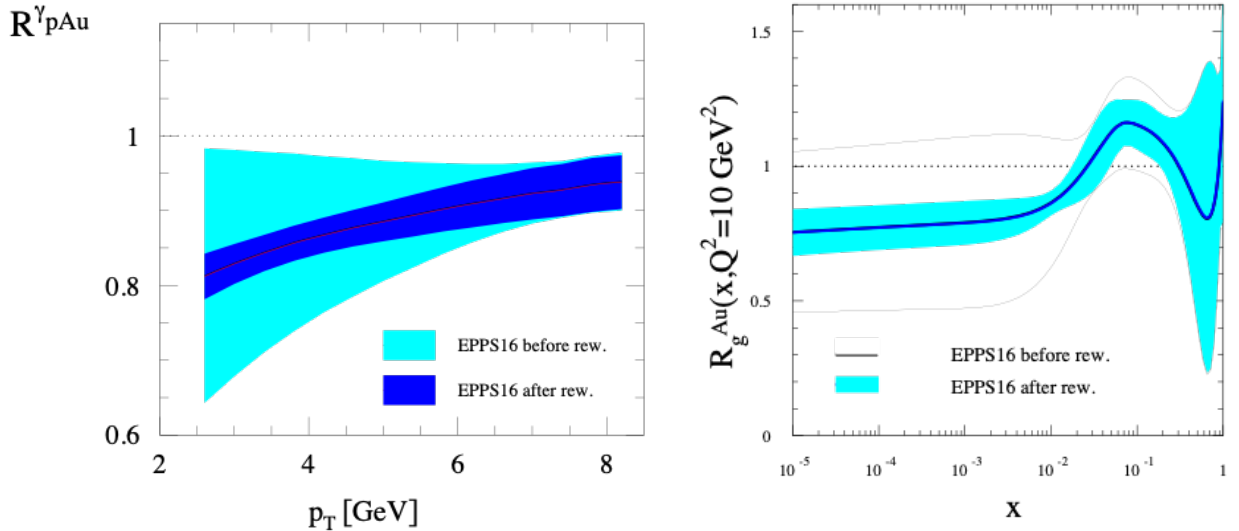


**Figure 80:** (left) The impact of the direct photon  $R_{pA}$  data measured in Run-15 (blue band) and for the anticipated statistics for the future  $p+Au$  run in 2024 (dark blue band) compared with the current uncertainties (cyan band) from EPPS-16. (right) The impact of the direct photon  $R_{pA}$  data measured in Run-15 and for the anticipated statistics for the future Run-24  $p+Au$  run on EPPS-16. The impact is shown on the nuclear suppression factor  $R_g$  of nPDF to the proton PDF, the grey bands represent the uncertainties before including the RHIC pseudo data.

2902 Figure 81 shows the kinematic coverage in  $x-Q^2$  of past, present, and future experiments  
 2903 capable of constraining nuclear parton distribution functions. The experiments shown pro-  
 2904 vide measurements that access the initial state parton kinematics on an event-by event basis  
 2905 (in a leading order approximation) while remaining insensitive to any nuclear effects in the  
 2906 final state. Some of the LHC experiments cover the same  $x$ -range as DY at forward pseudo-  
 2907 rapidities at RHIC but at a much higher scale  $Q^2$ , where nuclear modifications are already  
 2908 significantly reduced [300, 303, 304]. At intermediate  $Q^2$ , DY at RHIC will extend the low- $x$   
 2909 reach by nearly one decade compared to EIC.

2910 The biggest challenge of a DY measurement is to suppress the overwhelming hadronic  
 2911 background: the total DY cross-section is about  $10^{-5}$  to  $10^{-6}$  smaller than the corresponding  
 2912 hadron production cross-sections. Therefore, the probability of misidentifying a hadron  
 2913 track as a lepton has to be suppressed to the order of 0.1% while maintaining reasonable  
 2914 electron detection efficiencies. To that end, we have studied the combined electron/hadron

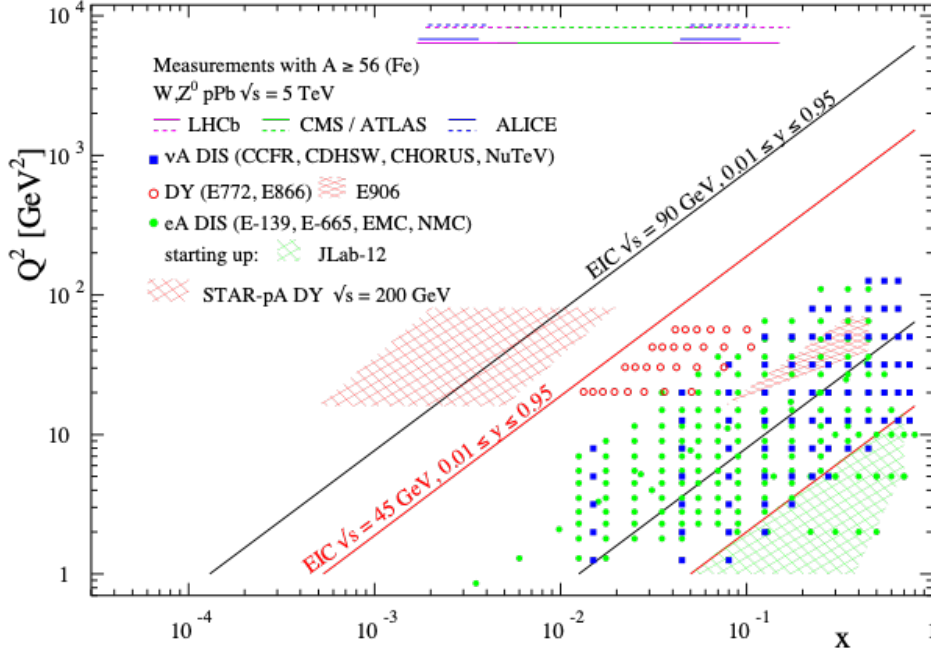


**Figure 81:** The kinematic coverage in  $x \sqrt{Q^2}$  of past, present and future experiments constraining nPDFs with access to the exact parton kinematics event-by-event and no fragmentation in the final state.

2915 discriminating power of the Forward Upgrade. It was found that by applying multivariate  
 2916 analysis techniques to the features of EM/hadronic shower development and momentum  
 2917 measurements we can achieve hadron rejection powers of 200 to 2000 for hadrons of 15 GeV  
 2918 to 50 GeV with 80% electron detection efficiency.

2919 The same procedure as for the direct photon  $R_{pA}$  was used to study the potential impact  
 2920 of the DY  $R_{pA}$  data for the EPPS-19 sets of nPDFs. We expect again a significant impact  
 2921 on the uncertainties of  $R_{pA}$  DY upon including the projected and properly randomized data.  
 2922 Clearly, the DY data from RHIC will be instrumental in reducing present uncertainties in  
 2923 nuclear modifications of sea quarks. Again, these data will prove to be essential in testing the  
 2924 fundamental universality property of nPDFs in the future when EIC data become available.

2925 STAR's unique detector capabilities will provide the first data on  $J/\Psi$ -production in  
 2926 ultra-peripheral collisions. This measurement provides access to the spatial gluon distri-  
 2927 bution by measuring the  $t$ -dependence of  $d\sigma/dt$ . As follows from the optical analogy, the  
 2928 Fourier-transform of the square root of this distribution yields the source distribution of the  
 2929 object probed. To study the gluon distribution in the gold nucleus, events need to be tagged  
 2930 where the photon is emitted from the proton. For both observables a measurement with  
 2931 different nuclei is required to pin down the  $A$ -dependence of nPDFs. The  $J/\Psi$ -production  
 2932 in ultra-peripheral collisions requires significantly more statistics than accumulated to date.

2933 **Gluon saturation:** Our understanding of the proton structure and of the nuclear  
 2934 interactions at high energy would be advanced significantly with the definitive discovery  
 2935 of the saturation regime [305–311]. Saturation physics would provide an infrared cutoff for  
 2936 perturbative calculations, the saturation scale  $Q_s$ , which grows with the atomic number of the  
 2937 nucleus  $A$  and with decreasing value of  $x$ . If  $Q_s$  is large it makes the strong coupling constant

2938 small,  $\alpha_s(Q_s^2) \ll 1$  allowing for perturbative QCD calculations to be under theoretical  
 2939 control.

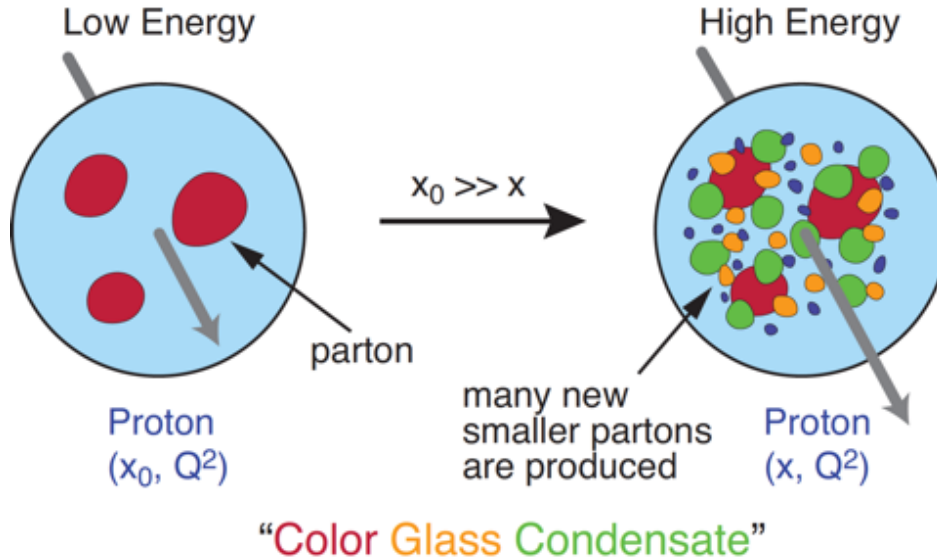


**Figure 82:** Proton wave function evolution towards small- $x$ .

2940 It is well known that PDFs grow at small- $x$ . If one imagines how such a high number of  
 2941 small- $x$  partons would fit in the (almost) unchanged proton radius, one arrives at the picture  
 2942 presented in Figure 82: the gluons and quarks are packed very tightly in the transverse plane.  
 2943 The typical distance between the partons decreases as the number of partons increases, and  
 2944 can get small at low- $x$  (or for a large nucleus instead of the proton). One can define the  
 2945 saturation scale as the inverse of this typical transverse inter-parton distance. Hence  $Q_s$   
 2946 indeed grows with  $A$  and decreasing  $x$ .

2947 The actual calculations in saturation physics start with the classical gluon fields (as gluons  
 2948 dominate quarks at small- $x$ ) [312–318], which are then evolved using the nonlinear small- $x$   
 2949 BK/JIMWLK evolution equations [319, 320, 320–328]. The saturation region can be well-  
 2950 approximated by the following formula:  $Q_s^2 \sim (A/x)^{1/3}$ . Note again that at small enough  
 2951  $x$  the saturation scale provides an IR cutoff, justifying the use of perturbative calculations.  
 2952 This is important beyond saturation physics, and may help us better understand small- $x$   
 2953 evolution of the TMDs.

2954 While the evidence in favor of saturation physics has been gleaned from the data col-  
 2955 lected at HERA, RHIC and the LHC, the case for saturation is not sealed and alternative  
 2956 explanations of these data exist. The EIC is slated to provide more definitive evidence for  
 2957 saturation physics [329]. To help the EIC complete the case for saturation, it is mandatory to  
 2958 generate higher-precision measurements in  $p$ +Au collisions at RHIC. These higher-precision  
 2959 measurements would significantly enhance the discovery potential of the EIC as they would  
 2960 enable a stringent test of universality of the CGC. We stress again that a lot of theoretical  
 2961 predictions and results in the earlier Sections of this document would greatly benefit from

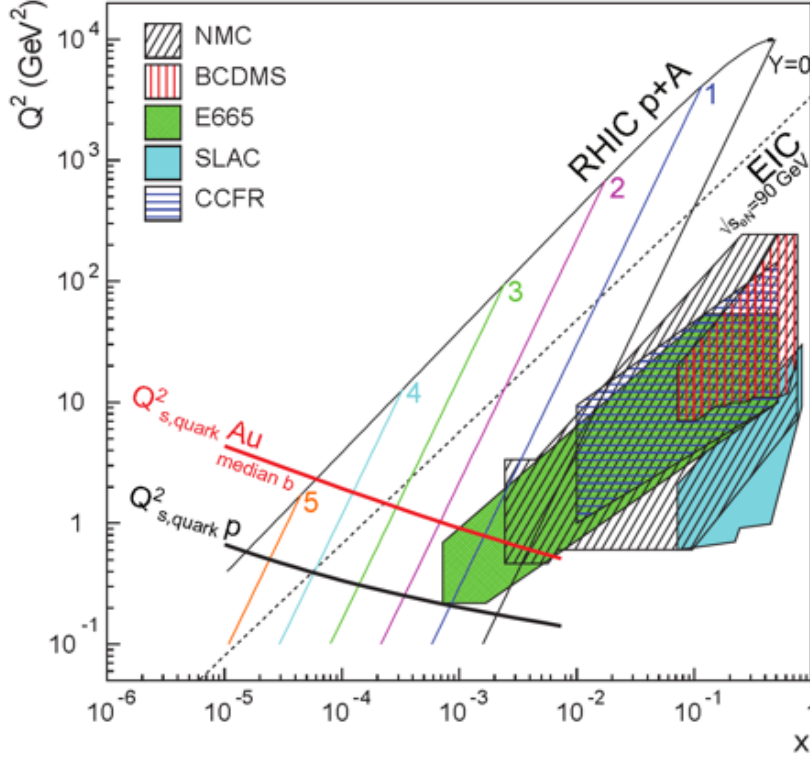


**Figure 83:** Kinematic coverage in the  $x - Q^2$  plane for  $p+A$  collisions at RHIC, along with previous  $e+A$  measurements, the kinematic reach of an electron-ion collider, and estimates for the saturation scale  $Q_s$  in Au nuclei and protons. Lines are illustrative of the range in  $x$  and  $Q^2$  covered with hadrons at various rapidities.

2962 saturation physics: the small- $x$  evolution of TMDs in a longitudinally or transversely polarized proton, or in an unpolarized proton, can all be derived in the saturation framework [330]  
 2963 in a theoretically better-controlled way due to the presence of  $Q_s$ . Hence saturation physics  
 2964 may help us understand both the quark and gluon helicity PDFs as well as the Sivers and  
 2965 Boer-Mulders functions.  
 2966

2967 The saturation momentum is predicted to grow approximately like a power of energy,  
 2968  $Q_s^2 \sim E^{\lambda/2}$  with  $\lambda \sim 0.2-0.3$ , as phase space for small- $x$  (quantum) evolution opens up. The  
 2969 saturation scale is also expected to grow in proportion to the valence charge density at the  
 2970 onset of small- $x$  quantum evolution. Hence, the saturation scale of a large nucleus should  
 2971 exceed that of a nucleon by a factor of  $A^{1/3} \sim 5$  (on average over impact parameters). RHIC  
 2972 is capable of running  $p+A$  collisions for different nuclei to check this dependence on the mass  
 2973 number. This avoids potential issues with dividing say  $p+Pb$  collisions in  $N_{part}$  classes [331].  
 2974 Figure 83 shows the kinematic coverage in the  $x-Q^2$  plane for  $p+A$  collisions at RHIC, along  
 2975 with previous  $e+A$  measurements and the kinematic reach of an EIC. The saturation scale for  
 2976 a Au nucleus and the proton is also shown. To access at RHIC a kinematic regime sensitive  
 2977 to saturation with  $Q^2 > 1 \text{ GeV}^2$  requires measurements at forward rapidities. For these  
 2978 kinematics the saturation scale is moderate, on the order of a few  $\text{GeV}^2$ , so measurements  
 2979 sensitive to the saturation scale are by necessity limited to semi-hard processes.

2980 Until today the golden channel at RHIC to observe strong hints of saturation has been  
 2981 the angular dependence of two-particle correlations, because it is an essential tool for testing  
 2982 the underlying QCD dynamics [331]. In forward-forward correlations facing the  $p(d)$  beam

2983 direction one selects a large- $x$  parton in the p(d) interacting with a low- $x$  parton in the  
 2984 nucleus. For  $x < 0.01$  the low- $x$  parton will be back-scattered in the direction of the large-  
 2985  $x$  parton. Due to the abundance of gluons at small  $x$ , the backwards-scattered partons  
 2986 are dominantly gluons, while the large- $x$  partons from the p(d) are dominantly quarks.  
 2987 The measurements of di-hadron correlations by STAR and PHENIX [332, 333], have been  
 2988 compared with theoretical expectations using the CGC framework based on a fixed saturation  
 2989 scale  $Q_s$  and considering valence quarks in the deuteron scattering off low- $x$  gluons in the  
 2990 nucleus with impact parameter  $b = 0$  [334, 335]. Alternative calculations [336] based on both  
 2991 initial and final state multiple scattering, which determine the strength of this transverse  
 2992 momentum imbalance, in which the suppression of the cross-section in  $d+Au$  collisions arises  
 2993 from cold nuclear matter energy loss and coherent power corrections have also been very  
 2994 successful to describe the data.

2995 The 2015  $p+Au$  run at RHIC has provided unique opportunities to study this channel in  
 2996 more detail at STAR. The high delivered integrated luminosities allow one to vary the trigger  
 2997 and associated particle  $p_T$  from low to high values and thus crossing the saturation boundary  
 2998 as shown in Figure 83 and reinstate the correlations for central  $p+A$  collisions for forward-  
 2999 forward  $\pi^0$ 's. Studying di-hadron correlations in  $p+A$  collisions instead of  $d+A$  collisions has  
 3000 a further advantage. In reference [337], the authors point out that the contributions from  
 3001 double-parton interactions to the cross-sections for  $dA \rightarrow \pi^0\pi^0 X$  are not negligible. They  
 3002 find that such contributions become important at large forward rapidities, and especially in  
 3003 the case of  $d+A$  scattering. Figure 84 shows the results for the di-hadron correlations for  $\pi^0$   
 3004 from the 2015  $p+p$  and  $p+Au$  run. Shown is the ratio of the area, the width and the level  
 3005 of pedestal of the backward peak for  $p+Au$  and  $p+p$  as function of the  $p_T$  of the trigger and  
 the associated  $\pi^0$  and the activity in the collision as measured by the BBC. The results show

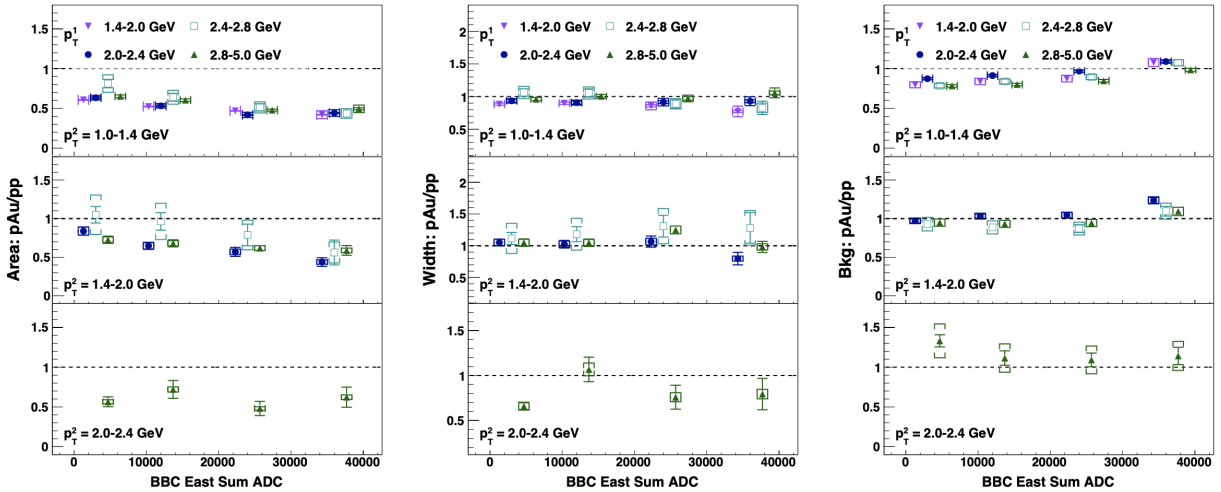
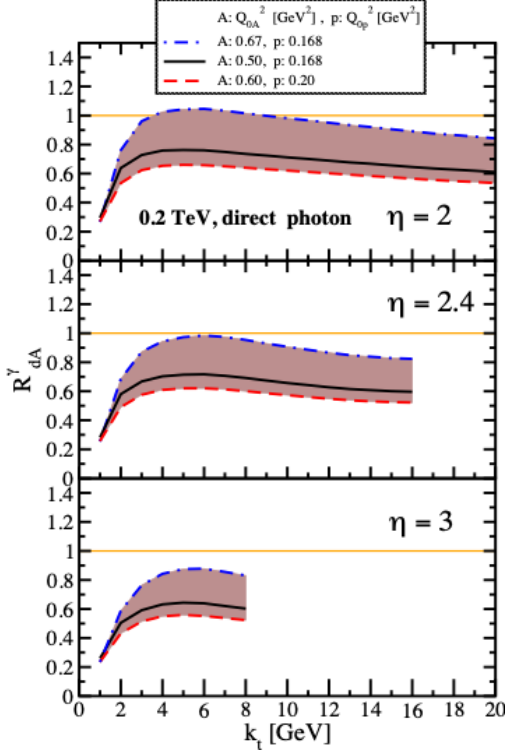


Figure 84: The results for the di-hadron correlations for  $\pi^0$  from the 2015  $p+p$  and  $p+A$  run.

3006 basically no change in the width of the backward peak and the background/pedestal the  
 3007 peak is sitting on shows only up to a 20% increase in  $p+Au$  to  $p+p$ . However, the area of the  
 3008



**Figure 85:** Nuclear modification factor for direct photon production in  $p(d)+A$  collisions at various rapidities at RHIC  $\sqrt{s} = 200$  GeV. The curves are the results obtained from Eq. (12) in Ref. [338] and the solution to rcBK equation using different initial saturation scales for a proton  $Q_{op}$  and a nucleus  $Q_{oA}$ . The band shows our theoretical uncertainties arising from allowing a variation of the initial saturation scale of the nucleus in a range consistent with previous studies of DIS structure functions as well as particle production in minimum-bias  $p+p$ ,  $p+A$  and  $A+A$  collisions in the CGC formalism, see Ref. [338] for details.

3009 backward peak shows a large suppression with increasing activity in the collision. For fixed  
 3010 activity the biggest suppression is observed for the smallest trigger  $p_T$  in combination with  
 3011 the smallest  $p_T$  for the associated  $\pi^0$ . This behaviour is consistent with different calculations  
 3012 based on the CGC formalism. This result is the first clean observable, which cannot yet  
 3013 be explained in a different framework than CGC and as such a clear hint for non-linear  
 3014 effects. With the Forward Upgrade several other channels, i.e charged di-hadron and di-jets  
 3015 correlations, will also be available, which will allow a rigorous test of the calculation in the  
 3016 CGC formalism. It is noted that these results are crucial for the equivalent measurements at  
 3017 an EIC, which are planned at close to identical kinematics, because only if non-linear effects  
 3018 are seen with different complementary probes, i.e., ep and  $p+A$ , one can claim a discovery  
 3019 of saturation effects and their universality.

3020 It is important to note that for the measurements to date in  $p(d)+A$  collisions both  
 3021 initial and final states interact strongly, leading to severe complications in the theoretical  
 3022 treatment (see [339, 340], and references therein). As described in detail in the Section  
 3023 above in  $p+A$  collisions, these complications can be ameliorated by removing the strong  
 3024 interaction from the final state, by using photons and Drell-Yan electrons. The Run-15  
 3025  $p+A$  run will for the first time provide data on  $R_{pA}$  for direct photons and therefore allow  
 3026 one to test CGC based predictions on this observable as depicted in Figure 85 (taken from  
 3027 Ref. [338]). The higher delivered integrated luminosity for the upcoming  $p+Au$  run in  
 3028 2024 together with the Forward Upgrade will enable one to study more luminosity hungry  
 3029 processes and/or complementary probes to the di- $\pi^0$  correlations, i.e. di-hadron correlations  
 3030 for charged hadrons, photon-jet, photon-hadron and di-jet correlations.

3031 We use direct photon plus jet (direct  $\gamma$  +jet) events as an example channel to indicate  
 3032 what can be done in 2024. These events are dominantly produced through the gluon Compton  
 3033 scattering process,  $g+q \rightarrow \gamma+q$ , and are sensitive to the gluon densities of the nucleon  
 3034 and nuclei in  $p+p$  and  $p+A$  collisions. Through measurements of the azimuthal correlations  
 3035 in  $p+A$  collisions for direct  $\gamma$  +jet production, one can study gluon saturation phenomena  
 3036 at small- $x$ . Unlike di-jet production that is governed by both the Weizsäcker-Williams and  
 3037 dipole gluon densities, direct  $\gamma$  +jet production only accesses the dipole gluon density, which  
 3038 is better understood theoretically [338, 341]. On the other hand, direct  $\gamma$  +jet production  
 3039 is experimentally more challenging due to its small cross-section and large background con-  
 3040 tribution from di-jet events in which photons from fragmentation or hadron decay could be  
 3041 misidentified as direct photons. The feasibility to perform direct  $\gamma$  +jet measurements with  
 3042 the Forward Upgrade in unpolarized  $p+p$  and  $p+Au$  collisions at  $\sqrt{s_{NN}} = 200$  GeV has been  
 3043 studied. PYTHIA-8.189 [342] was used to produce direct  $\gamma$  +jet and di-jet events. In order  
 3044 to suppress the di-jet background, the leading photon and jet are required to be balanced  
 3045 in transverse momentum,  $|\phi^\gamma - \phi^{jet}| > 2\pi/3$  and  $0.5 < \frac{p_T^\gamma}{p_T^{jet}} < 2$ . Both the photon and  
 3046 jet have to be in the forward acceptance  $1.3 < \eta < 4.0$  with  $p_T > 3.2$  GeV/ $c$  in 200 GeV  
 3047  $p+p$  collisions. The photon needs to be isolated from other particle activities by requiring  
 3048 the fraction of electromagnetic energy deposition in the cone of  $\Delta R=0.1$  around the photon  
 3049 is more than 95% of that in the cone of  $\Delta R=0.5$ . Jets are reconstructed by an anti- $k_T$   
 3050 algorithm with  $\Delta R=0.5$ . After applying these selection cuts, the signal-to-background ra-  
 3051 tio is around 3:1 [343]. The expected number of selected direct  $\gamma$  +jet events is around  
 3052 1.0M/0.9M at  $\sqrt{s_{NN}} = 200$  GeV in  $p+Au$  collisions for the proposed Run-24. We conclude  
 3053 that a measurement of direct photon-hadron correlation from  $p+Au$  collisions is feasible,  
 3054 which is sensitive to the gluon density in  $0.001 < x < 0.005$  in the Au nucleus where parton  
 3055 saturation is expected.

### 3056 **The final state:**

3057 **Nuclear fragmentation functions:** In spite of the remarkable phenomenological suc-  
 3058 cesses of QCD, a quantitative understanding of the hadronization process is still one of the  
 3059 great challenges for the theory. Hadronization describes the transition of a quark or gluon  
 3060 into a final state hadron. It is a poorly understood process even in elementary collisions.  
 3061 RHIC's unique versatility will make it possible to study hadronization in vacuum and in the  
 3062 nuclear medium, and additionally with polarized beams (see Sect. 3.2.1 for the latter).

3063 It has long been recognized that the hadron distributions within jets produced in  $p+p$   
 3064 collisions are closely related to the fragmentation functions that have typically been measured  
 3065 in  $e^+e^-$  collisions and SIDIS. The key feature of this type of observable is the possibility to  
 3066 determine the relevant momentum fraction  $z$  experimentally as the ratio of the hadron to the  
 3067 jet transverse momentum. Recently [344] a quantitative relationship has been derived in a  
 3068 form that enables measurements of identified hadrons in jets in  $p+p$  collisions to be included  
 3069 in fragmentation function fits on an equal footing with  $e^+e^-$  and SIDIS data. Furthermore,  
 3070 hadrons in  $p+p$  jets provide unique access to the gluon fragmentation function, which is

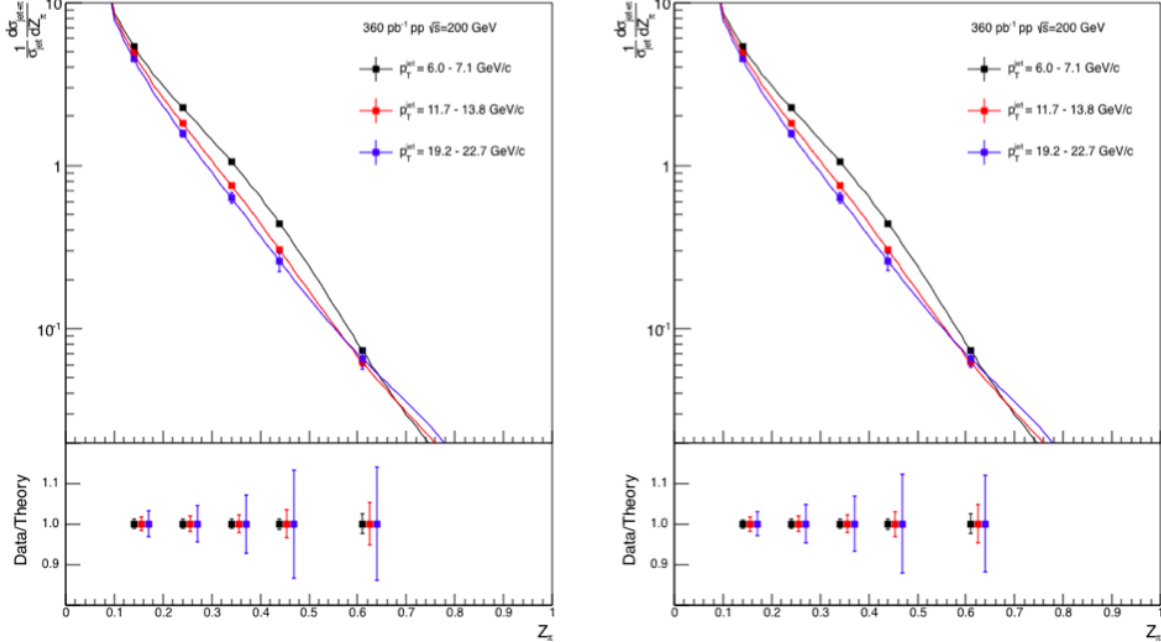


**Figure 86:** Anticipated precision for identified  $\pi^+$  (left) and  $\pi^-$  (right) within jets at  $|\eta| < 0.4$  in 200 GeV  $p+p$  collisions for three representative jet  $p_T$  bins. The data points are plotted on theoretical predictions based on the DSS14 pion fragmentation functions [344, 345]. Kaons and (anti)protons will also be measured, over the range from  $z < 0.5$  at low jet  $p_T$  to  $z < 0.2$  at high jet  $p_T$ , with uncertainties a factor of  $\sim 3$  larger than those for pions.

3071 poorly determined in current fits [345], in part due to some tension found in the inclusive  
 3072 high  $p_T$  pion yields measured by the PHENIX and ALICE collaborations. Here, the proposed  
 3073 measurements can provide valuable new insight into the nature of this discrepancy.

3074 This development motivated STAR to initiate a program of identified particle fragmen-  
 3075 tation function measurements using  $p+p$  jet data at 200 and 500 GeV from 2011, 2012, and  
 3076 2015. Figure 86 shows the precision that is anticipated for identified  $\pi^+$  and  $\pi^-$  in 200 GeV  
 3077  $p+p$  collisions for three representative jet  $p_T$  bins after the existing data from 2012 and 2015  
 3078 are combined with future 200 GeV  $p+p$  data from 2024. Identified kaon and (anti)proton  
 3079 yields will also be obtained, with somewhat less precision, over a more limited range of hadron  
 3080  $z$ . Once the 2017 data are fully analyzed, the uncertainties for 510 GeV  $p+p$  collisions will  
 3081 be comparable to that shown in Fig. 86 at high jet  $p_T$ , and a factor of  $\sim 2$  larger than shown  
 3082 in Fig. 86 at low jet  $p_T$ . Identified hadron yields will also be measured multi-dimensionally  
 3083 vs.  $j_T$ ,  $z$ , and jet  $p_T$ , which will provide important input for unpolarized TMD fits.

3084 Data from the HERMES experiment [289, 291, 346] have shown that production rates of  
 3085 identified hadrons in semi-inclusive deep inelastic  $e+A$  scattering differ from those in  $e+p$   
 3086 scattering. These differences cannot be explained by nuclear PDFs, as nuclear effects of  
 3087 strong interactions in the initial state should cancel in this observable. Only the inclusion of  
 3088 nuclear effects in the hadronization process allows theory to reproduce all of the dependencies  
 3089 ( $z$ ,  $x$ , and  $Q^2$ ) of  $R_{eA}$  seen in SIDIS, as shown in Fig. 87.

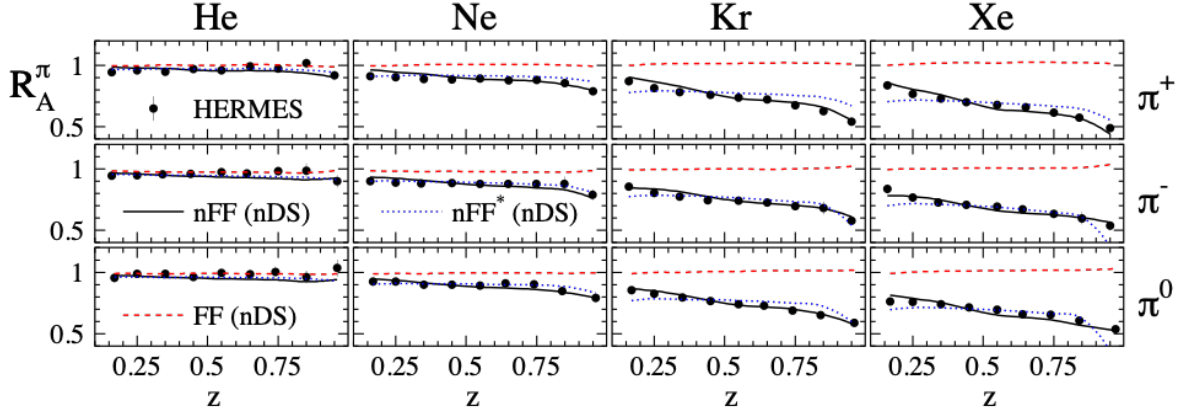


**Figure 87:**  $R_{eA}$  in SIDIS for different nuclei in bins of  $z$  as measured by HERMES [289, 291, 346]. The solid lines correspond to the results using effective nuclear FF [298] and the nDS medium modified parton densities [347]. The red dashed lines are estimates assuming the nDS medium modified PDFs but standard DSS vacuum FFs [348, 349] and indicate that nPDFs are insufficient to explain the data

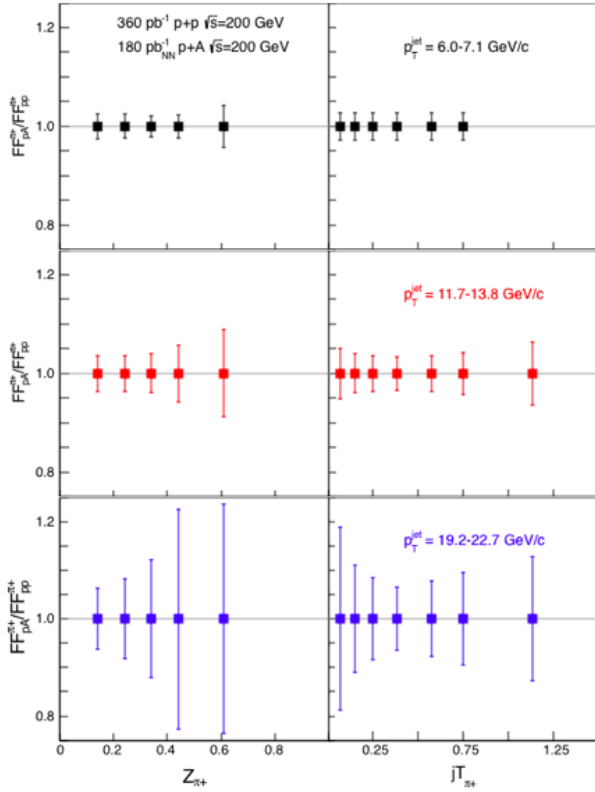


**Figure 88:** Anticipated precision for measurements of  $\pi^+$  fragmentation functions in  $p+A/p+p$  at  $|\eta| < 0.4$  vs.  $z$  and  $j_T$  in 2024 for three representative jet  $p_T$  bins. Uncertainties for  $\pi^-$  will be similar to those shown here for  $\pi^+$ , while those for kaons and (anti)protons will be a factor of  $\sim 3$  larger. Note that, to be species independent, the nucleon-nucleon equivalent luminosity is specified for  $p+Au$ .

3090 It is critical to see if these hadronization effects in cold nuclear matter persist at the higher  
3091  $\sqrt{s}$  and  $Q^2$  accessed at RHIC and EIC – both to probe the underlying mechanism, which is  
3092 not understood currently, and to explore its possible universality. The combination of  $p+p$   
3093 jet data from RHIC and future SIDIS data from EIC will also provide a much clearer picture  
3094 of modified gluon hadronization than will be possible with EIC data alone. Using the Run-15  
3095 200 GeV  $p+Au$  data, STAR will be able to make a first opportunistic measurement of these  
3096 hadron-jet fragmentation functions in nuclei, but the precision will be limited. Additional  
3097 data will be needed in 2024 in order to provide a sensitive test for universality, as shown in  
3098 Figure 88.

## 3099 4 Detector Updates, Operations, and Opportunities

3100 In this section we discuss the performance of the endcap Time of Flight (eTOF) in Run-20  
3101 and progress of the construction of the Forward upgrades. The iTPC and EPD were fully  
3102 integrated for Run-19.

### 3103 4.1 Status and Performance of the eTOF

3104 The full eTOF hardware installation was completed in Nov. 2018 followed by the first  
3105 data taking started in Feb. 2019 by recording about 580 M Au+Au events at  $\sqrt{s_{NN}} =$   
3106 19.6 GeV with an eTOF participation of 85%. However, due to several beam loss events  
3107 causing instantaneous high currents on the readout strips all eTOF preamplifier boards got  
3108 damaged and no further useful operation was possible during that year. It was decided to  
3109 replace all preamplifier boards with an improved version using ESD protection diodes on  
3110 the input. Beside minor issues eTOF showed an excellent performance during Run-20. A  
3111 reliable start-up procedure and control interface was implemented that allows the full system  
3112 to be controlled via only 2 commands issued by the shift crew. For Run-20 an improved clock  
3113 distribution method was installed offering a system synchronization in the order of 35 ps over  
3114 the full wheel. Figure 89 shows the width of the time distribution (red corresponds to the  
3115 Gaussian sigma and blue to the RMS) obtained by measuring the arrival time of injected  
3116 pulser signals on every TDC board. The stability of the system is demonstrated on the right  
3117 plot of Fig. 89. Here the mean of the time distribution width from all pulser channels is  
3118 plotted vs. the run number. The range of 130 runs reflects a time period of several days.

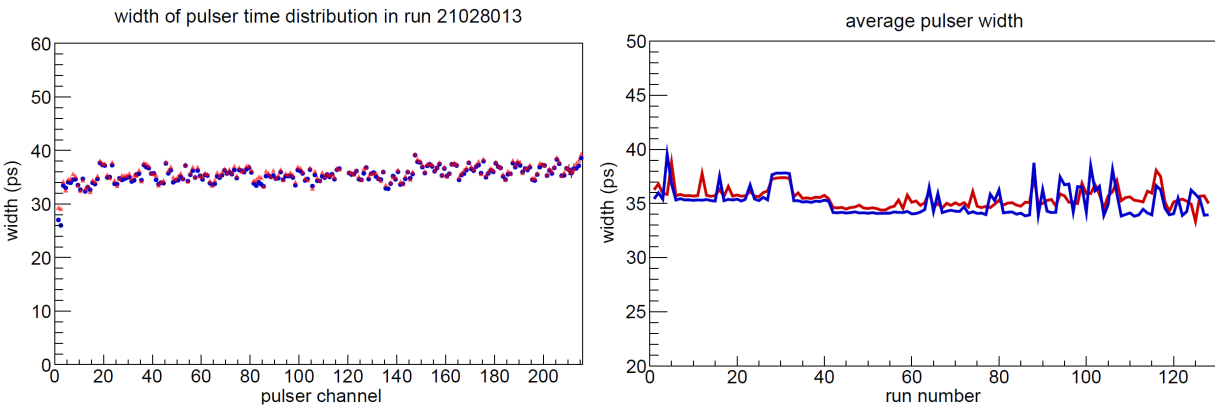


**Figure 89:** Left: Width of the time distribution obtained by measuring the arrival time of injected pulser signals on every GET4 board. Right: Mean of the time distribution width vs. the run number.

3119 All fixed target runs in 2020 were successfully completed and about 100 M events with  
3120 eTOF data were collected for each energy. For the  $\sqrt{s_{NN}} = 11.5$  GeV collider run 235 M  
3121 events with eTOF data were recorded. The eTOF performance remained stable also during  
3122 the Run-20b after the break due to COVID-19.

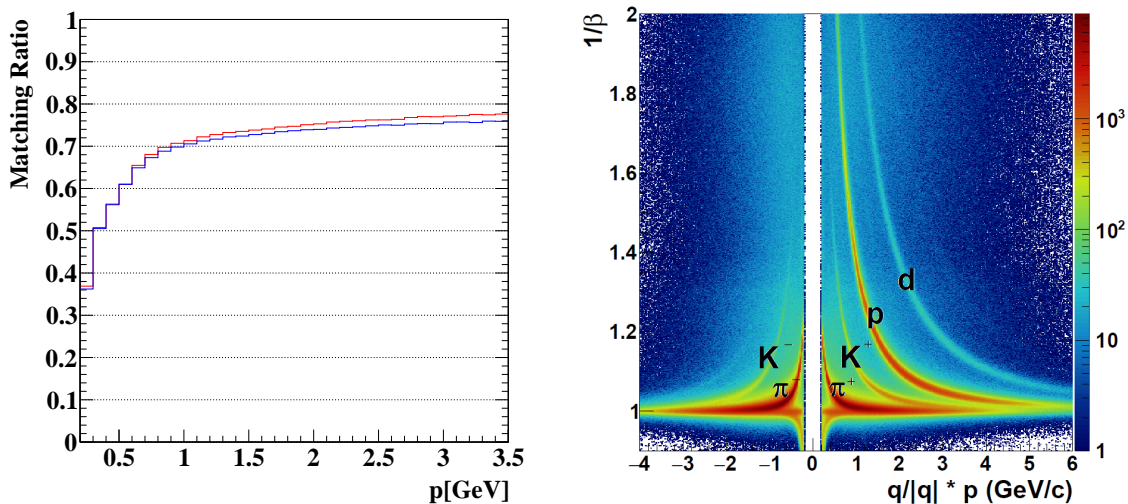


**Figure 90:** Left: Matching efficiency of MRPC hits in respect to the extrapolated TPC tracks as function of the particle momentum. Right:  $1/\beta$  as function of particle momentum. The separation of kaons from pions up to a momenta of 2.5 GeV/c demonstrates the PID capability of eTOF.

3123 In order to demonstrate the eTOF performance fixed target data at  $\sqrt{s_{NN}} = 7.7$  GeV were  
 3124 calibrated and the matching efficiency with the TPC has been deduced as function of the  
 3125 particle momentum (see left Fig.90). At a momentum of 1 GeV/c a matching efficiency of  
 3126 70% is obtained for both MRPC types (red and blue are different MRPC types with different  
 3127 electrode materials). Beyond 1 GeV/c the curve levels off at 75%. The time resolution (not  
 3128 shown here) was determined to be in the order of 80 ps. This good timing resolution is  
 3129 reflected in the  $1/\beta$  versus the particle momenta plot shown in the right Fig. 90. The narrow  
 3130 particle bands allow for a kaon to pion separation of up to a momentum of 2.5 GeV/c which  
 3131 demonstrates the excellent PID capability of eTOF.

3132 For the upcoming period no major hardware changes for eTOF are foreseen. During Run-  
 3133 20 one MRPC counter developed a high dark current and noise and will be replaced at the  
 3134 next shutdown. Due to COVID-19 travel restrictions it is planed to ship a fully assembled  
 3135 module (3 MRPC counters) to BNL as a replacement for the module housing the broken  
 3136 counter. On a different module it is planned to replace one GBTx readout card, which is  
 3137 currently not working. A substantial eTOF upgrade will be performed on the firmware side  
 3138 of the readout FPGAs, which can be done remotely. This implies also small adaptations in  
 3139 the control software. With this upgrade an improved startup reliability and a more stable  
 3140 operation is expected.

## 3141 4.2 Forward Upgrade

3142 STAR is constructing a forward detector system, realized by combining tracking with elec-  
 3143 tromagnetic and hadronic calorimeters for the years beyond 2021. It will have superior  
 3144 detection capability for neutral pions, photons, electrons, jets and leading hadrons covering

3145 a region of  $2.5 < \eta < 4$ . The design of the Forward Calorimeter System (FCS) is driven by  
3146 consideration of detector performance, integration into STAR and cost optimization. For  
3147 the electromagnetic calorimeter the refurbished PHENIX sampling EMCal is used, and the  
3148 hadronic calorimeter will be newly constructed as a sandwich iron scintillator plate sampling  
3149 type, based on the extensive STAR Forward Upgrade and EIC Calorimeter Consortium R&D.  
3150 The existing EPD will be used as a trigger detector especially for a 2 electron trigger. Both  
3151 calorimeters share the same cost-effective readout electronics, with SiPMs as photo-sensors.  
3152 This FCS system will have very good ( $\sim 10\%/\sqrt{E}$ ) electromagnetic and ( $\sim 50\%/\sqrt{E} + 10\%$ )  
3153 hadronic energy resolutions. In addition, a Forward Tracking System (FTS) is being con-  
3154 structed. The FTS will be capable of discriminating hadron charge sign for transverse  
3155 asymmetry and Drell-Yan measurements in  $p+A$ . In heavy ion collisions, measurements of  
3156 charged particle transverse momenta of  $0.2 < p_T < 2$  GeV/ $c$  with 20-30% momentum res-  
3157 olution are required. To keep multiple scattering and photon conversion background under  
3158 control, the material budget of the FTS must be small. Hence, the FTS design is based on  
3159 three Silicon mini-strip detectors that consist of disks with a wedge-shaped design to cover  
3160 the full azimuth and  $2.5 < \eta < 4.0$ ; they are read out radially from the outside to minimize  
3161 the material. The Si-disks are combined with four small-strip Thin Gap Chamber (sTGC)  
3162 wheels following the ATLAS design [350, 351]. The Si mini-strip disks will be placed in the  
3163 region  $z = 146.6 - 173.7$  cm. The 4 sTGC wheels would be placed 30 cm apart starting from  
3164  $z = 273$  cm. The Si-Disks readout is based on APV chips, which will reuse the readout chain  
3165 of the IST, which was part of the STAR HFT. For the sTGC the readout will be based on  
3166 the ATLAS VMM3 chip [352].

#### 3167 4.2.1 Status

3168 Following the successful directors review in November 2018, the project submitted a proposal  
3169 for a NSF MRI for construction of EMCAL and HCAL and the associated electronics. The  
3170 NSF MRI was approved in Summer 2019 and work has been ongoing on all aspects of the  
3171 upgrade. In August 2020, another successful directors review was conducted on the status  
3172 of the upgrades. No serious issues were found.

#### 3173 4.2.2 Forward Calorimetry System

3174 The platform that supports the HCAL and EMCAL was installed in 2019, followed by the  
3175 installation of the refurbished PHENIX EMCAL blocks. The installed EMCAL blocks are  
3176 depicted in Fig. 91. The HCAL absorber blocks are under production at Chapman Lake  
3177 Instrumentation and Getto Industrial Plating. The first sets of blocks have arrived at BNL.  
3178 The scintillating tiles have been produced and all 18200 are in hand. About 10,000 of these  
3179 have been polished at ACU and Valpo and are ready for installation. Other parts are being  
3180 fabricated at Rutgers, Temple and Ohio State. Front-end electronics cards with the SiPM  
3181 and readout for both EMCAL and HCAL are in production and testing is underway. The  
3182 front end cards will be readout by 78 DEP/ADC boards and 3 trigger processor boards  
3183 housed in 5 crates. About half have been delivered and are undergoing testing at BNL.

3184 All DAQ PCs and receiver cards have been installed. The installation will commence once  
3185 the Run-20b is completed by mid September, and key personnel has come to BNL. The  
3186 commissioning of the FCS will be continue during Run-21, and will be ready for Run-22.



**Figure 91:** A view of the installed forward ECal detector halves, left and right from the beam pipe.

### 3187 4.2.3 Forward Silicon Tracking

3188 The procedures for the Si-detector module fabrication has been developed and documented.  
3189 Several prototype mechanical structures with hybrids mounted have been produced and  
3190 two wedges were assembled with Si-sensors. Performance of two fully assembled prototype  
3191 wedges have been evaluated with cosmic ray data and show that all channels can be read out,

3192 the signal-to-noise meets requirements, and the efficiency is higher than 90%. The design  
3193 of the support structures and the interface to the detector modules is nearly complete. If  
3194 time allows in the upcoming shutdown a test installation of the support frame into STAR  
3195 is planned. The cooling system, which was used previously for the HFT IST sub-system,  
3196 has been revived and verification of its performance is on-going. An internal production  
3197 readiness review with external reviewers was held on August 3, and the initial steps of the  
3198 mass production have started. The review recommendations, which were useful, will be  
3199 implemented. Currently there is only limited schedule float for the installation in August  
3200 2021.

#### 3201 **4.2.4 sTGC Tracking**

3202 A full prototype module of the sTGC was designed and produced at Shandong University  
3203 and tested. This module is now at BNL to undergo testing with the n-pentane gas system  
3204 that is being built at BNL. Due to space constraints around the beam pipe the final detector  
3205 will have pentagon shaped modules. The design is complete and production has started  
3206 of the final pre-production module; mass production is expected to start in October. The  
3207 read-out electronics are based on the ATLAS VMM3 chip [352] developed for the same kind  
3208 of detector. The strips of each sTGC layer can be handled by 24 Front-End Boards (FEB).  
3209 In total 96 FEBs are needed for 4 sTGC layers. The FEBs are vertically inserted in the  
3210 sTGC chamber. The signals are send to Readout Boards (ROD) placed in standard VME  
3211 crates and interfaced to the STAR DAQ. The electronics design and fabrication is done at  
3212 USTC, Hefei. The FEB prototype boards have been tested, the prototype RDO is under  
3213 construction, and the VMM3 chips are being procured. The design of the installation and  
3214 mounting frames need to be finished. The n-pentane gas system and Interlocks have been  
3215 designed and have been approved.

#### 3216 **4.2.5 Software**

3217 The trigger algorithms for the FCS have been well defined and simulated, the FPGA codes  
3218 are currently under development.

3219 The forward tracking utilizing hits from the 4 sTGC planes and 3 Si-layers has been de-  
3220 veloped and good performance has been demonstrated. As forward tracking is very different  
3221 than mid-rapidity tracking new tools had to be developed. The tracking algorithm is based  
3222 on modern techniques and depends on GENFIT, a general purpose tracking toolkit and in  
3223 addition the iLCSoft KiTrack a Cellular Automata library are used to seed track finding.

## References

- 3224
- 3225 [1] STAR, L. Adamczyk *et al.*, Phys. Rev. C **96**, 024905 (2017), 1702.01108.
- 3226 [2] STAR, R. Kunnawalkam Elayavalli, PoS **HardProbes2018**, 090 (2018), 1903.12115.
- 3227 [3] STAR, J. Adam *et al.*, Phys. Rev. D **101**, 052004 (2020), 1912.08187.
- 3228 [4] STAR, J. Adam *et al.*, Phys. Rev. C **102**, 014905 (2020), 1911.12168.
- 3229 [5] STAR, J. Adam *et al.*, (2019), 1906.09363.
- 3230 [6] STAR, J. Adam *et al.*, (2020), 2003.02114.
- 3231 [7] STAR, J. Adam *et al.*, (2020), 2006.00582.
- 3232 [8] STAR, J. Adam *et al.*, Phys. Rev. D **100**, 052005 (2019), 1906.02740.
- 3233 [9] STAR, R. Licenik, Measurement of inclusive jet production in Au+Au collisions at  
3234  $\sqrt{s_{NN}} = 200$  GeV by the STAR experiment, 2020, 2008.10006.
- 3235 [10] STAR, N. R. Sahoo, Measurement of  $\gamma$ +jet and  $\pi^0$ +jet in central Au+Au collisions  
3236 at  $\sqrt{s_{NN}} = 200$  GeV with the STAR experiment, 2020, 2008.08789.
- 3237 [11] T. Sjöstrand *et al.*, Comput. Phys. Commun. **191**, 159 (2015), 1410.3012.
- 3238 [12] ATLAS, M. Aaboud *et al.*, Phys. Rev. Lett. **123**, 042001 (2019), 1902.10007.
- 3239 [13] CMS, S. Chatrchyan *et al.*, Phys. Rev. C **90**, 024908 (2014), 1406.0932.
- 3240 [14] STAR, S. Oh, Measurement of semi-inclusive jet fragmentation functions in Au+Au  
3241 collisions at  $\sqrt{s_{NN}} = 200$  GeV in STAR, 2020, 2008.08631.
- 3242 [15] STAR, L. Adamczyk *et al.*, Phys. Rev. Lett. **119**, 062301 (2017), 1609.03878.
- 3243 [16] SN0619 : A Proposal for STAR Inner TPC Sector Upgrade (iTPC) [https://drupal.](https://drupal.star.bnl.gov/STAR/starnotes/public/sn0619)  
3244 [star.bnl.gov/STAR/starnotes/public/sn0619](https://drupal.star.bnl.gov/STAR/starnotes/public/sn0619).
- 3245 [17] STAR, CBM eTOF Group, The CBM Collaboration eTOF Group, (2016), 1609.05102.
- 3246 [18] J. Adams *et al.*, Nucl. Instrum. Meth. A **968**, 163970 (2020), 1912.05243.
- 3247 [19] STAR, J. Adam *et al.*, Phys. Rev. C **98**, 014910 (2018), 1805.04400.
- 3248 [20] STAR, L. Adamczyk *et al.*, Nature **548**, 62 (2017), 1701.06657.
- 3249 [21] W.-T. Deng and X.-G. Huang, Phys. Rev. C **93**, 064907 (2016), 1603.06117.

- 3250 [22] STAR, J. Adams, Differential measurements of  $\Lambda$  polarization in Au+Au  
3251 collisions and a search for the magnetic field by STAR, in *the XXVII-*  
3252 *Ith International Conference on Ultra-relativistic Nucleus-Nucleus Collisions*, 2019,  
3253 <https://indico.cern.ch/event/792436/contributions/3535689/>.
- 3254 [23] I. Karpenko and F. Becattini, *Eur. Phys. J. C* **77**, 213 (2017), 1610.04717.
- 3255 [24] Y. Jiang, Z.-W. Lin, and J. Liao, *Phys. Rev. C* **94**, 044910 (2016), 1602.06580, [Erra-  
3256 tum: *Phys.Rev.C* 95, 049904 (2017)].
- 3257 [25] K. Schilling, P. Seyboth, and G. E. Wolf, *Nucl. Phys. B* **15**, 397 (1970), [Erratum:  
3258 *Nucl.Phys.B* 18, 332 (1970)].
- 3259 [26] STAR, S. Singha, Measurement of global spin alignment of  $k^*0$ ,  $k^*\pm$   
3260 and  $\phi$  vector mesons using the STAR detector at RHIC, in *the XXVII-*  
3261 *Ith International Conference on Ultra-relativistic Nucleus-Nucleus Collisions*, 2019,  
3262 <https://indico.cern.ch/event/792436/contributions/3535685/>.
- 3263 [27] R. Bryan and B. Scott, *Phys. Rev.* **177**, 1435 (1969).
- 3264 [28] M. Nagels, T. Rijken, and J. de Swart, *Phys. Rev. D* **17**, 768 (1978).
- 3265 [29] STAR, L. Adamczyk *et al.*, *Phys. Rev. Lett.* **115**, 222301 (2015), 1505.07812.
- 3266 [30] STAR, S. Huang, Explore the nuclei deformation with a expanding  
3267 QGP fireball, in *The 36th Winter Workshop on Nuclear Dynamics*, 2020,  
3268 <https://indico.cern.ch/event/841247/contributions/3740391/>.
- 3269 [31] G. Giacalone, *Phys. Rev. Lett.* **124**, 202301 (2020), 1910.04673.
- 3270 [32] U. Heinz and R. Snellings, *Ann. Rev. Nucl. Part. Sci.* **63**, 123 (2013), 1301.2826.
- 3271 [33] STAR, J. Adam *et al.*, (2020), 2006.13537.
- 3272 [34] ALICE, S. Acharya *et al.*, *Phys. Lett.* **B773**, 68 (2017), 1705.04377.
- 3273 [35] P. Alba *et al.*, (2017), 1711.05207.
- 3274 [36] B. Schenke, C. Shen, and P. Tribedy, *Phys. Rev.* **C99**, 044908 (2019), 1901.04378.
- 3275 [37] H. Song, S. A. Bass, U. Heinz, T. Hirano, and C. Shen, *Phys. Rev. Lett.* **106**, 192301  
3276 (2011), 1011.2783, [Erratum: *Phys.Rev.Lett.* 109, 139904 (2012)].
- 3277 [38] D. Teaney and L. Yan, *Phys. Rev.* **C83**, 064904 (2011), 1010.1876.
- 3278 [39] Z. Qiu and U. W. Heinz, *Phys.Rev.* **C84**, 024911 (2011), 1104.0650.
- 3279 [40] G. Denicol, H. Niemi, E. Molnar, and D. Rischke, *Phys. Rev. D* **85**, 114047 (2012),  
3280 1202.4551, [Erratum: *Phys.Rev.D* 91, 039902 (2015)].

- 3281 [41] W. Florkowski, R. Ryblewski, and M. Spaliński, Phys. Rev. D **94**, 114025 (2016),  
3282 1608.07558.
- 3283 [42] K. Dusling and R. Venugopalan, Phys. Rev. Lett. **108**, 262001 (2012), 1201.2658.
- 3284 [43] PHENIX, C. Aidala *et al.*, Nature Phys. **15**, 214 (2019), 1805.02973.
- 3285 [44] CMS, S. Chatrchyan *et al.*, Phys. Lett. B **724**, 213 (2013), 1305.0609.
- 3286 [45] STAR, R. A. Lacey, Long-range collectivity in small collision-systems with two- and  
3287 four-particle correlations @ STAR, in *28th International Conference on Ultrarelativistic*  
3288 *Nucleus-Nucleus Collisions*, 2020, 2002.11889.
- 3289 [46] L. D. McLerran and T. Toimela, Phys. Rev. D **31**, 545 (1985).
- 3290 [47] H. Weldon, Phys. Rev. D **42**, 2384 (1990).
- 3291 [48] R. Rapp and J. Wambach, Eur. Phys. J. A **6**, 415 (1999), hep-ph/9907502.
- 3292 [49] P. M. Hohler and R. Rapp, Phys. Lett. B **731**, 103 (2014), 1311.2921.
- 3293 [50] C. Jung and L. von Smekal, Phys. Rev. D **100**, 116009 (2019), 1909.13712.
- 3294 [51] H.-T. Ding *et al.*, Phys. Rev. D **83**, 034504 (2011), 1012.4963.
- 3295 [52] J. Atchison and R. Rapp, J. Phys. Conf. Ser. **832**, 012057 (2017).
- 3296 [53] R. Rapp and H. van Hees, Phys. Lett. B **753**, 586 (2016), 1411.4612.
- 3297 [54] R. Chatterjee, D. K. Srivastava, U. W. Heinz, and C. Gale, Phys. Rev. C **75**, 054909  
3298 (2007), nucl-th/0702039.
- 3299 [55] J. Deng, Q. Wang, N. Xu, and P. Zhuang, Phys. Lett. B **701**, 581 (2011), 1009.3091.
- 3300 [56] P. Mohanty *et al.*, Phys. Rev. C **85**, 031903 (2012), 1111.2159.
- 3301 [57] E. Speranza, A. Jaiswal, and B. Friman, Phys. Lett. B **782**, 395 (2018), 1802.02479.
- 3302 [58] STAR, L. Adamczyk *et al.*, Phys. Rev. Lett. **113**, 022301 (2014), 1312.7397, [Adden-  
3303 dum: Phys.Rev.Lett. 113, 049903 (2014)].
- 3304 [59] STAR, L. Adamczyk *et al.*, Phys. Rev. C **92**, 024912 (2015), 1504.01317.
- 3305 [60] STAR, L. Adamczyk *et al.*, Phys. Lett. B **750**, 64 (2015), 1501.05341.
- 3306 [61] STAR, J. Adam *et al.*, (2018), 1810.10159.
- 3307 [62] B. B. Brandt, A. Francis, H. B. Meyer, and H. Wittig, JHEP **03**, 100 (2013), 1212.4200.
- 3308 [63] STAR, J. Adam *et al.*, (2019), 1910.12400.

- 3309 [64] G. Baur, Nucl. Phys. Proc. Suppl. **184**, 143 (2008), 0711.2882.
- 3310 [65] C. Li, J. Zhou, and Y.-J. Zhou, Phys. Rev. D **101**, 034015 (2020), 1911.00237.
- 3311 [66] S. Klein, A. Mueller, B.-W. Xiao, and F. Yuan, (2020), 2003.02947.
- 3312 [67] STAR Collaboration, J. Adam *et al.*, Phys. Rev. Lett. **124**, 172301 (2020).
- 3313 [68] J. Adam *et al.*, Physics Letters B **797**, 134917 (2019).
- 3314 [69] STAR Collaboration, J. Adam *et al.*, Phys. Rev. Lett. **123**, 162301 (2019).
- 3315 [70] STAR Collaboration, J. Adam *et al.*, Phys. Rev. C **99**, 034908 (2019).
- 3316 [71] M. Djordjevic, Phys. Rev. Lett. **112**, 042302 (2014).
- 3317 [72] H. van Hees, M. Mannarelli, V. Greco, and R. Rapp, Phys. Rev. Lett. **100**, 192301  
3318 (2008).
- 3319 [73] S. Cao, G.-Y. Qin, and S. A. Bass, Phys. Rev. C **92**, 024907 (2015).
- 3320 [74] P. B. Gossiaux and J. Aichelin, Phys. Rev. C **78**, 014904 (2008).
- 3321 [75] M. Djordjevic and M. Djordjevic, Phys. Rev. C **90**, 034910 (2014).
- 3322 [76] STAR Collaboration, L. Adamczyk *et al.*, Phys. Rev. Lett. **118**, 212301 (2017).
- 3323 [77] STAR Collaboration, L. Adamczyk *et al.*, Phys. Rev. C **95**, 034907 (2017).
- 3324 [78] D. Kharzeev and R. D. Pisarski, Phys.Rev. **D61**, 111901 (2000), hep-ph/9906401.
- 3325 [79] D. Kharzeev, Phys.Lett. **B633**, 260 (2006), hep-ph/0406125.
- 3326 [80] S. A. Voloshin, Phys. Rev. Lett. **105**, 172301 (2010), 1006.1020.
- 3327 [81] W.-T. Deng, X.-G. Huang, G.-L. Ma, and G. Wang, Phys. Rev. C **97**, 044901 (2018),  
3328 1802.02292.
- 3329 [82] H.-J. Xu *et al.*, Phys. Rev. Lett. **121**, 022301 (2018), 1710.03086.
- 3330 [83] J. Hammelmann, A. Soto-Ontoso, M. Alvioli, H. Elfner, and M. Strikman, (2019),  
3331 1908.10231.
- 3332 [84] STAR 2017 BUR [https://drupal.star.bnl.gov/STAR/system/files/STAR\\_BUR\\_](https://drupal.star.bnl.gov/STAR/system/files/STAR_BUR_Run1718_v22_0.pdf)  
3333 [Run1718\\_v22\\_0.pdf](https://drupal.star.bnl.gov/STAR/system/files/STAR_BUR_Run1718_v22_0.pdf).
- 3334 [85] STAR, J. Adam *et al.*, (2019), 1911.00596.
- 3335 [86] STAR, J. Zhao, (2020), 2002.09410.

- 3336 [87] CMS, A. M. Sirunyan *et al.*, Phys. Rev. **C97**, 044912 (2018), 1708.01602.
- 3337 [88] H.-j. Xu *et al.*, Chin. Phys. **C42**, 084103 (2018), 1710.07265.
- 3338 [89] S. A. Voloshin, Phys. Rev. **C98**, 054911 (2018), 1805.05300.
- 3339 [90] J. Zhao, H. Li, and F. Wang, Eur. Phys. J. C **79**, 168 (2019), 1705.05410.
- 3340 [91] STAR, J. Adam *et al.*, (2020), arXiv:2006.05035.
- 3341 [92] STAR, P. Tribedy, Nucl. Phys. A **967**, 740 (2017), 1704.03845.
- 3342 [93] STAR, J. Adam *et al.*, (2020), arXiv:2006.04251.
- 3343 [94] STAR, Y. Lin, (2020), 2002.11446.
- 3344 [95] N. Magdy, S. Shi, J. Liao, N. Ajitanand, and R. A. Lacey, Phys. Rev. C **97**, 061901  
3345 (2018), 1710.01717.
- 3346 [96] A. Tang, Chin. Phys. C **44**, 054101 (2020), 1903.04622.
- 3347 [97] L. Finch and S. Murray, Phys. Rev. C **96**, 044911 (2017), 1801.06476.
- 3348 [98] STAR, M. Zurek, Longitudinal double-spin asymmetries for inclusive jets produced  
3349 in  $\sqrt{s} = 200$  GeV proton-proton collisions at STAR, in *Nuclear Physics Seminar,*  
3350 *Brookhaven National Laboratory*, 2020, <https://indico.bnl.gov/event/8632/>.
- 3351 [99] STAR, N. Lukow, Longitudinal double-spin asymmetries for dijets pro-  
3352 duced in  $\sqrt{s} = 200$  GeV proton-proton collisions at STAR, 2020,  
3353 <https://drupal.star.bnl.gov/STAR/blog/nlukow/dijet-all-2015-preliminary>.
- 3354 [100] STAR, L. Adamczyk *et al.*, Phys. Rev. Lett. **115**, 092002 (2015), 1405.5134.
- 3355 [101] STAR, L. Adamczyk *et al.*, Phys. Rev. **D95**, 071103 (2017), 1610.06616.
- 3356 [102] D. de Florian, R. Sassot, M. Stratmann, and W. Vogelsang, Phys. Rev. Lett. **113**,  
3357 012001 (2014), 1404.4293.
- 3358 [103] NNPDF, E. R. Nocera, R. D. Ball, S. Forte, G. Ridolfi, and J. Rojo, Nucl. Phys.  
3359 **B887**, 276 (2014), 1406.5539.
- 3360 [104] J. Adam *et al.*, Physical Review D **100** (2019).
- 3361 [105] STAR, T. Lin, Azimuthal Transverse Single-Spin Asymmetries of Charged Pions  
3362 Within Jets from Polarized pp Collisions at  $\sqrt{s} = 200$  GeV, in *Nuclear Physics Semi-*  
3363 *nar, Brookhaven National Laboratory*, 2020, <https://indico.bnl.gov/event/8633/>.

- 3364 [106] STAR, H. Liu, Measurement of transverse single-spin asymmetries for dijet production  
3365 in polarized p+p collisions at  $\sqrt{s} = 200$  GeV at STAR, in *Nuclear Physics Seminar,*  
3366 *Brookhaven National Laboratory*, 2020, <https://indico.bnl.gov/event/8633/>.
- 3367 [107] STAR, S. Heppelmann, Preview from RHIC Run 15 pp and pAu Forward Neutral  
3368 Pion Production from Transversely Polarized Protons, in *7th International Workshop*  
3369 *on Multiple Partonic Interactions at the LHC*, pp. 228–231, 2016.
- 3370 [108] STAR, Z. Zhu, Measurement of transverse single spin asymmetries at forward rapidities  
3371 by the STAR experiment at  $\sqrt{s} = 200$  and 500 GeV at STAR, in *Nuclear Physics*  
3372 *Seminar, Brookhaven National Laboratory*, 2020, <https://indico.bnl.gov/event/8632/>.
- 3373 [109] Z.-B. Kang, X. Liu, F. Ringer, and H. Xing, *JHEP* **11**, 068 (2017), 1705.08443.
- 3374 [110] Z.-B. Kang, A. Prokudin, F. Ringer, and F. Yuan, *Phys. Lett. B* **774**, 635 (2017),  
3375 1707.00913.
- 3376 [111] U. D’Alesio, F. Murgia, and C. Pisano, *Phys. Rev. D* **83**, 034021 (2011), 1011.2692.
- 3377 [112] J. K. Adkins, *Studying Transverse Momentum Dependent Distributions in Polarized*  
3378 *Proton Collisions via Azimuthal Single Spin Asymmetries of Charged Pions in Jets*,  
3379 PhD thesis, University of Kentucky, 2015, 1907.11233.
- 3380 [113] STAR, B. Abelev *et al.*, *Phys. Rev. Lett.* **99**, 142003 (2007), 0705.4629.
- 3381 [114] J. Cammarota *et al.*, (2020), 2002.08384.
- 3382 [115] STAR, E. Braidot, Suppression of Forward Pion Correlations in d+Au Interactions  
3383 at STAR, in *45th Rencontres de Moriond on QCD and High Energy Interactions*, pp.  
3384 355–338, 2010, 1005.2378.
- 3385 [116] STAR, M. Posik, *PoS DIS2019*, 028 (2019), 1908.08490.
- 3386 [117] NuSea, R. S. Towell *et al.*, *Phys. Rev.* **D64**, 052002 (2001), hep-ex/0103030.
- 3387 [118] SeaQuest, K. Nagai, *PoS DIS2018*, 033 (2018).
- 3388 [119] STAR, S. Fazio, Measurements of weak boson production with the STAR detector,  
3389 in *QCD Spin Physics: A Symposium to Honor Jacques Soffer, Brookhaven National*  
3390 *Laboratory*, 2019, <https://indico.bnl.gov/event/6274/>.
- 3391 [120] V. Bertone, I. Scimemi, and A. Vladimirov, *JHEP* **06**, 028 (2019), 1902.08474.
- 3392 [121] M. A. Stephanov, K. Rajagopal, and E. V. Shuryak, *Phys. Rev. D* **60**, 114028 (1999),  
3393 hep-ph/9903292.
- 3394 [122] M. Stephanov, *Phys. Rev. Lett.* **107**, 052301 (2011), 1104.1627.

- 3395 [123] STAR, J. Adam *et al.*, (2020), 2001.02852.
- 3396 [124] HADES, J. Adamczewski-Musch *et al.*, (2020), 2002.08701.
- 3397 [125] B. Ling and M. A. Stephanov, Phys. Rev. C **93**, 034915 (2016), 1512.09125.
- 3398 [126] STAR, L. Adamczyk *et al.*, Phys. Rev. **C96**, 044904 (2017), 1701.07065.
- 3399 [127] F. Becattini, J. Manninen, and M. Gazdzicki, Phys. Rev. C **73**, 044905 (2006), hep-  
3400 ph/0511092.
- 3401 [128] A. Andronic, P. Braun-Munzinger, and J. Stachel, Phys. Lett. B **673**, 142 (2009),  
3402 0812.1186, [Erratum: Phys.Lett.B 678, 516 (2009)].
- 3403 [129] J. Cleymans, D. Elliott, A. Keranen, and E. Suhonen, Phys. Rev. C **57**, 3319 (1998),  
3404 nucl-th/9711066.
- 3405 [130] J. Cleymans, A. Forster, H. Oeschler, K. Redlich, and F. Uhlig, Phys. Lett. B **603**,  
3406 146 (2004), hep-ph/0406108.
- 3407 [131] I. Kraus, J. Cleymans, H. Oeschler, K. Redlich, and S. Wheaton, Phys. Rev. C **76**,  
3408 064903 (2007), 0707.3879.
- 3409 [132] HADES, J. Adamczewski-Musch *et al.*, Phys. Lett. B **778**, 403 (2018), 1703.08418.
- 3410 [133] FOPI, K. Piasecki *et al.*, Phys. Rev. C **94**, 014901 (2016), 1602.04378.
- 3411 [134] A. Andronic, P. Braun-Munzinger, J. Stachel, and H. Stocker, Phys. Lett. B **697**, 203  
3412 (2011), 1010.2995.
- 3413 [135] C. Shen and S. Alzhrani, Phys. Rev. C **102**, 014909 (2020), 2003.05852.
- 3414 [136] NA49, T. Anticic *et al.*, Phys. Rev. **C83**, 014901 (2011), 1009.1747.
- 3415 [137] BRAHMS, I. Arsene *et al.*, Phys. Rev. Lett. **93**, 242303 (2004), nucl-ex/0403005.
- 3416 [138] Yu. B. Ivanov, Phys. Rev. **C87**, 064905 (2013), 1304.1638.
- 3417 [139] K. Dusling, W. Li, and B. Schenke, Int. J. Mod. Phys. **E25**, 1630002 (2016),  
3418 1509.07939.
- 3419 [140] L. He *et al.*, Phys. Lett. **B753**, 506 (2016), 1502.05572.
- 3420 [141] A. Kurkela, U. A. Wiedemann, and B. Wu, Kinetic transport is needed to reliably ex-  
3421 tract shear viscosity from pA and AA data, in Vol. arXiv:1805.04081, 2018, 1805.04081.
- 3422 [142] P. Romatschke, Eur. Phys. J. **C78**, 636 (2018), 1802.06804.
- 3423 [143] J. L. Nagle and W. A. Zajc, Ann. Rev. Nucl. Part. Sci. **68**, 211 (2018), 1801.03477.

- 3424 [144] B. Schenke, S. Schlichting, and R. Venugopalan, Phys. Lett. **B747**, 76 (2015),  
3425 1502.01331.
- 3426 [145] J. L. Nagle *et al.*, Phys. Rev. Lett. **113**, 112301 (2014), 1312.4565.
- 3427 [146] PHENIX, A. Adare *et al.*, Phys. Rev. Lett. **111**, 212301 (2013), 1303.1794.
- 3428 [147] STAR, S. Huang, Nucl. Phys. A **982**, 475 (2019).
- 3429 [148] B. Schenke, C. Shen, and P. Tribedy, (2020), 2005.14682.
- 3430 [149] P. Romatschke, Eur. Phys. J. C **75**, 305 (2015), 1502.04745.
- 3431 [150] C. Shen, J.-F. Paquet, G. S. Denicol, S. Jeon, and C. Gale, Phys. Rev. C **95**, 014906  
3432 (2017), 1609.02590.
- 3433 [151] Workshop on collectivity of small systems in high-energy collisions, 14-16 march 2019,  
3434 <https://indico.cern.ch/event/771998/>, Accessed May 2019.
- 3435 [152] STAR, STAR Public Note SN0644 - Technical Design Report for the iTPC Upgrade,  
3436 <https://drupal.star.bnl.gov/STAR/starnotes/public/sn0644>.
- 3437 [153] STAR, STAR Public Note SN0666 - An Event Plane Detector for STAR, <https://drupal.star.bnl.gov/STAR/starnotes/public/sn0666>.  
3438
- 3439 [154] S. Huang, Z. Chen, J. Jia, and W. Li, Phys. Rev. C **101**, 021901 (2020), 1904.10415.
- 3440 [155] Z. Citron *et al.* *Report from Working Group 5: Future physics opportunities for high-*  
3441 *density QCD at the LHC with heavy-ion and proton beams* Vol. 7 (, 2019), pp. 1159–  
3442 1410, 1812.06772.
- 3443 [156] ALICE, K. Aamodt *et al.*, Phys. Rev. Lett. **105**, 252302 (2010), 1011.3914.
- 3444 [157] PHENIX, S. S. Adler *et al.*, Phys. Rev. Lett. **94**, 232302 (2005), nucl-ex/0411040.
- 3445 [158] STAR, J. Adam *et al.*, Phys. Lett. **B784**, 26 (2018), 1804.08647.
- 3446 [159] ATLAS, M. Aaboud *et al.*, Eur. Phys. J. **C78**, 997 (2018), 1808.03951.
- 3447 [160] PHENIX, A. Adare *et al.*, Phys. Rev. Lett. **107**, 252301 (2011), 1105.3928.
- 3448 [161] ATLAS, G. Aad *et al.*, Phys. Rev. C **90**, 044906 (2014), 1409.1792.
- 3449 [162] STAR, B. I. Abelev *et al.*, Phys. Rev. Lett. **99**, 112301 (2007), nucl-ex/0703033.
- 3450 [163] CMS Collaboration, Phys. Lett. B **765**, 193 (2017), 1606.06198.
- 3451 [164] CMS Collaboration, Phys. Rev. Lett. **115**, 012301 (2015), 1502.05382.

- 3452 [165] ATLAS, M. Aaboud *et al.*, Phys. Lett. **B789**, 444 (2019), 1807.02012.
- 3453 [166] ALICE, S. Acharya *et al.*, Investigations of anisotropic flow using multi-particle  
3454 azimuthal correlations in pp, p-Pb, Xe-Xe, and Pb-Pb collisions at the LHC,  
3455 arXiv:1903.01790, 2019, 1903.01790.
- 3456 [167] PHENIX, C. Aidala *et al.*, Phys. Rev. Lett. **120**, 062302 (2018), 1707.06108.
- 3457 [168] A. Huss *et al.*, (2020), 2007.13758.
- 3458 [169] A. Huss *et al.*, (2020), 2007.13754.
- 3459 [170] K. J. Sun, L.-W. Chen, C. M. Ko, J. Pu, and Z. Xu, Phys. Lett. **B781**, 499 (2018),  
3460 1801.09382.
- 3461 [171] STAR, L. Adamczyk *et al.*, Phys. Rev. Lett. **112**, 032302 (2014), 1309.5681.
- 3462 [172] STAR, L. Adamczyk *et al.*, Phys. Rev. Lett. **113**, 092301 (2014), 1402.1558.
- 3463 [173] STAR, L. Adamczyk *et al.*, Phys. Lett. **B785**, 551 (2018), 1709.00773.
- 3464 [174] STAR, X. Luo, PoS **CPOD2014**, 019 (2015), 1503.02558.
- 3465 [175] X. Luo, Nucl. Phys. **A956**, 75 (2016), 1512.09215.
- 3466 [176] A. Bzdak, V. Koch, D. Oliinychenko, and J. Steinheimer, Phys. Rev. **C98**, 054901  
3467 (2018), 1804.04463.
- 3468 [177] STAR, J. Adam *et al.*, accepted by PRC **arXiv:1903.11778** (2019), 1903.11778.
- 3469 [178] STAR, D. Zhang, Light Nuclei ( $d$ ,  $t$ ) Production in Au + Au Collisions at  $\sqrt{s_{NN}} =$   
3470 7.7 - 200 GeV, in *28th International Conference on Ultrarelativistic Nucleus-Nucleus*  
3471 *Collisions*, 2020, 2002.10677.
- 3472 [179] H. Liu *et al.*, Phys. Lett. B **805**, 135452 (2020), 1909.09304.
- 3473 [180] M. Danysz *et al.*, Phys. Rev. Lett. **11**, 29 (1963).
- 3474 [181] D. Prowse, Phys. Rev. Lett. **17**, 782 (1966).
- 3475 [182] S. Aoki *et al.*, Prog. Theor. Phys. **85**, 1287 (1991).
- 3476 [183] H. Takahashi *et al.*, Nucl. Phys. A **721**, 951 (2003).
- 3477 [184] T. A. Rijken, M. Nagels, and Y. Yamamoto, Prog. Theor. Phys. Suppl. **185**, 14 (2010).
- 3478 [185] I. Arsene *et al.*, Phys. Rev. C **75**, 034902 (2007), nucl-th/0609042.
- 3479 [186] J. Harris *et al.*, Phys. Lett. B **153**, 377 (1985).

- 3480 [187] R. Stock, Phys. Rept. **135**, 259 (1986).
- 3481 [188] J. Molitoris and H. Stoecker, Phys. Rev. C **32**, 346 (1985).
- 3482 [189] H. Kruse, B. Jacak, and H. Stoecker, Phys. Rev. Lett. **54**, 289 (1985).
- 3483 [190] P. Danielewicz, R. Lacey, and W. G. Lynch, Science **298**, 1592 (2002), nucl-th/0208016.
- 3484 [191] W. Reisdorf, Heavy ion collisions in the 1A GeV regime: how well do we join up to  
3485 astrophysics?, in *International Workshop on Nuclear Symmetry Energy and Reaction*  
3486 *Mechanisms*, 2013, 1307.4210.
- 3487 [192] J. Aichelin and C. M. Ko, Phys. Rev. Lett. **55**, 2661 (1985).
- 3488 [193] KAOS, C. T. Sturm *et al.*, Phys. Rev. Lett. **86**, 39 (2001), nucl-ex/0011001.
- 3489 [194] C. Hartnack and J. Aichelin, J. Phys. G **28**, 1649 (2002).
- 3490 [195] C. Fuchs *et al.*, J. Phys. G **28**, 1615 (2002), nucl-th/0103036.
- 3491 [196] T. Klahn *et al.*, Phys. Rev. C **74**, 035802 (2006), nucl-th/0602038.
- 3492 [197] T. Fischer *et al.*, Nature Astron. **2**, 980 (2018), 1712.08788.
- 3493 [198] A. Aprahamian *et al.*, Reaching for the horizon: The 2015 long range plan for  
3494 nuclear science, 2015, The 2015 Long Range Plan for Nuclear Science “Reach-  
3495 ing for the Horizon” [http://science.energy.gov/~media/np/nsac/pdf/2015LRP/](http://science.energy.gov/~media/np/nsac/pdf/2015LRP/2015_LRPNS_091815.pdf)  
3496 [2015\\_LRPNS\\_091815.pdf](http://science.energy.gov/~media/np/nsac/pdf/2015LRP/2015_LRPNS_091815.pdf).
- 3497 [199] RHIC luminosity projection [https://www.rhichome.bnl.gov//RHIC/Runs/](https://www.rhichome.bnl.gov//RHIC/Runs/RhicProjections.pdf)  
3498 [RhicProjections.pdf](https://www.rhichome.bnl.gov//RHIC/Runs/RhicProjections.pdf).
- 3499 [200] The STAR Forward Calorimeter System and Forward Tracking System beyond  
3500 BES-II [https://drupal.star.bnl.gov/STAR/files/Proposal.ForwardUpgrade.](https://drupal.star.bnl.gov/STAR/files/Proposal.ForwardUpgrade.Nov_.2018.Review.pdf)  
3501 [Nov\\_.2018.Review.pdf](https://drupal.star.bnl.gov/STAR/files/Proposal.ForwardUpgrade.Nov_.2018.Review.pdf).
- 3502 [201] G. Denicol, A. Monnai, and B. Schenke, Phys. Rev. Lett. **116**, 212301 (2016),  
3503 1512.01538.
- 3504 [202] H. Niemi, G. S. Denicol, P. Huovinen, E. Molnar, and D. H. Rischke, Phys. Rev. **C86**,  
3505 014909 (2012), 1203.2452.
- 3506 [203] B. Schenke and S. Schlichting, Phys. Rev. **C94**, 044907 (2016), 1605.07158.
- 3507 [204] W. Li, Nucl. Phys. A **967**, 59 (2017), 1704.03576.
- 3508 [205] P. Bozek, W. Broniowski, and J. Moreira, Phys. Rev. **C83**, 034911 (2011), 1011.3354.
- 3509 [206] J. Jia and P. Huo, Phys. Rev. **C90**, 034915 (2014), 1403.6077.

- 3510 [207] L.-G. Pang, H. Petersen, G.-Y. Qin, V. Roy, and X.-N. Wang, Eur. Phys. J. **A52**, 97  
3511 (2016), 1511.04131.
- 3512 [208] CMS, V. Khachatryan *et al.*, Phys. Rev. C **92**, 034911 (2015), 1503.01692.
- 3513 [209] ATLAS, M. Aaboud *et al.*, Eur. Phys. J. C **78**, 142 (2018), 1709.02301.
- 3514 [210] STAR Collaboration, L. Adamczyk *et al.*, Manuscript under preparation (2016).
- 3515 [211] A. Behera, M. Nie, and J. Jia, Phys. Rev. Res. **2**, 023362 (2020), 2003.04340.
- 3516 [212] C. Shen and B. Schenke, Phys. Rev. **C97**, 024907 (2018), 1710.00881.
- 3517 [213] STAR, B. Abelev *et al.*, Phys. Rev. C **76**, 064904 (2007), 0706.0472.
- 3518 [214] Z.-T. Liang, J. Song, I. Upsal, Q. Wang, and Z.-B. Xu, (2019), 1912.10223.
- 3519 [215] Y. Xie, D. Wang, and L. P. Csernai, Eur. Phys. J. C **80**, 39 (2020), 1907.00773.
- 3520 [216] X.-L. Sheng, L. Oliva, and Q. Wang, Phys. Rev. D **101**, 096005 (2020), 1910.13684.
- 3521 [217] X.-L. Sheng, Q. Wang, and X.-N. Wang, (2020), 2007.05106.
- 3522 [218] A. Bazavov *et al.*, Phys. Rev. D **95**, 054504 (2017), 1701.04325.
- 3523 [219] S. Borsanyi *et al.*, JHEP **10**, 205 (2018), 1805.04445.
- 3524 [220] STAR, A. Pandav, (2020), 2003.12503.
- 3525 [221] STAR, F. Seck, Measurements of dielectron production in Au+Au collisions at  $\sqrt{s_{NN}}$   
3526 = 27, 54.4 and 200 GeV with the STAR experiment, in *28th International Conference*  
3527 *on Ultrarelativistic Nucleus-Nucleus Collisions (Quark Matter 2019)*, 2019.
- 3528 [222] H. Xing, C. Zhang, J. Zhou, and Y.-J. Zhou, The  $\cos 2\phi$  azimuthal asymmetry in  $\rho^0$   
3529 meson production in ultraperipheral heavy ion collisions, 2020, 2006.06206.
- 3530 [223] STAR, J. the STAR Collaboration, Adam *et al.*, Phys. Rev. Lett. **123**, 132302 (2019),  
3531 1904.11658.
- 3532 [224] W. Zha *et al.*, Phys. Rev. C **97**, 044910 (2018).
- 3533 [225] M. B. G. Ducati and S. Martins, Phys. Rev. D **97**, 116013 (2018).
- 3534 [226] W. Shi, W. Zha, and B. Chen, Phys. Lett. B **777**, 399 (2018), 1710.00332.
- 3535 [227] B. Chen, M. Hu, H. Zhang, and J. Zhao, Phys. Lett. B **802**, 135271 (2020), 1910.08275.
- 3536 [228] X. Guo, S. Shi, N. Xu, Z. Xu, and P. Zhuang, Phys. Lett. B **751**, 215 (2015),  
3537 1502.04407.

- 3538 [229] B. Chen, X. Du, and R. Rapp, Nucl. Part. Phys. Proc. **289-290**, 475 (2017),  
3539 1612.02089.
- 3540 [230] ALICE, J. Adam *et al.*, JHEP **05**, 179 (2016), 1506.08804.
- 3541 [231] ATLAS, M. Aaboud *et al.*, Eur. Phys. J. C **78**, 762 (2018), 1805.04077.
- 3542 [232] CMS, A. M. Sirunyan *et al.*, Phys. Rev. Lett. **118**, 162301 (2017), 1611.01438.
- 3543 [233] JETSCAPE, S. Cao *et al.*, Phys. Rev. C **96**, 024909 (2017), 1705.00050.
- 3544 [234] JETSCAPE, A. Kumar *et al.*, Jet quenching in a multi-stage Monte Carlo approach,  
3545 in *28th International Conference on Ultrarelativistic Nucleus-Nucleus Collisions*, 2020,  
3546 2002.07124.
- 3547 [235] Y. Mehtar-Tani and K. Tywoniuk, Phys. Rev. D **98**, 051501 (2018), 1707.07361.
- 3548 [236] Y. Mehtar-Tani and K. Tywoniuk, Nucl. Phys. A **979**, 165 (2018), 1706.06047.
- 3549 [237] B. Zakharov, (2020), 2003.10182.
- 3550 [238] L. Chen, G.-Y. Qin, S.-Y. Wei, B.-W. Xiao, and H.-Z. Zhang, Phys. Lett. B **773**, 672  
3551 (2017), 1607.01932.
- 3552 [239] D. A. Appel, Phys. Rev. D **33**, 717 (1986).
- 3553 [240] J. Blaizot and L. D. McLerran, Phys. Rev. D **34**, 2739 (1986).
- 3554 [241] ALICE, J. Adam *et al.*, JHEP **09**, 170 (2015), 1506.03984.
- 3555 [242] F. D’Eramo, K. Rajagopal, and Y. Yin, JHEP **01**, 172 (2019), 1808.03250.
- 3556 [243] ALICE, J. Norman.
- 3557 [244] A. J. Larkoski, S. Marzani, G. Soyez, and J. Thaler, JHEP **05**, 146 (2014), 1402.2657.
- 3558 [245] Y.-T. Chien and R. Kunnawalkam Elayavalli, (2018), 1803.03589.
- 3559 [246] J. Blaizot and Y. Mehtar-Tani, p. 217 (2016).
- 3560 [247] J.-w. Qiu and G. F. Sterman, Phys. Rev. D **59**, 014004 (1999), hep-ph/9806356.
- 3561 [248] K. Kanazawa, Y. Koike, A. Metz, and D. Pitonyak, Phys. Rev. D **89**, 111501 (2014).
- 3562 [249] L. Bland *et al.*, Physics Letters B **750**, 660 (2015).
- 3563 [250] Z.-B. Kang and J.-W. Qiu, Phys. Rev. Lett. **103**, 172001 (2009).
- 3564 [251] P. Sun, J. Isaacson, C. P. Yuan, and F. Yuan, Universal non-perturbative functions  
3565 for sidis and drell-yan processes, 2014, 1406.3073.

- 3566 [252] J. P. Ralston and D. E. Soper, Nuclear Physics B **152**, 109 (1979).
- 3567 [253] R. Jaffe and X.-D. Ji, Nucl. Phys. B **375**, 527 (1992).
- 3568 [254] P. Mulders and R. Tangerman, Nucl. Phys. B **461**, 197 (1996), hep-ph/9510301,  
3569 [Erratum: Nucl.Phys.B 484, 538–540 (1997)].
- 3570 [255] D. Sivers, Nuovo Cim. C **035N2**, 171 (2012), 1109.2521.
- 3571 [256] C. Alexandrou *et al.*, Phys. Rev. D **98**, 091503 (2018).
- 3572 [257] R. Jaffe and X.-D. Ji, Phys. Rev. Lett. **67**, 552 (1991).
- 3573 [258] J. C. Collins, S. F. Heppelmann, and G. A. Ladinsky, Nucl. Phys. B **420**, 565 (1994),  
3574 hep-ph/9305309.
- 3575 [259] L. Adamczyk *et al.*, Phys. Lett. B **780**, 332–339 (2018).
- 3576 [260] M. Radici and A. Bacchetta, Phys. Rev. Lett. **120**, 192001 (2018), 1802.05212.
- 3577 [261] J. Collins and J.-W. Qiu, Phys. Rev. D **75**, 114014 (2007).
- 3578 [262] T. C. Rogers and P. J. Mulders, Phys. Rev. D **81**, 094006 (2010).
- 3579 [263] X. Liu, F. Ringer, W. Vogelsang, and F. Yuan, Factorization and its breaking in dijet  
3580 single transverse spin asymmetries in  $pp$  collisions, 2020, 2008.03666.
- 3581 [264] Z.-B. Kang, K. Lee, D. Y. Shao, and J. Terry, The sivers asymmetry in hadronic dijet  
3582 production, 2020, 2008.05470.
- 3583 [265] F. Yuan, Phys. Rev. Lett. **100**, 032003 (2008).
- 3584 [266] F. Yuan, Phys. Rev. D **77**, 074019 (2008).
- 3585 [267] STAR, L. Adamczyk *et al.*, Phys. Rev. D **97**, 032004 (2018), 1708.07080.
- 3586 [268] M. Anselmino *et al.*, Phys. Rev. D **73**, 014020 (2006), hep-ph/0509035.
- 3587 [269] M. Anselmino *et al.*, Phys. Rev. D **75**, 054032 (2007).
- 3588 [270] J. Soffer, Phys. Rev. Lett. **74**, 1292 (1995).
- 3589 [271] U. D’Alesio, F. Murgia, and C. Pisano, Phys. Lett. B **773**, 300–306 (2017).
- 3590 [272] H1, ZEUS, F. Aaron *et al.*, Eur. Phys. J. C **72**, 2175 (2012), 1207.4864.
- 3591 [273] CMS, V. Khachatryan *et al.*, Phys. Rev. D **92**, 012003 (2015), 1503.08689.
- 3592 [274] S. L. Bultmann *et al.*, Phys. Lett. B **579**, 245 (2004), nucl-ex/0305012.

- 3593 [275] S. Bultmann *et al.*, Phys. Lett. B **632**, 167 (2006), nucl-ex/0507030.
- 3594 [276] pp2pp, S. Bultmann *et al.*, Phys. Lett. B **647**, 98 (2007), nucl-ex/0610022.
- 3595 [277] STAR, L. Adamczyk *et al.*, Phys. Lett. B **719**, 62 (2013), 1206.1928.
- 3596 [278] I. Helenius, in *Talk at 7th International Workshop*  
 3597 *shop on Multiple Partonic Interactions at the LHC*,  
 3598 <http://indico.ictp.it/event/a14280/session/266/contribution/1042/material/slides/0.pdf>.
- 3599 [279] STAR, C. Dilks, PoS **DIS2016**, 212 (2016), 1805.08875.
- 3600 [280] A. Airapetian *et al.*, Phys. Lett. B **693**, 11–16 (2010).
- 3601 [281] C. Adolph *et al.*, Phys. Lett. B **744**, 250–259 (2015).
- 3602 [282] D. Müller, D. Robaschik, B. Geyer, F.-M. Dittes, and J. Hořejši, Fortsch. Phys. **42**,  
 3603 101 (1994), hep-ph/9812448.
- 3604 [283] X.-D. Ji, Phys. Rev. Lett. **78**, 610 (1997), hep-ph/9603249.
- 3605 [284] A. Radyushkin, Phys. Lett. B **380**, 417 (1996), hep-ph/9604317.
- 3606 [285] M. Burkardt, Phys. Rev. D **62**, 071503 (2000), hep-ph/0005108, [Erratum: Phys.Rev.D  
 3607 66, 119903 (2002)].
- 3608 [286] S. Klein and J. Nystrand, Photoproduction of J / psi and Upsilon in pp and anti-p p  
 3609 collisions, in *5th Workshop on Small x and Diffractive Physics*, 2003, hep-ph/0310223.
- 3610 [287] S. R. Klein, J. Nystrand, J. Seger, Y. Gorbunov, and J. Butterworth, Comput. Phys.  
 3611 Commun. **212**, 258 (2017), 1607.03838.
- 3612 [288] J. Lansberg, L. Massacrier, L. Szymanowski, and J. Wagner, Phys. Lett. B **793**, 33  
 3613 (2019), 1812.04553.
- 3614 [289] HERMES, A. Airapetian *et al.*, Phys. Lett. B **577**, 37 (2003), hep-ex/0307023.
- 3615 [290] HERMES, A. Airapetian *et al.*, Nucl. Phys. B **780**, 1 (2007), 0704.3270.
- 3616 [291] HERMES, A. Airapetian *et al.*, Phys. Lett. B **684**, 114 (2010), 0906.2478.
- 3617 [292] W. Brooks and H. Hakobyan, Nucl. Phys. A **830**, 361C (2009), 0907.4606.
- 3618 [293] NuSea, M. Vasilev *et al.*, Phys. Rev. Lett. **83**, 2304 (1999), hep-ex/9906010.
- 3619 [294] DIS–2014 [https://indico.cern.ch/event/258017/contributions/1588381/  
 3620 attachments/453934/629277/pA\\_DIS2014\\_Paukkunen.pdf](https://indico.cern.ch/event/258017/contributions/1588381/attachments/453934/629277/pA_DIS2014_Paukkunen.pdf).

- 3621 [295] D. de Florian, R. Sassot, P. Zurita, and M. Stratmann, Phys. Rev. D **85**, 074028  
3622 (2012), 1112.6324.
- 3623 [296] PHENIX, S. Adler *et al.*, Phys. Rev. Lett. **98**, 172302 (2007), nucl-ex/0610036.
- 3624 [297] K. Eskola, H. Paukkunen, and C. Salgado, Nucl. Phys. A **855**, 150 (2011), 1011.6534.
- 3625 [298] R. Sassot, M. Stratmann, and P. Zurita, Phys. Rev. D **81**, 054001 (2010), 0912.1311.
- 3626 [299] K. J. Eskola, P. Paakkinen, H. Paukkunen, and C. A. Salgado, Eur. Phys. J. C **77**,  
3627 163 (2017), 1612.05741.
- 3628 [300] N. Armesto, H. Paukkunen, J. M. Penín, C. A. Salgado, and P. Zurita, Eur. Phys. J.  
3629 C **76**, 218 (2016), 1512.01528.
- 3630 [301] H. Paukkunen and P. Zurita, JHEP **12**, 100 (2014), 1402.6623.
- 3631 [302] E. Aschenauer *et al.*, (2014), 1409.1633.
- 3632 [303] H. Paukkunen, K. J. Eskola, and C. Salgado, Nucl. Phys. A **931**, 331 (2014), 1408.4563.
- 3633 [304] K. J. Eskola, H. Paukkunen, and C. A. Salgado, JHEP **10**, 213 (2013), 1308.6733.
- 3634 [305] L. Gribov, E. Levin, and M. Ryskin, Phys. Rept. **100**, 1 (1983).
- 3635 [306] E. Iancu and R. Venugopalan, The Color glass condensate and high-energy scattering  
3636 in QCD, in *In \*Hwa, R.C. (ed.) et al.: Quark gluon plasma\* 249-3363*, 2003, hep-  
3637 ph/0303204.
- 3638 [307] H. Weigert, Prog. Part. Nucl. Phys. **55**, 461 (2005), hep-ph/0501087.
- 3639 [308] J. Jalilian-Marian and Y. V. Kovchegov, Prog. Part. Nucl. Phys. **56**, 104 (2006),  
3640 hep-ph/0505052.
- 3641 [309] F. Gelis, E. Iancu, J. Jalilian-Marian, and R. Venugopalan, Ann. Rev. Nucl. Part. Sci.  
3642 **60**, 463 (2010), 1002.0333.
- 3643 [310] G. Giuliani, H. Zheng, and A. Bonasera, Prog. Part. Nucl. Phys. **76**, 116 (2014),  
3644 1311.1811.
- 3645 [311] Y. V. Kovchegov and E. Levin *Quantum chromodynamics at high energy* Vol. 33 (Cam-  
3646 bridge University Press, 2012).
- 3647 [312] A. H. Mueller and J.-w. Qiu, Nucl. Phys. B **268**, 427 (1986).
- 3648 [313] L. McLerran and R. Venugopalan, Phys. Rev. D **49**, 2233 (1994).
- 3649 [314] L. McLerran and R. Venugopalan, Phys. Rev. D **49**, 3352 (1994).

- 3650 [315] L. McLerran and R. Venugopalan, Phys. Rev. D **50**, 2225 (1994).
- 3651 [316] Y. V. Kovchegov, Phys. Rev. D **54**, 5463 (1996).
- 3652 [317] Y. V. Kovchegov, Phys. Rev. D **55**, 5445 (1997).
- 3653 [318] J. Jalilian-Marian, A. Kovner, L. McLerran, and H. Weigert, Phys. Rev. D **55**, 5414  
3654 (1997).
- 3655 [319] A. H. Mueller, Nucl. Phys. **B415**, 373 (1994).
- 3656 [320] A. H. Mueller and B. Patel, Nucl. Phys. B **425**, 471 (1994), hep-ph/9403256.
- 3657 [321] I. Balitsky, Nucl. Phys. **B463**, 99 (1996), hep-ph/9509348.
- 3658 [322] I. Balitsky, Phys. Rev. D **60**, 014020 (1999), hep-ph/9812311.
- 3659 [323] Y. V. Kovchegov, Phys. Rev. **D60**, 034008 (1999), hep-ph/9901281.
- 3660 [324] Y. V. Kovchegov, Phys. Rev. D **61**, 074018 (2000), hep-ph/9905214.
- 3661 [325] J. Jalilian-Marian, A. Kovner, and H. Weigert, Phys. Rev. D **59**, 014015 (1998),  
3662 hep-ph/9709432.
- 3663 [326] J. Jalilian-Marian, A. Kovner, A. Leonidov, and H. Weigert, Phys. Rev. D **59**, 014014  
3664 (1998), hep-ph/9706377.
- 3665 [327] E. Iancu, A. Leonidov, and L. D. McLerran, Phys. Lett. B **510**, 133 (2001), hep-  
3666 ph/0102009.
- 3667 [328] E. Iancu, A. Leonidov, and L. D. McLerran, Nucl. Phys. **A692**, 583 (2001), hep-  
3668 ph/0011241.
- 3669 [329] A. Accardi *et al.*, Eur. Phys. J. A **52**, 268 (2016), 1212.1701.
- 3670 [330] Y. V. Kovchegov and M. D. Sievert, Nucl. Phys. B **903**, 164 (2016), 1505.01176.
- 3671 [331] CMS, S. Chatrchyan *et al.*, Eur. Phys. J. C **74**, 2951 (2014), 1401.4433.
- 3672 [332] STAR, E. Braidot, Nucl. Phys. A **854**, 168 (2011), 1008.3989.
- 3673 [333] PHENIX, A. Adare *et al.*, Phys. Rev. Lett. **107**, 172301 (2011), 1105.5112.
- 3674 [334] C. Marquet, Nucl. Phys. A **796**, 41 (2007), 0708.0231.
- 3675 [335] J. L. Albacete and C. Marquet, Phys. Rev. Lett. **105**, 162301 (2010), 1005.4065.
- 3676 [336] Z.-B. Kang, I. Vitev, and H. Xing, Phys. Rev. D **85**, 054024 (2012), 1112.6021.
- 3677 [337] M. Strikman and W. Vogelsang, Phys. Rev. D **83**, 034029 (2011), 1009.6123.

- 3678 [338] J. Jalilian-Marian and A. H. Rezaeian, Phys. Rev. D **86**, 034016 (2012), 1204.1319.
- 3679 [339] J. L. Albacete and C. Marquet, Nucl. Phys. A **854**, 154 (2011), 1009.3215.
- 3680 [340] K. J. Eskola, H. Paukkunen, and C. A. Salgado, JHEP **07**, 102 (2008), 0802.0139.
- 3681 [341] A. H. Rezaeian, Phys. Rev. D **86**, 094016 (2012), 1209.0478.
- 3682 [342] T. Sjostrand, S. Mrenna, and P. Z. Skands, Comput. Phys. Commun. **178**, 852 (2008),  
3683 0710.3820.
- 3684 [343] Di-jet production from pythia8.189 is scaled down due to its overestimation of inclusive  
3685  $\pi_0$  yields compared to those reported by BRAHMS in phys. rev. lett. 98 (2007) 252001  
3686 and STAR in phys. rev. lett. 97 (2006) 152302.
- 3687 [344] T. Kaufmann, A. Mukherjee, and W. Vogelsang, Phys. Rev. D **92**, 054015 (2015),  
3688 1506.01415, [Erratum: Phys.Rev.D 101, 079901 (2020)].
- 3689 [345] D. de Florian, R. Sassot, M. Epele, R. J. Hernández-Pinto, and M. Stratmann, Phys.  
3690 Rev. D **91**, 014035 (2015), 1410.6027.
- 3691 [346] A. Khouaja *et al.*, Nucl. Phys. A **780**, 1 (2006).
- 3692 [347] D. de Florian and R. Sassot, Phys. Rev. D **69**, 074028 (2004), hep-ph/0311227.
- 3693 [348] D. de Florian, R. Sassot, and M. Stratmann, Phys. Rev. D **75**, 114010 (2007), hep-  
3694 ph/0703242.
- 3695 [349] D. de Florian, R. Sassot, and M. Stratmann, Phys. Rev. D **76**, 074033 (2007),  
3696 0707.1506.
- 3697 [350] V. Smakhtin *et al.*, Nucl. Instrum. Meth. **A598**, 196 (2009).
- 3698 [351] A. Abusleme *et al.*, Nucl. Instrum. Meth. **A817**, 85 (2016), 1509.06329.
- 3699 [352] Iakovidis, George, EPJ Web Conf. **174**, 07001 (2018).